Department of Physics
Indian Institute of Technology Guwahati
Ph.D. Thesis

Study of Magnetocaloric Effect in Off-stoichiometric Ni-Mn-Sb Heusler Compounds by Density Functional Theory and Monte Carlo Methods

Sheuly Ghosh

Supervisor: Prof. Subhradip Ghosh
October, 2020.

Study of Magnetocaloric Effect in Off-stoichiometric Ni-Mn-Sb Heusler Compounds by Density Functional Theory and Monte Carlo Methods

A thesis submitted by

Sheuly Ghosh

to

Indian Institute of Technology Guwahati
in partial fulfillment of the requirements
for the award of the degree of
Doctor of Philosophy in Physics

Department of Physics
Indian Institute of Technology Guwahati
Guwahati - 781039, Assam, India

Statement

The work contained in the thesis entitled "*Study of Magnetocaloric Effect in Off-stoichiometric Ni-Mn-Sb Heusler Compounds by Density Functional Theory and Monte Carlo Methods*" has been carried out at the Department of Physics, Indian Institute of Technology Guwahati, India by me under the supervision of Prof. Subhradip Ghosh. The material of this thesis has not been submitted elsewhere for any other degree. Works presented in the thesis are all my own unless referenced to the contrary in the text.

(Sheuly Ghosh) Date:
Roll No. - 156121017
Department of Physics
Indian Institute of Technology Guwahati
Guwahati - 781039, India

Disclaimer

The bibliography included in this thesis is, by no means complete but contains the ones which are consulted thoroughly by me. I apologize for inadvertently missing out some of the research papers, review articles and other scientific documents pertaining to the focus of this thesis which should also have been cited. For illustration purpose some of the figures in this thesis are taken from other sources and properly cited.

Certificate

It is certified that the work contained in the thesis entitled "*Study of Magnetocaloric Effect in Off-stoichiometric Ni-Mn-Sb Heusler Compounds by Density Functional Theory and Monte Carlo Methods*" by Ms. Sheuly Ghosh, a Ph.D. student of the Department of Physics, Indian Institute of Technology Guwahati is carried out under my supervision and has not been submitted elsewhere for the award of any other degree.

(Prof. Subhradip Ghosh)
Department of Physics
Indian Institute of Technology Guwahati
Guwahati - 781039, India

Date:

Dedicated to

my parents, my uncle and my brother

Acknowledgement

Foremost, I would like to express my sincere gratitude to my thesis supervisor Prof. Subhradip Ghosh, who expertly guided me as a tremendous mentor. His patience, motivation, and immense knowledge helped me in all the time of research and writing this thesis. I heartily thank him for allowing me to grow as a research scientist.

I would like to acknowledge my doctoral committee members - Prof. Perumal Alagarsamy, Prof. P. K. Padmanabhan, Prof. Gopal Das, for their useful suggestions during the yearly assessments of my research work. I would like to thank Dr. Biplab Sanyal at Uppsala University for fruitful discussions and suggestions. I thank to all HODs (Prof. Poulose Poulose and Prof. Subhradip Ghosh) during my Ph.D. I would like to thank all the technical assistants, the department's academic and non-academic staff, who helped me in various ways during my research period. I am also thankful to Param Ishan, IIT Guwahati, for the supercomputer facility. I thank the Department of Physics, IIT Guwahati, India, for allowing me to utilize the Newton cluster, funded under the FIST program by DST, India.

I would like to thank my senior group members, Dr. Debashish Das, Dr. Ashis Kundu and Dr. Srikrishna Ghosh, and my junior group member Mandira Das. My special thank goes to Dr. Ashis Kundu for his continuous support to familiarize me with different electronic structure packages. His constant encouragement to think and learn things independently is broadly acknowledged. I want to thank Kartik-da for always giving many suggestions, inspiration, and motivation for working hard.

I am fortunate enough to have a great friend circle, seniors, and juniors, who made the whole journey of my Ph.D. dynamic and full of life. I would like to thank Sourav-da, Kallol-da, Rishav, Shilpi, Sreemanti. I thank all my labmates for making the lab environment workable as well as sometimes relaxing also. I am fortunate to have my friends like Priya, Ruma, and Srijita to be like another family in IIT Campus far away from home. I had a lot of great moments with them, which I will never forget. I would like to thank my batchmates Krishnakanta, Anirban, Sneha, Susmita, Sunil, Joydeep.

I want to express the heartiest gratitude to an important person, Aparna Pisi, who was always present as a surprise savior in most crucial times of my life. Without her initiatives, I might not be allowed to pursue my higher education coming out of my little town.

Most importantly, I would like to thank my parents from the deepest heart, who always support me in every phase of my life. I heartily thank my uncle, who is always beside me, guided my education since my childhood, and always hear me in every problem I express. One most important person is my brother, an all-time friend in any situation. I heartily thank my husband, Dr. Ashis Kundu, who always supports me in every situation and motivates to work hard and makes me realize to handle difficult situations more practically. I must thank all of my other family members for always expressing positive vibes towards me with their unconditional love. I owe everything to them.

Abstract

Solid-state cooling or heating using magnetocaloric materials has emerged as an energy efficient green technology. The magnetocaloric effect (MCE) describes the thermal response of a magnetic material due to the application of a magnetic field which is quantified by isothermal magnetic entropy change (ΔS_{mag}) and the adiabatic temperature change (ΔT_{ad}). An extended search of new magnetocaloric materials exhibiting giant MCE, in an appropriate temperature range, as well as improving performances of the existing ones, is an active area of current research. Among different types of magnetocaloric materials, Ni-Mn based magnetic shape memory Heusler alloys are of great interest since they exhibit giant MCE associated with the first-order magneto-structural transition. In this thesis, we have investigated the Ni-Mn-Sb based Heusler systems where significant magnetocaloric effects are observed near room temperature. Our investigation focused on off-stoichiometric Ni-Mn-Sb and Fe, Co and Cu substituted Mn-excess Ni-Mn-Sb compounds. We investigated the impact of various factors, such as composition, site occupancy, magnetic structure, magnetic interactions on structural phase stability, transition temperatures, mechanical properties, and consequently the magnetocaloric parameters of compounds in Ni-Mn-Sb family. We have done first-principles Density Functional Theory (DFT) calculations in conjunction with Monte Carlo simulation method using model Hamiltonians which incorporated the magnetic, structural and magneto-structural degrees of freedom. We have developed a Monte Carlo simulation code and used the Heisenberg model, the BEG model and the q-state Potts model for computations of magnetocaloric parameters near a first-order magneto-structural transition and a second-order magnetic transition in substitutional Ni-Mn-Sb compounds. Our calculations reproduced the experimental results on systems where experiments were done and also predicted a few new compounds in the family that can exhibit significantly large magnetocaloric effect, near room temperature. In essence, the results presented in this thesis on Ni-Mn-Sb based Heusler compounds, on one hand, provides a protocol for identifying materials potentially useful for magnetocaloric applications, using results of DFT calculations and on the other hand, quantifies the magnetocaloric effects in those materials, thus paving ways for experimentalists to design new magnetocaloric materials.

Contents

Acknowledgement **xi**

Abstract **xii**

1 Introduction **1**

1.1 Thermodynamics of caloric effect 2

1.2 Magnetocaloric effect and its quantification 4

1.3 Historical origin of MCE 6

1.4 Applications 6

1.4.1 Magnetic refrigeration 7

1.4.2 Bio-medical applications 9

1.5 Phase transitions and maximum magnetocaloric effect 9

1.6 Criteria for promising magnetocaloric materials 12

1.7 Materials for magnetocaloric applications: status of the research . . . 13

1.7.1 Structure of Heusler compounds 16

1.7.2 Magnetic shape memory property 17

1.7.3 Results on MCE in Ni-Mn based Heusler alloys 19

1.7.3.1 Ni-Mn-Ga compounds 19

1.7.3.2 Ni-Mn-In compounds 21

1.7.3.3 Ni-Mn-Sn compounds 22

1.7.3.4 Ni-Mn-Sb compounds 23

1.7.4 Importance of Ni-Mn-Sb series 24

1.8 Importance of combined first-principles electronic structure calculations and Monte Carlo simulation based studies for investigation of MCE 26

1.9 Outline of the thesis 27

2 Methodology **33**
2.1 Density Functional Theory 33
2.1.1 The many-body Hamiltonian 34
2.1.2 The Born-Oppenheimer approximation 35
2.1.3 Hartree and Hartree-Fock Methods 35
2.1.4 The philosophy of DFT 36
2.1.4.1 Hohenberg-Kohn theorems 37
2.1.4.2 The Kohn-Sham ansatz 37
2.1.4.3 Approximations for the exchange-correlation energy functional 39
2.1.5 Methods implementing DFT for electronic structure calculations 40
2.1.5.1 Projector Augmented Wave (PAW) method 40
2.1.5.2 Korringa, Kohn and Rostoker (KKR) Green's Function method 44
2.1.5.3 Coherent Potential Approximation (CPA) 48
2.1.6 Calculation of physical quantities 49
2.1.6.1 Calculation of Elastic moduli 49
Bulk Modulus: 49
Elastic Constants: 50
2.1.6.2 Calculation of the magnetic exchange interactions . . 52
2.2 Monte Carlo Simulation (MCS) Method 53
2.2.1 Markov process 55
2.2.2 Metropolis algorithm 55
2.2.3 Calculation of Curie temperature (T_c) 56
2.2.4 Calculation of Magnetocaloric parameters 57
2.3 Summary 62

3 Role of composition, site ordering and magnetic structure for structural stability in Ni and Mn excess off-stoichiometric Ni_2MnSb **63**
3.1 Introduction 63
3.2 Computational Details 66
3.3 Results and Discussions 66
3.3.1 Site preference and magnetic ground state 66
3.3.2 Structural parameters and magnetic moments 72
3.3.3 Composition dependent structural phase stability 73

3.3.4 Dependence of phase stability on site-occupancy and magnetic structure . . . 75
3.3.5 Electronic structure . . . 78
3.3.6 Elastic properties and predictor of T_M . . . 80
3.4 Summary and Conclusions . . . 84

4 Understanding the origin of the magnetocaloric effects in substitutional Ni-Mn-Sb-Z (Z=Fe, Co, Cu) compounds 85
4.1 Introduction . . . 85
4.2 Computational Details . . . 87
4.3 Results and Discussions . . . 88
4.3.1 Site preferences and magnetic ground states in austenite phases 89
4.3.2 Magnetic moments in the austenite phases . . . 91
4.3.3 Structural phase transition and associated change in magnetic structure . . . 93
4.3.4 Magnetic exchange interactions . . . 96
4.3.5 Mechanical properties . . . 102
4.3.6 Variation in T_M and T_c^A . . . 104
4.3.7 Resolving discrepancy between theory and experiment for $Ni_2Mn_{1.52-y}Fe_ySb_{0.48}$: possible role of site occupancy . . . 108
4.4 Conclusions . . . 110

5 Cosubstitution in Ni-Mn-Sb Heusler compounds: realization of room temperature reversible magnetocaloric effect driven by second-order magnetic transition 113
5.1 Introduction . . . 113
5.2 Computational Details . . . 115
5.3 Results and Discussions . . . 117
5.3.1 Selection of compounds with potential to exhibit large MCE . 118
5.3.2 Quantification of parameters important for MCE: calculations of Curie temperature by MCS method (T_c^{MCS}) and changes in magnetic entropy (ΔS_{mag}) . . . 123
5.3.3 Analysis of structural phase stability from electronic structures 124
5.3.4 Understanding magnetic properties from effective exchange interactions . . . 126
5.4 Conclusions . . . 130

6 Giant magnetocaloric effect driven by first-order magneto-structural transition in cosubstituted Ni-Mn-Sb Heusler compounds **131**
6.1 Introduction . . . 131
6.2 Computational Details . . . 132
6.3 Results and Discussions . . . 134
6.3.1 Magnetic moment in austenite phase . . . 135
6.3.2 Martensitic transformation and magnetic structures across structural phases . . . 137
6.3.3 Curie temperature in austenite phase . . . 140
6.3.4 Prediction of new compounds . . . 141
6.3.5 Computation of the MCE parameters . . . 143
6.4 Conclusions . . . 150

7 Conclusions and scopes for future work **153**
7.1 Conclusions . . . 153
7.2 Scopes for future work . . . 156

Appendix **157**

A Benchmarking the In-house Monte Carlo Code **157**
A.1 Calculation of second order magnetic transition temperature (T_c) within Heisenberg model . . . 157
A.1.1 Ni_2MnGa and Mn_2NiGa . . . 157
A.1.2 $Ni_2Mn_{1+x}Sn_{1-x}$ . . . 158
A.1.3 Fe/Co substituted Mn_2NiGa . . . 159
A.2 Calculation of MCE parameters for $Ni_2Mn_{1.4}In_{0.6}$ near second-order magnetic transition . . . 161
A.3 Calculation of MCE parameters near first-order magneto-structural transition . . . 163
A.3.1 $Ni_{2.18}Mn_{0.82}Ga$ . . . 166
A.3.2 Fe substituted off-stoichiometric Ni_2MnGa . . . 167

Bibliography **169**

List of publications **183**

Chapter 1

Introduction

Human development has caused a depletion of natural energy resources and climate changes with unpredictable consequences. In recent times, it is necessary not only to focus on the primary energy source and avoid our dependence on non-renewable energy sources but also to dedicate substantial research efforts to improve the efficiency of energy conversion. Due to their universality, magnetic materials play an important role in improving the efficiency and performance of devices in electric power generation, conditioning, conversion, transportation, and other energy-use sectors of the economy [1, 2]. This constitutes a driving force for the improvement of magnetic materials for energy applications.

Among the different final uses of energy in the residential and commercial sectors, refrigeration and air conditioning account for a relevant fraction of electricity use. Rapid increases in the ownership of air conditioners are already occurring in many developing countries. At the same time, climate change is expected to make cooling demands even greater. Morna Isaac and Detlef van Vuuren of the Netherlands Environmental Assessment Agency assessed future residential-energy use for cooling in the world in the context of potential climate change. They estimated that by 2100 worldwide energy demand for air-conditioning could increase by 72% as a result of climate change alone [3]. Therefore, to fulfil the climate and energy goals, the heating and cooling sector must drastically reduce their energy consumptions and reduce the use of fossil fuels. Both these issues can be mitigated if caloric effects in solid materials are fully utilized since solid-state cooling or heating based on materials' caloric effect can come up as an energy-efficient green technology. Several researchers have concluded that caloric or ferroic [4–6] refrigeration and heat-pumping technologies, which are still in the research and development phase, are the most important options for the future.

Caloric effects occur as a consequence of materials' thermal response to changes of generalized displacement variables such as volume, strain, magnetization, polarization, etc. through the application or removal of their conjugated generalized forces or fields. The fields conjugated to volume, strain, magnetization, and polarization are pressure, stress, magnetic field, electric field, respectively. Changes in these give rise to different types of caloric effects, such as barocaloric [7], elastocaloric [8, 9], magnetocaloric [10–13] and electrocaloric effects [14, 15], respectively, which are utilized in solid-state technologies. Among these, the study of magnetocaloric effect (MCE) in magnetic materials is an expanding field of research nowadays. It occurs due to the interdependence of thermal and magnetic properties and is apparent as a change in material temperature. Magnetic materials displaying significant magnetocaloric effects are acknowledged to be potentially interesting with their possible applications in magnetic refrigerators. Conventional cooling technologies using vapor-compression refrigerators are bulky, heavy, energy inefficient, and pose environmental threats. On the other hand, magnetic refrigerators based on magnetocaloric materials are expected to be energetically more efficient and nature-friendly. Recently, MCE is also being suggested in bio-medical fields of applications like one of the malignant tumors treatment methods - hyperthermia [16]. Thus, research of the magnetocaloric effect in magnetic materials is topical both from fundamental and practical perspectives. The remainder of the introduction covers a basic and detailed concept of MCE with a brief review of theoretical and experimental backgrounds of magnetocaloric materials followed by the importance of materials chosen in this thesis and the outline of the thesis.

1.1 Thermodynamics of caloric effect

Thermodynamics provides a very convenient framework allowing us to establish a unified treatment at a macroscopic scale of caloric effects, regardless of the actual complexity of the particular system of interest [17–19]. A generic closed system can be described by n number of generalized displacement variables $\boldsymbol{X}_i$ (i=1,.....,n), $\boldsymbol{X}_i$s being volume, strain, magnetization, polarization etc. The Gibbs free energy (G) for the system can be expressed as

$$G = U - TS - \sum_{i}^{n} \boldsymbol{x}_i \,.\, \boldsymbol{X}_i \tag{1.1}$$

where U is the internal energy, T the temperature, S the entropy, and $\boldsymbol{x}_i$s are the generalized forces corresponding to displacement variables $\boldsymbol{X}_i$s. The initial internal energy (U) depends on $\{\boldsymbol{x}_i, S\}$ and the extreme condition of the free energy (G) leads to the relation $\boldsymbol{X}_i = \left(\frac{\partial U}{\partial \boldsymbol{x}_i}\right)_{S,\boldsymbol{x}_{j\neq i}}$. On the other hand, to quantify caloric effects, it is convenient to express differential changes of entropy in terms of differential changes of generalized forces or fields and temperature,

$$dS = \left(\frac{\partial S}{\partial T}\right)_{\boldsymbol{x}_i} dT + \sum_i^n \left(\frac{\partial S}{\partial \boldsymbol{x}_i}\right)_{T,\boldsymbol{x}_{j\neq i}} . d\boldsymbol{x}_i \tag{1.2}$$

With the definition of the heat capacity C at constant values of the fields, $C = T\left(\frac{\partial S}{\partial T}\right)_{\boldsymbol{x}_i}$ and considering the Maxwell relation,

$$\left(\frac{\partial S}{\partial \boldsymbol{x}_i}\right)_{T,\boldsymbol{x}_{j\neq i}} = \left(\frac{\partial \boldsymbol{X}_i}{\partial T}\right)_{\boldsymbol{x}_j} \tag{1.3}$$

the entropy differential can be written in the form,

$$dS = \frac{C}{T} dT + \sum_i^n \left(\frac{\partial \boldsymbol{X}_i}{\partial T}\right)_{\boldsymbol{x}_j} . d\boldsymbol{x}_i \tag{1.4}$$

In general, the two limits of interest correspond to isothermal and adiabatic variation of the field. With consideration of the two cases for variations of the field from 0 to a value of $\boldsymbol{x}_i$, equation (1.4) transforms to the relations,

$$\Delta S = \int_0^{x_i} \xi_i \, dx_i \tag{1.5}$$

$$\Delta T = -\int_0^{x_i} \frac{T}{C} \xi_i \, dx_i \tag{1.6}$$

where $\xi_i = \left(\frac{\partial X_i}{\partial T}\right)_{x_j}$ is the response function. In the first case, the caloric effect is quantified by the heat exchanged with the surroundings during the process, resulting in a change in the material's entropy. In the second case, it is measured by the corresponding change of temperature. For the cases of the electrocaloric,

barocaloric, elastocaloric effect, the relevant response functions are $\xi_P = \left(\frac{\partial P}{\partial T}\right)_{E,\ldots}$ (P is the polarization component in the direction of the applied electrical field E), $\xi_V = \left(\frac{\partial V}{\partial T}\right)_{p,\ldots}$ (V is volume and p is pressure), $\xi_\varepsilon = \left(\frac{\partial \varepsilon}{\partial T}\right)_{\sigma,\ldots}$ (σ is an uniaxial stress and ε the corresponding strain), respectively.

In a similar way, for the particular case of magnetocaloric effect (MCE), we are interested in, the response function is $\xi_M = \left(\frac{\partial M}{\partial T}\right)_{H,\ldots}$, where M is the component of the magnetization in the direction of the applied field H and the two magnetocaloric quantities, the isothermal magnetic entropy change ΔS_{mag} and the adiabatic temperature change ΔT_{ad} can be obtained as,

$$\Delta S_{mag} = \int_0^H \left(\frac{\partial M}{\partial T}\right)_H dH \tag{1.7}$$

$$\Delta T_{ad} = -\int_0^H \frac{T}{C}\left(\frac{\partial M}{\partial T}\right)_H dH \tag{1.8}$$

1.2 Magnetocaloric effect and its quantification

Magnetocaloric effect (MCE) is the heating or cooling i.e., the temperature change of a magnetic material due to the application of a magnetic field, quantified by the two quantities, isothermal magnetic entropy change (ΔS_{mag}) and the adiabatic temperature change (ΔT_{ad}). All magnetic materials intrinsically show MCE, although the intensity of the effect depends on the properties of each material. Two relevant processes are shown schematically in Fig. 1.1 in order to understand the origin of the two quantities ΔS_{mag} and ΔT_{ad}.

Entropy is a measure of the order in the magneto-thermodynamic system: a high order is related to low entropy and vice versa. The value of the entropy (S) of a magnetic material at constant pressure depends on both applied magnetic field, H and temperature, T, given by equation 1.9. The contributions are the lattice entropy (S_{lat}) caused by the vibrations of crystal lattice, electronic entropy (S_{el}) of material's free electrons, as for any solid, and the magnetic entropy (S_{mag}) due to magnetization of the material [19, 20]. The lattice and electronic entropy can be considered independent of the magnetic field and are dependent of temperature only. The magnetic entropy is highly dependent on both the magnetic field and the

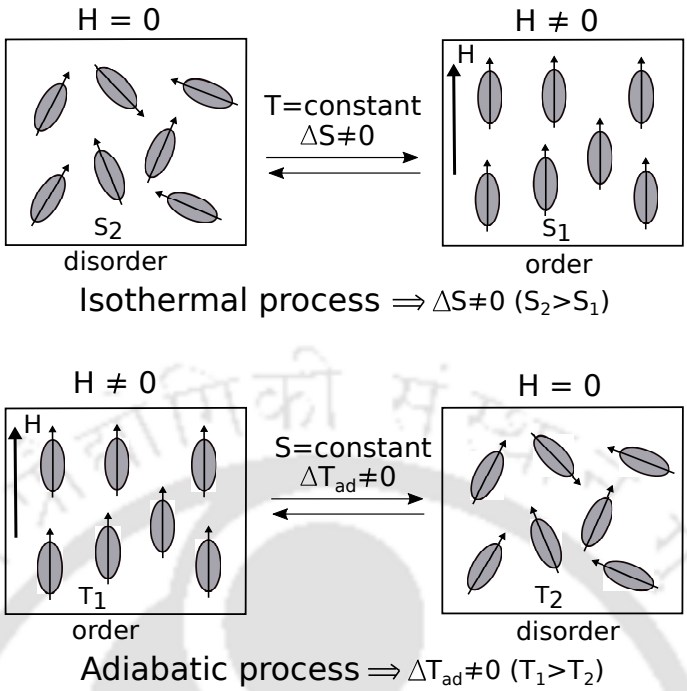

Figure 1.1: Schematic understanding of the two basic processes of the magnetocaloric effect, when a magnetic field (H) is applied or removed in a magnetic system: the isothermal process, which leads to an entropy change (ΔS), particularly the magnetic entropy change (ΔS_{mag}), and the adiabatic process, which yields an adiabatic change in temperature (ΔT_{ad}).

temperature.

$$S(T,H) = S_{lat}(T) + S_{el}(T) + S_{mag}(T,H) \tag{1.9}$$

In the isothermal process (see Fig. 1.1), in absence of magnetic field, the spins are randomly oriented. When the magnetic field (H) is applied isothermally, the spins get aligned in the direction of the applied field and the entropy decreases due to the decrease in the magnetic contribution (S_{mag}). Therefore the entropy change in the process at a constant temperature T is defined as $\Delta S_{mag} = S(T,H)$ - $S(T,0)$ = S_1 - S_2.

When the magnetic field (H) is removed adiabatically (see Fig. 1.1), the spins again become randomly oriented and the magnetic entropy increases. But as the total entropy does not change, the lattice entropy (and the electronic entropy in case of metals) in equation 1.9 must decrease by a comparable amount of the magnetic entropy increase. Consequently, the temperature of the material decreases. Thus the adiabatic temperature change is obtained as ΔT_{ad}=T_2 - T_1.

1.3 Historical origin of MCE

Interest in the connection between magnetism and heat goes back well over 150 years. In 1831 Faraday discovered that a time-varying magnetic flux would induce an electrical current, showing that currents can be generated by means other than the batteries. As part of his extended investigations on the mechanical value of heat, Joule considered the effects of induction currents. In 1843, Joule's work "On the Calorific Effects of Magneto-Electricity, and on the Mechanical Value of Heat" [21] made clear that the heat evolved by the electromagnetically induced current is indeed equal to that evolved by any other kind of electrical current. Following Joule's work, it was generally accepted that repeated magnetization and demagnetization of a ferromagnetic material gives rise to a temperature increase due to the heat dissipated by induction currents. However, it was also realized that there are other ways in which a magnetic field causes a temperature change. In 1917 and 1918, French and Swiss physicists P. Weiss and A. Piccard first discovered reversible heating of a Nickel sample near its Curie temperature (627 K) when a magnetic field was applied [22, 23]. They called it as a "novel magnetocaloric phenomenon". In the late 1920s, Debye [24] and Giauque [25] independently proposed an interpretation based on thermodynamics and suggested the possibility of cooling by adiabatic demagnetization. Such an interpretation was experimentally proved a few years later by Giauque and MacDougall [26].

1.4 Applications

The magnetocaloric effect (MCE) is considered to be one of the most important fundamental thermodynamic effects to be employed in various technological applications. Research is largely focused on environmentally-friendly magnetocaloric materials for their possible applications in magnetic refrigeration and other magnetic energy conversion technologies. Very recently, the magnetocaloric materials are also getting attention in the increasing number of medical applications, e.g., controllable delivery and release of drugs and bio-medical substances to defined locations in the human body and magnetic hyperthermia. In the following, we discuss the applications briefly.

1.4.1 Magnetic refrigeration

Modern society relies very much on readily available cooling. Next to the food storage and transport, air conditioning in buildings and cars gains more importance. Coulomb pointed out in his introductory talk at the Second International Conference on Magnetic Refrigeration at room temperature (Thermag II), 15% of the total worldwide energy consumption involves the use of refrigeration (air conditioning, freezing, chilling, etc.) [27]. Present cooling devices are primarily based on vapor compression technology and are not environmentally clean since it uses Chlorofluorocarbons (CFCs), greenhouse gases, and hazardous chemicals. Hence, the interest in alternative technologies as a new solid-state cooling technology competitive with the conventional vapor compression approach has grown considerably over the past few years, coinciding with rising international concerns about global warming due to ever-increasing energy consumption [28–31]. The magnetic refrigeration using magnetocaloric materials has been demonstrated to be a promising alternative that has great social effects and economic benefits [11–13, 18]. The use of highly energy-efficient magnetic cooling reduces consumption of fossil fuels, hence reducing Carbon dioxide emission. Magnetic refrigeration also offers considerable advantages such as small volume, chemical stability, low cost, non-toxicity, and lack of noise pollution. The cooling efficiency in magnetic refrigerators with working material gadolinium has been observed to reach 60% of the theoretical limit [32], compared to only about 45% in the best gas-compression refrigerators. However, room temperature magnetic refrigeration had been just a promise since Brown designed and built the first successful magnetic refrigerator prototype [33], devices being restricted to research laboratories. The situation has begun to change, as Haier, Astronautics Corporation of America and BASF, developed a domestic appliance of a wine cooler based on the principle of magnetic refrigeration [34]. While commercial magnetic refrigerators are still in the development stages, research efforts to develop new materials with improved MCE are focused on maximizing the cooling capacity and energy efficiency of this budding technology.

In general, a magnetic refrigerator comprises of a magnetic working material, a magnetizing-demagnetizing system, hot and cold heat exchangers and a heat transfer system with a thermal fluid responsible for pumping the heat between the working magnetic material and the hot and cold heat exchangers. Depending on the operating temperature, the heat-transfer medium may be water with antifreeze or air and, for very low temperatures, helium. The response of a magnetocaloric material to a magnetic field is similar to the response of gas to compression or expansion. The

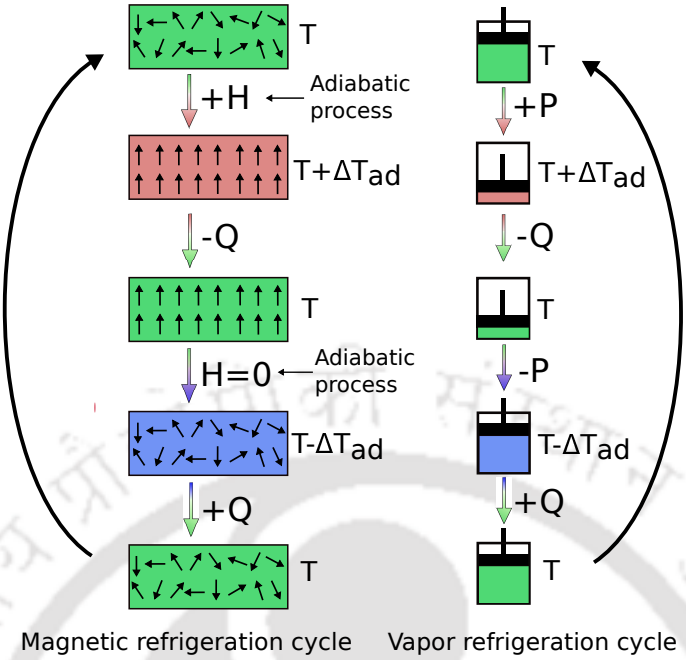

Figure 1.2: Analogy between magnetic refrigeration and conventional vapor refrigeration cycle.

analogy between the vapor compression refrigeration cycle and the magnetic refrigeration cycle is depicted in Fig. 1.2. There are four steps in a magnetic refrigeration cycle (see Fig. 1.2): (i) A magnetocaloric material is placed in an insulated environment. The application of an external magnetic field (H) adiabatically, makes the spins aligned, decreasing the material's magnetic entropy. Since the total entropy should remain unchanged, that material is heated. (ii) The added heat (Q) can then be removed by the thermal fluid or gas, while keeping the applied magnetic field constant. (iii) The magnetocaloric material is then demagnetized adiabatically, decreasing its temperature (ΔT_{ad}). (iv) The demagnetized material absorbs heat from the source or space to be cooled, and the cycle begins again. The magnetocaloric effect of a single material is not sufficient for achieving the temperature span required for magnetocaloric refrigeration and heat pumping devices. There are two options for increasing the temperature span of the magnetocaloric effect and achievement of magnetic refrigeration: the first utilizes a cascade system consisting of several interconnected thermodynamic cycles, while the second involves heat regeneration. A detailed information on these can be gained in Refs. [11, 35].

1.4.2 Bio-medical applications

One of the important applications of MCE is in the field of medical treatments. One possible application in this field is in the treatment of malignant tumors by method of hyperthermia [17, 36, 37]. The most promising means of cancer treatment with fundamentally new mechanisms of therapeutic effects on tumors are the method of hyperthermia [38–40]. In hyperthermia therapy, body tissue is exposed to high temperatures, between 40-45°C, to damage and kill cancer cells, usually with minimal injury to healthy tissues. Also, it makes cancer cells more sensitive to radiation. It is known that the temperature of about 39°C stimulates the growth of a tumor, and temperatures higher than that reduce the viability of a tumor cell. Application of local hyperthermia in combination with radiation and chemotherapy improves the results of cancer treatment by 20–40%. However, classical hyperthermia methods cause an uneven spread of heat inside the tumor and tissues and hence some pathological effects for the most important tissues and organs. Introducing magnetic nanoparticles allows more uniform dissemination of heat, reducing the side effects of classical hyperthermia. In conventional magnetic hyperthermia [41, 42], magnetic nanoparticles are subjected to alternating magnetic fields of few Gauss, which produce heat due to magnetic relaxation losses. However, the drawback of conventional hyperthermia is the lack of control of temperature, which may damage the healthy cells in the body and also has side effects like increased blood pressure. These problems can be avoided by using magnetocaloric materials, as it can provide controlled heating and was patented by Tishin [43]. The advantage of using magnetocaloric materials is that as soon as the magnetic field is removed, the cooling effect is generated, unlike in use of conventional magnetic materials where overheating persists even after removal of the magnetic field. Nanoparticles of rare-earth metals and other compounds those possess the high MCE values [44–47] are used in practical implementation of the method.

1.5 Phase transitions and maximum magnetocaloric effect

From the thermodynamic expressions of magnetocaloric parameters ΔS_{mag} and ΔT_{ad} (equations 1.7 and 1.8), it can be understood that maximum MCE in a material can be expected in the temperature ranges where phase transformations associated with the strong changes in magnetic states occur. Thus, the magnetocaloric mate-

rials can be tentatively divided into two groups [35, 48], (i) materials exhibiting a second-order magnetic phase transition and (ii) materials undergoing a first-order magneto-structural phase transition i.e., the structural transition is associated with a change in magnetization in the system. There are magnetocaloric materials also, showing both types of phase transitions. In Fig. 1.3, a schematic of the magnetic behavior with temperature and the possibility of obtaining maximum magnetocaloric effect near both types of transitions in a ferromagnetic material is illustrated. In Fig. 1.3(a), the green curve represents the magnetization, M vs. temperature, T curve in absence of an applied field. At the second-order magnetic transition temperature i.e., Curie temperature (T_c), the magnetization vanishes, and the ferromagnet turns into a paramagnet. The orange curve depicts the behavior of magnetization in presence of an external magnetic field H_1. Figure 1.3(b) shows the entropy of the material as a function of temperature in the vicinity of a second-order transition. With the application of a magnetic field, the magnetic moments align to some extent, which leads to a decrease of the magnetic entropy (orange curve) as discussed in section 1.2. This decrease in entropy (ΔS_{mag}) is observed under isothermal conditions, drawn as a vertical arrow. Under adiabatic conditions, the total entropy is constant, and the decrease in the magnetic contribution is compensated with an increase in the lattice entropy. Thus, the application of magnetic field results in a heating of the material by ΔT_{ad}, as indicated with a horizontal arrow. The obtained magnetocaloric effect is called the conventional magnetocaloric effect.

A conventional first-order transition is schematically illustrated in Fig. 1.3(c) and 1.3(d). In such a transition, a discontinuity is observed in both the magnetization and the total entropy curves. As shown in Fig. 1.3(c), the ferromagnetic phase is stable in the low-temperature region. Then at a temperature T_M, it transforms into the high-temperature phase with lower magnetization. In principle, the high-temperature phase would still be ferromagnetic up to its Curie temperature, which is illustrated by the extrapolated magnetization curve (green dashed line). However, this is prevented due to the magneto-structural transition. The application of a magnetic field results in the shift of the transition temperature T_M, since the magnetic field stabilizes the phase with higher magnetization. The positive shift of the transition temperature due to the application of magnetic field is the case of a conventional first-order transition. The corresponding total entropy diagram is shown in Fig. 1.3(d). In the entropy curve, a discontinuity is visible for the ideal

A detailed description of magnetocaloric effects associated with first- and second-order transitions is given in Philosophical Transactions of the Royal Society A: Mathematical, Physical and Engineering Sciences 374, 20150308 (2016), by Gutfleisch O *et al.*

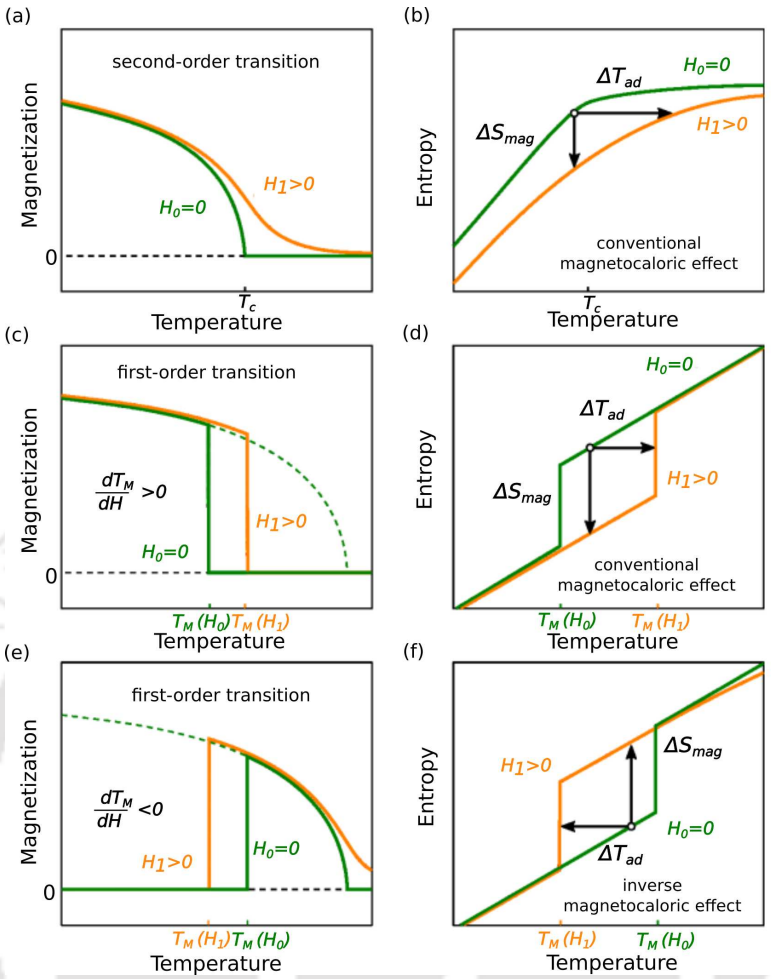

Figure 1.3: Schematic representation of the temperature-dependence of magnetization and the total entropy in absence and presence of a magnetic field in ((a)-(b)) a conventional second-order transition, ((c)-(d)) a conventional first-order transition, and ((e)-(f)) an inverse first-order transition. The figure is taken from ref. [48].

case. When the temperature is constant, the entropy decreases under applied field. Therefore, ΔS_{mag} is negative (vertical arrow) as it was the case for the second-order transition in Fig. 1.3(b). When a magnetic field is applied adiabatically, it increases the material's temperature (horizontal arrow). Thus, in this case, the obtained magnetocaloric effect is conventional.

In contrast to the conventional first-order transition, the inverse first-order transformation is schematically illustrated in Fig. 1.3(e) and 1.3(f). In the inverse case, the low-temperature structural phase has a magnetization lower than that in the high-temperature phase (shown in Fig. 1.3(e)). For this reason, the applied magnetic field shifts the transition temperature to lower value. The corresponding total entropy diagram is shown in Fig. 1.3(f). One can see that the positions of the green

and the orange curves are now exchanged in comparison to those in Fig. 1.3(d). As a result, the isothermal entropy change ΔS_{mag} is positive and the adiabatic temperature change ΔT_{ad} is negative i.e. when a magnetic field is applied adiabatically, it decreases the material's temperature. This is called as inverse magnetocaloric effect.

Materials undergoing first-order transitions have the advantages of exhibiting large magnetic entropy change and adiabatic temperature change i.e., giant MCE associated with the magneto-structural transition. However, these are accompanied by thermal hysteresis, rate-dependent behavior, and decreased cyclic performance. Conversely, second-order transition materials do not suffer from thermal hysteresis. But, their magnetocaloric responses are usually smaller than those of most first-order transition materials operating within the same temperature range. Therefore, a current goal of magnetocalorics is to combine the best from both types of materials, large response without hysteresis and a trade-off between static and cyclic performance. In the following section, magnetocaloric materials exhibiting either second-order, first-order, or both types of transitions will be discussed.

1.6 Criteria for promising magnetocaloric materials

In terms of the of existing parameters, typical for materials that exhibit significant magnetocaloric effect, the criteria for promising and efficient magnetocaloric materials are as follows [49, 50]:

i. A first-order field-induced transition should occur around the working temperature to utilize the associated entropy change. A large difference in magnetization (ΔM) between the high-temperature and low-temperature structural phases is also of great importance because substantial Zeeman energy, which is defined as $\Delta M.H$, is the key to first-order magneto-structural transition.

ii. The two parameters characterizing MCE, the magnetic field induced isothermal entropy change (ΔS_{mag}), and adiabatic temperature change (ΔT_{ad}), must be significant at a magnetic field as low as possible.

iii. The transition temperatures, i.e., the magneto-structural transition temperature (T_M) and magnetic transition temperature (T_c) should be easily tunable. They preferably should coincide near the room temperature.

iv. A low magnetic hysteresis, to avoid magnetic work losses due to the rotation

of domains in a magnetic refrigeration cycle.

v. A low heat capacity (C), since a high heat capacity increases the thermal load and more energy is required to heat the sample itself. It causes a loss in entropy, i.e., for a given ΔS_{mag}, ΔT_{ad} will be lower, as understood from equations 1.7 and 1.8.

vi. For magnetic refrigerants, a high refrigerant capacity (RC) is needed. Refrigerant capacity is a measure of how much heat can be transferred between the cold and hot sinks in one ideal refrigeration cycle, and it is calculated as:

$$RC = \int_{T_{cold}}^{T_{hot}} \Delta S(T)_{\Delta H} dT \tag{1.10}$$

Therefore, a substantial entropy change in a temperature range as wide as possible is needed. For any practical application, it is the amount of heat energy per unit volume transferred in one refrigeration cycle. Thus the denser the magnetic refrigerant, the more effective it is [51].

vii. Environmentally-friendly, affordable, abundant, and easily synthesizable materials are required.

1.7 Materials for magnetocaloric applications: status of the research

The interest in magnetic refrigeration as a new solid state cooling technology competitive with the conventional vapor compression approach has grown considerably over the past 25 years. However, for a technique to become a fully mature alternative, smart engineering and more detailed studies of the fundamental physical properties are needed. The potential of magnetic cooling has not gone unnoticed by fundamental sciences as well. The number of published papers per annum on the magnetocaloric effect has grown exponentially in the past few years. The following are the key results of research on magnetocaloric effects in various materials.

The research on magnetocaloric materials, associated with the second-order magnetic transition, has been centered in soft ferromagnets with T_c between 4 and 77 K,

suitable for applications such as helium and nitrogen liquefaction, and also in materials which order near room temperature to use their magnetocaloric properties in magnetic refrigeration, air conditioning, etc. MCE in paramagnets was used as the first practical application, the so-called adiabatic demagnetization. With this technique, ultra-low temperatures can be reached (m K-μ K). In 1927, the pioneering work of Giauque and MacDougall [25, 26] showed that using the paramagnetic salt $Gd_2(SO_4)_3{\cdot}8H_2O$, temperature lower than 1 K could be reached. The materials that display the largest MCE in the range of ∼10-80 K are intermetallic compounds containing lanthanide metals. The best of them are $REAl_2$ compounds, where RE = Er, Ho, Dy, $Dy_{0.5}Ho_{0.5}$ and Dy_xEr_{1-x} ($0 \leq x \leq 1$) [52–54], GdPd, and $RENi_2$ compounds, where RE=Gd [55], Dy and Ho [56].

MCE in the intermediate-temperature range (∼ 80 - 250 K) has not been studied much, since there are not many applications in this range due to the fact that the temperatures lie in between gas liquefaction temperature and room temperature. One of the best magnetic refrigerant materials in this temperature range is pure Dy [53, 57], with $\Delta T_{ad} \sim 12$ K at around 180 K for a magnetic field change of 7 T.

Magnetic refrigeration near room temperature is of special interest because of its great social effect and economic benefit. Brown in 1976 [33] observed a large MCE of Gd (T_c=293 K), the prototype MCE material at room temperature. However, the entropy changes of magnetocaloric materials reported subsequently are much smaller than that of Gd. This lanthanide has been extensively studied [53, 58–60], and ΔT_{ad} values at their Curie temperatures (T_c) are ∼ 6, 12, 16 and 20 K for magnetic field changes of 2, 5, 7.5 and 10 T, respectively. A variety of alloys using Gd and other rare-earths have been prepared to improve the MCE in Gd. Gd-RE (RE=Tb, Dy, Er, Ho, ...) [61, 62] have been studied, but the alloying only decreases T_c, which is not desirable. Also, the MCE value does not increase considerably in comparison with the pure Gd. The only intermetallic compounds that display a MCE as large as that of Gd are Gd_5Si_4 (with $T_c \sim 335$ K) and the germanium substituted solid solution $Gd_5(Si_xGe_{1-x})_4$, for $x \leq 0.5$, with T_c from ∼ 290 K to ∼ 335 K [63].

In second-order magnetic phase transitions, the existence of short-range order and spin fluctuations above the ordering temperature (T_c) brings about a reduction in the maximum possible magnetization change ($|(\partial M/\partial T)_H|$) value, and the maximum MCE is accordingly reduced. In contrast, a first-order phase transition, as discussed in section 1.5, ideally occurs at constant temperature (the structural transition temperature, T_M) and thus the $|(\partial M/\partial T)_H|$ value should be infinitely large. The existence of entropy change associated with the first-order structural transition

brings about an additional contribution to MCE, yielding the giant magnetocaloric effect. Thus extensive search for magnetocaloric materials with a first-order field-induced magnetic phase transition has been of great research interest in literature.

It was considered a milestone in magnetocaloric material research when the reversible giant MCE near room temperature in a series of Gd-Si-Ge alloys was first observed. $Gd_5(Si_xGe_{1-x})_4$ alloys with $0 \leq x \leq 0.5$, display a ΔS_{mag} at least two times larger than that of Gd near room temperature [64]. It was found by Gschneidner and his colleagues that the entropy change of $Gd_5Si_2Ge_2$ [65] associated with a first-order phase transition is $\sim 18\ \mathrm{J\,kg^{-1}\,K^{-1}}$ around 276 K for a field change of 5 T, which is significantly larger than that of Gd ($\sim 10\ \mathrm{J\,kg^{-1}\,K^{-1}}$) under a similar condition. This sparked a big interest in first-order magneto-structural transformations and triggered the development of promising new magnetocaloric materials. However, the price and critical resources of RE elements limit their large-scale utilization.

From this point of view, 3*d* transition metal compounds or ceramic manganites are good alternatives. Elaborate investigations into 3*d* transition metal compounds such as La-Fe-Si-based alloys, Mn-As-Sb compounds, Mn-Fe-P-based alloys etc have been encouraging [66–71]. These compounds exhibit a first-order magnetic-field-induced transformation from the paramagnetic phase to the ferromagnetic one, giving rise to a conventional giant MCE. Giant and inverse MCE were observed in the intermetallic compound FeRh. This alloy has a first-order ferromagnetic to antiferromagnetic phase transition at $T_M \sim 316$ K, which yields a MCE value as large as -8.4 K for a field change of 2.1 T [72].

The single largest 3*d* transition metal compound series with encouraging results in the context of adding more members in the family of magnetocaloric materials is the series of magnetic Heusler compounds with Ni and Mn as the 3*d* constituents. The simple structures of Heusler compounds, the large database of them and their cost-effectiveness have generated huge interests to explore possible magnetocaloric materials from the family. The Heusler compounds have been the subject of intensive research owing to a magneto-mechanical property i.e., the magnetic shape memory property. The shape memory effect (SME) describes restoring the original shape of an elastically deformed sample when heated. The property underlying the features of shape memory alloys is the martensitic phase transition (MPT), a diffusionless first-order structural solid-solid phase transition with displacive nature, often associated with phonon anomalies in the parent phase and related precursor phenomena. The term "martensite" is named in honor of the German metallographer A. Martens [73]. Upon cooling, the transition occurs from a high symmetry

cubic phase, known as parent phase or austenite, to a lower symmetry phase known as product phase or martensite. The temperature at which the martensites start to form is known as the martensitic-start temperature (T_s). Subsequently, the high-temperature parent phase, known as the austenite phase, becomes mechanically unstable and when the parent phase completely transforms to the martensite phase, the corresponding temperature is called the martensitic-finish temperature (T_f). The martensitic transformation temperature (T_M) is defined as an average of these two i.e. T_M=(T_s+T_f))/2. In the absence of any generalized external field, there are a certain number of twin-related martensitic domains or variants in the martensite phase, which are energetically equivalent but with different crystallographic orientations. These domains self-accommodate in such a way that the elastic energy is minimized. The consequence of the elastic energy stored in the lattice is that the transition does not occur at a constant temperature, but rather it spreads over a certain temperature range. The mechanism behind the shape memory property is: on cooling below T_s, in the absence of any uniaxial stress the martensitic phase has a polyvariant structure, with almost no shape change than in the high-temperature austenite phase; then application of uniaxial stress breaks the degeneracy of the martensitic variants, and by twin boundary motion those variants reorient in favorable orientation with the applied stress, resulting in a macroscopic change of shape. Finally, on heating, the alloy above temperature T_f transforms back to the cubic parent phase. Since the discovery of shape memory effect in Au-Cd [74], a wide variety of materials have been found, prominent among them being the Ni-Ti alloy [75]. In the next few sub-sections we provide an overview of the knowledge acquired so far about structure-property relationships in magnetic Heusler compounds in the context of magnetocaloric effects.

1.7.1 Structure of Heusler compounds

Heusler compounds, discovered by Fritz Heusler, are a remarkable class of intermetallic materials, comprising of more than 1500 members. Heusler compounds are symbolically denoted as X_2YZ, where X and Y are transition metal elements, and Z is the main group element. In general, the Heusler compound X_2YZ, crystallizes in a Cu_2MnAl-type structure i.e. the regular cubic $L2_1$ (space group no. 225; $Fm\bar{3}m$) structure where the X atoms occupy the Wyckoff position 8c((1/4, 1/4, 1/4) and (3/4, 3/4, 3/4)), the Y and Z atoms occupy the positions 4b(1/2, 1/2, 1/2) and 4a(0, 0, 0) respectively [76] (shown in Fig. 1.4(a)). However, another prototype of

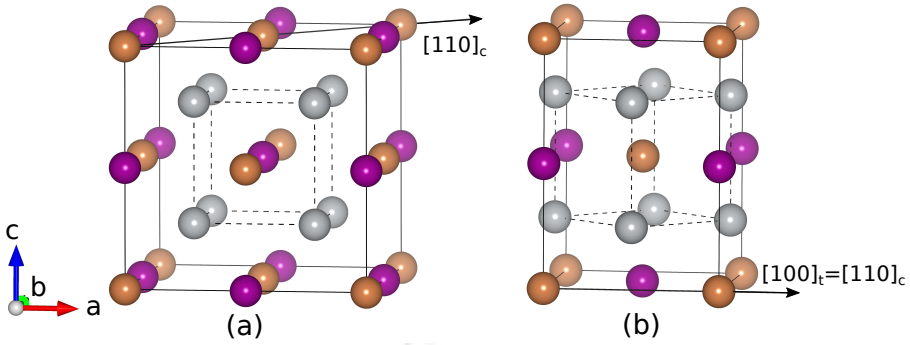

Figure 1.4: (a) Regular Cu_2MnAl-type cubic Heusler structure and (b) corresponding tetragonal structure representation of the same, with cell parameters relations: c_{tet}=c_{cubic} and a_{tet}=$a_{cub}/\sqrt{2}$.

the Heusler compound, called "inverse" Heusler, is formed in Hg_2CuTi (space group no. 216; $F\bar{4}3m$) structure. In the inverse Heusler structure, the atom at 4b site gets interchanged with atoms at the 8c site of regular Heusler alloy. Thus, the X atoms of X_2YZ compounds occupy the Wyckoff positions 4b(1/2, 1/2, 1/2) and 4d(3/4, 3/4, 3/4) whereas the Y and the Z atoms occupy the 4c(1/4, 1/4, 1/4) and 4a(0, 0, 0) positions respectively [76]. An alternative arrangement of the atoms can also be made as the 4a site is symmetric with 4b and 4c with 4d. Depending on the number of valence electrons of the constituent elements, a system crystallizes in the regular or inverse Heusler structure. If the number of valence electrons of the transition metal element Y is larger than that of the transition metal element X, the system crystallizes in the inverse Heusler structure [76–80]. Experimental and theoretical studies on numerous Heusler compounds established the above rules for site occupancies of X_2YZ Heusler compounds, albeit with few exceptions. A widely reported structural phase occurring in some of these compounds is the tetragonal derivative of the cubic structure. This tetragonal structure can be generated through a rotation of the cubic structure by 45° along [110] direction, as shown in Fig. 1.4(b). The cubic unit cell can be described in terms of tetragonal cell with c/a ratio of $\sqrt{2}$ and the corresponding relations between the cell parameters are a_{tet}=$a_{cub}/\sqrt{2}$ and c_{tet}=c_{cub}.

1.7.2 Magnetic shape memory property

A breakthrough in the research of shape memory materials came about with the discovery of magnetic shape memory alloys. The main trouble for practical application of the conventional shape memory effect was the slow response of the devices

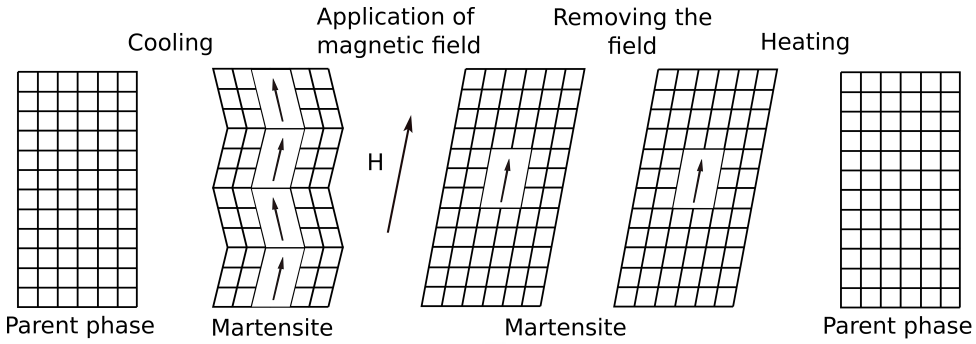

Figure 1.5: Schematic representation of the magnetic shape-memory effect. The arrows inside the variants indicate the corresponding direction of the easy axis. For high magnetocrystalline anisotropy of the martensitic phase, the magnetic field causes the rotation of the variants and hence a deformation of the compounds [81].

inherent to the thermal control of the effect. In contrast, it is easier to control the magnetic field rather than the temperature. The possibility of controlling shape memory effect due to an applied magnetic field opened up a research area aimed at designing a new generation of sensors and actuators which can operate at relatively high frequencies. The effects associated with magnetic shape memory originate from a different mechanism. In this case, it is a magneto-structural coupling of magnetic and martensitic variants at a mesoscopic length scale, which causes the length change by the re-orientation of the martensitic variants under the externally applied field. The mechanism giving rise to the magnetic shape memory effect is shown schematically in Fig. 1.5. In the martensitic state, the sample is a heterophase composed of several twin-related martensitic variants or structural domains (for simplicity, only two of these domains are shown in Fig. 1.5). At temperatures below the Curie temperature, there are magnetic domains within each martensitic variant with their magnetizations pointing along the easy axis and organized to minimize the magnetostatic energy. When a magnetic field is applied, there is the tendency of the magnetic moments to align along the magnetic field. If the magnetic anisotropy is weak, the magnetic moments will rotate within each martensitic variant. This will result in almost no change in the sample dimensions other than those corresponding to conventional magnetostriction. However, if the magnetic anisotropy is high, rotation of magnetic domains requires a significant increase in magnetic energy. Provided that the energy to move twin boundaries is low enough, there will be a rotation of the structural domains so that their easy axis becomes aligned with the externally applied field. In this case, the rotation of martensitic variants is promoted by the difference in the Zeeman energy between the variants. The result is a

significant change in the dimensions of the sample. Thus, in this process, the magnetic field plays the role that mechanical stress plays in conventional shape memory compounds. Shape memory is achieved on heating the compound above the reverse martensitic transition temperature, where all martensitic variants disappear, and the sample recovers its original shape.

Magnetic shape memory alloys (MSMAs) have raised intense interests in recent years as multifunctional materials due to the existence of strong coupling between structure and magnetism. Among different MSMAs, Ni-Mn-Z (Z=Ga, In, Sn, Sb) are of special interest nowadays [82–96]. The presence of first-order magneto-structural transition makes them promising to realize giant magnetocaloric effect.

1.7.3 Results on MCE in Ni-Mn based Heusler alloys

The Heusler type magnetic shape memory compounds can be tentatively divided into two groups: ferromagnetic and metamagnetic. Ferromagnetic shape memory compounds can be distinguished from metamagnetic shape memory ones by the nature of the magneto-structural interplay. In ferromagnetic shape memory materials, the interplay is dominated by the strong increase of magnetocrystalline anisotropy, induced by the symmetry changes taking place at the martensitic transitions. This class of interplay makes feasible a magnetic field induced variant reorganization and thus the magnetic shape memory effect. In the so-called metamagnetic compounds, the interplay is dominantly controlled by the symmetry induced change of exchange coupling and thus changes in magnetization. In this case, the applied field drives the magnetoelastic phase transition and therefore, metamagnetic shape memory compounds are expected to show better magnetocaloric properties. However, the first study dealing with magnetocaloric effect in Heusler compounds was carried out in Ni-Mn-Ga based compounds which belongs to the first category i.e. ferromagnetic shape memory alloys.

1.7.3.1 Ni-Mn-Ga compounds

The first reported data showed inverse magnetocaloric properties in $Ni_{2.06}Mn_{0.908}Ga_{1.032}$ with ΔS_{mag}=4.1 $J\,kg^{-1}\,K^{-1}$ at the austenite transition temperature 197 K in a field of 0.9 T. The obtained value is comparable to that of Gd (ΔS_{mag}=4.2 $J\,kg^{-1}\,K^{-1}$ in 1.5 T field) [97]. However, in a subsequent study a conventional effect, ΔS_{mag}=18.0 $J\,kg^{-1}\,K^{-1}$ in 5 T field at 300 K, was reported in a slightly

different composition $Ni_{2.104}Mn_{0.924}Ga_{0.972}$ [87]. It was later shown that the change in the magnetocaloric character was a consequence of the effect of composition on the magnetocrystalline anisotropy of the martensite phase. It was demonstrated that the inverse contribution to the magnetocaloric effect is dominant at low applied magnetic fields. It becomes less and less important while tuning the composition in such a way that the martensitic transition temperature (T_M) approaches the Curie temperature (T_c), due to the decrease of magnetocrystalline anisotropy of the martensitic phase [81, 98–100]. In particular, for compounds with both transitions very close to each other, the magnetocaloric effect is always conventional [101]. Since then many investigations were done on the Ni-Mn-Ga alloys series [102, 103] by varying the compositions slightly. The largest entropy change ΔS_{mag}=20.7±1.5 J kg^{-1} K^{-1} in a magnetic field of 1.8 T was reported in the $Ni_{2.18}Mn_{0.82}Ga$ alloy at the magneto-structural phase transition temperature (T_M) of 333.2 K [104]. The effect of substitution with different atoms was also studied in the Ni-Mn-Ga series. Both positive and negative entropy changes were observed when Fe substituted Ni-Mn-Ga. In $Ni_{2.18}Fe_{0.04}Mn_{0.8}Ga_{0.98}$, the maximum ΔS_{mag}=3.1 J kg^{-1} K^{-1} was observed in a field of 0.5 T. Maximum negative entropy change of ΔS_{mag}= -2.1 J kg^{-1} K^{-1} was experimentally observed in a field of 2 T. This was due to the separation of structural and magnetic transition temperatures [105]. Pathak *et. al.* [106] observed large inverse magnetic entropy changes in the vicinity of a field induced martensitic transition in $Ni_{2-x}Co_xMn_{1.28-y}Fe_yGa_{0.72}$ (ΔS_{mag}=31 J kg^{-1} K^{-1} for x=0.32 and y=0.36 near room temperature in 5 T). The relatively small hysteresis loss and large refrigeration capacity, tunability of the martensitic transition temperature through variation in Fe concentration make these compounds promising materials for applications. A strong magneto-structural coupling yields large magnetic entropy change of -12.8 J kg^{-1} K^{-1} and adiabatic temperature variation of 1.6 K in an external magnetic field change of 1.5 T in $Ni_2Mn_{0.72}Cu_{0.28}Ga$ [107]. First-principles calculations in conjunction with thermodynamic models were used for a detailed description of magnetic, martensitic and magnetocaloric properties of $Ni_{2+x}Mn_{1-x}Ga$ ($0.18 \leq x \leq 0.24$) Heusler alloys, undergoing a first-order magneto-structural phase transition [108]. The complex magnetic and structural properties of Co substituted Ni-Mn-Ga Heusler alloys have also been investigated [109].

In metamagnetic shape memory alloys of the Ni-Mn-Z (Z=In, Sn, Sb,...) family, inverse magnetocaloric effect is observed. This is associated with the martensitic transition for compositions with excess Mn atoms with respect to the 2:1:1 sto-

ichiometry. The decrease of magnetic moment at the transition is explained by considering the fact that due to the excess of Mn, neighboring Mn-Mn atoms couple antiferromagnetically in the martensite phase [110–112].

1.7.3.2 Ni-Mn-In compounds

MCE in Ni-Mn-In Heusler compounds with variable relative concentrations of the constituents has been observed. Low field inverse magnetocaloric effect associated with first-order martensitic transition was observed in $Ni_{2-x}Mn_{1.48+x}In_{0.52}$ (x=0.12, 0.16, 0.2) compounds. The results show that a small variation in Ni/Mn ratio significantly influences the martensitic transition temperature and the associated magnetic and magnetocaloric properties. In a low field change of 2 T, a large positive magnetic entropy change of 23.5 $J\,kg^{-1}\,K^{-1}$ with a net refrigeration capacity (RC) of 53 J/kg was obtained near room temperature (308 K) in the compound with x=0.12 [113]. MCE was also studied in high Ni content $Ni_{2.08}Mn_{1.92-x}In_x$ (x=0.62, 0.64, 0.66) compounds. The maximum entropy change was 22.3 $J\,kg^{-1}\,K^{-1}$ for x=0.66 at 270 K in 1.5 T [114]. Recently it has been shown that the unidirectional crystal growing technique may provide an effective approach to enhance the magnetocaloric effect of Mn-rich Heusler materials [115]. The results on the effect of the partial substitution of In by Si in $Ni_2Mn_{1.4}In_{0.6-x}Si_x$ ($0.04 \leq x \leq 0.2$) showed that the substitution of 20% In atoms by Si results in an increase in positive magnetic entropy change of more than 300% [116]. The peak values of positive magnetic entropy change in a magnetic field change of 5 T are found to be dependent upon composition and vary from 82 $J\,kg^{-1}\,K^{-1}$ for x=0.04 at 275 K to 124 $J\,kg^{-1}\,K^{-1}$ for x=0.12 at 239 K. Partial substitution of Mn with Fe and Cr in Ni-Mn-In alloys were also studied. It showed that the substitution with Cr increases the martensitic transition temperature, whereas in case of substitution with Fe, it decreases [117]. In $Ni_2Mn_{1.36}In_{0.64}$, substitution of Mn or Ni by Fe leads to increasing values of magnetic exchange parameters. In contrast, the substitution by Cr weakens the exchange interactions as the magnetic moment of Cr atoms is small compared with Mn and Fe moments. A large isothermal magnetic entropy change of 17.7 $J\,kg^{-1}\,K^{-1}$ with large effective refrigerant capacity (254 J/kg) near 270 K was observed in $Ni_2Mn_{1.3464}Cr_{0.0136}In_{0.64}$ [118]. $Ni_{1.8}Co_{0.2}Mn_{1.5}In_{0.5}$ single crystal shows a large entropy change of 30 $J\,kg^{-1}\,K^{-1}$ in an applied field of 7 T during the first-order magneto-structural transition at 355 K leading to a net refrigeration capacity of 267 J/kg, which is very encouraging for magnetic refrigeration applications [119]. A computational study was also done on quaternary Ni-Mn-In-Y Heusler compounds

to predict materials with better magnetocaloric properties. It was found that the inverse MCE increases if Mn is substituted by Y in comparison to the case when Y substitutes Ni. $Ni_2Mn_{1.31}Cu_{0.05}In_{0.64}$ where 5% Mn is replaced by Cu exhibits an inverse MCE which is twice as large compared to that in $Ni_2Mn_{1.36}In_{0.64}$ [120]. Computational studies by Monte Carlo and first-principles calculations show that by tuning the magnetic exchange interactions in $Ni_2Mn_{1.36}In_{0.64}$, the MCE can be enhanced [121, 122] and that can be realized experimentally by doping the host alloys with nonmagnetic or antiferromagnetic atoms e.g., B, Cu, Cr, etc.

1.7.3.3 Ni-Mn-Sn compounds

The giant inverse magnetocaloric effect in Ni-Mn-Sn compounds has its origin in a martensitic phase transformation that modifies the magnetic exchange interactions through the changes in their lattice parameters [123]. It was experimentally shown that Heusler-type $Ni_{0.50}Mn_{0.50-x}Sn_x$ alloys show structural and magnetic phase transformations in the narrow range $0.13 < x < 0.15$, for which an inverse MCE was observed (ΔS_{mag}=15 J kg^{-1} K^{-1} for x=0.15 and 18 J kg^{-1} K^{-1} for x=0.13 in 5 T field) which was at least three times larger than in the Ni-Mn-Ga compounds. The martensitic transition and magnetocaloric effects in $Ni_{2.04}Mn_{1.96-x}Sn_x$ (x=0.536-0.6) Heusler alloys were also investigated. The largest magnetic entropy change ΔS_{mag}=10.77 J kg^{-1} K^{-1} at about 268 K was obtained in $Ni_{2.04}Mn_{1.38}Sn_{0.58}$ alloy with a magnetic field change of 1.5 T [124]. In the bulk off-stoichiometric Heusler alloys with compositions $Ni_{1.76}Mn_{1.72}Co_{0.08}Sn_{0.44}$ and $Ni_{1.76}Mn_{1.72}Cu_{0.08}Sn_{0.44}$, the martensitic transition temperature of the parent alloy $Ni_{1.84}Mn_{1.72}Sn_{0.44}$ shifts to the lower temperatures upon Co and Cu substitution. Therefore, Co doping was explored to open a wide temperature window for a magneto-structural transformation. Tuning the Sn and Co content in $Mn_2Ni_{2-x-y}Sn_xCo_y$ (x=0.44, y=0 to x=0.24, y=0.56), martensitic transition temperature could be adjusted over the range 99 to 450 K, with the condition that T_M remains lower than the Curie temperature of the austenite phase (T_c^A) which varied from 288 K to 565 K. Thus a 351 K temperature window for the magneto-structural transformation was established [125]. A large magnetic entropy change of 29.5 J kg^{-1} K^{-1} with wide working temperature span of 14 K and large effective refrigeration capacity (RC) of 232 J/kg under a field of 5 T was obtained in $Ni_{1.624}Mn_{1.732}Sn_{0.4}Co_{0.244}$ alloy [126]. The study of the diverse properties provided knowledge to develop $Ni_{1.92}Mn_{1.56}Sn_{0.52-x}Si_x$ ($0.04 < x < 0.16$) alloys as a possible multifunctional materials [127]. Large magnetic entropy change was also observed in $Ni_{1.72}Mn_{1.84}Sn_{0.44}C_x$ (x=0, 0.08, 0.16, 0.32) compounds. W-

doping turned out to be an efficient tool to tailor properties of the Ni-Mn-Sn alloy [128]. Complementary computational study was done to optimize the magnetic and structural properties of Ni(Co,Cu)MnSn Heusler alloys for investigation of the magnetocaloric effect [129].

1.7.3.4 Ni-Mn-Sb compounds

In off-stoichiometric Sb-deficient Ni-Mn-Sb systems, giant inverse magnetocaloric effect has been observed near room temperature. The magnetic properties and magnetocaloric effect were studied in $Ni_{0.5}Mn_{0.5-x}Sb_x$ for x=0.1, 0.2, 0.3 and 0.4. It was seen that the properties were very sensitive to x and a negative entropy change of 1.0 $J\,kg^{-1}\,K^{-1}$ at 300 K in 1.2 T was obtained [130]. For a different composition ($Ni_2Mn_{2-x}Sb_x$, x=0.52) a large positive magnetic entropy change (9.1 $J\,kg^{-1}\,K^{-1}$) was observed in the vicinity of the martensitic transition at 287 K for a magnetic field change of 5 T [131], while a maximum positive magnetic entropy change of 19 $J\,kg^{-1}\,K^{-1}$ at 297 K for a magnetic field change of 5 T was found in $Ni_2Mn_{1.48+x}Sb_{0.52-x}$ for x=0.04 [132]. The magnetic properties and MCE were investigated in $Ni_{2-x}Mn_{1.52+x}Sb_{0.48}$ (x = -0.04, 0, 0.04, 0.08) ferromagnetic shape memory alloys. The positive magnetic entropy change was found to be 6.15 $J\,kg^{-1}\,K^{-1}$ for $Ni_{1.96}Mn_{1.56}Sb_{0.48}$ in a field of 1 T, with negligible hysteresis loss [133]. Investigations on $Ni_{2-x}Co_xMn_{1.56}Sb_{0.44}$ (x=0-0.44) ferromagnetic shape memory alloys showed that the temperatures of martensitic transition and magnetic transition in the austentite phase depend strongly on the Co concentration. Only for $0.28 \leq x \leq 0.36$, the martensitic transition is accompanied by a sudden change in magnetization. Maximum entropy changes of 7.3, 7.9, 8.9 $J\,kg^{-1}\,K^{-1}$ for x=0.28, 0.32, 0.36 were observed in the temperature range 288 - 312 K [134]. The effect of Co on the structural, magnetic and magnetocaloric properties of $Ni_{2-x}Co_xMn_{1.52}Sb_{0.48}$ (x=0, 0.08, 0.12, 0.16, 0.2) Heusler alloys was studied by Nayak *et. al.* Remarkable enhancement of MCE was observed near room temperature upon Co substitution. The maximum magnetic entropy change of 34 $J\,kg^{-1}\,K^{-1}$ was achieved for x=0.2 at 262 K in a field of 5 T and a value of 29 $J\,kg^{-1}\,K^{-1}$ was found near room temperature [135]. The effect of Ge substitution was also investigated in $Ni_{1.8}Co_{0.2}Mn_{1.52}Sb_{0.48-x}Ge_x$ (x=0-0.12). Decrease in the exchange interactions brought by Ge substitution could be understood from the reduction in magnetization of the austenite phase and increase in the martensitic transition temperature. The most remarkable feature in the system is the reduction of hysteresis with Ge substitution. The entropy changes were ΔS_{mag}=68, 39, 28 $J\,kg^{-1}\,K^{-1}$ for x=0, 0.04,

0.12 respectively in a field of 5 T near room temperature. Also the RC value was larger than that in the reported Ni-Mn-Sb systems [136]. Investigations were carried to observe the effect of substitution of Si and Ga in quaternary Ni-Co-Mn-Sb alloys. The compound $Ni_{1.84}Co_{0.16}Mn_{1.52}Sb_{0.44}Si_{0.04}$ exhibited a large positive magnetic entropy change of 70 $J\,kg^{-1}\,K^{-1}$ at 273.5 K for a field change of 5 T. The entropy change is much lower (ΔS_{mag}=13 $J\,kg^{-1}\,K^{-1}$ at 272.5 K in 5 T) [137] for $Ni_{1.84}Co_{0.16}Mn_{1.52}Sb_{0.44}Ga_{0.04}$. The magnetic hysteresis loss in Ni-Mn-Sb alloys was effectively reduced by Si-doping [138]. The effect of boron addition on the magnetic and magnetocaloric properties was studied in $Ni_2Mn_{1.52}Sb_{0.48}B_x$ for x=0.04, 0.08, 0.12. ΔS_{mag}=9.2 $J\,kg^{-1}\,K^{-1}$ in a field of 5 T was observed which is larger than the entropy change (7 $J\,kg^{-1}\,K^{-1}$) without boron [139]. A maximum positive magnetic entropy change of 14.2 $J\,kg^{-1}\,K^{-1}$ was observed for x=0.08 in $Ni_2Mn_{1.52-x}Fe_xSb_{0.48}$ at 288 K in a magnetic field change of 5 T [140]. In $Ni_2Mn_{1.48-x}Cr_xSb_{0.52}$ series, a large positive magnetic entropy change of 20 $J\,kg^{-1}\,K^{-1}$ in the vicinity of martensitic transition temperature was observed for x=0.04 in 5 T [141].

Thus, extensive literature on experimental investgations into MCE in the Ni-Mn based Heusler compounds is available. All these studies infer that the magneto-structural transition temperature (T_M), the magnetic transition temperature (T_c), mechanical properties, and associated MCE properties of Heusler compounds can be easily tuned by playing with the compositions. However, the results available are somewhat scattered, as apparently they are done on arbitrarily compositions. A systematic study leading to fundamental understanding of the MCE properties in these systems, which is still missing, and is of utmost importance for the development of existing magnetocaloric materials as well as discovering new efficient ones. In this thesis, we have addressed this in the context of Ni-Mn-Sb compounds.

1.7.4 Importance of Ni-Mn-Sb series

The off-stoichiometric Sb-deficient Ni-Mn-Sb systems are the newest addition to the list of Ni-Mn based Heusler compounds that show large MCE associated with a first-order magneto-structural transition near the room temperature. Extensive experimental investigations (as discussed in previous section 1.7.3.4) have revealed that MPT and associated properties in Ni-Mn-Sb compounds crucially depend on the concentration ratio of Ni, Mn and Sb. The systems investigated were always Sb-deficient and Mn-excess. This propels one to examine the role of composition

on the MCE related properties, in particular the impact on the martensitic phase transition. Coupled with this is the question regarding the impact of site ordering on the physical properties. In order to ramp up the MCE in these materials, some more experimental investigations have been carried out for the Mn-excess Sb-deficient off-stoichiometric Ni-Mn-Sb systems by substituting the Fe and Co atoms at Mn and Ni sites respectively. As a consequence, a large positive ΔS_{mag} near room temperature was obtained with $0.28 \leq x \leq 0.36$ in $Ni_{2-x}Co_xMn_{1.56}Sb_{0.44}$ alloys [134]. For a slightly different composition, $Ni_{2-x}Co_xMn_{1.52}Sb_{0.48}$, nearly 70% decrease in moment is observed associated with the martensitic transition and remarkable enhancement in ΔS_{mag} of 34 $Jkg^{-1}K^{-1}$ is achieved for x=0.2 at 262 K in a field of 5 T [135, 142]. A significant ΔS_{mag} value of 14.2 $Jkg^{-1}K^{-1}$ at 288 K under 5 T field was observed for x=0.08 in $Ni_2Mn_{1.52-x}Fe_xSb_{0.48}$ [140]. These results suggest that Fe, Co, and Cu substitutions at select sites of Ni-Mn-Sb Heusler compounds would help in improving their MCE properties. However, it crucially depends on the substituent, the site of substitution, and the composition. A systematic investigation into the impact of these three would throw light on the microscopic understanding, help interpret the experimental observations, and provide a roadmap to tune the compositions for maximizing the functional properties. Inspite of the obtained giant effect, one issue with the 3*d* elements substituted Ni-Mn-Sb compositions is that the working temperature i.e., the martensitic transformation temperature (T_M) decreases below the room temperature due to the substitution which is not desirable for practical applications. Thus it will be worthwhile to explore magnetocaloric materials in the Ni-Mn-Sb Heusler family, with improved giant effect, but, within the desired range of working temperature. In some recent studies, the strategy of substitution of at least two 3*d* elements simultaneously (cosubstitution) has been found to be useful in achieving the important magnetic and structural properties with better tuning and adopted successfully [143–145], which may work in the present context.

To this end, the motivation of my research work is two-fold. From the fundamental point of view, the motivation is to gain a deeper insight into the relations between the MCE and magnetic phase transitions, compositions, and related structural and magnetic properties of Heulser compounds. This insight serves as a guide in the search for new materials suitable for application. Using this, I next focus on finding potential materials exhibiting large magnetocaloric effect. I have chosen the Ni-Mn-Sb magnetic shape memory Heusler series since magneto-structural transitions and significant magnetocaloric effects are observed near room temperature. This, along with low cost of Sb and achievable negligible hysteresis loss [146], makes

Ni-Mn-Sb systems potential candidates for good magnetocaloric materials. Apart from that, there is quite a bit of scope left to investigate it theoretically.

1.8 Importance of combined first-principles electronic structure calculations and Monte Carlo simulation based studies for investigation of MCE

The discussions in the previous sections clearly demonstrate that it would be of great interest to understand the fundamental picture of structural, electronic and magnetic properties in the Ni-Mn-Sb based Heusler compounds behind the fascinating magnetocaloric effect. For a theoretician, the natural way to do this is by obtaining the solution of Schrödinger equation for electrons in real solids, where their quantum mechanical behaviour is determined. For such a many body interacting system, exact solution of the Schrödinger equation is not possible. The Density Functional Theory (DFT) [147, 148] which projects the many body interacting system onto a non-interacting single particle one; where the many body interactions are taken care of in an average way through a single term, has made the required breakthrough to arrive at parameter-free, first-principles methods so that robust and accurate results on materials properties can be obtained from their electronic structures. Integration of DFT based first-principles methods with advanced softwares made tackling of complex problems accurately within reasonable time period [149–155]. Over the years, application of these methods in calculating the electronic structures of magnetic ground states [156–159], dynamical properties of materials [160, 161] and simultaneous comparison of these results with experimental observations confirmed the accuracy of these methods. Various problems related to sub-lattice disordered alloys [162, 163] have also been encountered with these sophisticated tools. Over the years, these methods are widely accepted to predict properties of new materials where experimental evidence is not present. Therefore, the DFT based first-principles methods are the essential tool for fundamental understanding of materials.

To quantify MCE in materials, one needs to calculate the temperature dependent magnetic properties and the magnetocaloric parameters, which is beyond the scope of DFT based first-principles electronic structure calculations. However, the fundamental insights into the properties obtained from DFT calculations can be used to model the finite temperature calculations or even screen materials for further

investigation. In this regard, one important focus of my work goes in developing in-house computer code to quantitatively calculate the MCE parameters, ΔS_{mag} and ΔT_{ad}. Generally speaking, most of the work on MCE in Heusler compounds are experimental in nature. Only a few theoretical studies of MCE in the framework of molecular-field approximation [164–166], bond proportion model [167], and Monte Carlo simulations [108, 111, 168–170] have been performed. From a theoretical point of view, it is a demanding task to obtain all phases in a self-consistent way, which requires the *ab initio* evaluation of all magnetic exchange parameters, i.e., for each structure (austenite and martensite) and temperature and compare at each step of the calculation the corresponding free energies. In the literature, a unified description of structural and associated first-order magnetic phase transitions, i.e., magneto-structural transitions, has been successfully presented for Ni-Mn based Heusler alloys, by using a model Hamiltonian implementing Blume-Emery-Griffiths (BEG) and Potts model [108, 120, 169, 171–176]. The Hamiltonian allows to explore the richness of the phase diagram as well as the observed qualitative and quantitative behavior of MCE quantities are in a very good agreement with experiments. In this thesis, I have adopted the same strategy.

Thus, my work, on one hand, represents how a search for giant magnetocaloric materials can be initialized by observing the basic structural and magnetic properties obtained from first-principles calculations and on the other hand, how the temperature-dependent magnetic, structural and magneto-structural properties can be calculated with the in-house Monte Carlo method based code implemented on a thermodynamic model.

1.9 Outline of the thesis

In this dissertation, I have focused on detailed understanding of various important physical properties related to the magnetocaloric effect, as well as, predicting possibility of realizing efficient MCE in some new compounds in Ni-Mn based Heusler systems. My investigation is mainly focused on off-stoichiometric Ni-Mn-Sb and $3d$ elements (Fe, Co and Cu) substituted Mn-excess Ni-Mn-Sb compounds. In brief, I have systematically explored the impact of various factors, such as structural phase stability, site occupancy, magnetic structure, composition, magnetic interactions, mechanical properties, transition temperatures, and how they may affect the magnetocaloric properties in a system, by first-principles electronic structure calculations and Monte Carlo simulations. Simultaneously, the interpretations of

the existing experimental results are also made. Armed with the inputs from such study, I calculated the MCE parameters i.e., the isothermal magnetic entropy change (ΔS_{mag}) and the adiabatic temperature change (ΔT_{ad}) in these systems which leads to proposing new compounds in Fe, Co and Cu substituted Mn-excess Ni-Mn-Sb Heusler family with improved magnetocaloric effects.

Chapter 1 starts with a description on thermodynamics of caloric effect in general along with a focus on the magnetocaloric effect. This is followed by the important application areas of utilizing the MCE, specially in the field of magnetic refrigation. A review of literature studies on the important magnetocaloric materials has been done to find out the criterion for selecting efficient magnetocaloric materials and hence the importance of Ni-Mn based Heusler alloys in the context of our systems of interest is analyzed.

Chapter 2 contains a brief description of theoretical methods which are used for material simulations finding ground state properties. This chapter starts with a description of Density functional theory (DFT) [147, 148], the backbone of current day electronic structure calculations in complex materials. Various implementations of the DFT which are used in this work are then described. In this work, I have used two techniques: the projected augmented wave method (PAW) [177] and Korringa-Kohn-Rostoker Green's function method [150, 151] which are implemented in Vienna *Ab initio* Simulation Package (VASP) [178, 179] and Munich Spin-Polarized-Relativistic Korringa-Kohn-Rostoker (SPRKKR) [180] band structure program package, respectively. Apart from descriptions to obtain the ground-state charge densities and total energies within the two implementations, I have also provided descriptions regarding calculations of elastic moduli and magnetic exchange interactions. The magnetic exchange parameters have been used in two different approaches for estimation of the Curie temperature (T_c): the mean field approximation (MFA) [181] and the Monte Carlo simulations (MCS) [182]. Further the Monte Carlo simulation technique for simulating the systems incorporating the model Hamiltonian with BEG and Potts model [108, 111, 120, 172], as a tool to extend the zero-temperature *ab initio* calculations to finite temperatures and estimate the MCE parameters, has been discussed. The simultaneous modeling of structural, magnetic, and magnetoelastic degrees of freedom in cubic and tetragonal structures in my in-house Monte Carlo method based code and the simulation details have also been discussed.

Using DFT calculations, in **Chapter 3** we have performed a comprehensive and systematic investigation into the roles of composition, site occupancies and magnetic configurations affecting the structural stabilities in Ni and Mn-excess Ni_2MnSb. We find that the site occupancy pattern and associated magnetic alignment of Mn atoms play the central role in de-stabilizing the high temperature Heusler phase and consequently stabilizing a tetragonal martensite at low temperature. We find that unless the system is significantly Sb-deficient, a martensitic transformation leading to its functional properties, like MCE, is difficult to realize unless the system stays in a meta-stable state due to the process of annealing or is grown by non-equilibrium methods. Our calculations for Mn-excess Sb-deficient system reproduce the experimentally observed trends. The patterns in phase stability as obtained from our total energy calculations can be understood from the features in the densities of states in the minority spin bands. This work helps understand the reason behind experimentalists choice of Sb-deficient systems for observing functional properties like magnetocaloric effect in Ni-Mn-Sb. An important outcome of this work is the identification of $Ni_{2+x}MnSb_{1-x}$ as a potential new MCE compound where the martensitic transformation takes place even at high Sb composition. This input widens the scope of the experimentalists to explore functional properties in Ni-Mn-Sb systems. Shear modulus and electron to atom ratio (e/a) both turn out to be good predictors of structural transition temperature in Ni-Mn-Sb. The materials are also found to be ductile which is an advantage for their commercial usages.

In **Chapter 4** we have explored the potentials of Mn-excess, Sb-deficient Ni_2MnSb compounds as magnetocaloric materials by substitution of Ni and Mn by $3d$ transition metals Fe, Co, and Cu. Apart from being able to explain the trends of variations in quantities like the martensitic transformation temperature, magnetic transition temperature and the magnetic moments with compositions, observed in handful of experiments on this system, we have provided insights into the possibilities of significant magnetocaloric effects in this group of compounds; the ones which are yet to be synthesized. Thus our investigation unveiled the physics behind the variations of physical properties associated with the magnetocaloric effects, and also interpreted the available experimental results successfully. We found that the site occupancies of various atoms play an important role in the variations of the above mentioned physical quantities. The structural stabilities in these systems could be correlated to the magnetic exchange interactions and their variations. We predict that the compounds $Ni_2Mn_{1.5-y}Co_ySb_{0.5}$ and $Ni_2Mn_{1.5-y}Cu_ySb_{0.5}$; $y \sim 0.25$, can emerge as

materials exhibiting large magnetocaloric effects. In brief, this work systematically explores the physics behind occurence of magnetocaloric effect in substituted Ni-Mn-Sb compounds. The approach adopted and knowledge obtained from this work can be used to investigate a wider pool of materials, boosting the possibility of discovering more materials with large MCE.

In **Chapter 5** we explore potential room temperature magnetocaloric materials near second-order magnetic transition by cosubstitution in the Ni-Mn-Sb family, using Density functional theory in conjunction with model Hamiltonian. Materials showing reversible magnetocaloric effect near room temperature are desirable for green refrigeration technology. The compounds in magnetic Heusler family displaying significant magnetocaloric effect driven by first-order magneto-structural transitions are in vogue. Comparatively, the Heusler compounds, undergoing second-order magnetic transition near room temperature are less explored in the context of discovering significant magnetocaloric effect, though they can offer certain advantages like less energy cost and hysteresis loss. Our investigation on two cosubstituted families, $Ni_{2-x}Fe_xMn_{1+z-y}Cu_ySb_{1-z}$ and $Ni_{2-x}Co_xMn_{1+z-y}Cu_ySb_{1-z}$, discovers significant numbers of compounds with second-order phase transition near room temperature exhibiting substantial changes in magnetic entropy, comparable to that observed in the compounds showing inverse magnetocaloric effect near a first-order magneto-structural transition. We find that the cosubstitution provides a wider scope of tuning the physical parameters like magnetic moment and magnetic transition temperature as well as of stabilization of the Heusler phase down to very low temperatures. We provide a systematic way to select potential reversible magnetocaloric compounds and analyze our results from their electronic structures and magnetic exchange interactions. In brief, this work, thus, offers a broader scope of synthesis and exploration of large MCE near room temperature by cosubstitution in other compounds of the Heusler family.

In **Chapter 6** we have investigated the two cosubstituted families, $Ni_{2-x}Fe_xMn_{1+z-y}Cu_ySb_{1-z}$ and $Ni_{2-x}Co_xMn_{1+z-y}Cu_ySb_{1-z}$ to find materials probable to exhibit large magnetocaloric effect associated with the first-order magneto-structural transition, using the techniques employed in chapter 5. The compositions complementary to the ones investigated in chapter 5 are considered here. We have investigated the compositions on which experiments are done as well as the other potential ones. Our calculations turn out to be in good agreement with experimental

results. The compositions which our initial screening predicted to be the ones exhibiting large MCE, indeed came out to be that after the full thermodynamic study (*ab initio* + Monte Carlo), including both magnetic and structural contributions, were done. This study, thus, establishes cosubstitution in Ni-Mn-Sb as a route to achieve giant MCE.

In **Chapter 7** we summarize the outcome of the thesis and discuss the possible directions for extension of the present work.

In **Appendix** the benchmarking of our in-house Monte Carlo code is presented. The benchmarking is done by running calculations on a number of systems where results, both experimental and theoretical, pre-exist. The details of the benchmarking are discussed in the appendix.

Chapter 2

Methodology

In this chapter, we describe the theoretical methods which are used in this thesis. The investigations carried out are based on density functional theory (DFT) and Monte Carlo methods. Fundamental understandings of the magnetocaloric effect in Heusler compounds and modeling new ones involves a two-stage approach: Density Functional Theory based first-principles are used to predict the ground state properties and subsequently, the obtained information is used as inputs in Monte Carlo simulation which implements thermomagnetic models to extend the zero-temperature *ab initio* calculations to finite temperatures. In this chapter, we provide descriptions of two different implementations of DFT for calculations of ground state properties, that are used to obtain results presented in the thesis. Monte Carlo simulation methods based on Heisenberg model, Blume-Emery-Griffiths (BEG) and Potts model and how they are used to compute the temperature dependent magnetization behavior, transition temperatures (T_c, T_M) as well as to calculate the magnetocaloric quantities (ΔS_{mag} and ΔT_{ad}) in the presence of strong magneto-structural coupling in our systems, will be discussed then.

2.1 Density Functional Theory

In principle, all the information about a given system is contained within the corresponding quantum mechanical wavefunction. For a hydrogen atom, we can solve the Schrödinger equation exactly in order to get the wavefunction of the system. We can then determine the allowed energy states of the system. Unfortunately, it is impossible to solve the Schrödinger equation for an N-body system. Evidently, some approximations are to be invoked to render the problem solvable. Density functional theory (DFT) is a method to do that. DFT is a theory of electronic structure, based

on the electron density distribution $n(\mathbf{r})$, instead of the many-electron wave function $\Psi(\mathbf{r}_1, \mathbf{r}_2, \mathbf{r}_3,...)$. It has been used widely for solids, surfaces, defects, etc.

2.1.1 The many-body Hamiltonian

The nonrelativistic, time-independent many body Schrödinger equation for solving the electronic structure of a solid can be written as

$$\mathcal{H}\Psi = E\Psi \tag{2.1}$$

The equation describes all many-particle states Ψ of the system and their related energies E; $\mathcal{H}$ is the Hamiltonian. A many body system consists of N_p positivley charged nuclei and N electrons. Therefore, the many particle wavefunction Ψ is of the form,

$$\Psi = \Psi(\mathbf{r}_1, \mathbf{r}_2, ..., \mathbf{r}_i, ..., \mathbf{r}_N, \mathbf{R}_1, \mathbf{R}_2, ..., \mathbf{R}_I, ..., \mathbf{R}_{N_p}) \tag{2.2}$$

The electronic coordinates are given by $\mathbf{r}_i$ and nuclear coordinates are given by $\mathbf{R}_I$, where i and I are indices for electrons and nuclei, respectively. The Hamiltonian $\mathcal{H}$ can be written as

$$\begin{aligned}\mathcal{H} = -\frac{\hbar^2}{2}\sum_i \frac{\nabla_i^2}{m_i} + \frac{1}{2}\sum_{i\neq j}\frac{e^2}{|\mathbf{r}_i - \mathbf{r}_j|} - \frac{\hbar^2}{2}\sum_I \frac{\nabla_I^2}{M_I} \\ + \frac{1}{2}\sum_{I\neq J}\frac{Z_I Z_J e^2}{|\mathbf{R}_I - \mathbf{R}_J|} - \sum_{i,I}\frac{Z_I e^2}{|\mathbf{r}_i - \mathbf{R}_I|}\end{aligned} \tag{2.3}$$

m_i and M_I are mass of electron and nucleus, respectively. Z_I is charge of the nucleus. The first and third terms in the Hamiltonian are kinetic energies of electrons and nuclei, respectively. The second, fourth and fifth terms are Coulomb interactions between electrons and electrons, nuclei and nuclei and between electrons and nuclei, respectively. The many body Hamiltonian given by equation 2.3 is difficult to solve for solid state systems and approximations are required at different levels. In the next subsections, we discuss them.

2.1.2 The Born-Oppenheimer approximation

The many-body problem can be simplified by Born-Oppenheimer approximation [183]. The approximation uses the fact that the nuclei are much more massive than the electrons. Therefore, the time scale associated with nuclear motion is orders of magnitude larger than that of the electrons and hence the nuclei can be considered motionless. Thus, their kinetic energy can be neglected and the potential energy due to nucleus - nucleus interactions is merely a constant. Accordingly, under the Born-Oppenheimer approximation, the electrons can be considered as moving in the field of fixed nuclei and the many-body Hamiltonian in equation 2.3 reduces to electronic Hamiltonian, given as

$$\begin{aligned}\mathcal{H}_{elec} &= -\frac{\hbar^2}{2}\sum_i \frac{\nabla_i^2}{m_i} + \frac{1}{2}\sum_{i\neq j}\frac{e^2}{|\mathbf{r}_i - \mathbf{r}_j|} - \sum_{i,I}\frac{Z_I e^2}{|\mathbf{r}_i - \mathbf{R}_I|} \\ &= T_e + V_{ee} + V_{ext}\end{aligned} \tag{2.4}$$

T_e is the kinetic energy of the electrons, V_{ee} is the internal potential energy i.e. Coulomb energy due to electron-electron interaction and V_{ext} is the interaction with external potential energy due to interaction between electrons and nuclei.

2.1.3 Hartree and Hartree-Fock Methods

A first approach to find a wave function that minimizes the energy of the system is the Hartree approximation [184]. The initial ansatz was that the many-body wavefunction could be written as

$$\Psi(\mathbf{r}_1, \mathbf{r}_2, ..., \mathbf{r}_N) = \Psi_1(\mathbf{r}_1)\Psi_2(\mathbf{r}_2)...\Psi_N(\mathbf{r}_N) \tag{2.5}$$

From equation 2.5, it follows that the electrons are independent and interact only via the mean-field Coulomb potential, that include both the electrons-nuclei interaction and the mean field arising from the (N-1) other electrons. This yields one-electron Schrödinger equations of the form,

$$-\frac{\hbar^2}{2}\sum_i \frac{\nabla_i^2}{m_i} + V_{Hatree}(\mathbf{r})\Psi_i(\mathbf{r}) = \epsilon_i \Psi_i(\mathbf{r}) \tag{2.6}$$

Although the Hartree equations are numerically tractable via the self-consistent field method, such a crude approximation fails to capture essential elements of the physics. The Hatree potential (V_{Hatree}) considers potentials due to the electron density distribution and ionic lattice but neglects exchange and correlation effects, the manifestation of the Pauli exclusion principle, which disallows two identical particles to lie in the same quantum state. The Pauli exclusion principle for electrons demands that the many-body wavefunction must be anti-symmetric with respect to interchange of any two electron coordinates, i.e.,

$$\Psi(\mathbf{r}_1, \mathbf{r}_2, ..., \mathbf{r}_N) = -\Psi(\mathbf{r}_2, \mathbf{r}_1, ..., \mathbf{r}_N) \tag{2.7}$$

This is incorporated in the Hartree-Fock [185] method by construction of a many body wave function Ψ using a Slater determinant of single-particle orbitals Ψ_i :

$$\Psi = \frac{1}{\sqrt{N!}} \begin{vmatrix} \Psi_1(\mathbf{r}_1) & \Psi_2(\mathbf{r}_1) & \dots & \Psi_N(\mathbf{r}_1) \\ \Psi_1(\mathbf{r}_2) & \Psi_2(\mathbf{r}_2) & \dots & \Psi_N(\mathbf{r}_2) \\ \vdots & \vdots & \vdots & \vdots \\ \Psi_1(\mathbf{r}_N) & \Psi_2(\mathbf{r}_N) & \dots & \Psi_N(\mathbf{r}_N) \end{vmatrix} \tag{2.8}$$

The Hartree-Fock method treats the exchange in an exact way. However, the formalism neglects correlation effects altogether leading to inaccurate results in many cases. The requirement for a computationally reasonable scheme that successfully incorporates the effects of both exchange and correlation leads one to consider the conceptually simple and elegant density functional theory.

2.1.4 The philosophy of DFT

The density functional theory (DFT) considers the electron density $n(\mathbf{r})$ as the central variable that describes all physical properties of the system, rather than the many-body wavefunction. This conceptual difference with the wave function based methods leads to a remarkable reduction in difficulty. Whereas the many-body electronic wavefunction is a function of $3N$ variables, the electron density is a function of only three variables x, y, z - three Cartesian coordinates. An early version of the density functional theory was proposed by Thomas [186] and Fermi [187] where the kinetic energy was represented by one electron density. The electron-electron interactions was incorporated via a mean field approximation. However, the semi-classical Thomas Fermi approximation, in spite of pointing out the importance of

one electron density to obtain the ground state properties in a solid, failed to address the effects of exchange and correlation. A subsequent proposal by Dirac [188] that incorporates the exchange energy in terms of the electron density, failed to improve the method significantly. In 1964, Hohenberg and Kohn [147] provided the required breakthrough.

2.1.4.1 Hohenberg-Kohn theorems

Hohenberg and Kohn's approach is the backbone of current day DFT. It is based on the following remarkable simple theorems:

1. The external potential $V_{ext}(\mathbf{r})$ is uniquely determined by the electron density $n(\mathbf{r})$ so the total energy is a unique functional of the density $E[n]$ [149].

2. The true ground state density $n(\mathbf{r})$ minimizes the total energy functional $E[n]$ [149].

According to the above theorem, the ground state energy of interacting electrons in an external potential $V_{ext}(\mathbf{r})$ is described by an energy functional

$$E[n] = F[n] + \int V_{ext}(\mathbf{r})n(\mathbf{r})\,d\mathbf{r} \tag{2.9}$$

The first term $F[n]$ is a universal functional of the electron density $n(\mathbf{r})$ which includes the kinetic (T_e) and electron-electron interaction (V_{ee}) energies in equation 2.4. The second term represents interaction energy with the external potential. The total energy in the ground state (E_0) is realized through the minimization of $E[n]$. Therefore, the ground state density, in principle, uniquely determines the ground state properties of an interacting electronic system. This approach offers a perspective different than the conventional methods where many body wave functions are to be computed, which is often a difficult task.

2.1.4.2 The Kohn-Sham ansatz

The two theorems proved the existence of a universal functional, though they do not give any idea about the nature of the functional. Therefore, the Hohenberg-Kohn theorems first appeared not to be helpful for practical applications. The success of the DFT comes through using the Hohenberg and Kohn theorem in conjunction with the Kohn-Sham formalism [148]. The basic idea of Kohn and Sham is the introduction of a fictitious auxiliary non-interacting electron system in which the

electrons are moving within an effective Kohn-Sham potential, $V_{KS}(\mathbf{r})$. The single-particle Kohn-Sham orbitals are constrained to yield the same ground state density as that of the fully-interacting system, so that the Hohenberg-Kohn-Sham theorems are still valid. This mapping by Kohn and Sham resulted in a Schrödinger like equation for single particle which provides a variational total energy and thus the ground state single particle density to a good approximation.

$$(H_{ks} - \epsilon_i)\psi_i(\mathbf{r}) = 0 \tag{2.10}$$

$$H_{ks} = -\frac{1}{2}\nabla^2 + V_{KS} \quad (in\ Hartree\ units) \tag{2.11}$$

where,

$$V_{KS} = V_{ext}(\mathbf{r}) + V_{Hatree}(\mathbf{r}) + V_{xc}(\mathbf{r}) \tag{2.12}$$

The second term is called Hartree potential,

$$V_{Hartree} = \frac{1}{2}\int \frac{n(\mathbf{r})n(\mathbf{r}')}{|\mathbf{r} - \mathbf{r}'|}\, d\mathbf{r}d\mathbf{r}' \tag{2.13}$$

and the last term is exchange-correlation potential, defined as,

$$V_{xc} = \frac{\delta E_{xc}[n]}{\delta n(\mathbf{r})} \tag{2.14}$$

which includes electron-electron interaction beyond the Hartree term. The density is calculated from single-electron Kohn-Sham orbitals according to

$$n(\mathbf{r}) = \sum_{i=1}^{N} |\psi_i(\mathbf{r})|^2 \tag{2.15}$$

The total number of electron is obtained as

$$N = \int n(\mathbf{r})\, d\mathbf{r} \tag{2.16}$$

The self-consistent equations (2.9-2.16) are used to compute the ground state energy of an electronic system with

$$E_{ks} = T_s[n] + \int V_{ext}(\mathbf{r})n(\mathbf{r})\, dr + E_{Hartree}[n] + E_{xc}[n] \tag{2.17}$$

Addressing magnetism by incorporating spin dependent density is not too com-

plicated in DFT. In this case, the Kohn-Sham equations are solved separately for each spin channel. The charge density is obtained by adding up the densities of the two spin channels (n↑ + n↓), while the spin density is obtained as the difference of the electron densities between the two spin channels (n↑ - n↓).

2.1.4.3 Approximations for the exchange-correlation energy functional

In principle, the Kohn-Sham ansatz is exact, except for the exchange-correlation functional. The challenging part of the solution of Kohn-Sham equations lies in approximating the exchange-correlation functionals in which all of the complicated many-body effects are considered.

The simplest approach to obtain an approximate E_{xc} is the local density approximation (LDA) [148]. The LDA assumes that the variation of density in a solid is locally insignificant, and thus the electron density in a solid can be mimiced using that of the homogeneous electron gas, the exchange and correlation terms of which are known exactly. The E_{xc}, under LDA, is given by

$$E_{xc}^{LDA}[n] = \int n(\mathbf{r})\epsilon_{xc}^{hom}(n(\mathbf{r}))d^3r \tag{2.18}$$

where ϵ_{xc}^{hom} is the sum of the exchange and correlation energies of the homogeneous electron gas of density $n(\mathbf{r})$. Consideration of spin degrees of freedom of electrons modifies LDA to the local spin density approximation (LSDA).

LDA, however, ignores the exchange-correlation energy at point $\mathbf{r}$ due to nearby inhomogeneities in the electron density. In spite of this, the success of LDA is remarkable due to the fact that it gives the correct sum rule for the exchange-correlation hole. However, it failed upto the extent of producing wrong electronic ground state in some important cases.

An attempt to improve the LDA was made by introducing the gradient corrections on the electron density, the generalized gradient approximation (GGA) [189–191]. The GGA functional is given by

$$E_{xc}^{GGA}[n] = \int d^3r\, n(\mathbf{r})\, \epsilon_{xc}^{GGA}(n(\mathbf{r}), |\nabla n(\mathbf{r})|) \tag{2.19}$$

For systems where the charge density varies slowly, the GGA functional improves the results. Calculations presented in the thesis are done with the GGA functionals.

For strongly correlated systems, LDA, as well as the GGA, fail. For example,

band gaps of semiconductors are underestimated [192]. The reason for this behavior is found in the mean-field treatment of the Coulomb repulsion between the electrons, which does not take into account strong electronic correlations. In the formulation of LDA exchange-correlation functional, the potential of the Kohn-Sham orbitals does not depend on the occupancy of the orbitals. However, in case of strong on-site correlations, the addition of an electron to a localized site, already containing an electron, requires an additional energy U [193]. The "Hubbard U" in the Hubbard model, introduced by J. Hubbard in 1963, takes into account the on-site Coulomb repulsion by an additional term in the Hamiltonian [194]. The introduction of the "Hubbard U" in the energy functional of LDA gives rise to the so-called LDA+U method [195–197]. In a similar manner, a term that takes into account correlation effects can also be added to GGA exchange-correlation functional, which gives rise to the GGA+U method. The basic idea behind this method can be understood in the comprehensive review by Anisimov *et al.* [198]. The absolute value of the U can either be estimated from experimental observations [199, 200] or through different computational approaches [201–204].

2.1.5 Methods implementing DFT for electronic structure calculations

DFT based electronic structure methods are classified according to the representation that is used for the Kohn-Sham orbitals. Depending on the nature of the problem addressed, developing accurate and at the same time, efficient numerical representations for solving the Kohn-Sham equations is the biggest challenge in computational material science. In the atomic region, rapid oscillations of the wavefunctions require a fine grid and chemical environment has little effect on the shape of the wavefunction. Therefore, a small basis set would be sufficient if appropriately chosen. On the other hand, in interatomic region, the wavefunction is smooth but very flexible and responds strongly to the environment, which requires large basis sets. In this sub-section, we discuss two different implementations of DFT that are based upon two different basis sets. Both methods have been used in this thesis.

2.1.5.1 Projector Augmented Wave (PAW) method

From solid state point of view, the atoms can be considered as a perturbation of the free electron gas and a very widely used basis set in solid-state calculations is the plane wave expansion. A plane wave basis set has the advantage of being

mathematically simple, and is in principle complete, in contrast to localized basis sets. Exploiting the lattice periodicity using Bloch's theorem [205], the one-electron wavefunctions are expressed in terms of a Fourier expansion using plane waves as a basis set. This approach is of more general interest, also for non-periodic systems, which can be modeled by supercells. Bloch's theorem states that the wavefunction of an electron in a band can be expanded using a discrete set of plane waves. However, a plane wave basis set is poorly suited to expand electronic wavefunctions because a very large number of plane waves are required to expand the tightly bound core orbitals and to represent the rapid oscillations of the wavefunctions of the valence electrons in the core region. The construction of the pseudopotentials removes the rapid oscillations in the wave functions of the valence electrons in the core region, resulting in a smooth valence wavefunction there. Consequently, the pseudo-wavefunctions can be represented by a reasonable number of plane waves, making the method computationally tractable. In the following, we briefly describe the evolution of pseudopotentials which are widely used in the electronic structure calculations. This is important to understand the history and philosophy of the PAW method.

The norm-conserving pseudopotentials (NCPP) were the first in the block of pseudopotentials which were computationally tractable. The NCPPs are generated by putting up the constraint that the norm of the pseudo wave function is same as that of the all electron wave function within some cut-off distance $\mathbf{r}_c$. The condition is mathematically stated as,

$$\int_0^{\mathbf{r}_c} \psi^{PS*}(r)\psi^{PS}(r)r^2\ dr = \int_0^{\mathbf{r}_c} \psi^{AE*}(r)\psi^{AE}(r)r^2\ dr \tag{2.20}$$

ψ^{PS} and ψ^{AE} are the pseudo and all electron wave functions respectively. Though suitable for *sp* elements, this approach becomes intractable for transition metals and rare earth elements as very large plane wave basis sets are required for localized d and f states.

Within norm-conserving pseudopotentials scheme, the idea is that the considered pseudo-wavefunctions should match to the all-electron wavefunctions outside $\mathbf{r}_c$. However, inside $\mathbf{r}_c$, they are allowed to soften as much as possible. With norm-conservation criteria, it is unrealistic to make the pseudopotential dramatically smooth inside $\mathbf{r}_c$. A large plane wave basis set is required which slows down the convergence of the calculations. To overcome this issue, in 1990, Vanderbilt

proposed a new and radical idea for generating ultrasoft pseudopotentials [206–208]. Although this introduces some complications, it greatly reduces the number of plane waves required to construct the basis set. The three-fold complications inherent to the construction of ultrasoft pseudopotential are: (i) since the wavefunctions are not necessarily been normalized, they introduce a non-trivial overlap term in the secular equation, (ii) the pseudo charge density cannot simply be obtained with calculations $\sum \psi^* \psi$ as done with norm-conserving pseudopotentials. Rather, a term is needed to be added in the core region, (iii) relaxation of the norm conservation results in less transferable pseudopotentials. Nevertheless, usage of these pseudopotentials over the years in large-scale calculations proved their reliability in condensed matter calculations and most importantly, the cost of generating these kinds of pseudopotentials is negligible compared to the cost of calculations where they are used.

In spite of the enormous benefits in terms of speed and memory, the major drawback of pseudopotential method is that all the information of the full wave function is lost close to the nuclei which can influence the result obtained in cases of certain properties, such as hyperfine parameters and electric field gradients. Another disadvantage is that there are many adjustable parameters and degrees of freedom for the generation of the pseudopotentials. For this reason, a particular pseudopotential with fixed parameters may not give accurate results under all circumstances. A more general approach introduced by Peter Blöchl in 1994 is the Projector Augmented Wave (PAW) method [177]. The PAW method is a full-potential calculation which keeps the all-electron wavefunction. The main idea of PAW method was to divide the wave function into two parts: partial wave expansion in a sphere around the atom (atomic region) and envelope functions outside the spheres (interstitial region), which are connected by a linear transformation at the sphere radius. PAW unifies all-electron and pseudopotential approaches. A brief description of this formalism is as follows:

In the PAW method, the all electron wavefunction $|\psi_n>$ is represented by a smooth wavefunction after a linear transformation with operator T

$$|\psi_n> = T\,|\tilde{\psi}_n> \tag{2.21}$$

Around each atom, a augmented sphere ($|\mathbf{r} - \mathbf{R}^a| < r_c^a$) is constructed, where r_c^a is the cut-off radius, a is the atom index, $\mathbf{R}^a$ is the atom position. The linear

transformation operator T can be written as

$$T = 1 + \sum_a T^a \tag{2.22}$$

where T^a only acts in the augmentation sphere. Within the augmentation region, the smooth wavefunction can be expanded into smooth partial waves $\tilde{\phi}^a$

$$|\tilde{\psi}_n >= \sum_{ia} c^a_{ni} |\tilde{\phi}^a_i > \tag{2.23}$$

Similarly the all-electron wavefunction can be written as

$$|\psi_n >= \sum_{ia} c^a_{ni} |\phi^a_i > \tag{2.24}$$

The smooth partial wave after linear transformation operation

$$|\phi^a_i >= T\,|\tilde{\phi}^a_i >= (1 + T^a)\,|\tilde{\phi}^a_i > \tag{2.25}$$

As T^a only acts inside the augmented sphere, so the Eq. 2.25 at $r > r^a_c$

$$|\phi^a_i >= |\tilde{\phi}^a_i > \tag{2.26}$$

Now the true wavefunction are expressed as (using Eq 2.19 and 2.12)

$$|\psi_n >= |\tilde{\psi}_n > - \sum_{ia} c^a_{ni} |\tilde{\phi}^a_i > + \sum_{ia} c^a_{ni} |\phi^a_i > \tag{2.27}$$

As the transformation operator T is linear, the coefficient of the smooth partial wave must be scaler product and

$$c^a_{ni} =< \tilde{p}^a_i | \tilde{\psi}_n >\equiv \mathcal{P}^a_{ni} \tag{2.28}$$

where $\tilde{p}^a_i$ are some smooth projector operators. So the transformation operator T become

$$\mathcal{T} = \sum_a \sum_i (|\phi^a_i > - |\tilde{\phi}^a_i >) < \tilde{p}^a_i | \tag{2.29}$$

After the transformation in Eq. 2.29, the Kohn-Sham wavefunction is

$$\begin{aligned} |\psi_n> &= |\tilde{\psi}_n> + \sum_a \sum_i (|\phi_i^a> - |\tilde{\phi}_i^a>) < \tilde{p}_i^a | \tilde{\psi}_n > \\ &= |\tilde{\psi}_n> + \sum_a \Big(\sum_i (|\phi_i^a>< \tilde{p}_i^a | \tilde{\psi}_n > - |\tilde{\phi}_i^a>< \tilde{p}_i^a | \tilde{\psi}_n > \Big) \end{aligned} \tag{2.30}$$

From Eq. 2.30, the wavefunction can be decomposed as the sum of the smooth wavefunctions (smooth everywhere) and sum over the subtraction of one-centered all electron contribution and one-centered pseudo part. Using Eq. 2.30 in Eq. 2.21, one can obtain compact expression for various quantities in PAW method [179, 209–211]. Results presented throughout this thesis have been obtained using the Vienna *Ab Initio* Simulation Package (VASP) [212] using PAW potentials and the generalized gradient approximation (GGA) in the formulation of Perdew, Burke, and Ernzerhof (PBE) [190] as the exchange-correlation functional.

2.1.5.2 Korringa, Kohn and Rostoker (KKR) Green's Function method

To apply density functional theory (DFT) for studying the electronic structure of materials locally perturbed by defect atoms or more generally of disordered dilute and concentrated alloys, a periodic crystal with a large unit cell (supercell) is constructed for employing Bloch's theorem. The Green function methods are appropriate for such situations. The advantage of Green function methods is that the potential must be determined self-consistently only in the region where it noticeably differs from the one of the unperturbed host crystal. As a consequence, Green function methods correctly describe the embedding of the local environment of the defect atoms in the otherwise unperturbed surrounding perfect crystal. One popular scheme employing the Green function method is the Korringa-Kohn-Rostoker (KKR) method.

The KKR method for electronic structure calculation of materials was introduced in 1947 by Korringa [150] and in 1954 by Kohn and Rostoker [151]. In this approach, the scattering properties of each atom center are determined first by a scattering matrix. In the next step, the multiple-scattering theory is applied for solving the equation of one electron scattered at many different potentials (all atomic sites in the lattice). The single scattering and the multiple scattering problems are connected by a condition that the incident wave at each scattering center has to be equal to the sum of the outgoing waves from all the other scattering centers. Due to the above splitting, the structural part is separated from the potential part, which makes the

formalism tractable.

The significant development of the KKR method is made by construction of the Green function. This method is able to produce the crystal Green function accurately by relating it to the Green function of free space via the Dyson equation, which also works efficiently for a system with an impurity in the crystal. So, KKR method with Green function is an extremely robust technique for solving the impurity problem without the construction of huge supercells. This technique is particularly suited for metallic systems but can be also applied for semiconductors and insulators. The KKR Green's Function method can be straightforwardly applied to

1. Systems with impurity
2. Surfaces or arbitrarily layered systems
3. Disordered systems using appropriate alloy theory
4. Calculation of response functions and susceptibility

The key steps in the KKR Green's Function formalism are as described below.

Suppose that the system is composed of an assembly of non-overlapping spherical muffin-tin potentials centered on each lattice site of a crystal. Then, the crystal Green's function $G(\mathbf{r}, \mathbf{r}^{'}; E)$ can be evaluated from the free space Green's function $g(\mathbf{r}, \mathbf{r}^{'}; E)$ by

$$G(\mathbf{r}, \mathbf{r}^{'}; E) = g(\mathbf{r}, \mathbf{r}^{'}; E) + \int dr^{''} g(\mathbf{r}, \mathbf{r}^{''}; E) V(\mathbf{r}^{''}) G(\mathbf{r}^{''}, \mathbf{r}^{'}; E) \tag{2.31}$$

where $V(\mathbf{r}^{'})$ denotes the assembly of muffin-tin potentials. In reality, the above equation can not be used for calculations because of convergence problem. Instead, a cell-centered angular momentum based representation is introduced. Let's first consider the cell-centered representation of $g(\mathbf{r}, \mathbf{r}^{'}; E)$

$$\begin{aligned} g(\mathbf{r} + \mathbf{R_m}, \mathbf{r}^{'} + \mathbf{R_n}; E) &= g(\mathbf{r}, \mathbf{r}^{'} + \mathbf{R_n} - \mathbf{R_m}; E) \\ &= -i\sqrt{E} \sum_{L} J_L(\mathbf{r}) H_L(\mathbf{r}^{'} + \mathbf{R_n} - \mathbf{R_m}) \end{aligned} \tag{2.32}$$

where H_Ls are the Hankel functions. Using the addition theorem of Hankel functions,

$$H_L(\mathbf{r}^{'} + \mathbf{R_n} - \mathbf{R_m}; E) = \frac{i}{\sqrt{E}} \sum_{L^{'}} g_{LL^{'}}^{mn}(E) J_{L^{'}}(\mathbf{r}; E) \tag{2.33}$$

and utilizing the following abbreviations

$$\begin{aligned} J_L(\mathbf{r};E) &= j_\ell(\sqrt{E}r)Y_L(\mathbf{r}) \\ H_L(\mathbf{r};E) &= h_\ell(\sqrt{E}r)Y_L(\mathbf{r}) \end{aligned} \tag{2.34}$$

the free electron Green's function can be expressed as

$$\begin{aligned} &g(\mathbf{r}+\mathbf{R_m},\mathbf{r}^{'}+\mathbf{R_n};E) = -i\sqrt{E}\delta_{mn}\textstyle\sum_L J_L(r_<;E)H_L(r_>;E) \\ &+\textstyle\sum_{LL'} J_L(\mathbf{r};E)g^{mn}_{LL'}J_L(\mathbf{r}^{'};E) \end{aligned} \tag{2.35}$$

The structure constants are defined by

$$g^{mn}_{LL'}(E) = -4\pi i\sqrt{E}(1-\delta_{mn})\sum_{L''} i^{\ell-\ell'+\ell''}C^{L''}_{LL'}H_{L''}(R_m-R_n;E) \tag{2.36}$$

with the Gaunt coefficients

$$C^{L''}_{LL'} = \int d\Omega Y_{L''}(\mathbf{r})Y_{L'}(\mathbf{r})Y_L(\mathbf{r}) \tag{2.37}$$

Similarly, the crystal Green's function has the cell-centered representation as follows,

$$\begin{aligned} &G(\mathbf{r}+\mathbf{R_m},\mathbf{r}^{'}+\mathbf{R_n};E) = -i\sqrt{E}\delta_{mn}\textstyle\sum_L \mathcal{J}_L(r_<;E)\mathcal{H}_L(r_>;E) \\ &+\textstyle\sum_{LL'} \mathcal{J}_L(\mathbf{r};E)G^{mn}_{LL'}\mathcal{J}_L(\mathbf{r}^{'};E) \end{aligned} \tag{2.38}$$

with

$$\begin{aligned} \mathcal{J}_L(\mathbf{r};E) &= P_\ell(\sqrt{E}r)Y_L(\mathbf{r}) \\ \mathcal{H}_L(\mathbf{r};E) &= Q_\ell(\sqrt{E}r)Y_L(\mathbf{r}) \end{aligned} \tag{2.39}$$

The second term, in equation 2.35, represents the contribution of the multiple scattering or back scattering to the Green's function and produces the band structure. The relation between $G^{mn}_{LL'}(E)$ and $g^{mn}_{LL'}(E)$ can be obtained by inserting the above expressions for the Green's function into the integral equation

$$G^{mn}_{LL'}(E) = g^{mn}_{LL'}(E) + \sum_{L''m,} g^{mm^{'}}_{LL'}(E)t^{m^{'}}_{L''}G^{m^{'}n}_{L''L'}(E) \tag{2.40}$$

where t-matrix $t^{m^{'}}_{L''}$ is defined as

$$t^{m^{'}}_{L''} = \int\int d\mathbf{r_m}d\mathbf{r}^{'}_{\mathbf{m}}J_L(\mathbf{r}_{m'};E)t^{m^{'}}(\mathbf{r}_{m'},\mathbf{r}^{'}{}_{m'};E)J_{L'}(\mathbf{r}^{'}{}_{m'};E) \tag{2.41}$$

When the scattering centers are aligned periodically in the crystal, $G^{mn}_{LL'}$ and $g^{mn}_{LL'}$ can be Fourier transformed as,

$$G^{mn}_{LL'}(\mathbf{R}_m - \mathbf{R}_n; E) = \frac{1}{\tau}\int_{\tau} G_{LL'}(\mathbf{k}, E)e^{i\mathbf{k}(\mathbf{R_m}-\mathbf{R_n})}d\mathbf{k} \tag{2.42}$$

$$g^{mn}_{LL'}(\mathbf{R}_m - \mathbf{R}_n; E) = \frac{1}{\tau}\int_{\tau} g_{LL'}(\mathbf{k}, E)e^{i\mathbf{k}(\mathbf{R_m}-\mathbf{R_n})}d\mathbf{k} \tag{2.43}$$

where τ is the volume of the first Brillouin zone. Substituting them into equation 2.40, one gets

$$G_{LL'}(\mathbf{k}, E) = g_{LL'}(\mathbf{k}, E) + \sum_{L''} g_{LL'}(\mathbf{k}, E)t_{L''}G_{L''L'}(\mathbf{k}, E) \tag{2.44}$$

Finally,

$$G_{LL'}(\mathbf{k}, E) = \sum_{L''}[\delta_{L''L} - g_{L''L}(\mathbf{k}, E)t_L]g_{L''L}(\mathbf{k}, E) \tag{2.45}$$

Then, the crystal Green's function is given by

$$\begin{array}{l} G(\mathbf{r}+\mathbf{R_m}, \mathbf{r}^{'}+\mathbf{R_n}; E) = -i\sqrt{E}\delta_{mn}\sum_L \mathcal{J}_L(r_<; E)\mathcal{H}_L(r_>; E) \\ +\mathcal{J}_{Lm}(\mathbf{r})\int \frac{d\mathbf{k}}{\tau} exp(i\mathbf{k}.(\mathbf{R_m}-\mathbf{R_n}))\sum_{L''} g_{LL''}(\mathbf{k}, E)[1-tg(\mathbf{k}, E)]^{-1}_{L''L'}\mathcal{J}_{L'n}(\mathbf{r}^{'}) \end{array} \tag{2.46}$$

The band structure is then calculated by finding the zeros of the determinant of the matrix appearing in equation 2.45 for each $\mathbf{k}$

$$det|\delta_{LL'} - t_L(E)g_{LL'}(\mathbf{k}; E)| = 0 \tag{2.47}$$

The procedure determines the energy eigenvalues as a function of $\mathbf{k}$ and hence, yields an energy dispersion relation $E(\mathbf{k})$. The zeros of the KKR matrix give the poles of the Green's function; each pole corresponds to the eigenstate of the Hamiltonian.

In this thesis, we have extensively used this method for chemically disordered systems. The chemical disorder is treated by coherent potential approximation (CPA), which we discuss in the next section. We have used the Munich group's implementation of the KKR-CPA method as done in their SPRKKR package [180].

2.1.5.3 Coherent Potential Approximation (CPA)

For electronic structure calculations of chemically disordered systems, Coherent Potential Approximation (CPA) has been used widely. P. Soven was first to introduce the CPA method [213]. Later, D. W. Taylor has used this concept for phonons in random alloys [214]. In 1972, B. L. Gyorffy implemented this method in the framework of the multiple scattering theory using Green function technique [215]. Over the years, this method has been used to calculate lattice parameters, elastic constants, mixing enthalpy, etc., for disordered alloys with an accuracy similar to the ordered systems. The main approximation is that the disordered system can be replaced by an ordered effective medium, the potential of which is determined self-consistently. The single-site approximation is used to treat the impurity problem which means that the single impurity is placed in an effective medium and no information is provided about the individual potential and charge density beyond the sphere or polyhedra around this impurity. Let us consider a substitutional alloy $A_aB_bC_c$, . . . , where the atoms A, B, C, . . . are randomly distributed in the lattice sites. Here a, b, c, ... stand for the atomic fractions of the A, B, C, ... atoms, respectively. The Green's function g and the alloy potential P_{alloy} are used to characterize the above system. In real alloy, due to the disorder in the environment, the alloy potential varies uniformly around the same type of atoms. There are two important approximations within the CPA. The first approximation within the CPA is that the local potentials around a certain type of atoms from the alloy are the same, i.e., the effect of the local environment is neglected. These local potentials are described by the potential functions P_A, P_B, P_C, ... Second approximation is that the system is replaced by a monatomic set-up described by the site independent coherent potential $\tilde{P}$. Therefore, the real Green's function g is approximated by the coherent Green's function, $\tilde{g}$. For each alloy component i = A, B, C, . . . a single-site Green's function g_i is introduced. The main steps to construct the CPA effective medium are as follows.

First, the coherent Green's function is calculated from the coherent potential with an electronic structure method.

$$\tilde{g} = \left[S - \tilde{P}\right]^{-1} \tag{2.48}$$

here S denotes the structure constant matrix corresponding to the underlying lattice. Next, the Green's functions of the alloy components, g_is are determined by substituting the coherent potential of the CPA medium by the real atomic potential

P_i, which is given by

$$g_i = \tilde{g} + \tilde{g}\left(P_i - \tilde{P}\right) g_i;\ i = A, B, C \tag{2.49}$$

Finally, the average of the individual Green's functions should reproduce the single-site part of the coherent Green's functions, i.e.,

$$\tilde{g} = a g_A + b g_B + c g_C + ... \tag{2.50}$$

The above three equations are solved iteratively and the output $\tilde{g}$'s and g_i's are used to determine the electronic structure, charge density and total energy of random alloys [216].

2.1.6 Calculation of physical quantities

Elastic moduli and magnetic exchange parameters are the two important physical parameters, used in this thesis, can be obtained from DFT calculations. In the next sub-sections we briefly describe the approaches adopted to calculate these.

2.1.6.1 Calculation of Elastic moduli

The elastic moduli can be derived from the total energy $E(V)$ calculated as a function of volume V or strain e by DFT based methods. In the following, we describe how they are computed.

Bulk Modulus: The bulk modulus (B) describes the behaviour of the crystal volume or lattice parameters under hydrostatic pressure. It is evaluated from the energy-volume $E(V)$ relations. The bulk modulus can be obtained from the Birch-Murnaghan (B-M) isothermal equation of state which is a relationship between the total energy with crystal volume under hydrostatic pressure [217]. The third order B-M equation of state is given by

$$\begin{aligned} E(V) =& E_0 + \frac{9}{16} B V_0 \\ & \times \left\{ \left[\left(\frac{V_0}{V}\right)^{\frac{2}{3}} - 1 \right]^3 B_0' - \left[\left(\frac{V_0}{V}\right)^{\frac{2}{3}} - 1 \right]^2 \left[\left(4\frac{V_0}{V}\right)^{\frac{2}{3}} - 6 \right]^2 \right\} \end{aligned} \tag{2.51}$$

and the related pressure $P(V)$ is given by

$$P(V) = \frac{3B}{2}\left[\left(\frac{V_0}{V}\right)^{\frac{7}{3}} - \left(\frac{V_0}{V}\right)^{\frac{5}{3}}\right]\left\{1 + \frac{3}{4}(B_0' - 4)\left[\left(\frac{V_0}{V}\right)^{\frac{2}{3}} - 1\right]\right\}. \quad (2.52)$$

where V_0 is the equilibrium volume, V is the deformed volume, and B_0' is the derivative of the bulk modulus with respect to pressure. The value of B_0' is almost constant for many substances [218].

Elastic Constants: There are two standard methods for calculating the elastic constants from *ab initio* calculations. One is the energy-strain method and another is the stress-strain method. In this thesis, we employed the energy-strain method where the total energy is calculated as a function of the applied strain [216]. The applied strains are chosen at constant volume as the total energy depends on the volume much more strongly than on strain. The stain matrix $D(e)$, the elements of which are denoted by $e_1, e_2, ..., e_6$, transforms the lattice A with basis vectors x, y, z into the deformed lattice A' with basis vector x', y', z', i.e.

$$\begin{pmatrix} x' \\ y' \\ z' \end{pmatrix} = (D(e) + I)\begin{pmatrix} x \\ y \\ z \end{pmatrix} = \begin{pmatrix} (1+e_1)x & \frac{1}{2}e_6 y & \frac{1}{2}e_5 z \\ \frac{1}{2}e_6 x & (1+e_2)y & \frac{1}{2}e_4 z \\ \frac{1}{2}e_5 x & \frac{1}{2}e_4 y & (1+e_3)z \end{pmatrix} \quad (2.53)$$

where I is the 3×3 identity matrix. In practice, the $e_1, e_2, ..., e_6$ are expressed in terms of δ so that the change in E upon strain is written as

$$E(e_1, e_2, ..., e_6) = E(0) + \frac{1}{2}V \sum_{i,j=1,6} c_{ij} e_i e_j + O(\delta^3) \quad (2.54)$$

where c_{ij}s are the elastic constants. In general the Eq. 2.54 becomes

$$E(\delta) = E(0) + VC\delta^2 + O(\delta^3) \quad (2.55)$$

where C is the particular combination of elastic constants which is obtained by fitting $E(\delta)$ by a polynomial of δ

$$C = \frac{C_2}{V} \quad (2.56)$$

C_2 is the second order coefficient of the polynomial [216].

For a cubic lattice there are three independent elastic constants C_{11}, C_{12} and C_{44}. The corresponding strains are given in the Table 2.1. The compliances of the cubic phase can be obtained from the elastic constants using the following relations:

$$\begin{aligned} S_{44} &= \frac{1}{C_{44}}, \\ S_{11} - S_{12} &= \frac{1}{C_{11} - C_{12}}, \\ S_{11} + S_{12} &= \frac{C_{11}}{(C_{11} - C_{12})(C_{11} + C_{12})}, \end{aligned} \tag{2.57}$$

Table 2.1: Strain for the calculation of elastic constants in the cubic systems. ΔE is the energy change upon strain and V is the equilibrium volume of the lattice.

Strain	Parameter	$\Delta E/V$
C1	$e_1 = e_2 = e_3 = \delta$	$\frac{3}{2}(C_{11} + 2C_{12})\delta^2$
C2	$e_1 = \delta, e_2 = -\delta, e_3 = \frac{\delta^2}{1-\delta^2}$	$(C_{11} - C_{12})\delta^2 + O(\delta^4)$
C3	$e_3 = \frac{\delta^2}{1-\delta^2}, e_6 = \delta$	$2C_{44}\delta^2 + O(\delta^4)$

Throughout this thesis, the strains have been varied from 0.00 to 0.05 with intervals of 0.01. Total energies are calculated for monoclinic and orthorhombic deformations and the elastic moduli (C_{11}, C_{12} and C_{44}) are then obtained by fitting the variation of total energies on the respective strain tensors to a 4th order polynomial equation. In the cubic lattice, the bulk modulus (B) is defined by $B = \frac{1}{3}(C_{11} + 2C_{12})$. The shear elastic modulus (C') is defined by $C' = \frac{1}{2}(C_{11} - C_{12})$. For mechanical stability in the cubic lattice, the conditions are

$$C_{44} > 0, \quad C_{11} > |C_{12}|, \quad C_{11} + 2C_{12} > 0 \tag{2.58}$$

Apart from these, other elastic moduli are relevant when the material is polycrystalline. In a polycrystalline material, the single-crystal grains are randomly oriented. On a large scale, such materials can be considered to be quasi-isotropic or isotropic in a statistical sense. So suitable averaging methods based on statistical mechanics are needed to calculate the polycrystalline elastic moduli. There are two approximation methods to derive the isotropic elastic modulus. They are the Voigt [219] and Reuss [220] averaging methods, which represent the upper and lower bounds respectively of the isotropic elastic modulus. As there are only three independent elastic constants in the cubic crystal, the shear modulus in the Voigt

method is

$$G_V = \frac{1}{5}(C_{11} - C_{12} + 3C_{44}) \tag{2.59}$$

The corresponding one in Reuss method is

$$G_R = \frac{5}{S4_{11} - 4S_{12} + 3S_{44}} \tag{2.60}$$

Finally, the shear modulus (G) are typically the average of Voigt and Reuss elastic moduli based on Hill approximation [221, 222] which is expressed as following:

$$G = \frac{1}{2}(G_R + G_V), \tag{2.61}$$

However, in cases of a number of ferromagnetic Heusler compounds, it was found out that G_v using Voigt formalism is closer to the experimental results [223, 224]. Hence G has been approximated as G_v. The Pugh ratio (G_v/B) and Cauchy pressure (C^P) are the two other important quantities characterising the mechanical properties of a material. Pugh ratio G_v/B [225–227], related to the resistance of the material to plastic deformation, measures whether material is more ductile or more brittle. Compounds having a Pugh ratio greater than 0.57 are considered to be more brittle. On the other hand, Cauchy pressure C^P, calculated as C^P=(C_{12}-C_{44}), provides insight to the nature of bonding in a material with cubic symmetry [228]. A positive value of Cauchy pressure indicates more metallic bonding in the system, while a negative value implies a stronger covalent bonding [229].

2.1.6.2 Calculation of the magnetic exchange interactions

The magnetic pair exchange parameters are computed in order to understand the nature of the magnetic interactions of the systems studied in this thesis. They are efficiently calculated using the multiple-scattering Green's function formalism as implemented in the SPRKKR code [230]. In this approach, the spin part of the Hamiltonian is mapped to a Heisenberg model:

$$H_{Heisenberg} = -\sum_{\mu,\nu}\sum_{i,j} J_{ij}^{\mu\nu} \mathbf{e}_i^{\mu}.\mathbf{e}_j^{\nu} \tag{2.62}$$

μ, ν represent different sublattices; i, j represent atomic positions; and $\mathbf{e}_i^{\mu}$ denotes the unit vector along the direction of magnetic moment at site i belonging to sublattice μ. The $J_{ij}^{\mu\nu}$ are magnetic exchange interactions which are computed from energy difference due to the small orientation of a pair of spins resulting a perturbation in spin-density which within the formulation of Lichtenstein *et al.* [231], based on magnetic force theorem [232] takes the following form

$$J_{ij} = \frac{1}{4\pi}\int_{-\infty}^{E_F} d\epsilon \, \mathrm{Im\ Tr}(\Delta_{\mathrm{i}}\hat{\mathrm{T}}_{\sigma}^{\mathrm{ij}}\Delta_{\mathrm{j}}\hat{\mathrm{T}}_{\sigma\prime}^{\mathrm{ji}}) \tag{2.63}$$

where Δ_i= ($\hat{t}_{i\sigma}^{-1}$-$\hat{t}_{i\sigma\prime}^{-1}$), σ is the spin index, $\hat{t}$ is the single scattering matrix and $\hat{T}$ is the scattering path operator related to the off-diagonal elements of the Green's function. Tr is the trace over the orbital indices of the scatting matrix. Positive (negative) values for J_{ij} indicate ferromagnetic (antiferromagnetic) coupling between atoms i and j.

2.2 Monte Carlo Simulation (MCS) Method

The Monte Carlo simulation method can be considered as an appropriate tool to extend the zero-temperature *ab initio* calculations to finite temperatures. The problems using Monte Carlo method [233] are solved in a stochastic manner, which depends on a sequence of random numbers generated during the simulation so that the equilibrium state at a given temperature T is reached. This method is widely used in statistical physics for computation of the "average" macroscopic observables of a system for which the Hamiltonian (H) is assumed to be known. If the temperature (T) is zero, the system must be in a state of lowest energy.

The thermal average of any observable $A(\mathbf{x})$ in the canonical ensemble is defined as,

$$\langle A(\mathbf{x})\rangle_T = \frac{1}{Z}\int d\mathbf{x}\, e^{-H(\mathbf{x})/k_BT} A(\mathbf{x}) \tag{2.64}$$

$$Z = \int d\mathbf{x}\, e^{-H(\mathbf{x})/k_BT} \tag{2.65}$$

The vector $\mathbf{x}$ in phase space represents the set of variables describing the degrees of freedom of the system. For example, the spin degrees of freedom, $\mathbf{x} = (S_1, S_2, S_3, ..., S_N)$ in case of Ising Hamiltonian. A central property of statistical physics is the probability density ρ which describes the statistical weight with which

the configuration $\mathbf{x}$ occurs in thermal equilibrium:

$$\rho(\mathbf{x}) = \frac{1}{Z} e^{-H(\mathbf{x})/k_B T} \tag{2.66}$$

The probability density ρ is the normalized Boltzmann factor. A problem arises due to the fact that the exact description in equation 2.66 contains an overwhelming amount of information, impossible to compute. Thus, an approximation for the exact equation 2.64 is required. The idea of the Monte Carlo simple sampling method is to substitute the exact equation, where integration is performed over all states $\{\mathbf{x}\}$ with their proper weights $\rho(\mathbf{x})$, using only a characteristic subset of phase space points $\{\mathbf{x}_1, \mathbf{x}_2, ..., \mathbf{x}_L\}$ that are used as a statistical sample. In numerical integration routines integrals are replaced by sums. Thus, in the limit $M \to \infty$ the discrete sum in Eq. 2.67 approximates equation 2.64.

$$\overline{A(\mathbf{x})} = \frac{\sum_{i=1}^{L} e^{-H(\mathbf{x}_i)/k_B T} A(\mathbf{x}_i)}{\sum_{i=1}^{L} e^{-H(\mathbf{x}_i)/k_B T}} \tag{2.67}$$

There are two common routines to choose the points $\mathbf{x}_i$. In the simple sampling technique the points $\mathbf{x}_i$ are set up with equal probability. They are chosen randomly or according to a regular grid. But this procedure has severe disadvantages, especially at low temperatures, where only few states dominate the sum in Eq. 2.67 while the main part of the phase space points are irrelevant. In order to cure this problem the method of importance sampling has been introduced in which the points $\mathbf{x}_i$ are chosen with a certain probability $\mathrm{P}(\mathbf{x}_i)$. This ensures that only the points which matter, are selected. Equation 2.67 is then written as,

$$\overline{A(\mathbf{x})} = \frac{\sum_{i=1}^{L} e^{-H(\mathbf{x}_i)/k_B T} \mathrm{P}^{-1}(\mathbf{x}_i)\, A(\mathbf{x}_i)}{\sum_{i=1}^{L} e^{-H(\mathbf{x}_i)/k_B T} \mathrm{P}^{-1}(\mathbf{x}_i)} \tag{2.68}$$

The most natural choice for $\mathrm{P}(\mathbf{x}_i)$ would be $\mathrm{P}(\mathbf{x}_i) \propto exp[-H(\mathbf{x}_i)/k_B T]$. Then the Boltzmann factor cancels out and equation 2.67 reduces to a simple arithmetic average:

$$\overline{A(\mathbf{x})} = \frac{1}{L}\sum_{i=1}^{L} A(\mathbf{x}_i) \tag{2.69}$$

Thus the observables i.e. energy, magnetization etc. are be obtained. For the construction of the points according to the Boltzmann distribution the so called Markov process is used.

2.2.1 Markov process

Following the Markov process, a new state $\mathbf{x}_i'$ is constructed from a given state $\mathbf{x}_i$ with respect to a given transition probability $\mathrm{W}(\mathbf{x}_i \to \mathbf{x}_i')$. Based on a given starting state a chain of states is built, known as Markov chain, finally resulting in the states with Boltzmann distribution $\mathrm{P}_{eq}(\mathbf{x}_i) = \frac{1}{Z} exp[-H(\mathbf{x}_i)/k_B T]$. A sufficient condition to achieve this is to impose the principle of detailed balance

$$P_{eq}(\mathbf{x}_i)\, W(\mathbf{x}_i \to \mathbf{x}_i') = P_{eq}(\mathbf{x}_i')\, W(\mathbf{x}_i' \to \mathbf{x}_i) \tag{2.70}$$

Equation 2.70 implies that only the energy change $\delta H = H(\mathbf{x}_i') - H(\mathbf{x}_i)$ defines the ratio of the transition probabilities for a "move" $\mathbf{x}_i' \to \mathbf{x}_i$ and the inverse move $\mathbf{x}_i \to \mathbf{x}_i'$,

$$\frac{W(\mathbf{x}_i \to \mathbf{x}_i')}{W(\mathbf{x}_i' \to \mathbf{x}_i)} = \frac{P_{eq}(\mathbf{x}_i')}{P_{eq}(\mathbf{x}_i)} = exp[-\delta H/k_B T] \tag{2.71}$$

As Eq. 2.71 is ambiguous, several options for the choice of W exist. One of them is given by the Metropolis algorithm.

2.2.2 Metropolis algorithm

In the Metropolis algorithm [234] the transition probabilities are given as

$$\begin{aligned} W(\mathbf{x}_i \to \mathbf{x}_i') &= exp(-\delta H/k_B T), \quad if\ \delta H > 0 \\ &= 1, \qquad\qquad\qquad\quad \text{Otherwise} \end{aligned} \tag{2.72}$$

The transition to the new state will be realized in case the new state is lower

in energy. If this is not the case the transition will only occur with the probability given by the exponent. The algorithm proceeds as follows: first an appropriate starting state $\mathbf{x}_i$ is set up. Then a new state $\mathbf{x}'_i$ is chosen randomly. As a next step the energy difference $\delta H = H(\mathbf{x}'_i) - H(\mathbf{x}_i)$ is calculated and the transition is carried out if $\delta H < 0$, i.e. if the energy of the new state is lower than the energy of the old state. Otherwise, the exponent $R = exp(-\frac{\delta H}{k_B T})$ has to be calculated which defines the transition probability. This is implemented in the simulation by choosing randomly a number $0 < r < 1$. If $r < R$, the system will adopt the new state. Otherwise, it remains in the old state. The random selection of a new state is carried out again and the whole procedure is repeated.

2.2.3 Calculation of Curie temperature (T_c)

Using the MCS method, the second order magnetic transition temperature i.e. the Curie temperature (T_c) is estimated. Heisenberg model (Eq. 2.62) is considered to construct the Hamiltonian. In this model, $\mathbf{e}_i = (e_i^x, e_i^y, e_i^z)$ is a classical Heisenberg spin variable and $|\mathbf{e}_i| = 1$ at lattice site i. We have used the magnetic exchange interaction ($J_{ij}^{\mu\nu}$), calculated using SPRKKR code [180]. In the MC simulations, the initial spin states are randomly sampled and the acceptance or rejection of the spin states is determined by Metropolis algorithm [234]. For a given site, the components of spin state are randomly chosen in the following manner [182]: two random numbers r_1 and r_2 are chosen in the interval of [0, 1] to produce a vector with two components $\xi_1 = 1-2r_1$ and $\xi_2 = 1-2r_2$. The length of the vector is determined by $\xi^2 = \xi_1^2 + \xi_2^2$. If $\xi^2 < 1$, then the new spin components are $e^x = 2\xi_1\sqrt{1-\xi^2}$, $e^y = 2\xi_2\sqrt{1-\xi^2}$ and $e^z = 1 - \xi^2$. After selecting the new spin components, we calculate the change in energy (ΔH) of the system. If ΔH is negative then the new spin state is accepted. Otherwise, the new spin state is accepted with probability $e^{-\Delta H/k_B T}$. The above procedure is continued for all the sites. When all the sites are covered, one Monte Carlo step is finished. The system evolves using MC algorithm for several MC steps till it reaches equilibrium that is, when the total energy of the system does not change significantly with MC step. The statistics are then calculated from the significant number of configurations. The total magnetization is calculated using the Eq. 2.73. The Curie temperature is estimated from the susceptibility [176, 223], (Eq. 2.74).

$$M = \langle \sum_i \mathbf{e}_i \rangle_T / N \tag{2.73}$$

$$\chi = \frac{1}{N} \sum_i^N \frac{\langle M^2 \rangle - \langle M \rangle^2}{k_B T} \tag{2.74}$$

where N is the number of sites.

It is worth mentioning that we have used another approach for calculation of T_c, the mean field approximation (MFA) [181]. This is done in order to check the qualitative consistency in the computed results. The MFA is known to overestimate or underestimate T_c while the MCS method is more accurate quantitatively. The Curie temperature within the mean field approximation for a multi-sublattice material can be obtained by solving the system of coupled equations [181, 223, 235]

$$\langle \mathbf{e}^\mu \rangle = \frac{2}{3k_B T} \sum_\nu J_0^{\mu\nu} \langle \mathbf{e}^\nu \rangle \tag{2.75}$$

where $\langle \mathbf{e}^\nu \rangle$ is the average z component of $\mathbf{e}_i^\nu$ and $J_0^{\mu\nu} = \sum_i J_{0i}^{\mu\nu}$. Eq. 2.75 can be expressed in the form of an eigenvalue matrix problem

$$(\mathbf{\Theta} - T\mathbf{I})\mathbf{E} = 0 \tag{2.76}$$

$\Theta_{\mu\nu} = \frac{2}{3k_B T} J_0^{\mu\nu}$, $\mathbf{I}$ is a unit matrix and $\mathbf{E}$ is the vector of $\langle \mathbf{e}^\nu \rangle$. The largest eigenvalue of matrix $\mathbf{\Theta}$ determines the value of the Curie temperature [181].

2.2.4 Calculation of Magnetocaloric parameters

For estimation of the MCE parameters, i.e., isothermal change in magnetic entropy (ΔS_{mag}) or adiabatic temperature change (ΔT_{ad}) under an applied magnetic field, we have used Monte Carlo simulation on a model Hamiltonian that uses the degenerate Blume-Emery-Griffiths (BEG) model and a mixed q-states Potts model. The Hamiltonian was chosen such that it accommodates, along with magnetic and structural degrees of freedom, the coupling between the two [108, 111, 120, 172]. The Monte Carlo simulation using the classical Heisenberg Hamiltonian treats the spins as classical variables which may take on continuous values and hence does not reproduce the saturation value of the magnetic entropy [111]. Thus, in order

to calculate the saturation value of the magnetic entropy, we have used the q-state Potts model, in which the spin variables can take discrete values.

The model Hamiltonian ($H_{BEG-Potts}$) consists of three parts: (a) the magnetic contribution due to the magnetic degrees of freedom of the system, H_m; (b) the elastic contribution due to the structural transformation from cubic to tetragonal phases, H_{els}; and (c) the contribution arising from the coupling of magnetic and structural interactions, H_{int}.

$$H_{BEG-Potts} = H_m + H_{els} + H_{int} \tag{2.77}$$

The magnetic subsystem is described by a mixed q-states Potts model [111, 171, 172, 175, 176], which allows for both first- and second-order phase transitions, where q is the number of spin states for magnetic atoms.

$$H_m = -\sum_{<i,\,j>}^{NN} J_{ij}\delta_{S_i,\,S_j} - g\mu_B\mu_0 H_{ext}\sum_{i}^{N}\delta_{S_i,\,S_g} \tag{2.78}$$

Here, the first term represents the magnetic interactions at different lattice sites; $J_{i,j}$ being the exchange parameters involving sites i and j, S_i the spin defined on the lattice site $i = 1, 2, ..., N$ and N the total number of atoms considered in the simulation cell. The second term represents the coupling of the spin system to the external magnetic field H_{ext} along the direction of ghost spin variable S_g. μ_{B} is the Bohr magneton, g is the Lande factor (here g=2).

The degenerate Blume-Emery-Griffiths (BEG) model [173, 174], which allows one to describe the interaction between the elastic variables, was used to address the mutual influence of magnetic ordering and structural transitions. The energy of the system undergoing structural transformation can be represented by,

$$H_{els} = -J\sum_{<i,\,j>}^{NN}\sigma_i\sigma_j - K\sum_{<i,\,j>}^{NN}(1-\sigma_i^2)(1-\sigma_j^2) - k_BT\ln(p)\sum_{i}(1-\sigma_i^2) \\ -K1g\mu_B\mu_0 H_{ext}\sum_{i}^{NN}\delta_{\sigma_g\sigma_i}\sum_{<i,\,j>}^{NN}\sigma_i\sigma_j \tag{2.79}$$

where σ is the strain parameter. It denotes the structural state of the lattice site and takes the value 0 for cubic or undistorted state, +1 or -1 for the tetragonal

or distorted state. J and K are structural exchange constants for tetragonal and cubic states respectively, p is the degeneracy factor characterizing the number of tetragonal states, $K1$ is the dimensionless magneto-elastic interaction, and T is the temperature of the system. The third term accounts for the higher configurational entropy in the cubic phase. The last term accounts for the energy contribution due to the changes in the structural states under the influence of the external magnetic field. The structural states are coupled to the external magnetic field through the ghost spin state σ_g. The sign of the magneto-elastic parameter, $K1$, indicates the favored structural state (cubic or tetragonal), in presence of an external magnetic field. For $K1 > 0$, energy is removed from the system in a tetragonal state, so that the tetragonal (distorted) state is favored over cubic state by the external magnetic field, while for $K1 < 0$, energy is added to the system in a tetragonal state so that the cubic state is favored. In essence, $K1 > (<)0$ if T_M increases(decreases) in the presence of external magnetic field.

$$H_{int} = 2 \sum_{<i,\,j>}^{NN} U_{ij}\delta_{S_i,\,S_j}(\frac{1}{2} - \sigma_i^2)(\frac{1}{2} - \sigma_j^2) - \frac{1}{2}\sum_{<i,\,j>}^{NN} U_{ij}\delta_{S_i,\,S_j} \tag{2.80}$$

In the magneto-elastic part (equation 2.80) of the Hamiltonian, the first term describes the effective coupling of magnetic sub-lattice to the modulation of the lattice, while the last term renormalizes the spin-spin interaction. U_{ij} is the magneto-elastic interaction parameter.

This Hamiltonian (equation 2.77) was used for Monte Carlo calculations using the following procedure:

1. For all the magnetic and lattice sites in the supercell, values of initial spin (S_i) and strain (σ_i) were chosen as 1.

2. First, one arbitrary lattice site was chosen, and the initial elastic energy contribution ($H_{els}^{initial}$) from that site was calculated using equation 2.79. For $\sigma_i = 0$, the site's energy contribution was calculated on a cubic lattice, while for $\sigma_i = +1$ or $\sigma_i = -1$, the energy was calculated on a tetragonal lattice. This was also done while calculating the magnetic and coupled contributions of the Hamiltonian.

3. For the same site i, the strain parameter σ_i was changed randomly. The elastic energy of the new configuration, H_{els}^{final}, was calculated. The change in the

elastic energy of the system, $(H_{els}^{final} - H_{els}^{initial})$, was then computed.

4. The new system configuration i.e., the lattice with a new strain parameter on that particular site was accepted or rejected based on the Metropolis algorithm [182, 236, 237]. If $H_{els}^{final} \leq H_{els}^{initial}$, The new system configuration was accepted; else a ratio R is calculated

$$R = \exp(-(H_{els}^{final} - H_{els}^{initial})/k_B T) \tag{2.81}$$

A random number (r; 0 < r < 1) is generated, and if $R > r$, the new configuration was accepted.

5. The next step was to find the new spin state for the site i. The total energy of the system, $H^{initial}$, was calculated using equation 2.77. The spin state of site i was then changed randomly, and the energy of the new configuration, H^{final}, was calculated. The new system configuration (site i with new spin parameter) was then accepted or rejected based on the Metropolis Algorithm, as described in the previous step.

6. The steps (2) - (5) were then repeated by moving through the lattice sites. Once all the lattice sites were swept, one Monte Carlo step (MCS) was completed.

At a given temperature, the system was first equilibrated by repeating the above Monte Carlo steps. Then the magnetic order parameter (m) and strain order parameter (ε) of the equilibrated system for a given temperature were calculated as,

$$\mathrm{m} = \frac{1}{N} \sum_{i}^{n} \frac{(q_i N_i^{max} - N_i)}{q_i - 1} \tag{2.82}$$

$$\varepsilon = \frac{1}{N} \sum_{i} \sigma_i \tag{2.83}$$

Where i in equation (2.82) denotes a magnetic atom type, n the total number of magnetic atom types, q_i the total number of spin states of the atom of type i, N_i^{max} is the maximum number of atoms of type i with the same spin state, N_i is the total

number of atoms of type i, N is the total number of atoms in the system.

The magnetic specific heat ($C_{\rm mag}$), the magnetic entropy ($S_{\rm mag}$) and total specific heat, $C = C_{\rm lat} + C_{\rm mag}$ with lattice and magnetic contributions were then calculated. We have neglected the electronic part of the specific heat. For the lattice heat, we have used the standard Debye approximation. Finally, the magnetocaloric parameters i.e. the isothermal changes in magnetic entropy (ΔS_{mag}) and the adiabatic temperature change (ΔT_{ad}) due to the application of an external field, were calculated by equation (2.87) and (2.88) respectively.

$$C_{mag}(T, H_{ext}) = \frac{1}{N}\sum_{i}^{N} \frac{\langle H^2\rangle - \langle H\rangle^2}{k_B T^2} \tag{2.84}$$

$$\mathrm{S}_{mag}(T, H_{ext}) = \frac{1}{N}\int_0^T dT \frac{C_{mag}(T, H_{ext})}{T} \tag{2.85}$$

$$C_{lat}(T, \Theta_{\rm D}) = 9RN_i\Big\{4\Big(\frac{T}{\Theta_{\rm D}}\Big)^3 \int_0^{\Theta_{\rm D}/T} dx \frac{x^3}{e^x - 1} - \Big(\frac{\Theta_{\rm D}}{T}\Big)\frac{1}{e^{(\Theta_{\rm D}/T)} - 1}\Big\} \tag{2.86}$$

$$\Delta S_{mag}(T, H_{ext}) = S_{mag}(T, H_{ext}) - S_{mag}(T, 0) \tag{2.87}$$

$$\Delta T_{ad}(T, H_{ext}) = -T\frac{\Delta S_{mag}(T, H_{ext})}{C(T, H_{ext})} \tag{2.88}$$

We have developed the code implementing this method to calculate the magnetocaloric quantities for the systems of interest in this thesis. The benchmarking of our in-house Monte Carlo code is presented in the appendix by running calculations on a number of systems where results, both experimental and theoretical, pre-exist.

2.3 Summary

In this chapter, we have briefly described the computational techniques i.e., DFT based methods for the calculations of ground state properties and Monte Carlo simulations for calculations of temperature-dependent magneto-structural properties relevant for the study of the materials investigated in this thesis. We have extensively used two different implementations of DFT: PAW method as implemented in the VASP and Green's function based KKR method as implemented in the SPRKKR package. Armed with the information from the *ab initio* methods, finite temperature properties are calculated with the in-house Monte Carlo code, using various model Hamiltonians. Various thermodynamic models like Heisenberg, q-state Potts and BEG models have been used to construct the model Hamiltonians. We have provided a comprehensive discussion of the models and the contexts in which they are used.

Chapter 3

Role of composition, site ordering and magnetic structure for structural stability in Ni and Mn excess off-stoichiometric Ni_2MnSb

3.1 Introduction

The most important feature driving the giant magnetocaloric effect in a material is the presence of first-order martensitic phase transition (MPT) accompanied with a significant change in magnetization. Unlike the prototype magnetic shape memory Ni-Mn-Ga family, Ni-Mn-Z (Z=In, Sn, Sb) Heusler alloys undergo MPT from high temperature $L2_1$ parent austenite phase to a low temperature tetragonal or orthorhombic martensite phase resulting in many exotic properties, only in off-stoichiometric compositions with substantial Z-deficiency [113, 238–241]. The off-stoichiometric Sb-deficient Ni-Mn-Sb systems exhibit giant magnetocaloric effect associated with the MPT near room temperature [130, 132] drawing special attention. Extensive experimental investigations, as discussed in chapter 1, have revealed that MPT and associated properties in Ni-Mn-Sb alloys crucially depend on the concentration ratio of Ni, Mn and Sb. The martensitic transformation is observed in $Ni_2Mn_{1+x}Sb_{1-x}$ alloys for $x \geq 0.4$ [242]. Complex magnetic structure with short-range correlations are also predicted. The observed decrease of magnetic moment with increasing electron-atom ratio e/a; a behaviour opposing the general trend in Heusler compounds, is attributed to the presence of these anti-ferromagnetic corre-

The contents of this chapter are published in Physical Review B **99**, 064112 (2019)

lations. Similar features are observed by Khan *et al.* [243]. Experiments on systems with low Sb concentration (between 0.44 and 0.48) with either Ni content being fixed [96, 132] or varying in a way to make the system Ni-deficient [146, 243], observed significant inverse magnetocaloric effect and exchange bias. All these experimental results pointed towards the presence of substantial anti-ferromagnetic interactions present due to excess amount of Mn occupying presumably the Sb sites. The experiments, though wonderfully established the potential multi-functional traits in Ni-Mn-Sb systems, certain fundamental questions remain to be answered. The systems investigated were always Sb-deficient and Mn-excess. This propels one to examine the role of composition on the properties, in particular the impact on the stabilities of the high-temperature austenite and the low-temperature martensite phases. Coupled with this is the question regarding the impact of site ordering in the system on its physical properties. Previous studies on off-stoichiometric Ni-Mn-Z (Z=Sn, Ga, In) showed that in the off-stoichiometric compositions, the excess atom does not always prefer to occupy the deficient atom site. The magnetic structure, as a consequence of this, also plays an important role in deciding the phase stability and the associated properties. For example, Hu *et al.* [244] showed that, for most of the off-stoichiometric Ni_2MnGa, though the excess atoms of the rich component occupy the deficient atom sites, in cases of Ga-rich alloys, the excess Ga atoms always prefer the Mn sites irrespective of whether the system is Mn-deficient or not. For Ni-deficient Ga-excess Ni_2MnGa systems, some of the Mn atoms move to the Ni sites and the excess Ga atoms occupy the Mn sites. For $Ni_2Mn_{1+x}Sn_{1-x}$, it was shown that the experimental phase diagram for Curie temperature can be verified only when an intermixing of Mn and Sn atoms is considered [223]. Li *et al.* [245] suggested a possibility of Mn-In ordering for Mn-excess off-stoichiometric $Ni_2Mn_{1+x}In_{1-x}$ compositions. They showed that magnetic ordering in the system can affect the martensitic phase transition significantly. It was found that if there is ferromagnetic (FM) coupling between the Mn atoms at Mn and In sites then no MPT occurs whereas for anti-ferromagnetic (AFM) coupling, MPT occurs in the system. For $Mn_2Ni_{1+x}Sn_{1-x}$ [246] also, an intricate relation between the site occupancy, magnetic ordering and the stability of the martensite phase was observed. Thus a knowledge of the site-occupancy will be essential for Ni-Mn-Sb systems for investigation of its physical properties. Detailed and systematic investigation about the effects of site ordering and magnetic structure on phase stability for compositions beyond those considered in the experiments would help understand the fundamental physics of the system and help choose the composition ranges where practical

applications due to the presence of MPT are most suitable.

Since relative stabilities of phases is central towards other novel features of this system, finding a good predictor for martensitic transformation temperature (T_M) is important. The electron-atom ratio (e/a) has been identified to be a predictor of T_M for systems undergoing martensitic transformations: a larger e/a indicates a higher T_M [247–249]. However, such a connection is coarse grained and fails in some situations. For the same e/a ratio, changes in atomic order (site occupancy) also can change the T_M. For example, replacement of Ga by Al or In and variations in the long-range atomic order changed T_M without altering the e/a ratio [250–253]. This is also true for Ni-Mn-Sb alloys. Although T_M varies as e/a for $Ni_2Mn_{1+x}Sb_{1-x}$ [242] and for $Ni_{2-x}Mn_{1.56+x}Sb_{0.44}$ [146], Khan *et al.* [254] concluded from their experiments on $Ni_{2+x}Mn_{1.52-x}Sb_{0.48}$ that rather than the e/a, the hybridization between Ni and excess Mn $3d$ states is responsible for variations in the T_M. On the other hand, for some compounds undergoing MPT, T_M is found to be closely related to elastic shear modulus C': the lower the shear modulus, calculated in the austenite phase, the higher the T_M will be [255, 256]. Various off-stoichiometric Ni_2MnGa alloys also show this T_M dependence on C' [244, 257]. The total energy difference ΔE between the high temperature parent austenite phase and the low temperature tetragonal martensite phase is another quantity to correlate T_M and C' with the composition of the compounds. A higher ΔE corresponds to a higher T_M [258, 259]. It is therefore, of fundamental interest, to correlate the trend of variation in T_M for off-stoichiometric Ni-Mn-Sb compositions with these physical quantities and decide the best predictor of T_M.

In this chapter, we present a systematic study over the entire composition range in Mn and Ni-excess off-stoichiometric Ni_2MnSb systems to explore the importances of various physical factors affecting the phase stability. To this end, we have systematically explored the importances of composition, atomic ordering and magnetic structure and the consequences on phase stability and various properties. The microscopic origin of the observed features has been interpreted from the composition, site-ordering and magnetic ordering dependent electronic structures. We have tried to address the reasons behind choice of Sb-deficient systems in experiments, how critical the role of relative compositions of Ni and Mn are in effecting martensitic transformation, how site occupancy and magnetic structure are intricately related with one another to impact the phase stability and also provided a predictor for martensitic transformation temperature, one that is independent of the details of the off-stoichiometry.

3.2 Computational Details

In the present work, electronic structure calculations were done with spin-polarized density functional theory (DFT) based projector augmented wave (PAW) method as implemented in Vienna *Ab initio* Simulation Package (VASP) [177–179]. The valence electronic configurations used for the Ni, Mn and Sb PAW pseudopotentials are $3d^8 4s^2$, $3d^6 4s$ and $5s^2 5p^3$, respectively. For all calculations, we have used the Perdew-Burke-Ernzerhof implementation of generalized gradient approximation for exchange-correlation functional [190]. An energy cut off of 550 eV and a Monkhorst-Pack $11 \times 11 \times 11$ k-mesh was used for self consistent calculations. A larger k-mesh of $15 \times 15 \times 15$ was used for the density of states calculations of all the structures. The convergence criteria for the total energies and the forces on individual atoms were set to 10^{-6} eV and 10^{-2} eV/Å respectively for all calculations. The elastic constants for the compounds are calculated using energy-strain method for high-temperature cubic austenite phases, as discussed in Chapter 2.

3.3 Results and Discussions

In the present work, we have focused on understanding the physics related to MPT and the trend in associated properties with compositional changes considering four off-stoichiometric Ni_2MnSb systems: (1) $Ni_2Mn_{1+x}Sb_{1-x}$ (sys1), (2) $Ni_{2-x}Mn_{1+x}Sb$ (sys2), (3) $Ni_{2+x}Mn_{1-x}Sb$ (sys3) and (4) $Ni_{2+x}MnSb_{1-x}$ (sys4). The modelling with any arbitrary composition within the formalism employed, requires large supercell and hence is computationally demanding. Hence, we have considered compositions with $x = 0, 0.25, 0.50$ and 0.75. To model the chemical substitution we have taken a 16-atom conventional cubic cell. Thus, chemical substitution of 25%, 50% and 75% can be modelled by successive replacement of the atoms of one of the constituents. For example, to make a 25% Mn-excess $Ni_2Mn_{1.25}Sb_{0.75}$ composition, one Sb atom out of the four in the conventional cell is to be replaced with one Mn atom. Such modelling strategy has worked for many other substituted systems in the Heusler family [144, 246, 260].

3.3.1 Site preference and magnetic ground state

Site-occupancy of different atoms for a fixed composition of a system has great importance in deciding the physical properties. Sánchez-Alarcos *et al.* [253] showed that quenching temperature and the subsequent heat treatment change the degree

of the $L2_1$ long-range atomic order i.e. the site occupancy of the alloy and this is a very important issue affecting the martensitic transformation temperature (T_M) in Ni_2MnGa based alloys. Hence before proceeding with investigation on the phase stability and other physical properties, the preferred site-occupation patterns are decided for all the systems considered.

For each of the four systems and compositions considered, possible configurations due to different site occupancy and magnetic structures are listed in Table 3.1 and Table 3.2. At high temperature regular Heusler $L2_1$ cubic structure of Ni_2MnSb [146, 261], the Sb atoms and Mn atoms occupy 4a (0, 0, 0) and 4b (0.50, 0.50, 0.50) Wyckoff positions respectively and Ni atoms occupy the 8c ((0.25, 0.25, 0.25) and (0.75, 0.75, 0.75)) sites [Figure 3.1(a)]. Taking the Mn-excess at Sb site, $Ni_2Mn_{1+x}Sb_{1-x}$ (sys1) system as an example, for $x = 0.25$, there exist two different possible site-occupation configurations: (i) the normal site occupation [Figure 3.1(b)] where 25% excess Mn atoms occupy the deficient Sb sub-lattice and (ii) the abnormal site occupation [Figure 3.1(c)] where 25% excess Mn atoms occupy the Ni sub-lattice and consequently the Ni atoms occupy the deficient Sb sub-lattice. For $x = 0.50$ and $x = 0.75$, the same way there are three and four different possible site-occupation configurations respectively. For all the cases, configuration "S-a" is the normal site-occupation configuration. For all compositions, the following nomenclature has been followed : if there are two types of a particular atom, say X, present, then X atom at its original site is denoted as X1, whereas it is denoted as X2 at other than its own site. If there are three types of a particular atom X present then X1 is the atom at its own site, X2 is the atom at the site originally for any other constituent but the constituent has deficiency in its composition with respect to Ni_2MnSb, X3 is the atom at site other than these two.

The preferred site-occupancy and the corresponding ground state magnetic configuration for a particular system and composition is determined by comparing the electronic energies (E_0) and the free energies (F) of the configurations considered. The stable site-occupancy is determined by the relative free energy ΔF; the reference being the energy of the configuration with normal site occupancy and the magnetic structure corresponding to that which produces the lowest energy E_0. The relative free energy is determined as,

$$\Delta F = \Delta E_0 - T\Delta S \tag{3.1}$$

The entropy S includes contributions from chemical mixing, lattice vibrations

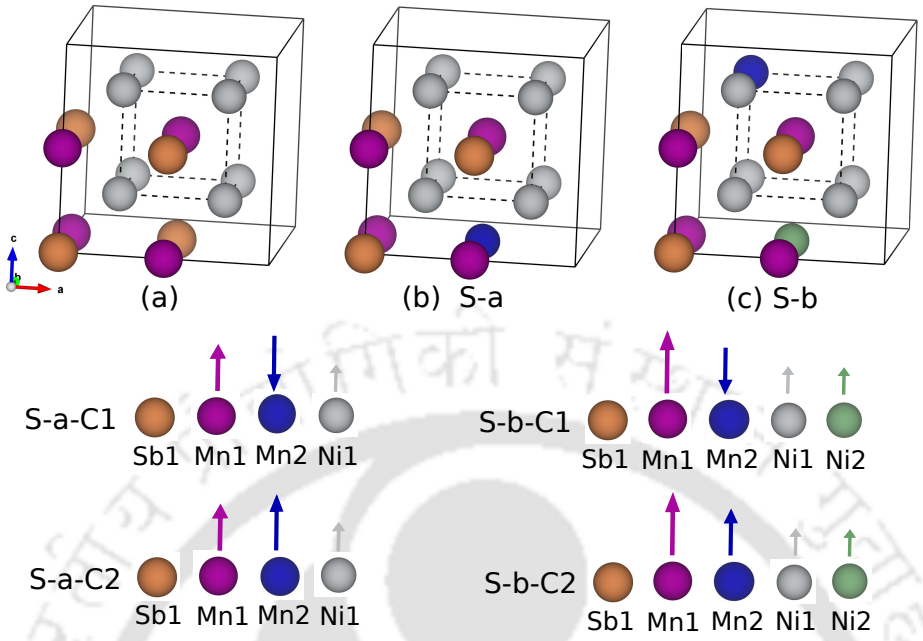

Figure 3.1: 16-atom supercells for (a) stoichiometric Ni_2MnSb and (b)-(c) off-stoichiometric $Ni_2Mn_{1+x}Sb_{1-x}$ (sys1) with x=0.25 for (b) normal site-occupation configuration ("S-a") and (c) abnormal site-occupation configuration ("S-b") respectively. "S-a-C1" - "S-a-C2" indicate the possible different magnetic configurations corresponding to "S-a" site configuration and "S-b-C1" - "S-b-C2" indicate the same corresponding to "S-b". Different types of atoms have been referred by their corresponding colour. The arrows indicate the spin orientations of the atoms with respect to z axis. An uparrow indicates positive z direction or spin up. The magnetic configurations "C1" and "C2" are explained in Table 3.1

.

and magnetic excitations,

$$S = S_{mix} + S_{vib} + S_{mag} \tag{3.2}$$

The chemical mixing entropy for a given configuration is determined as

$$S_{mix} = -\frac{1}{4} k_B \sum_{i=1}^{n} \sum_{j=1}^{4} x_{ij} ln x_{ij} \tag{3.3}$$

Where x_{ij} is the concentration of i^{th} component at j^{th} sublattice, n is the number of components at corresponding sub-lattices, k_B is the Boltzmann constant. For compositions considered in this chapter, the 8c site is treated as two degenerated

sublattices where different types of atoms are present at equal concentrations. The entropy difference between configurations due to lattice vibrations is approximated by the high-temperature expansion and given as [262]

$$\Delta S_{vib} \sim 3k_B \left(\Delta\Theta/\Theta\right) \tag{3.4}$$

In the simplest approximation, the Debye temperatures Θ are proportional to $\sqrt{rB}$ [263], where r is the Wigner-Seitz radius and B is the bulk modulus. The contributions of the magnetic excitations to the entropy is calculated invoking the Disordered Local Moment [264] to approximate the fully spin disordered phase. In the mean field approximation, the entropy due to magnetic disorder is given as [265]

$$S_{mag} = k_B \sum_i ln(\mu_i + 1) \tag{3.5}$$

μ_i is the magnetic moment of the i-th component. In all cases, the contribution of ΔS_{vib} is at least 1 to 2 orders of magnitude smaller than that of ΔS_{mix}. Similarly, ΔS_{mag} is at most of the order of ΔS_{vib} in some cases (For example, ΔS_{mag} for S-b-C1 configuration of sys1 with $x = 0.25$ is only 0.00367 meV/K) even after consideration of fully spin disordered phase. Therefore, the contributions from lattice vibrations and magnetic excitations are neglected in total ΔS as at ambient condition of T=300 K and at typical annealing temperature of the order of 1000 K, their contributions are not significant enough towards ΔF. In what follows, in Table 3.1 and Table 3.2, alongside ΔE_0, the relative energy with respect to the minimum total energy, we present only the values of ΔS_{mix}. It can be noted that even at the typical annealing temperature of the order of 1000 K, the ΔF comprising of contributions of only mixing entropy, will have the same trend as ΔE_0. Therefore, in the temperature range of interest, the mixing entropy cannot change the relative stability of the different site occupations and magnetic configurations. Thus, consideration of the relative electronic energy (ΔE_0) is sufficient to determine the preferred site and the magnetic configuration.

From Table 3.1, it can be seen that for all the compositions in Mn-excess off-stoichiometric systems (i.e. sys1 and sys2), the normal site occupation (i.e. "S-a") where excess Mn atoms occupy the deficient atom sub-lattice, is preferred over the abnormal ones and for all of the preferred site-occupation configurations,

Table 3.1: Relative electronic energy ΔE_0 (in meV/atom) and relative mixing entropy ΔS_{mix} (in meV/K per atom) considering the electronic energy and the mixing entropy of the normal site-occupation configuration with lowest energy magnetic configuration as reference for Mn-excess systems in their $L2_1$ phases: $Ni_2Mn_{1+x}Sb_{1-x}$ (sys1) and $Ni_{2-x}Mn_{1+x}Sb$ (sys2) with x=0.25, 0.50 and 0.75. "S-a" to "S-d" and "C1" to "C4" denote possible site-occupation configurations and possible magnetic configurations respectively. Boldface indicates the most stable configuration for the corresponding composition.

(i) $Ni_2Mn_{1+x}Sb_{1-x}$ (sys1)

Composition	Site Config.	Site Occupancy			Magnetic Config.	Name	ΔE_0	ΔS_{mix}
		4a site	4b site	8c site				
$x = 0.25$	**S-a**	$\mathbf{Sb1_{0.75}Mn2_{0.25}}$	**Mn1**	$\mathbf{Ni1_2}$	**C1 (Ni1↑ Mn1↑ Mn2↓)**	**S-a-C1**	0.00	0.00
$\mathbf{Ni_2Mn_{1.25}Sb_{0.75}}$					C2 (Ni1↑ Mn1↑ Mn2↑)	S-a-C2	11.70	0.00
	S-b	$Sb1_{0.75}Ni2_{0.25}$	Mn1	$Ni1_{1.75}Mn2_{0.25}$	C1 (Ni1↑ Ni2↑ Mn1↑ Mn2↓)	S-b-C1	33.61	0.00812
					C2 (Ni1↑ Ni2↑ Mn1↑ Mn2↑)	S-b-C2	55.51	0.00825
$x = 0.50$	**S-a**	$\mathbf{Sb1_{0.50}Mn2_{0.50}}$	**Mn1**	$\mathbf{Ni1_2}$	**C1 (Ni1↑ Mn1↑ Mn2↓)**	**S-a-C1**	0.00	0.00
$\mathbf{Ni_2Mn_{1.50}Sb_{0.50}}$					C2 (Ni1↑ Mn1↑ Mn2↑)	S-a-C2	15.32	0.00
	S-b	$Sb1_{0.50}Ni2_{0.50}$	Mn1	$Ni1_{1.50}Mn2_{0.50}$	C1 (Ni1↑ Ni2↑ Mn1↑ Mn2↓)	S-b-C1	38.58	0.0242
					C2 (Ni1↑ Ni2↑ Mn1↑ Mn2↑)	S-b-C2	90.36	0.0242
	S-c	$Sb1_{0.50}Mn2_{0.25}Ni2_{0.25}$	Mn1	$Ni1_{1.75}Mn3_{0.25}$	C1 (Ni1↑ Ni2↑ Mn1↑ Mn2↓ Mn3↓)	S-c-C1	30.98	0.0237
					C2 (Ni1↑ Ni2↑ Mn1↑ Mn2↑ Mn3↑)	S-c-C2	55.36	0.0237
					C3 (Ni1↑ Ni2↑ Mn1↑ Mn2↓ Mn3↑)	S-c-C3	44.67	0.0237
					C4 (Ni1↑ Ni2↑ Mn1↑ Mn2↑ Mn3↓)	S-c-C4	36.86	0.0237
$x = 0.75$	**S-a**	$\mathbf{Sb1_{0.25}Mn2_{0.75}}$	**Mn1**	$\mathbf{Ni1_2}$	**C1 (Ni1↑ Mn1↑ Mn2↓)**	**S-a-C1**	0.00	0.00
$\mathbf{Ni_2Mn_{1.75}Sb_{0.25}}$					C2 (Ni1↑ Mn1↑ Mn2↑)	S-a-C2	15.02	0.00
	S-b	$Sb1_{0.25}Ni2_{0.75}$	Mn1	$Ni1_{1.25}Mn2_{0.75}$	C1 (Ni1↑ Ni2↑ Mn1↑ Mn2↓)	S-b-C1	35.40	0.0285
					C2 (Ni1↑ Ni2↑ Mn1↑ Mn2↑)	S-b-C2	139.32	0.0285
	S-c	$Sb1_{0.25}Mn2_{0.25}Ni2_{0.50}$	Mn1	$Ni1_{1.50}Mn3_{0.50}$	C1 (Ni1↑ Ni2↑ Mn1↑ Mn2↓ Mn3↓)	S-c-C1	50.35	0.0345
					C2 (Ni1↑ Ni2↑ Mn1↑ Mn2↑ Mn3↑)	S-c-C2	124.78	0.0345
					C3 (Ni1↑ Ni2↑ Mn1↑ Mn2↓ Mn3↑)	S-c-C3	85.97	0.0345
					C4 (Ni1↑ Ni2↑ Mn1↑ Mn2↑ Mn3↓)	S-c-C4	44.10	0.0345
	S-d	$Sb1_{0.25}Mn2_{0.50}Ni2_{0.25}$	Mn1	$Ni1_{1.75}Mn3_{0.25}$	C1 (Ni1↑ Ni2↑ Mn1↑ Mn2↓ Mn3↓)	S-d-C1	36.27	0.0265
					C2 (Ni1↑ Ni2↑ Mn1↑ Mn2↑ Mn3↑)	S-d-C2	74.86	0.0265
					C3 (Ni1↑ Ni2↑ Mn1↑ Mn2↓ Mn3↑)	S-d-C3	45.42	0.0265
					C4 (Ni1↑ Ni2↑ Mn1↑ Mn2↑ Mn3↓)	S-d-C4	35.72	0.0265

(ii) $Ni_{2-x}Mn_{1+x}Sb$ (sys2)

Composition	Site Config.	Site Occupancy			Magnetic Config.	Name	ΔE_0	ΔS_{mix}
		4a site	4b site	8c site				
$x = 0.25$	**S-a**	**Sb1**	**Mn1**	$\mathbf{Ni1_{1.75}Mn2_{0.25}}$	**C1 (Ni1↑ Mn1↑ Mn2↓)**	**S-a-C1**	0.00	0.00
$\mathbf{Ni_{1.75}Mn_{1.25}Sb}$					C2 (Ni1↑ Mn1↑ Mn2↑)	S-a-C2	7.52	0.00
	S-b	$Sb1_{0.75}Mn2_{0.25}$	Mn1	$Ni1_{1.75}Sb2_{0.25}$	C1 (Ni1↑ Ni2↑ Mn1↑ Mn2↓)	S-b-C1	98.41	0.0121
					C2 (Ni1↑ Ni2↑ Mn1↑ Mn2↑)	S-b-C2	128.76	0.0121
$x = 0.50$	**S-a**	**Sb1**	**Mn1**	$\mathbf{Ni1_{1.50}Mn2_{0.50}}$	**C1 (Ni1↑ Mn1↑ Mn2↓)**	**S-a-C1**	0.00	0.00
$\mathbf{Ni_{1.50}Mn_{1.50}Sb}$					C2 (Ni1↑ Mn1↑ Mn2↑)	S-a-C2	20.75	0.00
	S-b	$Sb1_{0.50}Mn2_{0.50}$	Mn1	$Ni1_{1.50}Sb2_{0.50}$	C1 (Ni1↑ Mn1↑ Mn2↓)	S-b-C1	110.85	0.0149
					C2 (Ni1↑ Mn1↑ Mn2↑)	S-b-C2	141.96	0.0149
	S-c	$Sb1_{0.75}Mn3_{0.25}$	Mn1	$Ni1_{1.50}Mn2_{0.25}Sb2_{0.25}$	C1 (Ni1↑ Mn1↑ Mn2↓ Mn3↓)	S-c-C1	95.09	0.0195
					C2 (Ni1↑ Mn1↑ Mn2↑ Mn3↑)	S-c-C2	137.95	0.0195
					C3 (Ni1↑ Mn1↑ Mn2↑ Mn3↓)	S-c-C3	108.98	0.0195
					C4 (Ni1↑ Mn1↑ Mn2↓ Mn3↑)	S-c-C4	119.32	0.0195
$x = 0.75$	**S-a**	**Sb1**	**Mn1**	$\mathbf{Ni1_{1.25}Mn2_{0.75}}$	**C1 (Ni1↑ Mn1↑ Mn2↓)**	**S-a-C1**	0.00	0.00
$\mathbf{Ni_{1.25}Mn_{1.75}Sb}$					C2 (Ni1↑ Mn1↑ Mn2↑)	S-a-C2	36.12	0.00
	S-b	$Sb1_{0.25}Mn2_{0.75}$	Mn1	$Ni1_{1.25}Sb2_{0.75}$	C1 (Ni1↑ Mn1↑ Mn2↓)	S-b-C1	93.44	0.0121
					C2 (Ni1↑ Mn1↑ Mn2↑)	S-b-C2	161.2	0.0121
	S-c	$Sb1_{0.50}Mn3_{0.50}$	Mn1	$Ni1_{1.25}Mn2_{0.25}Sb2_{0.50}$	C1 (Ni1↑ Mn1↑ Mn2↓ Mn3↓)	S-c-C1	106.33	0.0252
					C2 (Ni1↑ Mn1↑ Mn2↑ Mn3↑)	S-c-C2	161.19	0.0252
					C3 (Ni1↑ Mn1↑ Mn2↑ Mn3↓)	S-c-C3	116.57	0.0252
					C4 (Ni1↑ Mn1↑ Mn2↓ Mn3↑)	S-c-C4	127.57	0.0252
	S-d	$Sb1_{0.75}Mn3_{0.25}$	Mn1	$Ni1_{1.25}Mn2_{0.50}Sb2_{0.25}$	C1 (Ni1↑ Mn1↑ Mn2↓ Mn3↓)	S-d-C1	87.43	0.0224
					C2 (Ni1↑ Mn1↑ Mn2↑ Mn3↑)	S-d-C2	149.99	0.0224
					C3 (Ni1↑ Mn1↑ Mn2↑ Mn3↓)	S-d-C3	124.21	0.0224
					C4 (Ni1↑ Mn1↑ Mn2↓ Mn3↑)	S-d-C4	106.82	0.0224

Table 3.2: Relative electronic energy ΔE_0 (in meV/atom) and relative mixing entropy ΔS_{mix} (in meV/K per atom) considering the electronic energy and the mixing entropy of the normal site-occupation configuration with lowest energy magnetic configuration as reference for Ni-excess systems in their $L2_1$ phases: $Ni_{2+x}Mn_{1-x}Sb$ (sys3) and $Ni_{2+x}MnSb_{1-x}$ (sys4) with x=0.25, 0.50 and 0.75. "S-a" to "S-d" and "C1" to "C4" denote possible site-occupation configurations and corresponding magnetic configurations respectively. Boldface indicates the most stable configuration for the corresponding composition.

(iii) $Ni_{2+x}Mn_{1-x}Sb$ (sys3)

Composition	Site Config.	Site Occupancy			Magnetic Config.	Name	ΔE_0	ΔS_{mix}
		4a site	4b site	8c site				
$x = 0.25$ **$Ni_{2.25}Mn_{0.75}Sb$**	**S-a**	**Sb1**	**$Mn1_{0.75}Ni2_{0.25}$**	**$Ni1_2$**	**C2 (Ni1↑ Ni2↑ Mn1↑)**	**S-a-C2**	0.00	0.00
	S-b	$Sb1_{0.75}Ni2_{0.25}$	$Mn1_{0.75}Sb2_{0.25}$	$Ni1_2$	C2 (Ni1↑ Ni2↑ Mn1↑)	S-b-C2	140.28	0.0123
$x = 0.50$ **$Ni_{2.50}Mn_{0.50}Sb$**	**S-a**	**Sb1**	**$Mn1_{0.50}Ni2_{0.50}$**	**$Ni1_2$**	**C2 (Ni1↑ Ni2↑ Mn1↑)**	**S-a-C2**	0.00	0.00
	S-b	$Sb1_{0.50}Ni2_{0.50}$	$Mn1_{0.50}Sb2_{0.50}$	$Ni1_2$	C2 (Ni1↑ Ni2↑ Mn1↑)	S-b-C2	170.75	0.015
	S-c	$Sb1_{0.75}Ni3_{0.25}$	$Mn1_{0.50}Ni2_{0.25}Sb2_{0.25}$	$Ni1_2$	C2 (Ni1↑ Ni2↑ Ni3↑ Mn1↑)	S-c-C2	164.36	0.0194
$x = 0.75$ **$Ni_{2.75}Mn_{0.25}Sb$**	**S-a**	**Sb1**	**$Mn1_{0.25}Ni2_{0.75}$**	**$Ni1_2$**	**C2 (Ni1↑ Ni2↑ Mn1↑)**	**S-a-C2**	0.00	0.00
	S-b	$Sb1_{0.25}Ni2_{0.75}$	$Mn1_{0.25}Sb2_{0.75}$	$Ni1_2$	C2 (Ni1↑ Ni2↑ Mn1↑)	S-b-C2	148.74	0.0121
	S-c	$Sb1_{0.50}Ni3_{0.50}$	$Mn1_{0.25}Ni2_{0.25}Sb2_{0.50}$	$Ni1_2$	C2 (Ni1↑ Ni2↑ Ni3↑ Mn1↑)	S-c-C2	204.67	0.0252
	S-d	$Sb1_{0.75}Ni3_{0.25}$	$Mn1_{0.25}Ni2_{0.50}Sb2_{0.25}$	$Ni1_2$	C2 (Ni1↑ Ni2↑ Ni3↑ Mn1↑)	S-d-C2	170.92	0.0224

(iv) $Ni_{2+x}MnSb_{1-x}$ (sys4)

Composition	Site Config.	Site Occupancy			Magnetic Config.	Name	ΔE_0	ΔS_{mix}
		4a site	4b site	8c site				
$x = 0.25$ **$Ni_{2.25}MnSb_{0.75}$**	S-a	$Sb1_{0.75}Ni2_{0.25}$	Mn1	$Ni1_2$	C2 (Ni1↑ Ni2↑ Mn1↑)	S-a-C2	0.00	0.00
	S-b	**$Sb1_{0.75}Mn2_{0.25}$**	**$Mn1_{0.75}Ni2_{0.25}$**	**$Ni1_2$**	**C1 (Ni1↑ Ni2↑ Mn1↑ Mn2↓)**	**S-b-C1**	-15.78	0.012
					C2 (Ni1↑ Ni2↑ Mn1↑ Mn2↑)	S-b-C2	-6.94	0.0123
$x = 0.50$ **$Ni_{2.50}MnSb_{0.50}$**	S-a	$Sb1_{0.50}Ni2_{0.50}$	Mn1	$Ni1_2$	C2 (Ni1↑ Ni2↑ Mn1↑)	S-a-C2	0.00	0.00
	S-b	**$Sb1_{0.50}Mn2_{0.50}$**	**$Mn1_{0.50}Ni2_{0.50}$**	**$Ni1_2$**	**C1 (Ni1↑ Ni2↑ Mn1↑ Mn2↓)**	**S-b-C1**	-9.75	0.0149
					C2 (Ni1↑ Ni2↑ Mn1↑ Mn2↑)	S-b-C2	4.14	0.0149
	S-c	**$Sb1_{0.50}Mn2_{0.25}Ni2_{0.25}$**	**$Mn1_{0.75}Ni3_{0.25}$**	**$Ni1_2$**	**C1 (Ni1↑ Ni2↑ Ni3↑ Mn1↑ Mn2↓)**	**S-c-C1**	-9.78	0.0195
					C2 (Ni1↑ Ni2↑ Ni3↑ Mn1↑ Mn2↑)	S-c-C2	-2.67	0.0195
$x = 0.75$ **$Ni_{2.75}MnSb_{0.25}$**	S-a	$Sb1_{0.25}Ni2_{0.75}$	Mn1	$Ni1_2$	C2 (Ni1↑ Ni2↑ Mn1↑)	S-a-C2	0.00	0.00
	S-b	**$Sb1_{0.25}Mn2_{0.75}$**	**$Mn1_{0.25}Ni2_{0.75}$**	**$Ni1_2$**	**C1 (Ni1↑ Ni2↑ Mn1↓ Mn2↑)**	**S-b-C1**	-6.72	0.0121
					C2 (Ni1↑ Ni2↑ Mn1↑ Mn2↑)	S-b-C2	2.23	0.0121
	S-c	$Sb1_{0.25}Mn2_{0.50}Ni2_{0.25}$	$Mn1_{0.50}Ni3_{0.50}$	$Ni1_2$	C1 (Ni1↑ Ni2↑ Ni3↑ Mn1↑ Mn2↓)	S-c-C1	-1.88	0.0252
					C2 (Ni1↑ Ni2↑ Ni3↑ Mn1↑ Mn2↑)	S-c-C2	0.73	0.0252
	S-d	$Sb1_{0.25}Mn2_{0.25}Ni2_{0.50}$	$Mn1_{0.75}Ni3_{0.25}$	$Ni1_2$	C1 (Ni1↑ Ni2↑ Ni3↑ Mn1↑ Mn2↓)	S-d-C1	2.39	0.0224
					C2 (Ni1↑ Ni2↑ Ni3↑ Mn1↑ Mn2↑)	S-d-C2	0.78	0.0224

magnetic configuration "C1" is the ground state in which the Mn atom at its original sub-lattice (denoted as Mn1) and the Mn atom at the deficient atom sub-lattice (denoted as Mn2) align antiparallel. Previous experimental and theoretical investigations [266, 267] also showed a ferrimagnetic coupling between the Mn1 and Mn2 atoms in Sb-deficient Mn-excess Ni-Mn-Sb compositions. For Ni-excess systems, as has been shown in Table 3.2, depending upon the deficiency of Mn or Sb in the systems, preferred site occupancy can be the normal or abnormal. For Mn-deficient system (sys3), normal site-occupation configuration ("S-a") with "C2" magnetic structure is stable for all the compositions. For Sb-deficient system (sys4), it is the abnormal one which has the lowest energy for each of the compositions. In this

system, for both 25% and 75% substitutions "S-b-C1", where the excess Ni atoms prefer the Mn sub-lattice although the compositions have Sb deficiency, is the lowest energy configuration whereas, for x=0.50, almost same energy for "S-b-C1" and "S-c-C1" suggests that these configurations may co-exist in the alloy.

3.3.2 Structural parameters and magnetic moments

The equilibrium lattice constants for the minimum energy configurations for each system and composition in the $L2_1$ phases are listed in Table 3.3. The variations in the lattice constants with x for all systems can be understood from the relative sizes of the atomic radii (the atomic radii of Mn, Ni and Sb are 1.40 Å, 1.35 Å, 1.45 Å respectively) of the constituents. The trend in the variation of our calculated lattice constants agrees well with the experimental results available for Mn-excess Sb-deficient system (sys1) [242, 243].

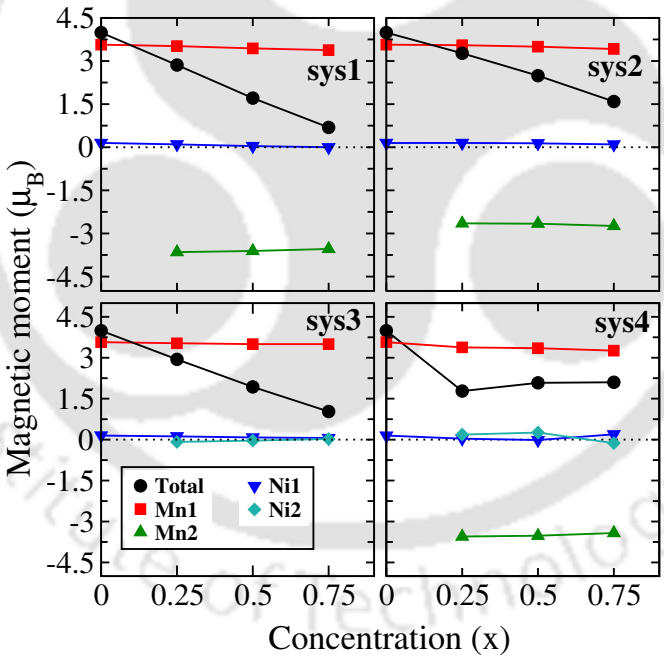

Figure 3.2: Calculated total magnetic moment in $\mu_B/f.u.$ and atomic magnetic moments (for atom-name convention see Section. 3.3.1) as a function of concentration of excess atom x for all four systems: $Ni_2Mn_{1+x}Sb_{1-x}$ (sys1), $Ni_{2-x}Mn_{1+x}Sb$ (sys2), $Ni_{2+x}Mn_{1-x}Sb$ (sys3) and $Ni_{2+x}MnSb_{1-x}$ (sys4) in their minimum energy configurations as indicated in Table 3.1 and Table 3.2.

In Fig. 3.2 and Table 3.3, we show the variations in the total and atomic magnetic moments in the $L2_1$ phase as a function of composition for each of the four systems considered. For sys1, sys2 and sys3, the total moments decrease with x while for

Table 3.3: Calculated values of electron to atom ratio (e/a), equilibrium lattice constant (a_0), total magnetic moment (M_A) of the four Ni-Mn-Sb systems in their $L2_1$ phases. The total energy difference (ΔE) between the austenite($L2_1$) and the martensite(tetragonal) phases [the equilibrium value of tetragonal distortion (c/a) is given in parentheses], the corresponding volume change ($|\Delta V|/V$) with respect to $L2_1$ structure, are given. Reported values of lattice constants in the literature are also given.

Composition	Configuration	e/a	a_0(Å)	$\Delta E(c/a)$ (meV/atom)	$\lvert\Delta V\rvert/V$ (%)	M_A ($\mu_B/f.u.$)	$a_0^{Lit.}$(Å)
Ni_2MnSb	S-a-C2	8.00	6.06	-	-	3.99	6.027 [243], 6.0031 [242]
$Ni_2Mn_{1.25}Sb_{0.75}$	S-a-C1	8.125	6.00	2.56(1.28)	0.54	2.86	6.018 [243] (x=0.24)
$Ni_2Mn_{1.50}Sb_{0.50}$	S-a-C1	8.25	5.94	25.14(1.32)	1.60	1.71	5.98 [243], 5.97 [268]
$Ni_2Mn_{1.75}Sb_{0.25}$	S-a-C1	8.375	5.86	55.32(1.36)	1.69	0.69	-
$Ni_{1.75}Mn_{1.25}Sb$	S-a-C1	7.8125	6.09	-	-	3.27	-
$Ni_{1.50}Mn_{1.50}Sb$	S-a-C1	7.625	6.10	-	-	2.49	-
$Ni_{1.25}Mn_{1.75}Sb$	S-a-C1	7.4375	6.12	-	-	1.59	-
$Ni_{2.25}Mn_{0.75}Sb$	S-a-C2	8.1875	6.04	-	-	2.94	-
$Ni_{2.50}Mn_{0.50}Sb$	S-a-C2	8.375	6.01	-	-	1.93	-
$Ni_{2.75}Mn_{0.25}Sb$	S-a-C2	8.5625	5.98	-	-	1.03	-
$Ni_{2.25}MnSb_{0.75}$	S-b-C1	8.3125	5.96	13.3(1.31)	0.55	1.78	-
$Ni_{2.50}MnSb_{0.50}$	S-b-C1	8.625	5.88	54.88(1.38)	1.75	0.00	-
	S-c-C1	8.625	5.88	36.46(1.34)	1.22	2.08	-
$Ni_{2.75}MnSb_{0.25}$	S-b-C1	8.9375	5.78	61.05(1.40)	2.30	2.10	-

sys4, the variation is non-monotonic. Also, there is no uniform trend in the variation of the total moment with (e/a). For sys1, the trend agrees well with the experimental observation [243]. Our calculations establish the prediction based upon experimental results [96, 243] that the decrease in moment with increase in Mn content is due to anti-parallel alignment of Mn1 and Mn2. Same is true for sys2. For Ni-excess, Mn-deficient system (sys3), the same trend is observed, albeit not because of anti-parallel alignment of Mn atoms at different sites but because of decrease in the Mn content, the largest contributor to the total magnetic moment. The non-monotonic trend seen in sys4 can be attributed to the presence of Mn and Ni at two different sites. The trends in the atomic moments suggest that the moment of each constituent element remains nearly constant across systems and compositions. Thus, the trends in the total moment are controlled by concentration alone.

3.3.3 Composition dependent structural phase stability

After ascertaining the ground-state atomic and magnetic configurations of each of the four systems considered, we now investigate the relative stabilities of the $L2_1$ austenite and the tetragonal martensite phases. This investigation will shed light on the dependence of the stability of the high temperature austenite phase on the details of composition. We proceed to do this by distorting the $L2_1$ structure along

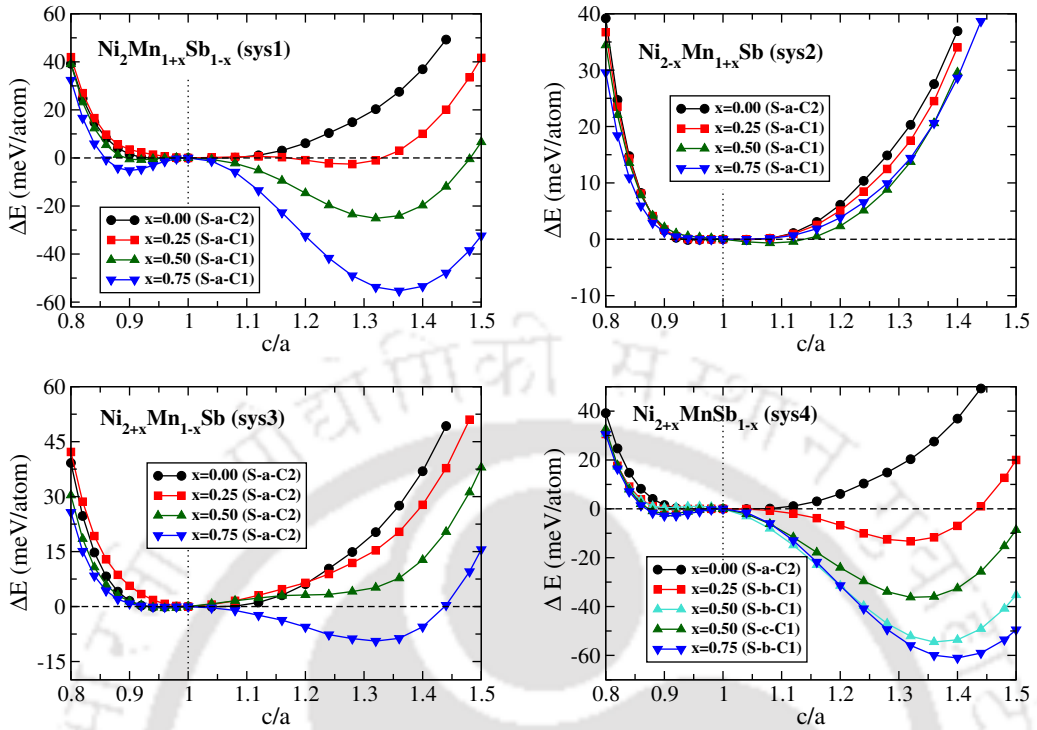

Figure 3.3: The variations of total energy difference (ΔE) between the austenite($L2_1$) and the martensite(tetragonal) phases as a function of tetragonal distortion i.e. c/a ratio for all four systems with different compositions and at their minimum-energy configurations.

z axis and computing the total energy as a function of the tetragonal distortion, given by (c/a). This is done for the ground state configuration for each system and each composition. In each case, the composition with $x = 0.50$ required special treatment. Due to finite size of the 16 atom supercell, two crystallographic inequivalent directions appear in the supercell only for compositions with $x = 0.50$. In this case, the tetragonal distortion can be applied parallel to or perpendicular to the plane defined by the two atoms which are deficient with respect to stoichiometric composition of 2:1:1 (8:4:4 in 16 atom supercell) for sys1, sys3 and sys4 and by the two atoms which are excess in sys2. Accordingly, the total energies are computed with respect to both distortions and averaged. The results are presented in Fig. 3.3.

For sys1 i.e. Mn-excess and Sb-deficient system, it can be seen that the stability of the austenite $L2_1$ phase decreases with the increasing concentration x of the excess Mn atoms at the expense of Sb atoms. The increase of ΔE (see Table 3.3) with x suggests that as the Sb(Mn) concentration gradually decreases(increases), the martensitic transformation would take place at higher temperature. This trend is in good agreement with the experimental observations [132, 146, 243] that the

martensitic transformation temperature T_M increases with decrease in Sb concentration for $Ni_2Mn_{1+x}Sb_{1-x}$ alloys. For sys2 and sys3, those are the two systems where Sb concentration is that of the stoichiometric Ni_2MnSb, the austenite phase is stable throughout the entire composition range considered. In case of sys3, a weak tendency towards de-stabilization of the austenite phase is observed when $x = 0.75$. For sys4 i.e. Ni-excess and Sb-deficient system, the tetragonal phase is stable for all compositions with ΔE as large as $\sim$61 meV/atom for $x = 0.75$. Our calculations, thus, suggest that the $L2_1$ phase in Ni-Mn-Sb system can be destabilized leading to a martensitic transformation only when Sb content in the system is about 12.5% (25%) or less for Mn-excess(Ni-excess) systems. This also suggests why experiments to observe functional properties driven by martensitic phase transformation were always done at compositions with Sb content around 12.5%.

3.3.4 Dependence of phase stability on site-occupancy and magnetic structure

Site ordering and magnetic structure can affect the possibility of a martensitic transformation in Heusler alloys. Ghosh *et al.* [269] observed that depending on annealing time, site occupancy in $Ni_2Mn_{1.46}Sn_{0.54}$ can change, affecting the magnetocaloric properties as a consequence. In $Ni_2Mn_{1+x}In_{1-x}$, it was observed that the martensitic phase transformation happens only when the Mn atoms at different sites align anti-parallel [245]. We therefore examine the dependencies of the relative stabilities of the two phases on the site occupancy configurations and the magnetic structures. We do so by picking up only those configurations corresponding to each of the four systems and compositions which have energies in their $L2_1$ phases lying right above the corresponding ground state energies and computing their total energy surfaces as a function of tetragonal distortions. In choosing the configurations from Table 3.1 and Table 3.2 following this procedure, we have made exceptions in only two cases: (i) in sys1, for $x = 0.75$ i.e. $Ni_2Mn_{1.75}Sb_{0.25}$ composition, though "S-b-C1" has lower energy than "S-d-C1", we have chosen "S-d-C1" to compare, in order to maintain the same site-occupancy pattern as that of $x = 0.25$ and 0.50 compositions, (ii) in sys4, since an abnormal configuration is always the lowest energy one, we have considered the normal configuration for the purpose of comparison even though it is not the one having energy right above the minimum. The configurations picked up are marked by enclosing boxes around them in Table 3.1 and Table 3.2. For these calculations optimized lattice constants corresponding to each configuration

have been used. The results are presented in Fig. 3.4.

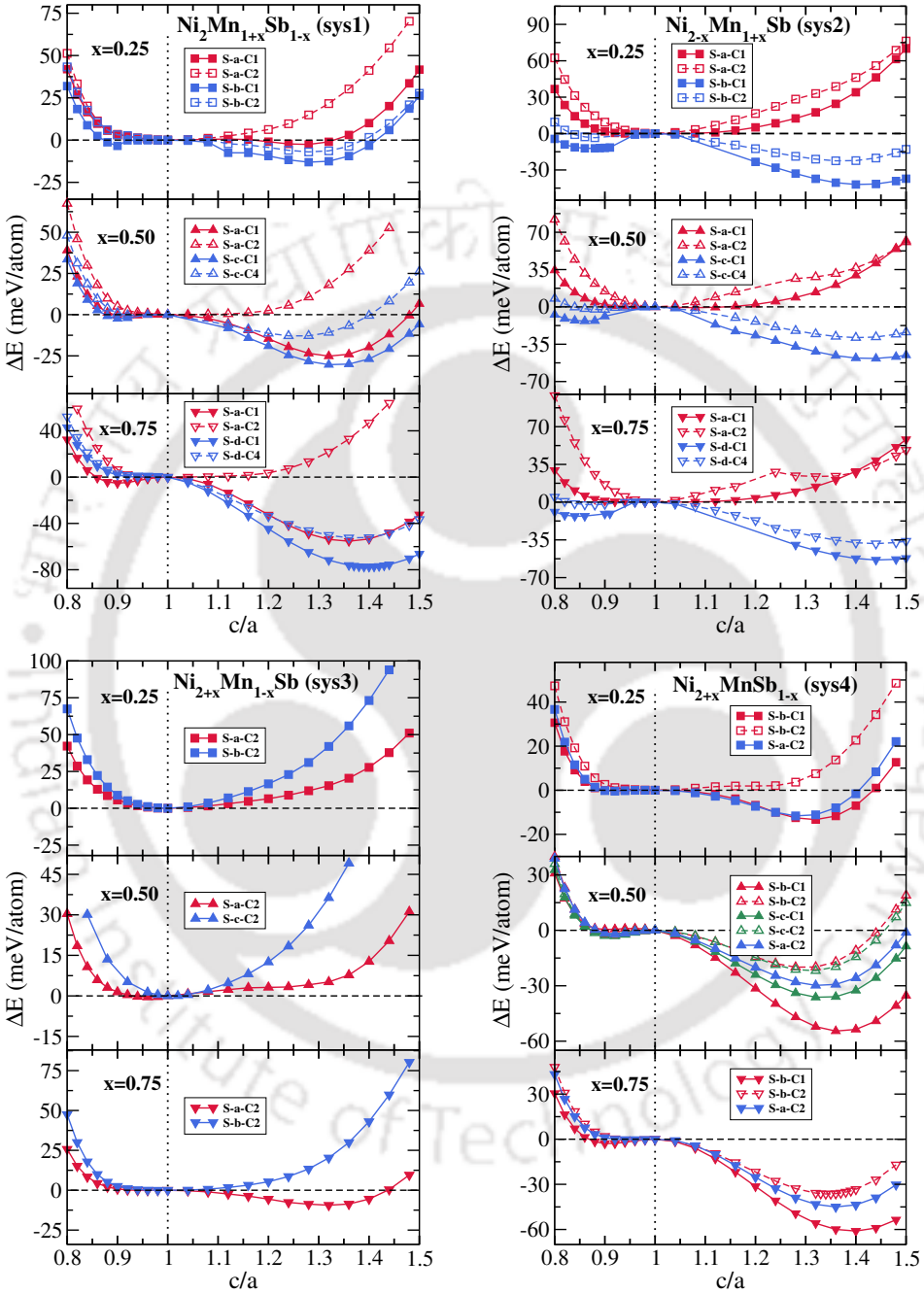

Figure 3.4: The variations of total energy difference (ΔE) between the austenite($L2_1$) and the martensite(tetragonal) phases as a function of tetragonal distortion i.e. c/a ratio for all four systems with different compositions for different site occupancies and magnetic configurations. The red curves correspond to the minimum energy configurations and the blue curves are the ones with energies right above them. Solid curves with filled symbols indicate ground state magnetic configurations and the dashed curves with open symbols are the ones with energies right above them, for each site-occupation configuration.

We divide the systems into two categories: (i) ones with Sb concentration equal to that of Ni_2MnSb, but with excess-Mn or excess-Ni (sys2 and sys3 respectively), (ii) Sb-deficient ones, but with excess-Mn or excess-Ni (sys1 and sys4 respectively), for the purpose of discussion. For the category (i), the total energy results suggest that an abnormal site-occupancy where Mn atoms occupy Sb sites also is the key factor de-stabilizing the austenite phase, effecting a martensitic transformation. Thus, irrespective of whether site-occupancy is normal or abnormal, the austenite phase is nearly stable across compositions in sys3, as in such a Mn-deficient system, Mn can occupy its own site only. In sys2, the abnormal site-occupancy leads to de-stabilization of the austenite phase across compositions as in "abnormal" occupancy patterns considered here, extra Mn atoms occupy both Ni and Sb sites. For the category (ii), both site-ordering and spin alignment of Mn atoms at different sites contribute towards phase stability along with the content of Sb. In sys1, with the highest Sb-content ($Ni_2Mn_{1.25}Sb_{0.75}$), a parallel alignment between Mn atoms at its original site and at Sb site with normal site configuration produces minimum total energy in the $L2_1$ phase. The stability is disturbed when the alignment is anti-parallel leading to a rather shallow minima for $c/a \neq 1$. With an abnormal site configuration where excess Mn occupies Ni site rather than Sb site, the de-stabilisation of the austenite phase becomes prominent, and the alignment of Mn spins do not matter. As Sb-content decreases, the martensitic phase becomes stable for abnormal site-configuration, irrespective of the magnetic structure. However, with normal site configuration, a magnetic structure where Mn moments align parallel stabilize the austenite phase. Thus, the ferromagnetic ordering stabilizes the austenite phase in this system when site-occupancy is normal. The opposite picture is seen in case of sys4, which is Ni-excess and Sb-deficient. Barring the highest Sb-content compound, the austenite phase is significantly de-stabilized irrespective of site-occupancy configurations and orientation of Mn spins. Hence, we can conclude that in order to de-stabilize the austenite phase and effect a martensitic transformation in the Ni-Mn-Sb family, the requirements are an abnormal site occupancy and the presence of Mn at Sb site apart from its own site, with their moments aligning anti-parallel. This means that controlling the site ordering by manipulating the annealing or preparing the sample by non-equilibrium methods may see potential benefits in Ni-Mn-Sb system with regard to functional properties associated with the volume conserving martensitic transformation.

3.3.5 Electronic structure

In this subsection, we try to understand the microscopic physics behind composition, site occupancy and magnetic structure dependent stabilities of the austenite phase of Ni-Mn-Sb systems as discussed in the previous two subsections. We do this by computing the total and partial electronic densities of states of each compound with various compositions, normal and abnormal site occupancies and different magnetic structures of Mn atoms. In order to analyse the stability of the $L2_1$ phase of Ni_2MnSb, we also take recourse to the total and partial densities of states for the same in Fig. 3.5. It is well known for Ni-Mn based shape memory systems that the occurrence of martensitic stability or the lack of it can be linked to the relative strengths of two factors: the Jahn-Teller effect manifested by substantial densities of states at the Fermi level and the covalent bonding due to Ni and the main group element manifested in a pseudo-gap in the occupied parts. Fig. 3.5 suggests that, in the $L2_1$ phase for Ni_2MnSb, a pseudo-gap at around -1.2 eV is formed in the spin-down state. Partial densities of states suggest that this pseudo-gap is formed mainly due to the hybridization between the $3d$ states of Ni and $5p$ states of Sb resulting in strong covalent bonding that stabilizes the $L2_1$ phase down to low temperature. Thus, a competition between the strength of the Jahn-Teller instability and the strength of the covalent bond due to Ni d and Sb p minority states explains the phase stability in Ni-Mn-Sb too.

In order to understand the dependencies of phase stability on composition, site occupancy and magnetic structure for the four considered off-stoichiometric Ni-Mn-Sb systems, we analyze the electronic structures of the minority bands close to Fermi levels as shown in Figs. 3.6, 3.7, 3.10, 3.11 for sys1 to 4 respectively. The densities of states are presented for those configurations for which the total energy curves were discussed in Fig. 3.4.

For sys1, in Fig. 3.6, we first compare the electronic structures corresponding to two magnetic structures "C1" and "C2" with the same normal site occupancy "S-a". We find that with the magnetic configuration being "C2", where Mn1 and Mn2 align parallel, the pseudo-gap in the minority band around -1.2 eV persists for all compositions and in fact becomes wider with increasing x. The structure at the Fermi level, on the other hand has no significant difference due to changed magnetic configuration. This persisting pseudo-gap explains the stability of the $L2_1$ structure when two Mn atoms align parallel. The origin of this can be understood from the partial densities of states (Fig. 3.8). The pseudo-gap originating out of Ni and Sb hybridization could not be suppressed in "C2", as unlike "C1", the Mn2 do

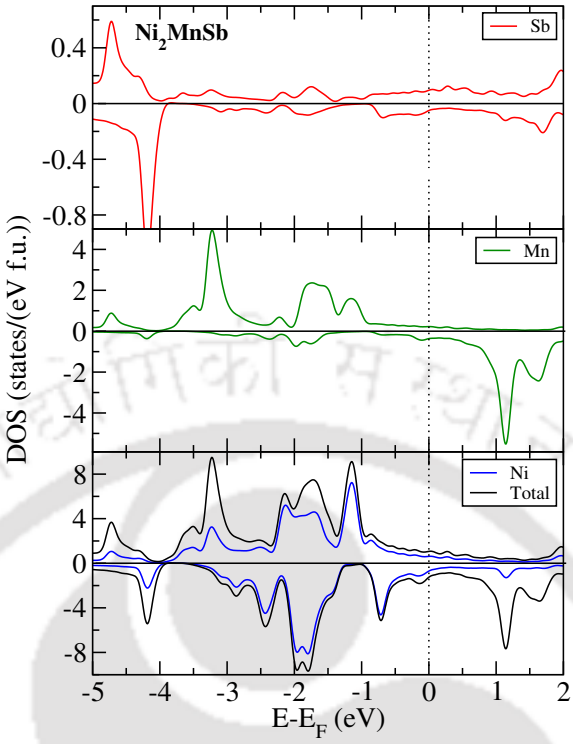

Figure 3.5: Total and partial densities of states for $L2_1$ phase of Ni_2MnSb. The zero energy is set at Fermi energy (E_F).

not have states in this energy range. Next we analyze the effects of site-occupancy patterns by inspecting the densities of states with "S-b", "S-c" and "S-d" (Fig. 3.6) configurations. From partial densities of states in Fig. 3.9, we find that for all abnormal configurations, irrespective of the magnetic structures, the pseudo-gap around -1.2 eV in stoichiometric Ni_2MnSb gradually becomes narrower due to Ni1, Mn2 (Mn at Sb site) and Mn3 (Mn at Ni site) states in the down band. Also a peak around -0.3 eV seen in $x = 0.25$ composition gradually shifts towards the Fermi level as x increases and finally fermi level falls on a peak in $x = 0.75$ which is mainly due to the states of Sb1, Ni1 and Mn3 atoms amplifying the Jahn-Teller instability in the system and driving it towards the martensitic transformations for both magnetic configurations as shown in Fig. 3.4. Thus for sys1, for normal configurations, the Ni1 and Mn2 states decrease the strength of covalent bonding with increase in Mn2, only when there is an anti-parallel coupling between Mn1 and Mn2, bringing in the structural instability as Jahn-Teller effect gains strength in relative sense. For abnormal site occupations, once again the hybridization between the spin down bands of Ni and Mn atoms at various sites aligning anti-parallel boosts the Jahn-Teller instability driving a phase transition.

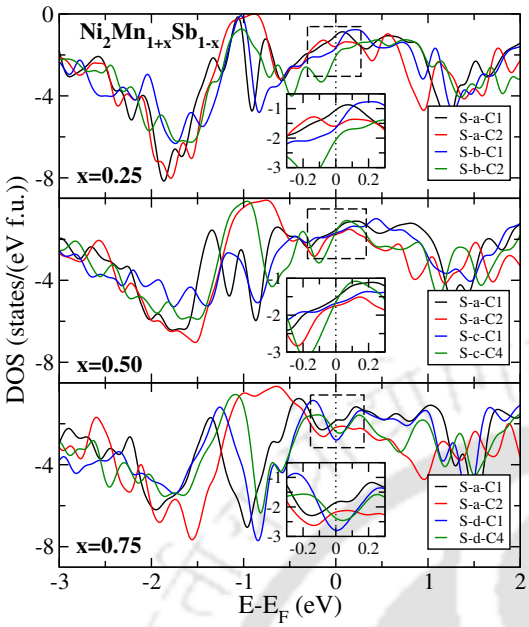

Figure 3.6: The total minority spin states (DOS) for $Ni_2Mn_{1+x}Sb_{1-x}$ (sys1) (x=0.25, 0.50, 0.75) in $L2_1$ phase with different site occupancies and magnetic configurations used in Fig. 3.4. The zero energy is set at Fermi energy (E_F). The insets show the zoomed view of total densities of states near Fermi level.

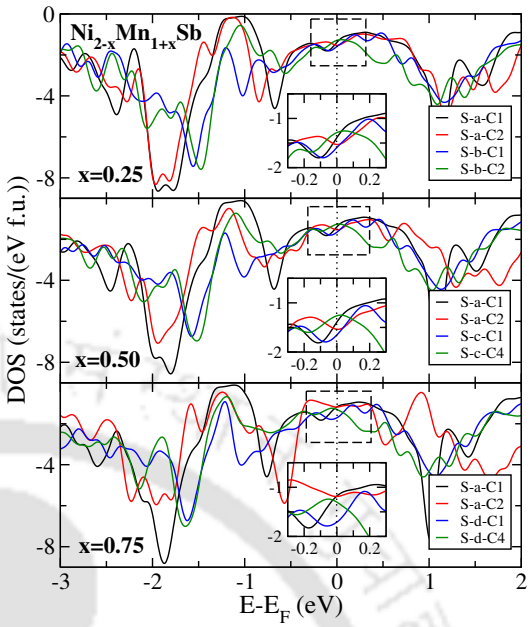

Figure 3.7: The total minority spin states (DOS) of $Ni_{2-x}Mn_{1+x}Sb$ (sys2) (x=0.25, 0.50, 0.75) in $L2_1$ phase with different site occupancies and magnetic configurations used in Fig. 3.4. The zero energy is set at Fermi energy (E_F). The insets show the zoomed view of total densities of states near Fermi level.

In a similar way, we can infer from Fig. 3.7, Fig. 3.10 and Fig. 3.11 that (i) for sys2, the changes in the hybridizations due to changes in site-occupancy configurations can induce instability in the $L2_1$ phase; the decisive factors being the deficiency of Sb at its own site and presence of anti-parallel Mn-Mn interactions (ii) the absence of Mn at any other site than its own in sys3 is the key factor behind absence of any pronounced Jahn-Teller instability irrespective of configurations and thus behind the stability of the $L2_1$ phases throughout and (iii) the hybridizations between Sb1, Ni1 and Ni2 minority bands in sys4 drive the system towards martensitic instability.

3.3.6 Elastic properties and predictor of T_M

Finally, in search of a predictor for T_M, we compute the composition dependence of elastic moduli. The results, apart from deciding on a predictor for T_M, provided insights into the mechanical properties and the nature of bonding in Ni-Mn-Sb. In case of Ni-Mn based Heusler alloys, the elastic modulus C' in the austenite phase

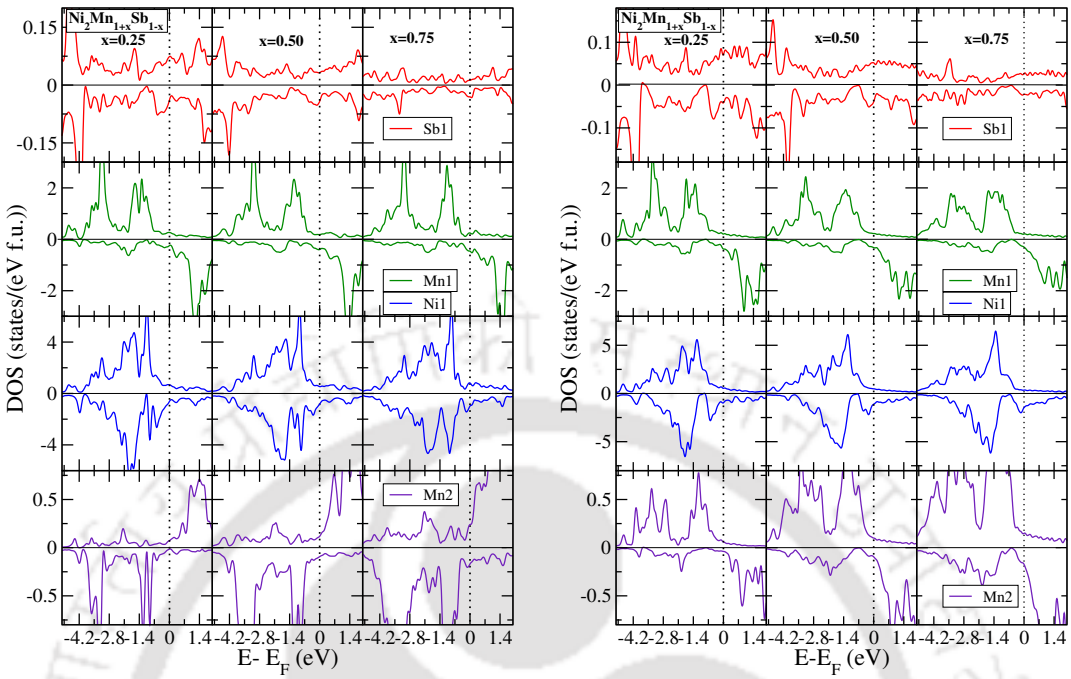

Figure 3.8: Partial densities of states of $Ni_2Mn_{1+x}Sb_{1-x}$ (sys1) in $L2_1$ phase for "S-a-C1" (left) and "S-a-C2" (right) configurations. The zero energy is set at Fermi energy (E_F)

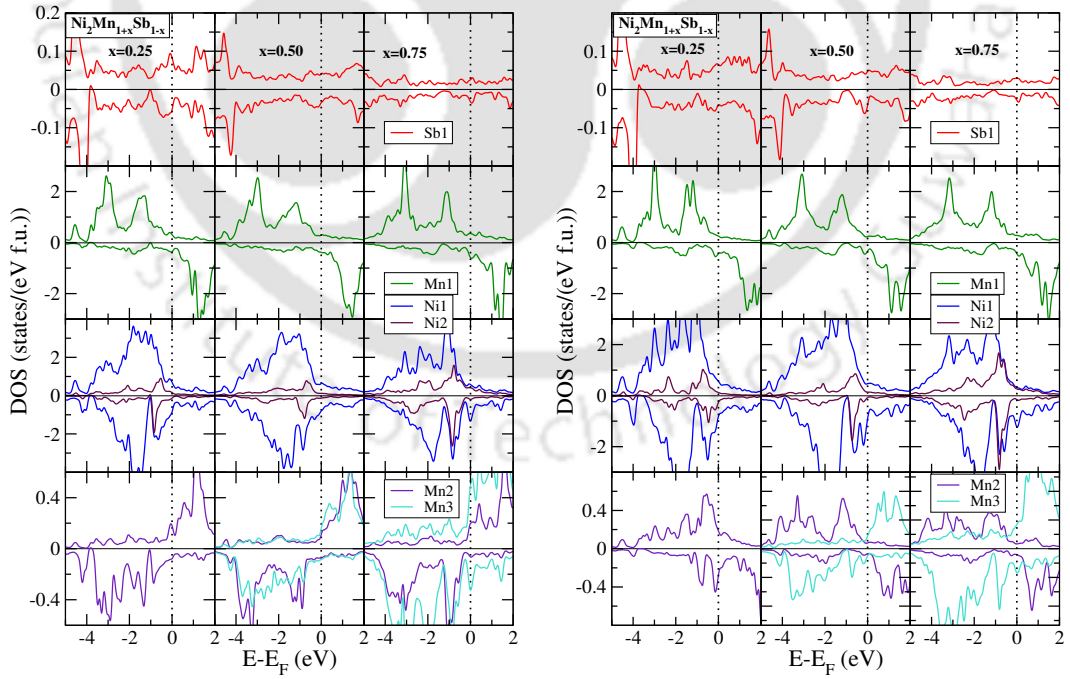

Figure 3.9: Partial densities of states in the $L2_1$ phase of $Ni_2Mn_{1+x}Sb_{1-x}$ (sys1) for "S-b-C1", "S-c-C1", "S-d-C1" (for x=0.25, 0.50, 0.75 respectively) (left) and "S-b-C2", "S-c-C4", "S-d-C4" (for x=0.25, 0.50, 0.75 respectively) (right) configurations. The zero energy is set at Fermi energy (E_F).

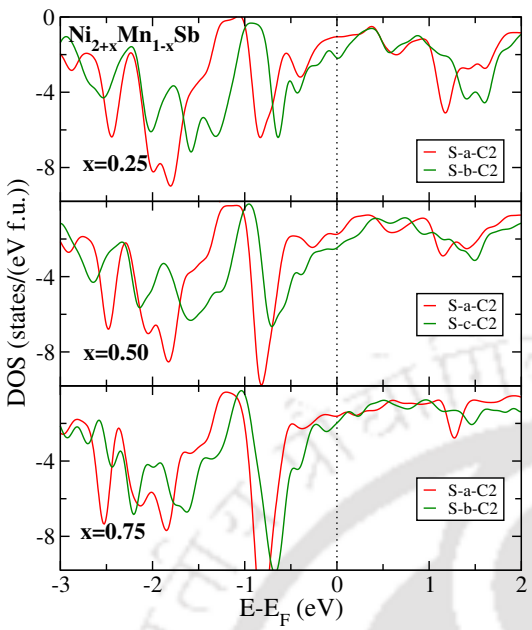

Figure 3.10: The total minority spin states (DOS) of $Ni_{2+x}Mn_{1-x}Sb$ (sys3) (x=0.25, 0.50, 0.75) in $L2_1$ phase with different site occupancies and magnetic configurations used in Fig. 3.4. The zero energy is set at Fermi energy (E_F).

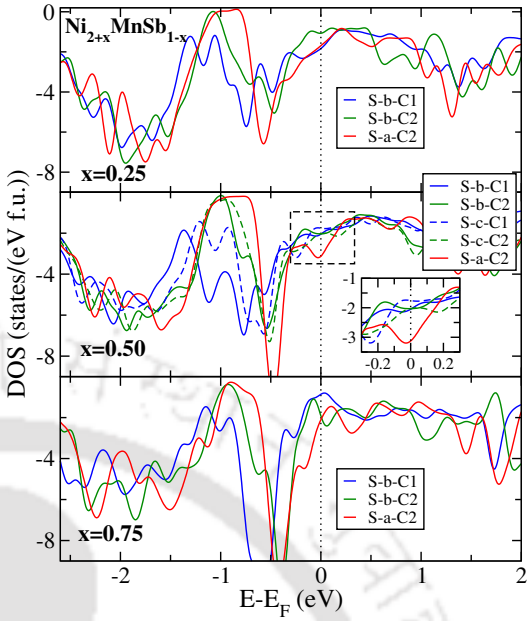

Figure 3.11: The total minority spin states (DOS) of $Ni_{2+x}MnSb_{1-x}$ (sys4) (x=0.25, 0.50, 0.75) in $L2_1$ phase with different site occupancies and magnetic configurations used in Fig. 3.4. The zero energy is set at Fermi energy (E_F).

has been found to be a good predictor for T_M [270–272]. The (e/a) and ΔE, the energy difference between $L2_1$ and tetragonal phases, are the other two quantities found to be good predictors in certain cases. In Fig. 3.12, we show the composition dependence of C' for each of the four systems in $L2_1$ phases. Calculations are done in their respective minimum energy configurations. For sys1 and sys4, we find gradual softening of C' indicating instability in the $L2_1$ phase. This is consistent with the results obtained from the total energy calculations. In fact negative C' at all compositions of sys4 indicates that the $L2_1$ structure is unstable across compositions. In sys1, a small positive C' for $x = 0.25$ is consistent with a shallow minimum for $(c/a) \neq 1$ in the total energy curve. For sys2, C' has little variation with composition while for sys3, we see positive C' for $x = 0.25, 0.50$ which is consistent with the stable $L2_1$ phase at low temperature as seen from Fig. 3.3. The trends of ΔE shown in Fig. 3.12 for sys1 and sys4 are consistent with variations in C'; a decreasing(increasing) $C'(\Delta E)$ indicating increasing stability of the tetragonal phase and increasing value of T_M. For sys1, this is consistent with the experimental results where T_M increases with x [146]. It is also to be noted that for sys1 and

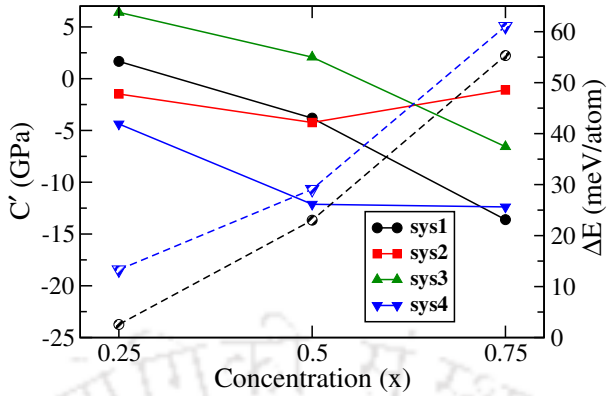

Figure 3.12: The calculated shear elastic constant C' in $L2_1$ phase as a function of concentration of excess atom x for all four systems: $Ni_2Mn_{1+x}Sb_{1-x}$ (sys1), $Ni_{2-x}Mn_{1+x}Sb$ (sys2), $Ni_{2+x}Mn_{1-x}Sb$ (sys3) and $Ni_{2+x}MnSb_{1-x}$ (sys4) in their respective minimum energy configurations. The dashed lines represent the variation in ΔE (defined in Table 3.3) with x.

sys4 where our calculations predict martensitic transformations, ΔE increases with (e/a) meaning that T_M varies as (e/a). Consequently, for Ni-Mn-Sb systems both C' and (e/a) can be good predictors for T_M.

Table 3.4: The calculated elastic moduli in the $L2_1$ phase for all four systems: $Ni_2Mn_{1+x}Sb_{1-x}$ (sys1), $Ni_{2-x}Mn_{1+x}Sb$ (sys2), $Ni_{2+x}Mn_{1-x}Sb$ (sys3) and $Ni_{2+x}MnSb_{1-x}$ (sys4) (x=0.00, 0.25, 0.50, 0.75) in their minimum energy configurations.

Composition	Configuration	B (GPa)	C' (GPa)	C_{44} (GPa)	C_{11} (GPa)	C_{12} (GPa)	G_v (GPa)	G_v/B	C^P=C_{12}-C_{44} (GPa)
Ni_2MnSb	S-a-C2	138.0	0.16	76.79	138.31	137.99	45.54	0.33	61.20
$Ni_2Mn_{1.25}Sb_{0.75}$	S-a-C1	140.8	1.67	86.21	143.03	139.69	52.10	0.37	53.48
$Ni_2Mn_{1.50}Sb_{0.50}$	S-a-C1	141.5	-3.81	94.86	136.42	144.04	55.18	0.39	49.18
$Ni_2Mn_{1.75}Sb_{0.25}$	S-a-C1	140.4	-13.61	108.58	122.25	149.48	60.37	0.43	40.89
$Ni_{1.75}Mn_{1.25}Sb$	S-a-C1	136.1	-1.48	72.46	129.63	132.59	43.55	0.32	60.12
$Ni_{1.50}Mn_{1.50}Sb$	S-a-C1	123.9	-4.24	67.17	118.25	126.72	38.41	0.31	59.55
$Ni_{1.25}Mn_{1.75}Sb$	S-a-C1	117.8	-1.09	66.95	116.35	118.53	40.05	0.34	51.58
$Ni_{2.25}Mn_{0.75}Sb$	S-a-C2	145.8	6.40	81.14	154.34	141.53	51.03	0.35	60.39
$Ni_{2.50}Mn_{0.50}Sb$	S-a-C2	150.7	2.08	82.88	153.48	149.31	51.24	0.34	66.44
$Ni_{2.75}Mn_{0.25}Sb$	S-a-C2	157.4	-6.57	85.52	148.64	161.78	48.79	0.31	76.25
$Ni_{2.25}MnSb_{0.75}$	S-b-C1	144.2	-4.37	93.55	138.37	147.12	54.79	0.38	53.57
$Ni_{2.50}MnSb_{0.50}$	S-b-C1	152.7	-12.13	108.16	136.53	160.79	59.55	0.39	52.63
	S-c-C1	151.8	-9.25	110.03	139.47	157.97	62.24	0.41	47.94
$Ni_{2.75}MnSb_{0.25}$	S-b-C1	160.3	-12.39	117.23	143.78	168.56	65.72	0.41	51.33

In Table 3.4, we show in detail the values of various elastic modulus for each compound. We calculated Pugh ratio (G_v/B) and Cauchy pressure (C^P) to get an idea about the brittleness and the nature of bonding in the compounds. Pugh ratio G_v/B [225, 226], where G_v is the isotropic shear modulus under Voigt formalism [219]

related to the resistance of the material to plastic deformation, measures whether a material is more ductile or more brittle. Compounds having a Pugh ratio greater than 0.57 are considered to be more brittle. On the other hand, Cauchy pressure C^P provides insight to the nature of bonding in a material with cubic symmetry [228]. A positive value of Cauchy pressure indicates the presence of more metallic bonding in the system while a negative value implies a stronger covalent bonding [229]. The tabulated values in Table 3.4 imply that Ni-Mn-Sb compounds are ductile in nature and the bonding is largely metallic.

3.4 Summary and Conclusions

In this chapter, we have performed a comprehensive and systematic investigation into the roles of composition, site occupancies and magnetic configurations affecting the structural stabilities in Ni- and Mn-excess Ni_2MnSb by *ab initio* calculations. We find that the site occupancy pattern and associated magnetic alignment of Mn atoms play the central role in de-stabilizing the high temperature Heusler phase and consequently stabilizing a tetragonal martensite at low temperature. It has been found that unless the system is significantly Sb-deficient, a martensitic transformation leading to the shape-memory effect and associated functional properties is difficult to realize unless the system stays in a meta-stable state due to the process of annealing or is grown by non-equilibrium methods. Our calculations for Mn-excess Sb-deficient system reproduce the experimentally observed trends. The patterns in phase stability as obtained from our total energy calculations can be understood from the features in the densities of states in the minority spin bands. This work helps understand the reason behind experimentalists choice of Sb-deficient systems for observing functional properties like magnetocaloric effect in Ni-Mn-Sb. An important outcome of this work is the identification of $Ni_{2+x}MnSb_{1-x}$ as a potential new shape memory alloy where the martensitic transformation takes place even at high Sb composition. This input widens the scope of the experimentalists to explore functional properties in Ni-Mn-Sb systems. Shear modulus and electron to atom ratio (e/a) both turn out to be good predictors of T_M in Ni-Mn-Sb. The materials are also found to be ductile which is an advantage for their commercial usages.

Chapter 4

Understanding the origin of the magnetocaloric effects in substitutional Ni-Mn-Sb-Z (Z=Fe, Co, Cu) compounds

4.1 Introduction

In the previous chapter, we performed a comprehensive and systematic investigation into the role of composition on structural stabilities in Ni and Mn-excess Ni_2MnSb. The electronic structure analysis clearly revealed that to realize a martensitic phase tranformation, the required criterion is the anti-parallel alignment between Mn atoms occupying different sites. This is the reason behind choosing Mn-excess and Sb-deficient compositions in all experimental investigations in Ni-Mn-Sb Heusler compounds [96, 130, 132, 242, 243] that eventually exhibit giant magnetocaloric effect. Along with the presence of MPT, high-performance magnetocaloric materials should meet at least the following important requirements: (1) the materials should possess a good value of magnetization in the high-temperature phase. A large difference in magnetization (ΔM) between the high-temperature austenite and low-temperature martensitic phases is also of great importance because substantial Zeeman energy, which is defined as $\Delta M.H$, is the key to first-order magneto-structural transition; (2) the first-order magneto-structural transition temperature (T_M) and the second-order magnetic transition temperature (T_c^A) in the austenite phase should be close and must be near room temperature; (3) the materials should

The contents of this chapter are published in Physical Review B **101**, 024109 (2020)

have good mechanical stability during operation.

In this regard, one major disadvantage with the off-stoichiometric Mn-excess, Z-deficient Ni-Mn-Z (Z=In, Sn, Sb) Heusler alloys is that the value of ΔM is limited due to the low value of magnetization in the high-temperature austenite phase, which arises because of the antiparallel alignment between the Mn atoms occupying different crystallographic sites. To overcome this, recently, several experimental studies have been done on Ni-Mn-Z compounds considering substitution of either of the constituents with another $3d$ transition element (i) to get a larger ΔM near the structural transition, (ii) to tune the transition temperatures (T_M and T_c^A) and bring them close to each other, (iii) to improve the mechanical properties. Positive changes in several counts were observed for substitution of Co, Cu and Fe at different sites and in different proportions [93, 273–285]. Some recent investigations have also been carried out for the Mn-excess Sb-deficient off-stoichiometric Ni-Mn-Sb systems by substituting the Fe and Co atoms at Mn and Ni sites respectively. As a consequence, a large positive ΔS_{mag} near room temperature was obtained with $0.28 \leq x \leq 0.36$ in $Ni_{2-x}Co_xMn_{1.56}Sb_{0.44}$ alloys [134]. For a slightly different composition, $Ni_{2-x}Co_xMn_{1.52}Sb_{0.48}$, nearly 70% decrease in moment is observed associated with the martensitic transition and remarkable enhancement in ΔS_{mag} of 34 $J\,kg^{-1}\,K^{-1}$ is achieved for $x = 0.2$ at 262 K in a field of 5 T near room temperature [135, 142]. A significant ΔS_{mag} value of 14.2 $J\,kg^{-1}\,K^{-1}$ at 288 K under 5 T field was observed for $x = 0.08$ in $Ni_2Mn_{1.52-x}Fe_xSb_{0.48}$ [140]. Thus, the Ni-Mn-Sb based Heusler alloys show a possibility to be proved as emerging materials, showing significant MCE properties with the substitution of $3d$-transition elements. However, the improvement in MCE properties due to the substitution crucially depends on the substituent, the site of substitution, and the composition. What is nevertheless lacking is a systematic investigation into the impacts of substitution with different $3d$-elements. Such an investigation would throw light on the microscopic understanding of these factors, help interpret the experimental observations, and provide a roadmap to tune the compositions for maximizing the functional properties.

In this chapter, we have considered Fe, Co and Cu substituted Ni-Mn-Sb systems to address these issues. We specifically considered the compound $Ni_2Mn_{1.5}Sb_{0.5}$, relative concentrations of the elements being around the mostly studied experimental composition, as the parent one, and systematically substitute Ni and Mn by Fe, Co, and Cu, varying the concentrations of the substituents. We mainly address the following: (i) the effect on the magnetization in the high temperature phase and whether and how the substitutions improve ΔM (ii) in what way the substitutions

impact the structural phase stabilities, the magnetic exchange interactions, the mechanical properties, the characteristic temperatures (T_M and T_c^A) and (iii) how the information from (i) and (ii) can be correlated to the magnetocaloric properties of the Ni-Mn-Sb compounds. In light of these, we also attempt to interpret the experimental observations in Fe substituted [140] and Co substituted [134, 135, 142] compounds which highlight the important role of atomic ordering in the system.

4.2 Computational Details

Electronic structure calculations were done with spin-polarized density functional theory (DFT) based projector augmented wave (PAW) method as implemented in Vienna *Ab initio* Simulation Package (VASP) [177–179]. The valence electronic configurations used for the Mn, Fe, Co, Ni, Cu and Sb PAW pseudopotentials are $3d^6 4s$, $3d^7 4s$, $3d^8 4s$, $3d^8 4s^2$, $3d^{10} 4s$ and $5s^2 5p^3$, respectively. For all calculations, we have used the Perdew-Burke-Ernzerhof implementation of generalized gradient approximation for exchange-correlation functional [190]. An energy cut off of 550 eV and a Monkhorst-Pack $11 \times 11 \times 11$ k-mesh were used for self-consistent calculations. The convergence criteria for the total energies and the forces on individual atoms were set to 10^{-6} eV and 10^{-2} eV/Å respectively for all calculations. The stabilities of the compounds are checked by computing the formation energies, defined by:

$$E_f = E_{tot} - \sum_i n_i E_i \tag{4.1}$$

E_{tot} is the total energy of the systems, i represents the atoms in the unit cell, and n_i is the concentration of the i-th atom. E_i is the total energy of the element i in its bulk ground state. We have considered bcc-Mn, bcc-Fe, hcp-Co, fcc-Ni, fcc-Cu, and trigonal-Sb as ground-state structures in their elemental phases. The elastic constants for the compounds are calculated using the energy-strain method only for high-temperature cubic austenite phases.

To study the variation of Curie temperatures with concentrations, we have calculated the magnetic pair exchange parameters using multiple scattering Green function formalism as implemented in SPRKKR code [230], as described in Chapter 2. In order to calculate the energy differences by the SPRKKR code, full potential spin-polarized scalar relativistic Hamiltonian with angular momentum cut-off

$l_{max} = 3$ is used along with a converged k-mesh for Brillouin zone integrations. The Green's functions were calculated for 32 complex energy points distributed on a semi-circular contour in the complex plane. The energy convergence criterion was set to 10^{-5} eV for the self-consistent cycles. Here we used the equilibrium lattice parameters, and the optimized atomic positions from the projector augmented wave calculation using VASP package. These exchange parameters are then used for the calculations of Curie temperatures (T_c^A) in the austenite phase. The Curie temperatures are estimated with two different approaches: the mean-field approximation (MFA) [223, 286] and the Monte Carlo simulation (MCS) method [182, 236] in order to check the qualitative consistency in the results and to obtain a reliable estimate of the quantity as the MFA is known to overestimate T_c^A while the MCS method is more accurate quantitatively. The Monte Carlo simulations have been carried out using Metropolis algorithm [182, 236]. Magnetic exchange interactions $J_{ij}^{\mu\nu}$ for upto 20 neighbours surrounding each atom have been considered in the Heisenberg Hamiltonian, as described in chapter 2. At each temperature, 80000 Monte Carlo steps have been performed to equilibriate the systems containing 8192 atoms. The Curie temperatures are obtained from the resulting M-T relationship, where M is the total magnetic moment of the system and T the temperature.

4.3 Results and Discussions

In the present chapter, we have dealt with Fe, Co and Cu substituted $Ni_2Mn_{1.50}Sb_{0.50}$ compounds with substitutions done both at Ni and Mn sites to get a comparative understanding of how they affect the properties as a function of composition. We, thus, have considered two different systems: (i) $Ni_2Mn_{1.50-y}Z_ySb_{0.50}$(referred as Z@Mn) and (ii) $Ni_{2-y}Z_yMn_{1.50}Sb_{0.50}$(referred as Z@Ni) with Z=Fe, Co and Cu for $y = 0, 0.25, 0.50$ (shown in Table 4.1). The systems are modelled with a 16-atom conventional cubic cell. For example, to make a 25% Fe-substituted $Ni_2Mn_{1.25}Fe_{0.25}Sb_{0.50}$ composition, one Mn atom out of the six in the conventional cell of $Ni_2Mn_{1.50}Sb_{0.50}$ is replaced with one Fe atom (Fig. 4.1(d)), as done elsewhere [144, 246, 260]. Though the experiments have been done with much smaller concentrations of the substituents, we had to restrict ourselves with above mentioned values of y as modelling of experimental compositions would require computationally demanding larger supercells.

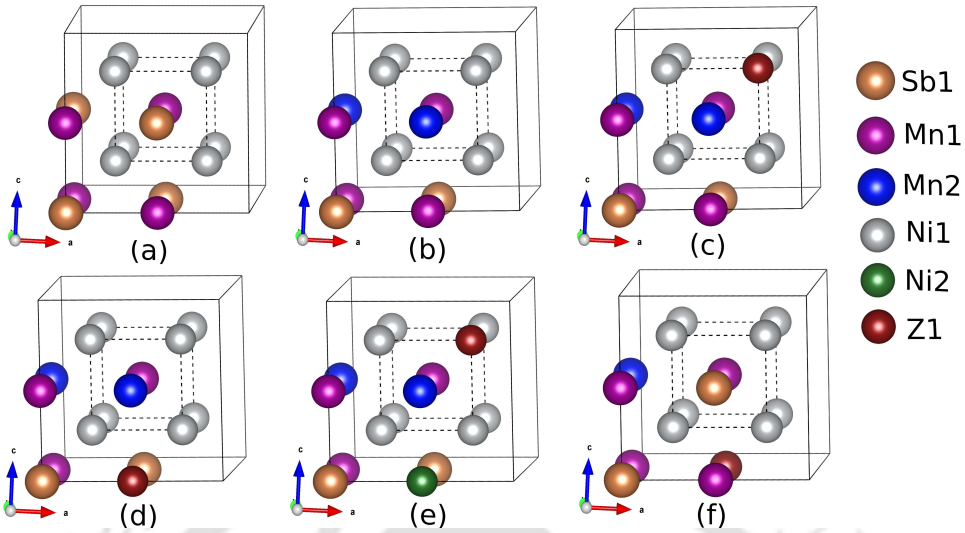

Figure 4.1: Sixteen-atom supercell for (a) stoichiometric Ni_2MnSb (b) off-stoichiometric $Ni_2Mn_{1.50}Sb_{0.50}$, and (c) 3*d*-element substituted $Ni_{2-y}Z_yMn_{1.50}Sb_{0.50}$ (Z=Fe, Co and Cu) (d) $Ni_2Mn_{1.50-y}Fe_ySb_{0.50}$ (e) $Ni_2Mn_{1.50-y}Co_ySb_{0.50}$ and (f) $Ni_2Mn_{1.50-y}Cu_ySb_{0.50}$ with y=0.25 compositions for their corresponding preferred site-configurations as mentioned in Table 4.1.

4.3.1 Site preferences and magnetic ground states in austenite phases

The configurational ordering of the constituent elements in the crystal lattice affects both the martensitic transformation characteristics and the magnetic properties of Ni-Mn-based alloys [223, 253, 269]. First-principles calculations [229, 287, 288] also demonstrated that the substituent 3*d*-transition metals do not always prefer to occupy the sites of substitutions. Therefore, we first focus on the determination of the site preferences and the associated magnetic ground states of the substituted $Ni_2Mn_{1.5}Sb_{0.5}$ compounds in their high-temperature austenite phases, by comparing total energies of various possible site ordered and magnetic configurations at fixed compositions. The results are shown in Table 4.1.

The results suggest the following (see Fig. 4.1): substitutions at Mn sites show that the different substituents prefer different sites. While the substituting Fe atoms prefer to occupy the Mn sublattices, Co atoms prefer the Ni sublattices forcing the Ni to occupy the substituted Mn sublattices. Substituting Cu atoms, on the other hand, prefer the Sb sublattices. In case of substitutions at Ni sites, all three substituents have preferences for the sites of substitution only, corroborating the experimental predictions in case of Co substituted $Ni_2Mn_{1.52}Sb_{0.48}$ [289]. Regarding the preferred magnetic configurations, it can be concluded that for both Fe and Cu

Table 4.1: Preferred site-occupancies, corresponding possible magnetic configurations, and their relative electronic energies ΔE_0 (in meV/atom) are shown. "C1" to "C4" denote possible magnetic configurations for Z=Fe, Co and Cu substituted (i) $Ni_2Mn_{1.50-y}Z_ySb_{0.50}$(Z@Mn) and (ii) $Ni_{2-y}Z_yMn_{1.50}Sb_{0.50}$(Z@Ni) systems. The atom X at its original site in $L2_1$ lattice is denoted as X1, whereas it is denoted as X2 when it occupies any other site. The reference energy in each case is that of "C1" or "C3" (when "C1" is not possible) magnetic configuration. Boldface indicates the ground state magnetic configuration for the corresponding composition.

(i) $Ni_2Mn_{1.50-y}Z_ySb_{0.50}$

Composition	Site Occupancy 4a site	4b site	8c site	Mag. Configurations	ΔE_0
Z=Fe					
$Ni_2Mn_{1.50}Sb_{0.50}$(y=0.00)	$Sb1_{0.50}Mn2_{0.50}$	Mn1	$Ni1_2$	**C1(Mn1↑ Mn2↓ Ni1↑)**	0.00
				C2(Mn1↑ Mn2↑ Ni1↑)	15.32
$Ni_2Mn_{1.25}Fe_{0.25}Sb_{0.50}$($y$=0.25)	$Sb1_{0.50}Mn2_{0.50}$	$Mn1_{0.75}Fe1_{0.25}$	$Ni1_2$	C1(Mn1↑ Mn2↓ Ni1↑ Fe1↓)	0.00
				C2(Mn1↑ Mn2↑ Ni1↑ Fe1↓)	-3.15
				C3(Mn1↑ Mn2↓ Ni1↑ Fe1↑)	-26.10
				C4(Mn1↑ Mn2↑ Ni1↑ Fe1↑)	-1.20
$Ni_2MnFe_{0.50}Sb_{0.50}$(y=0.50)	$Sb1_{0.50}Mn2_{0.50}$	$Mn1_{0.50}Fe1_{0.50}$	$Ni1_2$	C1(Mn1↑ Mn2↓ Ni1↑ Fe1↓)	0.00
				C2(Mn1↑ Mn2↑ Ni1↑ Fe1↓)	-16.94
				C3(Mn1↑ Mn2↓ Ni1↑ Fe1↑)	-36.17
				C4(Mn1↑ Mn2↑ Ni1↑ Fe1↑)	-3.34
Z=Co					
$Ni_2Mn_{1.50}Sb_{0.50}$(y=0.00)	$Sb1_{0.50}Mn2_{0.50}$	Mn1	$Ni1_2$	**C1(Mn1↑ Mn2↓ Ni1↑)**	0.00
				C2(Mn1↑ Mn2↑ Ni1↑)	15.32
$Ni_2Mn_{1.25}Co_{0.25}Sb_{0.50}$($y$=0.25)	$Sb1_{0.50}Mn2_{0.50}$	$Mn1_{0.75}Ni2_{0.25}$	$Ni1_{1.75}Co1_{0.25}$	**C3(Mn1↑ Mn2↓ Ni1,Ni2↑ Co1↑)**	0.00
				C4(Mn1↑ Mn2↑ Ni1,Ni2↑ Co1↑)	12.02
$Ni_2MnCo_{0.50}Sb_{0.50}$(y=0.50)	$Sb1_{0.50}Mn2_{0.50}$	$Mn1_{0.50}Ni2_{0.50}$	$Ni1_{1.50}Co1_{0.50}$	C3(Mn1↑ Mn2↓ Ni1,Ni2↑ Co1↑)	0.00
				C4(Mn1↑ Mn2↑ Ni1,Ni2↑ Co1↑)	-0.69
Z=Cu					
$Ni_2Mn_{1.50}Sb_{0.50}$(y=0.00)	$Sb1_{0.50}Mn2_{0.50}$	Mn1	$Ni1_2$	**C1(Mn1↑ Mn2↓ Ni1↑)**	0.00
				C2(Mn1↑ Mn2↑ Ni1↑)	15.32
$Ni_2Mn_{1.25}Cu_{0.25}Sb_{0.50}$($y$=0.25)	$Sb1_{0.50}Mn2_{0.25}Cu1_{0.25}$	Mn1	$Ni1_2$	**C3(Mn1↑ Mn2↓ Ni1↑ Cu1↑)**	0.00
				C4(Mn1↑ Mn2↑ Ni1↑ Cu1↑)	6.80
$Ni_2MnCu_{0.50}Sb_{0.50}$(y=0.50)	$Sb1_{0.50}Cu1_{0.50}$	Mn1	$Ni1_2$	**C4(Mn1↑ Ni1↑ Cu1↑)**	0.00

(ii) $Ni_{2-y}Z_yMn_{1.50}Sb_{0.50}$

Composition	Site Occupancy 4a site	4b site	8c site	Mag. Configurations	ΔE_0
Z=Fe					
$Ni_2Mn_{1.50}Sb_{0.50}$(y=0.00)	$Sb1_{0.50}Mn2_{0.50}$	Mn1	$Ni1_2$	**C1(Mn1↑ Mn2↓ Ni1↑)**	0.00
				C2(Mn1↑ Mn2↑ Ni1↑)	15.32
$Ni_{1.75}Fe_{0.25}Mn_{1.50}Sb_{0.50}$($y$=0.25)	$Sb1_{0.50}Mn2_{0.50}$	Mn1	$Ni1_{1.75}Fe1_{0.25}$	C1(Mn1↑ Mn2↓ Ni1↑ Fe1↓)	0.00
				C2(Mn1↑ Mn2↑ Ni1↑ Fe1↓)	25.13
				C3(Mn1↑ Mn2↓ Ni1↑ Fe1↑)	-13.07
				C4(Mn1↑ Mn2↑ Ni1↑ Fe1↑)	-4.26
$Ni_{1.50}Fe_{0.50}Mn_{1.50}Sb_{0.50}$($y$=0.50)	$Sb1_{0.50}Mn2_{0.50}$	Mn1	$Ni1_{1.50}Fe1_{0.50}$	C1(Mn1↑ Mn2↓ Ni1↑ Fe1↓)	0.00
				C2(Mn1↑ Mn2↑ Ni1↑ Fe1↓)	38.84
				C3(Mn1↑ Mn2↓ Ni1↑ Fe1↑)	-22.73
				C4(Mn1↑ Mn2↑ Ni1↑ Fe1↑)	-13.68
Z=Co					
$Ni_2Mn_{1.50}Sb_{0.50}$(y=0.00)	$Sb1_{0.50}Mn2_{0.50}$	Mn1	$Ni1_2$	**C1(Mn1↑ Mn2↓ Ni1↑)**	0.00
				C2(Mn1↑ Mn2↑ Ni1↑)	15.32
$Ni_{1.75}Co_{0.25}Mn_{1.50}Sb_{0.50}$($y$=0.25)	$Sb1_{0.50}Mn2_{0.50}$	Mn1	$Ni1_{1.75}Co1_{0.25}$	**C3(Mn1↑ Mn2↓ Ni1↑ Co1↑)**	0.00
				C4(Mn1↑ Mn2↑ Ni1↑ Co1↑)	5.77
$Ni_{1.50}Co_{0.50}Mn_{1.50}Sb_{0.50}$($y$=0.50)	$Sb1_{0.50}Mn2_{0.50}$	Mn1	$Ni1_{1.50}Co1_{0.50}$	C3(Mn1↑ Mn2↓ Ni1↑ Co1↑)	0.00
				C4(Mn1↑ Mn2↑ Ni1↑ Co1↑)	-3.04
Z=Cu					
$Ni_2Mn_{1.50}Sb_{0.50}$(y=0.00)	$Sb1_{0.50}Mn2_{0.50}$	Mn1	$Ni1_2$	**C1(Mn1↑ Mn2↓ Ni1↑)**	0.00
				C2(Mn1↑ Mn2↑ Ni1↑)	15.32
$Ni_{1.75}Cu_{0.25}Mn_{1.50}Sb_{0.50}$($y$=0.25)	$Sb1_{0.50}Mn2_{0.50}$	Mn1	$Ni1_{1.75}Cu1_{0.25}$	**C3(Mn1↑ Mn2↓ Ni1↑ Cu1↑)**	0.00
				C4(Mn1↑ Mn2↑ Ni1↑ Cu1↑)	17.74
$Ni_{1.50}Cu_{0.50}Mn_{1.50}Sb_{0.50}$($y$=0.50)	$Sb1_{0.50}Mn2_{0.50}$	Mn1	$Ni1_{1.50}Cu1_{0.50}$	**C3(Mn1↑ Mn2↓ Ni1↑ Cu1↑)**	0.00
				C4(Mn1↑ Mn2↑ Ni1↑ Cu1↑)	18.90

substitutions, the Mn1 atoms align parallel with Ni1, Ni2, and Z(=Fe, Cu) atoms and align anti-parallel with the Mn2 atoms; the configuration denoted as "C3". In cases of Co substitutions, though the Mn atoms have anti-parallel alignments for smaller concentrations (i.e., "C3" configuration), with increase in Co concentration, they align parallel making the "C4" magnetic configuration as the ground state. However, in $Ni_2MnCo_{0.50}Sb_{0.50}$ the energy difference between the "C3" and "C4" configurations is small indicating that a mixed phase of these two can be present. This implies that Co acts as a "ferromagnetic activator" in Ni-Mn-Sb alloys, as is seen in other Ni-Mn based Heusler alloys [283, 290–293].

4.3.2 Magnetic moments in the austenite phases

As was discussed in Section 4.1, significant enhancement of magnetic moment in the austenite phases leading to a possibility of large ΔM is one of the motivations for substitutions of Ni and Mn with other $3d$ elements. That there is a correlation between enhancement of magnetization in the austenite phase and a large MCE for Ni-Mn-Sb system could be observed in the experiment on the compound where Co substituted Ni. An enhancement in magnetization in the austenite phase along with a significant MCE was observed [135, 142, 293]. In order to understand the qualitative and quantitative trends in magnetizations due to substitutions of different elements at different sites and with different concentrations, we have calculated the total and atomic moments of all compounds as a function of compositions. The results are shown in Fig. 4.2 and Table 4.2. In Fig. 4.2, we present simultaneously the variations in the moments when concentrations of the substituting element are between 0 and 25% as well as between 25% and 50%, that is when the concentrations could be chosen arbitrarily. These calculations are done by SPRKKR code, which implements the KKR-CPA method that uses single-site mean-field technique to address the substitutional disorder and hence does not require constructions of supercell. This was necessary in order to mimic the experimental compositions as much as possible and at the same time, to find whether the qualitative changes in the moments with compositions indeed follow the trends as computed using supercells where concentrations of the substituents are varied by larger percentages. The lattice constants used for the calculations with KKR-CPA for arbitrary concentrations are taken by interpolating the lattice constants obtained from supercell calculations, presented in Table 4.2.

We find that Fe-substitution at the Mn1 sites in $Ni_2Mn_{1.50}Sb_{0.50}$ lead to a slight

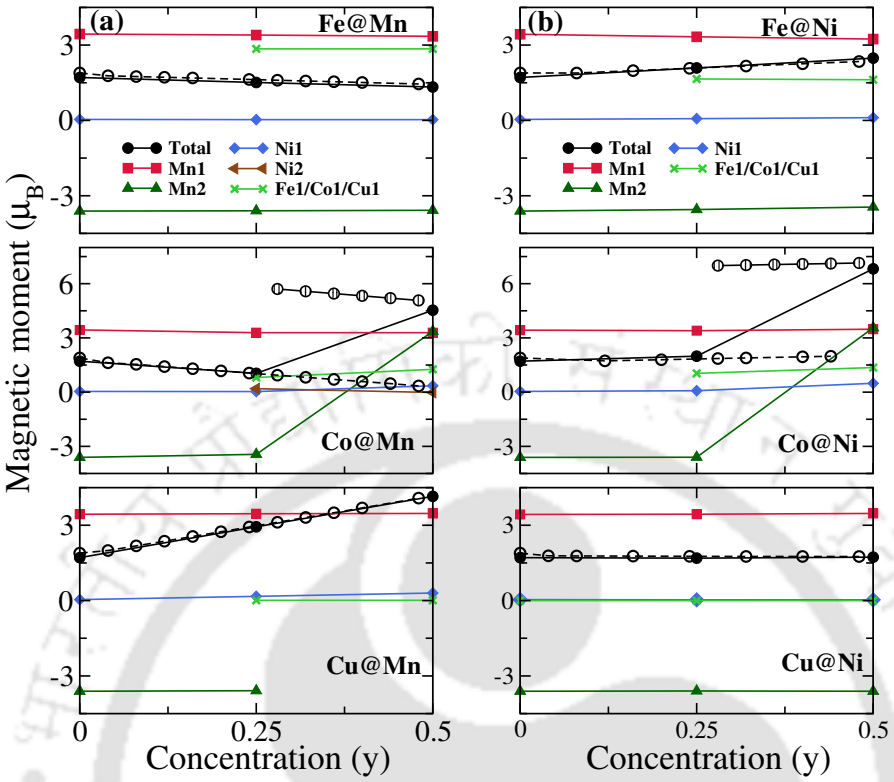

Figure 4.2: Calculated total magnetic moment and atomic magnetic moments (in $\mu_B/f.u.$) (for atom-name convention see Table 4.1) as a function of concentration y of substituting elements, Z=Fe, Co and Cu for (a) $Ni_2Mn_{1.50-y}Z_ySb_{0.50}$(Z@Mn) and (b) $Ni_{2-y}Z_yMn_{1.50}Sb_{0.50}$(Z@Ni) systems in their lowest energy magnetic configurations as indicated in Table 4.1. Variations of total magnetic moments with y calculated by SPRKKR code [230], are presented by dashed lines with open symbols. For Co-substituted systems, magnetic moments both for "C3"(dashed lines with open circles) and "C4"(solid lines with marked circles) magnetic configurations for $y > 0.25$ are shown.

decrease in total magnetic moments with increase in the concentration of Fe, although the atomic moments hardly change. This is due to the lower moments on Fe atoms in comparison to the substituted Mn1 atoms. When Fe substitutes Ni, the total magnetic moment increases with Fe concentration as stronger magnet Fe replaces Ni. In case of Cu substituting Mn, we find remarkable increase in the total moment as Cu concentration increases. This occurs as the Cu atoms, instead of occupying the Mn1 sites, replace Mn2 atoms at the Sb sites, thus decreasing the negative contributions from Mn2 atoms to the overall moment. This does not happen when Cu replaces Ni. Co-substitutions at either Mn or Ni sites present an interesting picture. When Co substitutes Mn or Ni, the magnetic configuration up to at least $y = 0.25$ is "C3". Since Co always occupies Ni sites irrespective of whether Mn or Ni is substituted, leaving Mn2 as it is, the moment decreases when Mn is substituted, as the net

positive contribution to the total moment goes down with weaker magnet Co replacing Mn. When Ni is substituted, the net moment increases with y, albeit weakly, as Co moment is greater than that of Ni. Quantitatively the results of supercell calculations (by VASP) and KKR-CPA calculations (by SPRKKR) have excellent agreements, and reproduce experimental results well, as KKR-CPA calculated moment value of 1.99 $\mu_B/f.u.$ for $Ni_{1.8}Co_{0.2}Mn_{1.50}Sb_{0.50}$ is in good agreement with the experimental value of 1.85 $\mu_B/f.u.$ for $Ni_{1.8}Co_{0.2}Mn_{1.52}Sb_{0.48}$ composition [289]. For $y = 0.5$, we found that although the lowest energy magnetic configuration "C4", the energy difference between "C3" and "C4" is extremely low, even less than 1 meV per atom for Mn-substituted compound. This gives rise to the possibility of mixed magnetic phases comprising of both "C3" and "C4". However, in our calculations, we have considered only "C4" for $y = 0.5$ in the supercell calculations while both configurations are considered for all y between 0.25 and 0.5 in KKR-CPA calculations. We find that for $y = 0.5$, both supercell and KKR-CPA produce identical results, a high magnetic moment which is expected as the Mn spins align in "C4". The configuration "C3" leads to gradual quenching of the total moment as Co replaces Mn1, an extrapolation of the behavior for $y \leq 0.25$. However, for Co replacing Ni, the total moment does not change appreciably due to the proximity of the atomic moments of the two.

Thus, substitution with Co provides us with a possibility for large magnetic moment in the austenite phase when $y \sim 0.25$ and subsequently a large value of ΔM as desired may be realized. However, since there is a good possibility of mixed magnetic phases of the two configurations, the actual moment may not be that high as the net moment will be a weighted average of moments of the two magnetic configurations. Even then, the net magnetic moment is expected to be higher than the cases where Fe or Cu are substituted.

4.3.3 Structural phase transition and associated change in magnetic structure

Compositions exhibiting the structural phase transition near room temperature and associated with a change in the magnetic structure are of great importance. Chemical substitution in Ni-Mn based ternary compounds has been proved to be an effective way to tune the stability of the austenite phase or in other words, to adjust T_M and to increase ΔM. As discussed in Section 4.1, different investigations conclude that Fe, Co, Cu substitutions at Mn and Ni sites in Mn-excess Ni-Mn-(Ga, In, Sn)

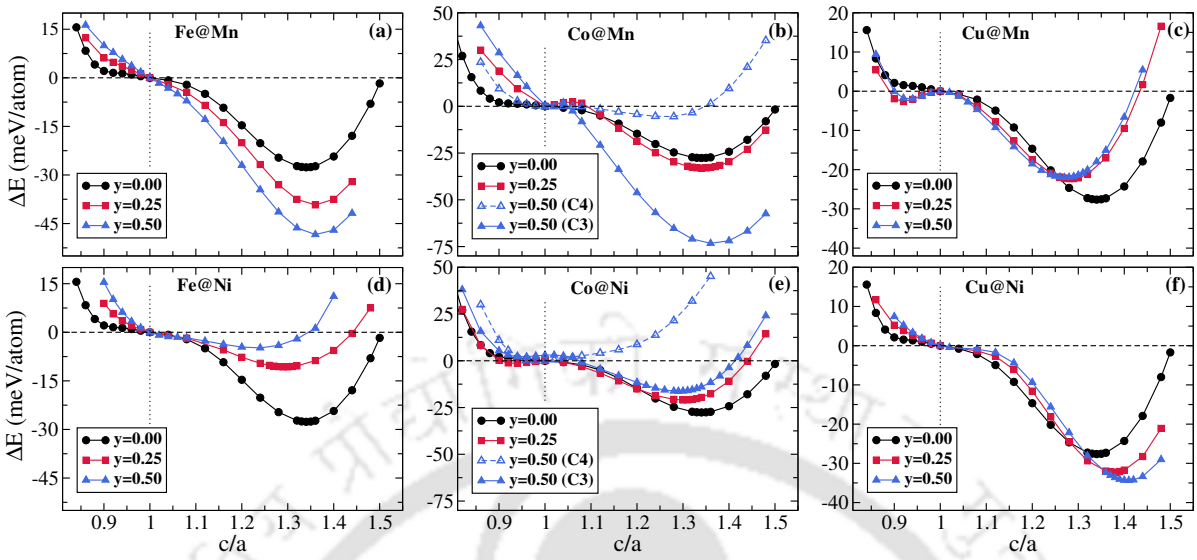

Figure 4.3: The variations of total energy difference (ΔE) between the austenite($L2_1$) and the martensite(tetragonal) phases as a function of tetragonal distortion i.e. c/a ratio for ((a)-(c)) $Ni_2Mn_{1.50-y}Z_ySb_{0.50}$(Z@Mn) and ((d)-(f)) $Ni_{2-y}Z_yMn_{1.50}Sb_{0.50}$(Z@Ni) (Z=Fe, Co and Cu) systems for considered values of y and at their ground state magnetic configurations (as in Table 4.1). Results where the magnetic configurations are different in the martensitic phases (for Co substitution with $y = 0.50$) are also shown.

alloys tune the thermodynamic parameters related to the magnetic and structural transformations and consequently the MCE [134, 135, 140, 142, 289, 294]. Therefore, in this section, we have systematically investigated the effects of substitution of different elements with different concentrations and at various sites on the stability of the austenite phase of $Ni_2Mn_{1.5}Sb_{0.5}$. We also look into the possible changes in the magnetic configurations due to the structural transitions from cubic austenite to a tetragonal martensitic phase that can result in a large (ΔM) in these compounds. Although, the quantification of ΔM and comparison with experiments cannot be directly done in this way due to the fact that the experimental samples may not lead to the tetragonal martensites immediately after the MPT and at the temperatures where experimental measurements were carried out, the calculations surely can provide important insights into the possible trends and outcomes in regard to expectation of large ΔM.

To study the structural phase stability for a particular composition, we have distorted the lowest energy $L2_1$ structure at that composition along each of the possible crystallographic inequivalent directions and computed the total energy as a function of the tetragonal distortion given by (c/a), as done in the previous chapter. Due to the finite size of the 16 atom supercell, different atomic distributions in the planes,

Table 4.2: Calculated values of equilibrium lattice constant (a_0), formation energies (E_f) and total magnetic moment (M_A) of the systems under considerations in their austenite phases with corresponding ground state magnetic configurations are shown. The total energy difference (ΔE) between the austenite($L2_1$) and the martensite(tetragonal) phases [the equilibrium value of tetragonal distortion (c/a) is given in parentheses], the total magnetic moment (M_M) in the non-modulated martensitic phases and the differences in magnetic moments between the austenite and martensite phases (ΔM) are also shown.

Composition	Mag. Config.	a_0 (Å)	E_f (eV/f.u.)	$\Delta E(c/a)$ (meV/atom)	M_A ($\mu_B/f.u.$)	M_M ($\mu_B/f.u.$)	$\lvert\Delta M\rvert$ ($\mu_B/f.u.$)
$Ni_2Mn_{1.50}Sb_{0.50}$	C1	5.94	-0.55	27.64(1.34)	1.71	1.55	0.16
$Ni_2Mn_{1.25}Fe_{0.25}Sb_{0.50}$	C3	5.92	-0.42	39.23(1.36)	1.51	1.46	0.05
$Ni_2MnFe_{0.50}Sb_{0.50}$	C3	5.91	-0.29	48.38(1.36)	1.33	1.37	0.04
$Ni_{1.75}Fe_{0.25}Mn_{1.50}Sb_{0.50}$	C3	5.92	-0.45	10.68(1.29)	2.09	1.88	0.21
$Ni_{1.50}Fe_{0.50}Mn_{1.50}Sb_{0.50}$	C3	5.91	-0.33	4.81(1.24)	2.48	-	-
$Ni_2Mn_{1.25}Co_{0.25}Sb_{0.50}$	C3	5.89	-0.63	33.00(1.34)	1.04	0.93	0.11
$Ni_2MnCo_{0.50}Sb_{0.50}$	C4	5.87	-0.66	73.26(1.36)	4.53	0.09	4.44
$Ni_{1.75}Co_{0.25}Mn_{1.50}Sb_{0.50}$	C3	5.93	-0.67	20.97(1.30)	1.99	1.94	0.05
$Ni_{1.50}Co_{0.50}Mn_{1.50}Sb_{0.50}$	C4	5.95	-0.79	16.27(1.29)	6.82	1.95	4.87
$Ni_2Mn_{1.25}Cu_{0.25}Sb_{0.50}$	C3	5.92	-0.49	22.30(1.28)	2.94	3.06	0.12
$Ni_2MnCu_{0.50}Sb_{0.50}$	C4	5.90	-0.43	22.00(1.27)	4.15	4.15	0.00
$Ni_{1.75}Cu_{0.25}Mn_{1.50}Sb_{0.50}$	C3	5.95	-0.44	32.23(1.38)	1.69	1.64	0.05
$Ni_{1.50}Cu_{0.50}Mn_{1.50}Sb_{0.50}$	C3	5.98	-0.33	34.35(1.41)	1.73	1.76	0.03

perpendicular to which distortion is given, define two crystallographic inequivalent directions for most of the compositions considered here. Further, for the purpose of investigation of any possible changes in the magnetic structures in the martensitic phases from that in the cubic phases, we have also checked energy profiles for all the possible magnetic configurations listed in Table 4.1 at each composition, considering the reference energy as the energy of the austenite ground state for the corresponding composition. In Fig. 4.3, we summarize the results and show the energy profiles of the configurations which provide the minimum energy in each case.

Figure 4.3(a) shows that, when Fe is substituted at Mn site in $Ni_2Mn_{1.5}Sb_{0.5}$, the stability of the austenite phase decreases with increasing concentration of Fe as is apparent from the growing difference in energy (ΔE) (Table 4.2) between the austenite and the martensite phases, implying that T_M increases with Fe concentration. This is completely in contrast with the qualitative behavior observed in the experiment [140]. We address this anomaly in detail as a special case in Section 4.3.7. Fe substituting Ni, on the other hand, enhances the stability of the austenite phase. For 50% Fe-substitution, the total energy curve has a shallow minimum, and thus the possibility of a martensitic instability is slim. Thus the relative

phase stability due to Fe substitution is dependent on the atom that is being substituted. For both cases, no changes in magnetic structures have been observed near the structural phase transition, and as a result, ΔM are also found to be very small. Substitution of Cu, in place of either Ni or Mn, does not affect the relative phase stability significantly. As the Fig. 4.3(c) and Fig. 4.3(f) suggest, ΔE does not change appreciably with y, implying that T_M remains almost unchanged even when concentration of the substituents are high. In both cases, the magnetic structures do not change across phases, as is clear from the results in Table 4.2. Co-substitution turns out to be very interesting as compared to the other two cases. With increase of Co concentration substituting Mn, ΔE first increases moderately in the lower concentration range ($y \leq 0.25$), and no changes in magnetic structure across phases are observed, resulting in a lower value of ΔM. Further increase in Co concentration brings in a change in the magnetic structure in austenite phase as was discussed in the previous section; however, the magnetic structure remains same in the martensitic phase with Mn spins still aligned anti-parallel, leading to a ΔM value of 4.44 $\mu_B/f.u.$. Simultaneously, we find a substantial increase in ΔE, implying a greater martensitic instability in the system. Large ΔM coupled with a large T_M indicate better prospect for MCE. Similar jump in ΔM is observed in case of Co substituting Ni. However, the ΔE decreases in this case with y. This is consistent with the experimental observation in $Ni_{2-y}Co_yMn_{1.52}Sb_{0.48}$ with $y = 0.2$ [135]. Incidentally, large MCE has been found in this compound. Thus, our results in Co-substituted compounds indicate that they are potential materials for large MCE near a magneto-structural transition of the first order.

4.3.4 Magnetic exchange interactions

The inter-atomic magnetic exchange interactions provide the understanding behind the evolution of magnetic transitions and the occurrence of MCE in cases of magneto-structural transitions as observed in Ni-Mn-Z compounds [121, 123, 132, 144, 171, 172, 295, 296]. In this section, we investigate the effects of substitutions of different constituents of $Ni_2Mn_{1.5}Sb_{0.5}$ at different sites and with different concentrations, on the magnetic exchange interactions in their austenite phases, and try to correlate with the results obtained in Sections 4.3.2 and 4.3.3. We then exclusively discuss the reasons behind large MCE observed in experiment on $Ni_{2-y}Co_yMn_{1.52}Sb_{0.48}$ in light of these.

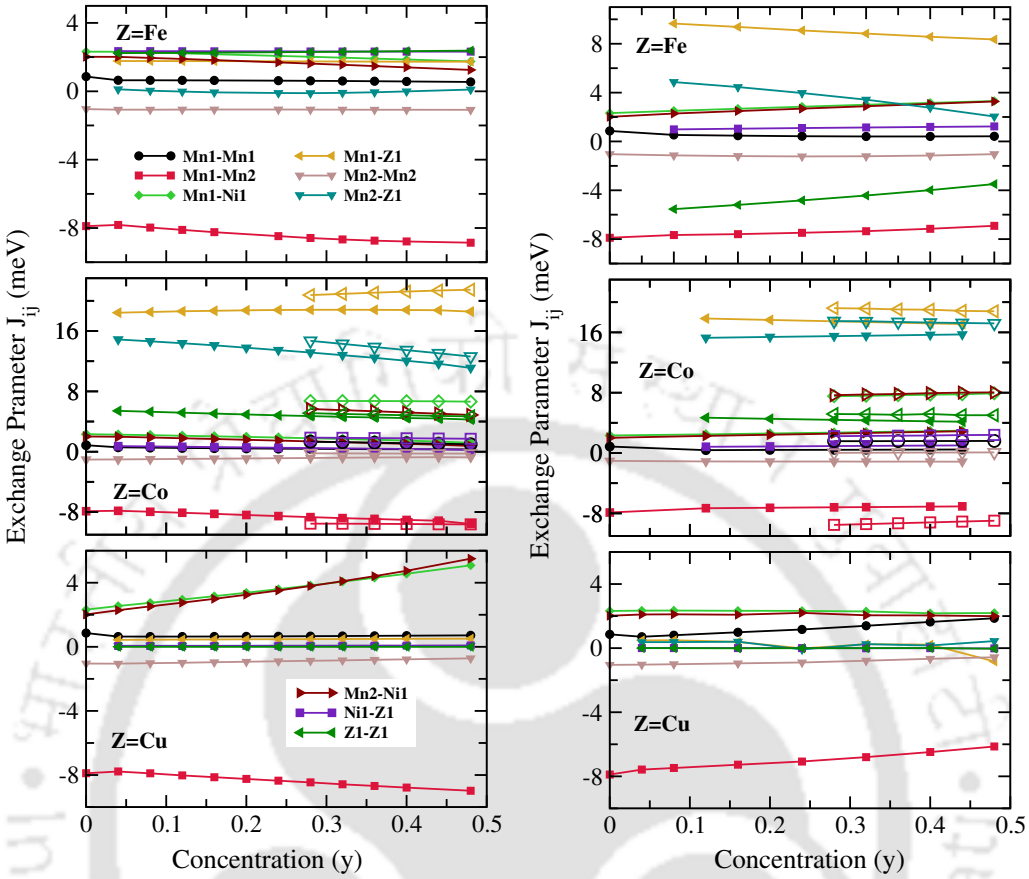

Figure 4.4: The dependence of the inter-atomic magnetic exchange parameters in the first coordination shell (for different pair of atoms) for (left panel) $Ni_2Mn_{1.52-y}Z_ySb_{0.48}$(Z@Mn) and (right panel) $Ni_{2-y}Z_yMn_{1.52}Sb_{0.48}$(Z@Ni) with Z=Fe, Co and Cu systems in their austenite phases. Calculations in each case are done at the ground state magnetic configuration. The composition of the parent compound ($y = 0$), in each case, is considered to be the ones in the experiments [134, 135, 140, 142, 289, 294], and are nominally different from that of $Ni_2Mn_{1.5}Sb_{0.5}$. For Co-substituted systems, magnetic exchange parameters both for "C3"(closed symbols) and "C4"(open symbols) magnetic configurations for $y > 0.25$ are shown.

Figure 4.4 shows the trends in variations of various nearest neighbor inter-atomic magnetic exchange coupling strengths as a function of the substituents concentration. Only the variations in the first coordination shells are considered as these are the dominant interactions. We find that, in each case of substitution, the overall ferromagnetic interactions increase due to the predominantly ferromagnetic interactions between the Ni-Z, Mn-Z, and Z-Z pairs. When Mn is substituted by Fe, there is a competition between the ferromagnetic coupling of Ni-Fe, Mn1-Fe, and antiferromagnetic coupling of Mn1-Mn2 pairs. The antiferromagnetic interaction of Mn1-Mn2 pairs increases with the concentration of Fe and compensates for the weak increase in the ferromagnetic interactions with y. The small negative changes

in the magnetic moment with y can be correlated to such variations in the exchange interactions. In complete contrast to this, substitution of Fe at Ni sites amplify the ferromagnetic Mn-Fe interactions, along with a simultaneous weakening of the anti-ferromagnetic interactions(Mn1-Mn2, Fe-Fe) as y increases. The increase in the magnetic moment with y is an artifact of this. Almost no variations in the magnetic moment of compounds when Ni is substituted by Cu can be understood from the minimal variations in both ferromagnetic and anti-ferromagnetic exchange interactions with Cu concentration. In contrast, The significant strengthening in Ni-Mn ferromagnetic interactions when Cu substitutes Mn can be correlated to the increase in the magnetic moment of the corresponding compound. Co substitutions, both at Mn and Ni sites, give rise to the largest ferromagnetic coupling strengths, which is due to very strong ferromagnetic exchange interactions between the Co and Mn atoms. Ferromagnetic interactions between Mn-Ni and Co-Co pairs strengthen it further. For higher concentrations ($y > 0.25$) the parallel alignment of the Mn atoms (as in "C4" magnetic configuration) magnifies the ferromagnetic interactions further. This explains the large value of moment at high concentrations of Co. Overall, it can be concluded that substitutions of magnetic $3d$-elements in $Ni_2Mn_{1.5}Sb_{0.5}$ magnify ferromagnetic exchange interactions in the system, and thus in general, leads to a higher value of magnetic moment with respect to the parent compound.

We next focus on understanding of the occurrence of large ΔM and the possible connection to significant MCE in some of the substituted Mn-excess, Sb-deficient Ni_2MnSb compounds. For this purpose, we consider $Ni_2Mn_{1.52}Sb_{0.48}$ compound and investigate the behavior of magnetic exchange interactions, in both austenite and martensite phases, when Fe, Co and Cu substitute Ni and Mn with the concentration of the substituent being 0.24. The reason for picking this particular composition is the observation of large MCE for compositions close to this [142] in the compound where Co substitutes Ni. In Fig. 4.5, we show the results for parent composition $Ni_2Mn_{1.52}Sb_{0.48}$ and Co substituted $Ni_{1.76}Co_{0.24}Mn_{1.52}Sb_{0.48}$ to interpret the experimental observations. In the parent composition $Ni_2Mn_{1.52}Sb_{0.48}$, the austenite phase is dominated by the Mn1-Mn2 nearest-neighbor antiferromagnetic (AFM) interactions. In the tetragonal martensite phase, this AFM interaction gets almost four times magnified and shows an oscillatory behavior in the second and third coordination shells. As a result, not much difference between the magnetic moments in the two phases is expected to occur. This proposition is consistent with the results on $Ni_2Mn_{1.5}Sb_{0.5}$ (Table 4.2). When Co substitutes Ni, the Mn1-Mn2 AFM interaction strength remains the same as the pristine compound in the martensitic phase, while

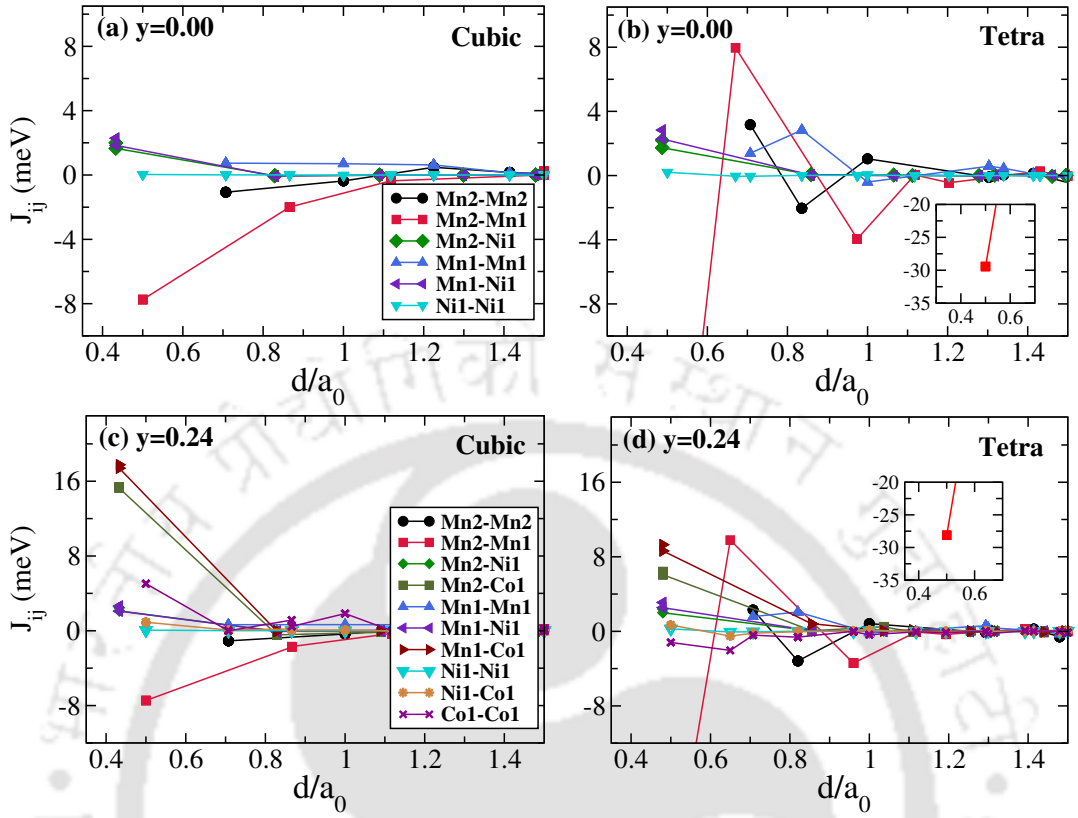

Figure 4.5: Inter-atomic magnetic exchange interactions in (a)-(b)parent composition $Ni_2Mn_{1.52}Sb_{0.48}$ and (c)-(d) $Ni_{2-y}Co_yMn_{1.52}Sb_{0.48}$ with $y = 0.24$ in the cubic (c/a $= 1$) and tetragonal (c/a $\neq 1$) phases as a function of distance d(in units of lattice constant a_0) between the pair of atoms.

the ferromagnetic interactions gain slightly. But, in the austenite phase, the Mn-Co ferromagnetic interactions amplify more than five times in comparison to the dominant ferromagnetic interactions in the pristine compound. As a result, the magnetic moments in the two phases would differ substantially, in comparison to that in the pristine compound. This, therefore, perfectly explains the experimentally observed large ΔM and large MCE. Another highlight of these calculations is observation of a correlation between the qualitative nature of the variations in the exchange interactions and relative stabilities of the structural phases. Experimentally it was observed that for Co-substitution at Ni site in $Ni_2Mn_{1.52}Sb_{0.48}$, T_M decreases with the substituent concentration implying that this substitution stabilizes the austenite phase. The nature of magnetic exchange interactions in Fig. 4.5(c) suggests that the strong ferromagnetic interactions stabilize the austenite phase.

Analysis of the figures 4.6-4.8 lead to the following: (i) for Fe substitution at Mn site, AFM couplings are stronger in the austenite phase, in comparison to the parent

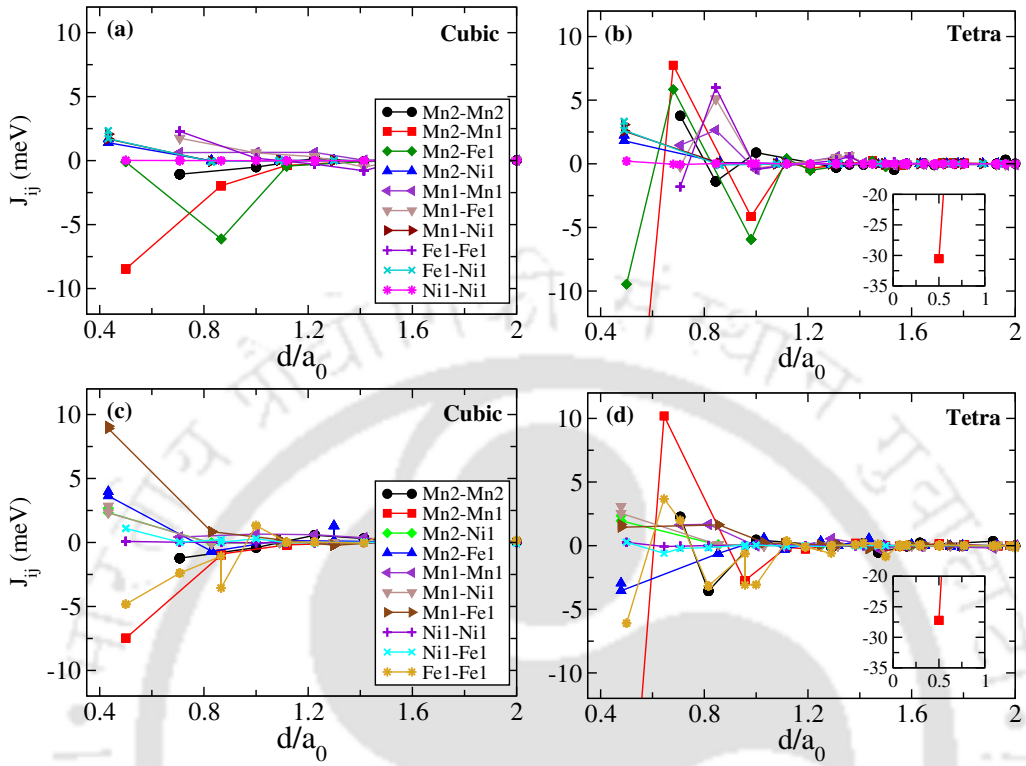

Figure 4.6: Inter-atomic magnetic exchange interactions in (a)-(b) $Ni_2Mn_{1.52-y}Fe_ySb_{0.48}$ ($y = 0.24$) and (c)-(d) $Ni_{2-y}Fe_yMn_{1.52}Sb_{0.48}$ ($y = 0.24$) in the cubic (c/a $= 1$) and tetragonal (c/a $\neq 1$) phases as a function of distance d(in units of lattice constant a_0) between the pair of atoms.

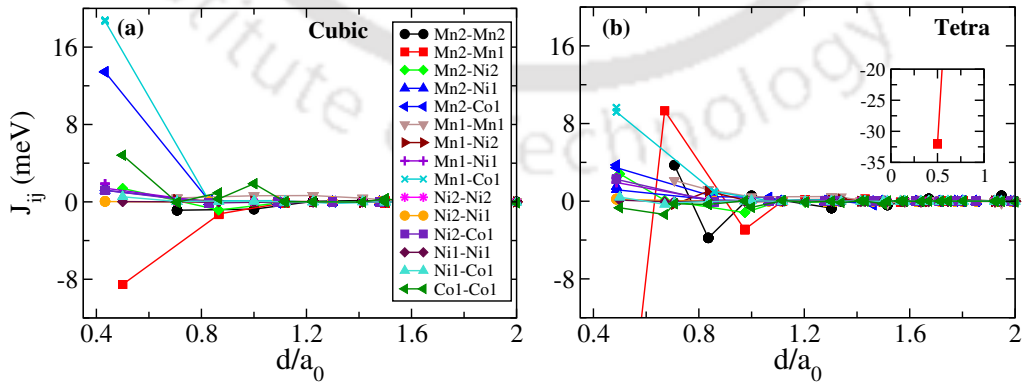

Figure 4.7: Inter-atomic magnetic exchange interactions in $Ni_2Mn_{1.52-y}Co_ySb_{0.48}$ ($y = 0.24$) in the (a) cubic (c/a $= 1$) and (b) tetragonal (c/a $\neq 1$) phases as a function of distance d(in units of lattice constant a_0) between the pair of atoms.

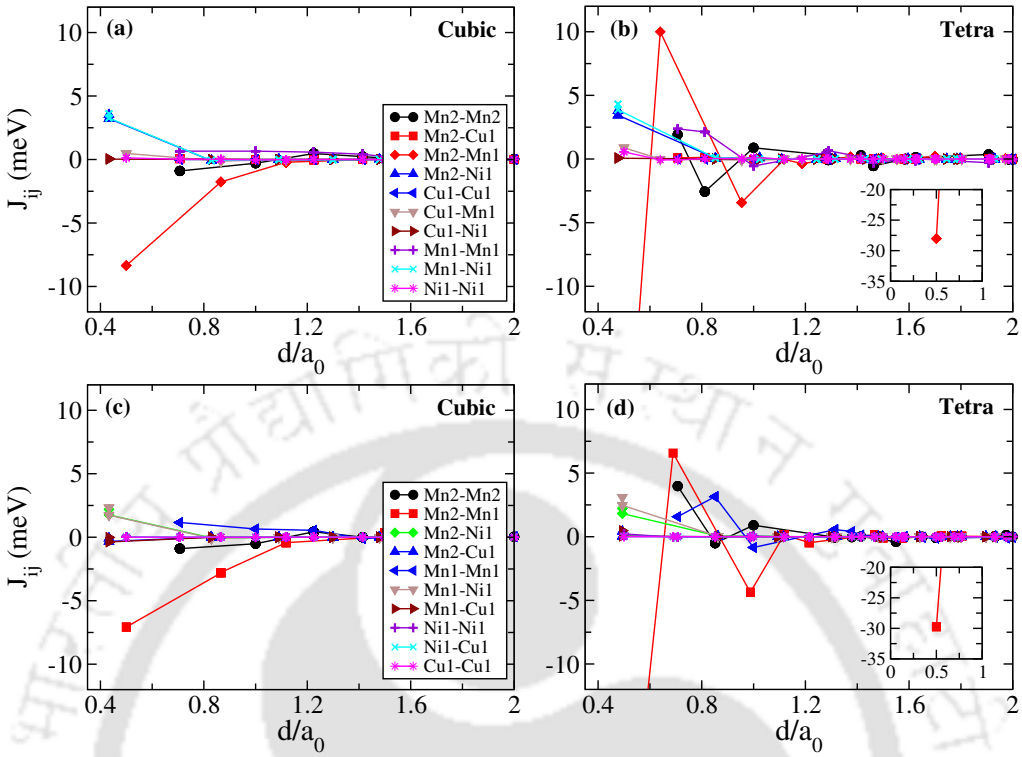

Figure 4.8: Inter-atomic magnetic exchange interactions in (a)-(b) $Ni_2Mn_{1.52-y}Cu_ySb_{0.48}$ ($y = 0.24$) and (c)-(d) $Ni_{2-y}Cu_yMn_{1.52}Sb_{0.48}$ ($y = 0.24$) in the cubic ($c/a = 1$) and tetragonal ($c/a \neq 1$) phases as a function of distance d(in units of lattice constant a_0) between the pair of atoms.

compound, due to AFM Mn2-Fe interactions on top of already existing Mn1-Mn2 one. In tetragonal phase, the AFM interactions magnify, mainly due to stronger Mn2-Fe interactions. Moreover, Mn1-Mn2 and Mn2-Fe interactions are oscillatory in nature. This implies that ΔM may not be very large in this system; (ii) Fe substitution at the expense of Ni leads to substantial increase in the FM components in the exchange interactions in the austenite phase, due to strong Mn-Fe FM interactions. In the martensitic phase, the nature of the interactions are not too different from that in the parent compound; (iii) ferromagnetic interactions become dominant upon substitution of Co at Mn site, in both phases. The many-fold stronger FM interactions in austenite phases and the presence of large AFM interaction in martensitic phases can explain the reason behind large ΔM when Co is substituted; (iv) nature of interactions in Cu substituted compounds are more or less similar to that in the parent compound. Combining these with the results on the relative stability of structural phases of various compounds, occurrence of large ΔM from our calculations and experimental observation of large MCE in Co-substituted (at Ni site) $Ni_2Mn_{1.48}Sb_{0.52}$ [130, 132], we can infer that strong FM interactions stabilize

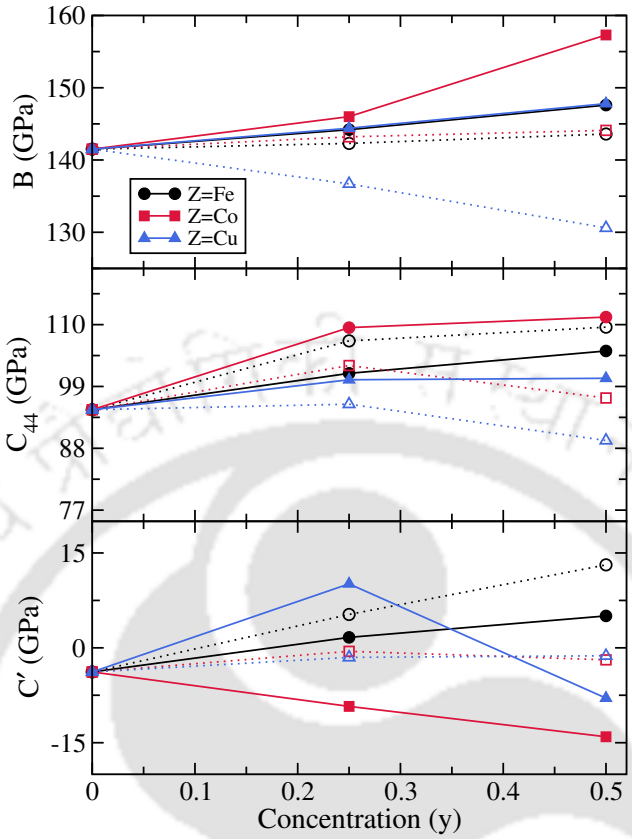

Figure 4.9: The variations in bulk modulus B, shear elastic constants C_{44} and C' as a function of concentration y of substituents, Z=Fe, Co and Cu, in the austenite phases of the considered two systems: $Ni_2Mn_{1.50-y}Z_ySb_{0.50}$(closed symbols) and $Ni_{2-y}Z_yMn_{1.50}Sb_{0.50}$(open symbols).

the austenite phase, reducing the T_M and that the observed large MCE is due to strikingly different nature of dominant magnetic interactions across structural phase transitions, in these compounds.

4.3.5 Mechanical properties

MCE materials with coupled magneto-structural transitions often suffer from cracking and fatigue, which severely limits their usefulness. Quaternary off-stoichiometric Ni-Mn based Heusler compounds are found to exhibit better mechanical properties such as ductility, corrosion resistance, machinability, all of which ease manufacturing and increase the product longevity. For example, Fe-addition improves the toughness of Ni-Mn-Ga alloys without sacrificing its magnetic and thermoelastic properties [229, 281]. In this section, we, therefore, explore the changes in the mechanical properties of $Ni_2Mn_{1.5}Sb_{0.5}$ compounds upon substitution by the fourth

Table 4.3: The calculated values of Pugh ratio G_v/B and Cauchy pressure C^P of the systems under consideration in their austenite phases with ground state magnetic configurations for corresponding compositions.

Composition	Mag. Config.	G_v/B	C^P(GPa)
$Ni_2Mn_{1.50}Sb_{0.50}$	C1	0.39	49.19
$Ni_2Mn_{1.25}Fe_{0.25}Sb_{0.50}$	C3	0.43	41.77
$Ni_2MnFe_{0.50}Sb_{0.50}$	C3	0.44	38.93
$Ni_2Mn_{1.50}Sb_{0.50}$	C1	0.39	49.19
$Ni_{1.75}Fe_{0.25}Mn_{1.50}Sb_{0.50}$	C3	0.47	31.68
$Ni_{1.50}Fe_{0.50}Mn_{1.50}Sb_{0.50}$	C3	0.49	25.31
$Ni_2Mn_{1.50}Sb_{0.50}$	C1	0.39	49.19
$Ni_2Mn_{1.25}Co_{0.25}Sb_{0.50}$	C3	0.42	42.70
$Ni_2MnCo_{0.50}Sb_{0.50}$	C4	0.45	40.12
$Ni_2Mn_{1.50}Sb_{0.50}$	C1	0.39	49.19
$Ni_{1.75}Co_{0.25}Mn_{1.50}Sb_{0.50}$	C3	0.43	40.85
$Ni_{1.50}Co_{0.50}Mn_{1.50}Sb_{0.50}$	C4	0.41	44.81
$Ni_2Mn_{1.50}Sb_{0.50}$	C1	0.39	49.19
$Ni_2Mn_{1.25}Cu_{0.25}Sb_{0.50}$	C3	0.46	33.78
$Ni_2MnCu_{0.50}Sb_{0.50}$	C4	0.39	52.65
$Ni_2Mn_{1.50}Sb_{0.50}$	C1	0.39	49.19
$Ni_{1.75}Cu_{0.25}Mn_{1.50}Sb_{0.50}$	C3	0.42	41.86
$Ni_{1.50}Cu_{0.50}Mn_{1.50}Sb_{0.50}$	C3	0.41	42.05

element.

Compounds having a Pugh ratio (G_v/B) greater than 0.57 are considered to be more brittle [225, 226]. On the other hand, a positive value of Cauchy pressure (C^P) indicates the bonding in the compound to be more metallic, while a negative value implies a stronger covalent bonding [228, 229], as discussed is Chapter 2. To calculate the Pugh ratio and Cauchy pressure, at first we have calculated the Bulk modulus (B) and the elastic moduli (C_{44} and C') for all the compounds, in their austenite phases. The results are shown in Fig. 4.9. We find that the bulk modulus decreases for all the cases where Mn is substituted. The bulk modulus does not change when Fe and Co substitute Ni but decreases appreciably when Cu replaces Ni. These trends in B are consistent with the trends in the variations of lattice constants, as shown in Table 4.2. Positive C_{44} for all the compositions satisfies one of the stability criteria for cubic crystals. A negative C' indicates the instability in the $L2_1$ phase and that the system is prone to a structural transformation. The values of C' explains the observed martensitic instabilities in the compounds and will be discussed later in Section 4.3.6 in detail. Then G_v/B and C^P are calculated

using the relations in Chapter 2 for all the compounds. The results are shown in Table 4.3. The results imply that substitution of Fe, Co, or Cu keeps the Ni-Mn-Sb compounds ductile and the nature of bonding largely metallic.

4.3.6 Variation in T_M and T_c^A

A large MCE i.e., ΔS_{mag}, is usually obtained at a temperature near T_M in cases of first-order magneto-structural transitions, typical for Ni-Mn based Heusler compounds. However, small ΔS_{mag} may also be observed near T_c^A, the magnetic transition temperature in the austenite phase, in a second-order magnetic transition. The largest MCE can be obtained if these two temperatures are as close as possible and near room temperature for operational purposes. Attempts [102, 103, 297], thus, have been made to bring these two temperatures closer by adjusting the composition so that T_M increases and T_c^A decreases. Success in this approach has been achieved in case of $Ni_{2.18}Mn_{0.82}Ga$ by substitution of the magnetic components with another transition metal from the $3d$ series [104, 275, 279, 280, 298]. After investigating the role of the substituents in achieving a large ΔM and the underlying physics therein in section 4.3.3 and section 4.3.4, thus pinpointing the materials which can potentially be exhibiting significant MCE, it becomes necessary to explore how T_M and T_c^A behave with substitution of Fe, Co or Cu in $Ni_2Mn_{1.5}Sb_{0.5}$; more so as the experimental results on Ni-Mn-Sb compounds with compositions close to the parent compound considered in this work suggest that the two temperatures are quite close [134, 142, 289, 294] and near room temperature, varying between 260-330 K.

Calculation of T_M requires computations of free energies, including contributions from phonon and magnetic excitations, apart from the electronic one. This becomes computationally prohibitive for off-stoichiometric compounds like the ones considered here. Therefore, in this work, we could only look at the qualitative variations in T_M as a function of composition for the compounds considered here, by studying the variations of quantities which are related to T_M [244, 287, 299, 300], and are calculated here. The e/a ratio has been found to be a good predictor for composition dependence of T_M in Ni-Mn based Heusler alloys. T_M is found to follow e/a [247–249], albeit with exceptions in some cases: Fe substituted Ni-Mn-Sb being one [140]. For a few notable cases like Ni-Mn-Ga compounds [287], the electron density $n=((e/a)\times n_1)/V_{cell}$, scales with T_M, n_1 being the average number of atoms contained in the unit cell of volume V_{cell} [301]. The total energy difference (ΔE) between the austenite and the martensite phases is found to be another predictor of

Table 4.4: Calculated values of all predicting observables of martensitic transition temperature, T_M: electron to atom ratio (e/a), electron density (n), total energy difference (ΔE) between the austenite($L2_1$) and the martensite(tetragonal) phases, tetragonality of the martensite phase ($\mid c/\mathrm{a}-1 \mid$) and shear modulus (C') of the austenite phase for all the six types of considered systems. In the last column trend in T_M and Curie temperature (T_c^A) in the austenite phase have been concluded by observing the trend in more reliable quantity C' and values of T_c^A calculated through Monte Carlo Simulation in Fig. 4.10, respectively.

Composition	Mag. Config.	e/a	n	ΔE (meV/atom)	$\mid c/\mathrm{a}-1 \mid$	C' (GPa)	Trends in T_M and T_c^A
$Ni_2Mn_{1.50}Sb_{0.50}$	C1	8.25	0.630	27.64	0.34	-3.81	T_M decreases,
$Ni_2Mn_{1.25}Fe_{0.25}Sb_{0.50}$	C3	8.3125	0.641	39.23	0.36	1.65	T_c^A decreases slightly
$Ni_2MnFe_{0.50}Sb_{0.50}$	C3	8.375	0.649	48.38	0.36	5.04	
$Ni_2Mn_{1.50}Sb_{0.50}$	C1	8.25	0.630	27.64	0.34	-3.81	T_M decreases,
$Ni_{1.75}Fe_{0.25}Mn_{1.50}Sb_{0.50}$	C3	8.125	0.627	10.68	0.29	5.28	T_c^A decreases
$Ni_{1.50}Fe_{0.50}Mn_{1.50}Sb_{0.50}$	C3	8.00	0.620	4.81	0.24	13.12	
$Ni_2Mn_{1.50}Sb_{0.50}$	C1	8.25	0.630	27.64	0.34	-3.81	T_M increases,
$Ni_2Mn_{1.25}Co_{0.25}Sb_{0.50}$	C3	8.375	0.656	33.00	0.34	-9.26	T_c^A decreases
$Ni_2MnCo_{0.50}Sb_{0.50}$	C4	8.50	0.672	73.26	0.36	-14.06	
$Ni_2Mn_{1.50}Sb_{0.50}$	C1	8.25	0.630	27.64	0.34	-3.81	T_M decreases,
$Ni_{1.75}Co_{0.25}Mn_{1.50}Sb_{0.50}$	C3	8.1875	0.628	20.97	0.30	-0.55	T_c^A increases slightly
$Ni_{1.50}Co_{0.50}Mn_{1.50}Sb_{0.50}$	C4	8.125	0.617	16.27	0.29	-1.90	
$Ni_2Mn_{1.50}Sb_{0.50}$	C1	8.25	0.630	27.64	0.34	-3.81	T_M decreases in the beginning
$Ni_2Mn_{1.25}Cu_{0.25}Sb_{0.50}$	C3	8.50	0.656	22.30	0.28	15.64	and then increases,
$Ni_2MnCu_{0.50}Sb_{0.50}$	C4	8.75	0.682	22.00	0.27	-7.95	T_c^A decreases
$Ni_2Mn_{1.50}Sb_{0.50}$	C1	8.25	0.630	27.64	0.34	-3.81	T_M and T_c^A remains
$Ni_{1.75}Cu_{0.25}Mn_{1.50}Sb_{0.50}$	C3	8.3125	0.631	32.23	0.38	-1.51	almost constant
$Ni_{1.50}Cu_{0.50}Mn_{1.50}Sb_{0.50}$	C3	8.375	0.627	34.35	0.41	-1.26	

T_M [229, 288, 302]. A larger value of ΔE implies a higher stability of the martensite phase at zero temperature and thus a higher T_M. The tetragonality of the martensite phase quantified by $\mid c/\mathrm{a}-1 \mid$ is also found to follow variations in T_M in cases of Ni-Mn-(Ga, In) compounds [245, 247, 303]. The best predictor of T_M for Ni-Mn based Heusler alloys, so far, has been the shear modulus C' in the austenite phase. This is due to the fact that the shear modulus is associated with the softening of the acoustic phonon branch that drives the martensitic transformation in these systems. Important physical factors like site ordering and magnetic structure are all taken care of in the variation of this quantity [255, 256]. Calculations on off-stoichiometric Ni-Mn-Sb compositions, in the previous chapter, also showed that for Ni-Mn-Sb systems, (e/a), ΔE, C' can be good predictors for T_M.

In Table 4.4, we compile the trends in variations of these five quantities as a function of composition for the six compounds considered, to qualitatively understand the variations in T_M. With increase in Fe concentration at the expense of Mn, the e/a ratio, electron density n, $\mid c/\mathrm{a}-1 \mid$ and ΔE increases, suggesting increase in T_M with Fe concentration, while the increase in C' with concentration of Fe suggests the stabilization of the austenite phase, an opposite trend. This later trend is in agree-

ment with the experimental observation [140], which shows a decrease in T_M with Fe concentration. Even though we consider the trends in C' as the authentic one, this particular system exhibits discrepancy between theory and experiment with regard to the trend in the magnetic moment in the austenite phase, as mentioned earlier. We discuss the origin of this discrepancy and possible solution in Section 4.3.7. For compounds with Fe substituting Ni, the trends in all five quantities are consistent, indicating lowering of T_M with Fe concentration. Though there are no experimental observations available on compositions close to $Ni_{2-y}Fe_yMn_{1.5}Sb_{0.5}$, Fe substitution at Ni sites for similar systems Ni-Mn-(Ga, In, Sn) show the same trend in variation of T_M [280, 284]. Our result for this system, therefore, is consistent. In case of Co-substitution, irrespective of whether Mn or Ni is substituted, all five quantities show the same trend, which implies that T_M increases(decreases) with Co concentration, when Co substitutes Mn(Ni). The available experimental results [134, 135, 142] for $Ni_{2-y}Co_yMn_{1.52}Sb_{0.48}$ are in agreement with this. For Cu substitution at Mn site, both e/a and n increase wheres ΔE decreases slightly, implying contrasting trends in T_M. On the other hand, C' initially increases with Cu for the low concentrations, consistent with the trend seen in ΔE, predicting a slight decrease in T_M, only to decrease for higher concentrations. For compounds where Cu substitutes Ni, ΔE and C', too, show opposite trends. However, changes in all the quantities are very small, indicating that the T_M remains almost constant with respect to the parent compound. In absence of experiments on this system, this cannot be verified. Nevertheless, it is noteworthy that other Ni-Mn based Heulser compounds show almost the same trend for Cu substitution [275, 304].

The variation in Curie temperature (T_c^A) in the austenite phase for all the considered systems, calculated by Mean-field approximation (MFA) and Monte Carlo simulation (MCS) methods, have been shown in Fig. 4.10. It can be seen that the overall trend remains almost same for most of the cases, irrespective of the method used, and that the calculated values, in general, are overestimated in comparison to experiments. For Fe substitution at Mn site, T_c^A, calculated by the MCS method, slightly decreases with Fe concentration wheres with MFA calculation, a substantial decrease in T_c^A is observed. On the other hand, when Fe is substituted at Ni site, same trend of T_c^A decreasing linearly with Fe concentration is found from calculations by either method. We find the same for Co substituted compounds. For compounds with Co substituting Mn, T_c^A decreases with Co concentration when "C3" magnetic configuration is considered. For "C4" magnetic configuration in the higher concentration range, same trend is observed ; the values of T_c^A are larger

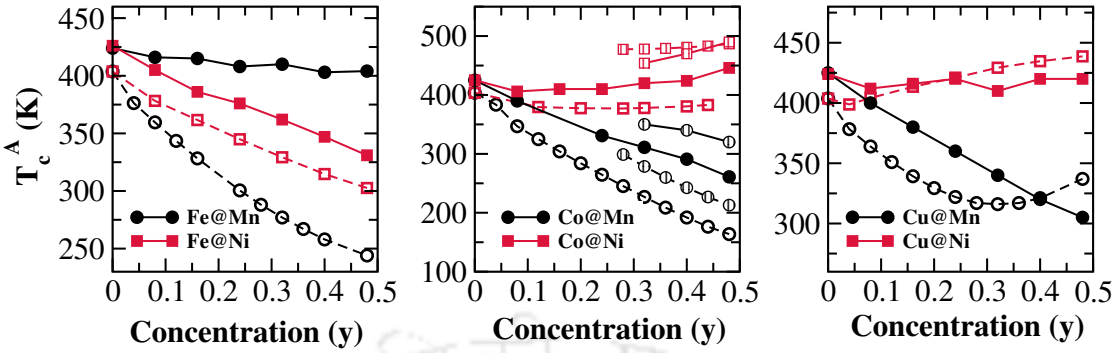

Figure 4.10: Calculated Curie temperatures (T_c^A) as a function of substituents (Z=Fe, Co, Cu) concentration for $Ni_2Mn_{1.52-y}Z_ySb_{0.48}$(Z@Mn) and $Ni_{2-y}Z_yMn_{1.52}Sb_{0.48}$(Z@Ni) systems. Closed symbols and Open symbols represent results calculated by Monte Carlo Simulation (MCS) and Mean Field Approximation (MFA) methods, respectively. For Co-substituted systems, Curie temperatures in "C4" magnetic configuration for $y > 0.25$ are shown with marked circles.

though. For compounds with Co substituting Ni, the T_c^A slightly increases with Co concentration. For compounds with Cu substitution, T_c^A decreases linearly when substitution is done at Mn site, whereas for substitution at Ni site T_c^A remains almost constant when calculated with MCS method. T_c^A calculated by MFA shows a different trend for substitution at Mn site for which T_c^A first decreases in the low concentration range, and then it increases in the higher concentration range.

In Table 4.4 we have summarized the above discussion with regard to variations in T_M and T_c^A. Among the compounds which showed promises as magnetocaloric materials by means of large ΔM, the Co-substituted ones at concentrations of Co more than 25%, $Ni_2Mn_{1.5-y}Co_ySb_{0.5}$ can have T_M and T_c^A very close, desirable for large MCE. In this case, if we take into account the fact that our calculated T_c^A is overestimated by around 50 K, the T_c^A can be very close to room temperature for $y \sim 0.25$. On the other hand, a crude estimation of T_M can be done from the values of ΔE. If the ΔE of the parent compound is mapped to 260 K, the possible T_M by extrapolation from experimental results [132, 146, 305] on compounds with compositions close to it, then T_M will be close to 300 K for $y \sim 0.25$. This, together with large ΔM, will make this compound with this composition a desirable material for MCE. $Ni_{2-y}Co_yMn_{1.5}Sb_{0.5}$ will not be as effective since its T_c^A will be around 350 K for $y \sim 0.25$ while the T_M will be around 220 K, as per the crude estimation from ΔE. Although the ΔM is very low, the compound $Ni_2Mn_{1.5-y}Cu_ySb_{0.5}$ exhibits the possibility of almost coincidence of T_M and T_c^A as the former remains almost constant, and the later rapidly decreases towards room temperature.

Table 4.5: All possible site-occupation configurations ("S-a" to "S-e") and corresponding ground state magnetic configurations of $Ni_2Mn_{1.50-y}Fe_ySb_{0.50}$ (y=0 and 0.25) with their relative electronic energies ΔE_0 (in meV/atom), considering the electronic energy of the "S-a" configuration as reference one.

Composition	Site Config.	Site Occupancy 4a site	4b site	8c site	Mag. Configurations	ΔE_0
$Ni_2Mn_{1.50}Sb_{0.50}$	S-a	$Sb1_{0.50}Mn2_{0.50}$	Mn1	$Ni1_2$	C1 (Mn1↑ Mn2↓ Ni1↑)	0.00
$Ni_2Mn_{1.25}Fe_{0.25}Sb_{0.50}$	S-a	$Sb1_{0.50}Mn2_{0.25}Fe1_{0.25}$	Mn1	$Ni1_2$	C3(Mn1↑ Mn2↓ Ni1↑ Fe1↑)	0.00
	S-b	$Sb1_{0.50}Mn2_{0.50}$	$Mn1_{0.75}Fe1_{0.25}$	$Ni1_2$	C3(Mn1↑ Mn2↓ Ni1↑ Fe1↑)	-4.06
	S-c	$Sb1_{0.50}Mn2_{0.25}Ni2_{0.25}$	Mn1	$Ni1_{1.75}Fe1_{0.25}$	C3(Mn1↑ Mn2↓ Ni1,Ni2↑ Fe1↑)	5.80
	S-d	$Sb1_{0.50}Mn2_{0.50}$	$Mn1_{0.75}Ni2_{0.25}$	$Ni1_{1.75}Fe1_{0.25}$	C3(Mn1↑ Mn2↓ Ni1,Ni2↑ Fe1↑)	-3.09
	S-e	$Sb1_{0.50}Mn2_{0.25}Ni2_{0.25}$	$Mn1_{0.75}Fe1_{0.25}$	$Ni1_{1.75}Mn3_{0.25}$	C3(Mn1↑ Mn2↓ Mn3↑ Ni1,Ni2↑ Fe1↑)	32.90

4.3.7 Resolving discrepancy between theory and experiment for $Ni_2Mn_{1.52-y}Fe_ySb_{0.48}$: possible role of site occupancy

In the absence of experimental results for most of the systems considered in this work, the validation of our findings largely dependent upon agreement with the results of only a couple of experiments on Fe and Co substituting Mn and Ni respectively in $Ni_2Mn_{1.52}Sb_{0.48}$, a composition very close to the one considered here. In case of the system with Co substituting Ni, we observed a good agreement for the trends in magnetic moment and T_M [142]. For the system where Fe substitutes Mn, following discrepancies between our calculations and the experimental observations [140] were found: (i) the magnetic moment of the system, decreases with Fe concentration as per our calculations, in complete disagreement with the trend observed in the experiment and (ii) although the variation of C', the most reliable predictor of T_M, with Fe concentration, suggesting a lowering of T_M, in agreement with the experimental findings, the trend in ΔE, another predictor, and a useful one, as it can provide a quantitative estimate of T_M, implies the opposite. In this section, we attempt to find the origin of the discrepancy and resolve it.

The possible origin of the discrepancy is the difference between the site ordering obtained in our calculation and the actual one generated during the experiment. The site ordering in an experimental sample depends on the thermal treatment. To resolve whether the site ordering is behind the observed discrepancy, we have done a detailed investigation considering all possible site occupancy of the constituent atoms in the Fe-doped $Ni_2Mn_{1.25}Fe_{0.25}Sb_{0.50}$ system. The energies of the ground state magnetic configurations, for each pattern of site occupancy, are summarized in Table 4.5. We, then, have calculated the magnetic moments as a function of Fe concentration between 0 and 0.25, for each site occupancy configuration of Table 4.5. The results are shown in Fig. 4.11(a). We find that the magnetic moment

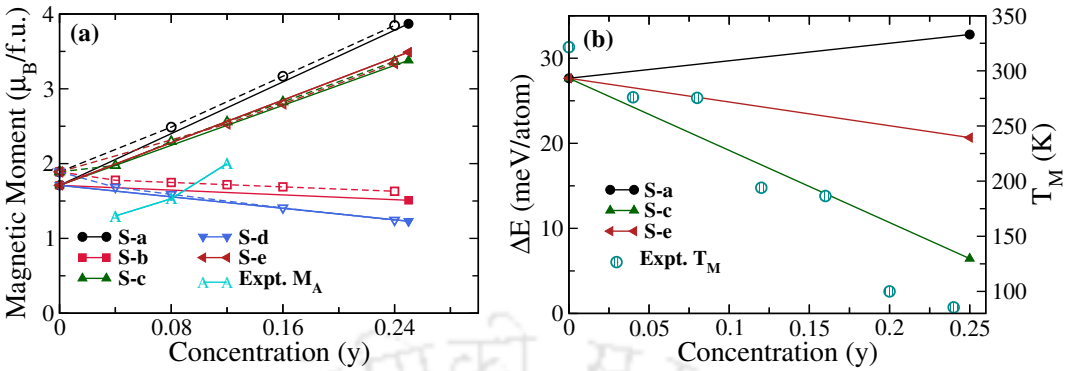

Figure 4.11: Variations in the (a) total magnetic moments with y for various site configurations (Table 4.5) for $Ni_2Mn_{1.50-y}Fe_ySb_{0.50}$ system in their austenite phases calculated with VASP (closed symbols with solid line) and for $Ni_2Mn_{1.52-y}Fe_ySb_{0.48}$ calculated by SPRKKR (open symbols with dashed line). Experimental values of the total moment are added for comparison; (b) total energy differences (ΔE) between the austenite and martensite phases of $Ni_2Mn_{1.50-y}Fe_ySb_{0.50}$ with y, for select site configurations. Experimental values of T_M [140] are given for comparing trends.

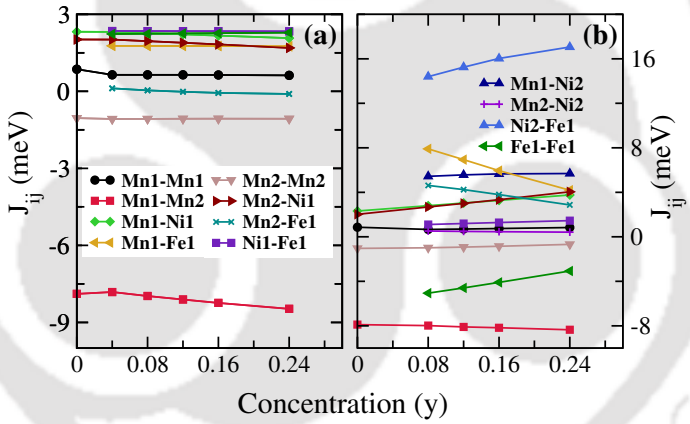

Figure 4.12: The dependence of the inter-atomic magnetic exchange parameters in the first coordination shell (for different pairs of atoms) for $Ni_2Mn_{1.52-y}Fe_ySb_{0.48}$ in their austenite phases for site configurations (a) "S-b" and (b) "S-c".

increases monotonically with Fe concentration, as observed in experiments, for all configurations except "S-b" and "S-d". It is to be noted that the configuration "S-b" has the lowest energy for this compound and has been considered for calculations of physical properties throughout the chapter. Since the configurations "S-a", "S-c", "S-e" reproduce the experimentally observed trend of the magnetic moment, we next calculate the energy profiles of this system as a function of (c/a) for these three configurations and compute ΔE in each case (shown in Fig. 4.11(b)). In the figure, experimentally obtained T_M are shown to find out the proximity of trends in variations of T_M with one or more of the calculated ΔE. We find that the configu-

ration "S-c", one where the substituent Fe atoms occupy the Ni sites while Ni atoms occupy the vacant Sb sites, provide the best agreement to the experiments, in terms of trends in magnetic moment of the austenite phase and the T_M. That this configuration provides the same trend in T_M as the experiment, is further established when our calculated shear modulus C′ is found to increase with Fe concentration (see Table 4.6). The calculated T_c^A provides further credence to "S-c" being the site occupancy configuration realized in the experiment since its trend with Fe concentration also agrees to that in the experiment. The total energies of "S-b" and "S-c" are only 10 meV per atom apart. Thus, occurrence of the "S-c" configuration during the heat treatment of the sample has substantial possibility. To conclude, the experimental results on $Ni_2Mn_{1.52-y}Fe_ySb_{0.48}$ can be consistently interpreted by taking into consideration the role of site occupancies.

Table 4.6: Calculated values of shear modulus C' and Curie temperature (T_c^A) in the austenite phase for $Ni_2Mn_{1.50-y}Fe_ySb_{0.50}$ as a function of Fe concentration for "S-c" site configuration with ground state "C3" magnetic configuration.

Concentration(y)	C' (GPa)	T_c^A (K)
0.00	-3.81	425
0.08	-	382
0.16	-	346
0.24	5.61	310

In order to gain further insights into the connection between the site occupancies, large magnetic moment in the austenite phase, and subsequently the MCE in this particular compound, we look at the variations in the magnetic exchange interactions as a function of y. The detailed comparison of the nearest neighbor inter-atomic magnetic exchange for "S-b" and "S-c" configurations is in Fig. 4.12. We find that substantially large ferromagnetic interactions in "S-c" configuration, the greatest being in the Ni2-Fe pair, makes the difference. The presence of large ferromagnetic interactions in the austenite phase produces a large moment, lends more stability to the austenite phase (T_M reduces), and can be correlated with the large MCE observed experimentally.

4.4 Conclusions

In this chapter, we have explored the potentials of Mn-excess, Sb-deficient Ni_2MnSb compounds, as magnetocaloric materials upon substitution of Ni and Mn by $3d$ transition metals Fe, Co, and Cu. Apart from being able to explain the trends of

variations in quantities like the martensitic transformation temperature, magnetic transition temperature and the magnetic moments with compositions, observed in handful of experiments on this system, we have provided insights into the possibilities of significant magnetocaloric effects in compounds which are yet to be synthesized. We found that the site occupancies of various atoms play an important role in the variations of the above mentioned physical quantities. The structural stabilities in these systems could be correlated to the magnetic exchange interactions and their variations. We predict that the compounds $Ni_2Mn_{1.5-y}Co_ySb_{0.5}$ and $Ni_2Mn_{1.5-y}Cu_ySb_{0.5}$; $y \sim 0.25$, can emerge as materials with large magnetocaloric effects. In conclusion, this work systematically explores the physics behind occurrence of magnetocaloric effect in substituted Ni-Mn-Sb compounds. The approach adopted and knowledge obtained from this work can be used to investigate a wider pool of materials, boosting the possibility of discovering more materials with large MCE.

Chapter 5

Cosubstitution in Ni-Mn-Sb Heusler compounds: realization of room temperature reversible magnetocaloric effect driven by second-order magnetic transition

5.1 Introduction

In the previous chapters, it has been seen that the compounds in magnetic Heusler family displaying significant magnetocaloric effect driven by first-order magneto-structural transitions are in vogue. Comparatively, the Heusler compounds, undergoing second-order magnetic transition near room temperature are less explored in the context of discovering significant magnetocaloric effect. The second-order transition can offer certain advantages like less energy cost and hysteresis loss.

In general, MCE obtained due to first-order transition [89, 123, 132, 306, 307], is higher compared to those obtained in the vicinity of a second-order magnetic transition. However, the materials exhibiting large MCE near a first-order magneto-structural transformation suffer from several disadvantages. The martensitic phase transition costs high energy, which translates into significant hysteresis loss and low efficiency for cooling applications. They also suffer from cracking and fatigue, which severely limit their lifetimes. It is, therefore, of utmost importance, to explore magnetocaloric materials in Heusler family exhibiting only second-order magnetic phase

The contents of this chapter are published in Physical Review Materials **4**, 025401 (2020)

transitions. They show full reversible effects and have limited mechanical drawbacks. The superior mechanical properties such as ductility, corrosion resistance, machinability of these materials ease manufacturing and bolster product longevity.

Accordingly, some of the recent studies focused on the exploration of large MCE in magnetic Heusler compounds in the vicinity of a second-order magnetic phase transition. Singh *et al.* [308] experimentally investigated the composition $Ni_2Mn_{1.4}In_{0.6}$ and found a significant negative entropy change (ΔS_{mag}) of 3.3 $J\,kg^{-1}\,K^{-1}$ and 6.3 $J\,kg^{-1}\,K^{-1}$ in an applied field of 2 T and 5 T, respectively, associated with a second-order transition near room temperature (315 K); the ΔS_{mag} being comparable to the benchmark material Gd [33] as magnetic refrigerant. A reversible magnetic entropy change of 1.02 $J\,kg^{-1}\,K^{-1}$ with moderate refrigeration capacity was obtained across the second-order magnetic transition near room temperature (305 K) in $Mn_{1.58}Fe_{0.34}Ni_{1.64}Sn_{0.44}$ [309] upon a variation of magnetic field by 1.4 T only. A tuneable and fully reversible MCE across the ferro-paramagnetic transition was also realized in $Ni_{1.92}Mn_{1.44}In_{0.64-x}Sn_x$ compounds [310]. The following three major factors behind the large MCE near a second-order phase transition were noted in these experiments: (i) the austenite phase of the system should be stable in the range of operational temperature, (ii) the magnetization should be high and (iii) second-order magnetic transition temperature i.e. the Curie temperature (T_c) must be close to the room temperature for practical refrigeration applications.

Gd, the prototype material for MCE, has a large magnetic moment ($\approx$ 7.5 $\mu_B/f.u.$) [33] produced by $4f$ electrons. Therefore, for $3d$ transition metal based Ni-Mn-Z Heuslers, the target is to achieve a magnetic moment as close to it. Since the largest contribution to the magnetic moment in Ni-Mn-Z compounds comes from the Mn atoms, it is expected that Mn-excess compounds would help increase magnetic moments. The overwhelming majority of Ni-Mn-Z compounds, exhibiting MCE, undergo a first-order magneto-structural transformation. This is typically achieved in Z-deficient, Mn-excess systems. However, contrary to the intuition, the magnetic moments of such systems are less than the ones of the stoichiometric compounds Ni_2MnZ because of the anti-parallel alignments of Mn spins. One possible way to overcome the dominant anti-ferromagnetic interaction originating from Mn-Mn interactions in these systems is to substitute Mn or Ni by another transition metal. The substituent, however, should be able to infuse significant ferromagnetic interactions in the system amplifying the net magnetic moment. This has been done in several systems showing first-order magneto-structural transitions, with promising outcomes [93, 273–280, 284]. Investigations showed that there is a delicate balance

of relative compositions of the elements that has to be achieved in order to obtain not only a large magnetic moment but also a desirable martensitic transformation temperature and Curie temperature, simultaneously.

In the previous chapter, we found the proof of this delicate balance upon substitutions of Ni and Mn by Fe, Co, and Cu. The motivation there was to understand the roles of the substituent, the composition and the substituted elements on magnetic and thermodynamic properties relevant to MCE, and interpret the origin of large MCE in $Ni_2Mn_{1.48+x}Sb_{0.52-x}$ [132], $Ni_{2-x}Co_xMn_{1.56}Sb_{0.44}$ [134], $Ni_{2-x}Co_xMn_{1.52}Sb_{0.48}$ [135, 142], and $Ni_2Mn_{1.52-x}Fe_xSb_{0.48}$ [140]. We found that (i) substitution of Mn with Cu brings the magnetization up, and the T_c down, close to the room temperature, (ii) substitution of Ni with Fe(Co) bolsters the magnetization, reduces(increases only slightly) T_c and provides more stability to the austenite phase. This indicates that in order to explore off-stoichiometric Ni-Mn-Sb to our advantage, in the context of large room temperature MCE near a second-order phase transition, substitutions of at least two elements simultaneously(cosubstitution) can be useful. This strategy has been adopted earlier successfully [143–145], for materials undergoing first-order magneto-structural transitions.

In what follows, in present chapter, we have explored possible members in the co-substituted $Ni_2Mn_{1+z}Sb_{1-z}$ family which are promising in exhibiting magnetocaloric effect near room temperature by adopting a strategy of substituting specific elements at select sites. The search for compounds with target properties was narrowed down further by imposing certain criteria based upon available information. We have found a good number of materials with significant changes in entropy due to the second-order magnetic phase transition, that can be useful for cooling applications. The greater significance of this investigation is that it opens up possibilities to discover more such materials in the Heusler family by adopting the same strategy.

5.2 Computational Details

In the present work, electronic structure calculations are done with spin-polarized density functional theory (DFT) based projector augmented wave (PAW) method as implemented in Vienna *Ab initio* Simulation Package (VASP)[177–179]. The valence electronic configurations used for the Mn, Fe, Co, Ni, Cu and Sb PAW pseudopotentials are $3d^64s$, $3d^74s$, $3d^84s$, $3d^84s^2$, $3d^{10}4s$ and $5s^25p^3$, respectively. For all calculations, we use the Perdew-Burke-Ernzerhof implementation of generalized gradient approximation for exchange-correlation functional [190]. An energy cut off

of 550 eV, and a Monkhorst-Pack $11 \times 11 \times 11$ k-mesh was used for self-consistent calculations. A larger k-mesh of $15 \times 15 \times 15$ is used for the density of states calculations of all the structures. The convergence criteria for the total energies and the forces on individual atoms are set to 10^{-6} eV and 10^{-2} eV/Å respectively. The stabilities of the compounds against decomposition into its components are checked by computing the formation energies, defined by:

$$E_f = E_{tot} - \sum_i n_i E_i \tag{5.1}$$

E_{tot} is the total energy of the systems, i represents the atoms in the unit cell, and n_i is the concentration of the i-th atom. E_i is the total energy of the element i in its bulk ground state. We have considered bcc-Mn, bcc-Fe, hcp-Co, fcc-Ni, fcc-Cu, and trigonal-Sb as ground-state structures in their elemental phases.

To compute the Curie temperature T_c of a compound, we first calculate the magnetic pair exchange parameters using multiple scattering Green function formalism as implemented in SPRKKR code [230]. In order to calculate the energy differences by the SPRKKR code, full potential spin-polarized scalar relativistic Hamiltonian with angular momentum cut-off $l_{max} = 3$ is used along with a converged k-mesh for Brillouin zone integrations. The Green's functions are calculated for 32 complex energy points distributed on a semi-circular contour in the complex plane. The energy convergence criterion is set to 10^{-5} eV for the self-consistent cycles. These exchange parameters are then used for the calculation of T_c. The Curie temperatures are estimated with two different approaches: the mean-field approximation (MFA) [223, 286] and the Monte Carlo simulation (MCS) method [182, 229, 236]. The Monte Carlo simulations have been carried out using Metropolis algorithm [182, 236]. Magnetic exchange interactions $J_{ij}^{\mu\nu}$ for upto 20 neighbours surrounding each atom have been considered in the Heisenberg Hamiltonian, as described in chapter 2. At each temperature, 80000 Monte Carlo steps have been performed to equilibriate the systems containing 8192 atoms. The Curie temperatures are obtained from the resulting M-T relationship, where M is the total magnetic moment of the system and T the temperature.

For estimation of the changes in magnetic entropy (ΔS_{mag}) due to the application of a magnetic field, we use the Potts model [175, 176] instead of Heisenberg

model, as discussed in Chapter 2. The Monte Carlo simulation using the classical Heisenberg Hamiltonian treats the spins as classical variables which may take on continuous values and hence does not reproduce the saturation value of the magnetic entropy [111]. Thus, in order to calculate the saturation value of the magnetic entropy, we have used the q-state Potts model, in which the spin variables can take discrete values.

5.3 Results and Discussions

Taking a cue from findings in the previous chapter and available experimental results [132, 134, 135, 140, 142], as discussed in the section 5.1, we choose two cosubstituted Mn-excess, Sb-deficient Ni-Mn-Sb families: (i) $Ni_{2-x}Fe_xMn_{1+z-y}Cu_ySb_{1-z}$ (denoted as Fe@Ni-Cu@Mn) and (ii) $Ni_{2-x}Co_xMn_{1+z-y}Cu_ySb_{1-z}$ (denoted as Co@Ni-Cu@Mn). It is to be noted that the concentration of Sb is also a variable, as the content of Sb is a critical parameter in the stabilization of the austenite phase, as understood in chapter 3. The austenite ($L2_1$ Heusler) phase of the systems (space group 225) is modeled by a 16 atom conventional cubic cell with the number of positions for Ni, Mn, and Sb being 8, 4 and 4 respectively. The cosubstituted systems are generated by replacing the atoms by the substituents in a systematic way. As a consequence of the size of the cell, compositions with arbitrary x, y or z cannot be modeled. In our work, x and z vary independently, the ranges being 0 to 1.5 and 0.25 to 0.75, respectively. The variable y is constrained to be less than or equal to the value of z. Each variable can be changed by an amount of 0.25 only, due to the finite size of the cell.

We first optimize the site occupancy and magnetic structures for each of the systems considered, by minimizing the total energy for each composition. We find that the optimized configurations exactly mimic the ones found in the previous two chapters, chapter 3 and Chapter 4, on Mn-excess, Sb-deficient Ni_2MnSb and single substituted (by Fe, Co or Cu) $Ni_2Mn_{1.5}Sb_{0.5}$ systems.

After obtaining the ground state atomic order (site occupancy pattern) and magnetic configurations, we calculate the magnetic moments and Curie temperatures T_c in their austenite phases. The T_c is calculated by the MFA method. The calculations are done by first fixing z that is the excess concentration of Mn with respect to the stoichiometric composition Ni_2MnSb, and then varying x and y independently. The results are shown in Fig. 5.1.

5.3.1 Selection of compounds with potential to exhibit large MCE

In order to get significant MCE near room temperature, arising out of a second-order magnetic transition, large magnetic moment in the austenite phase and a T_c close to room temperature are the requirements. The other requirement is that the austenite phase is stable down to low temperatures, or in other words, no MPT occurs, from the point of view of DFT results at T=0 K. Accordingly, we adopt the following strategy to choose the compounds for final investigations:

(i) From the results on magnetic moments and T_c^{MFA}, as shown in Fig.5.1, we select only those compositions (the ranges of x, y, z) whose magnetic moment $M_{\rm A}$ in the austenite phase satisfies the criterion $M_{\rm A} \geq 4.5\ \mu_{\rm B}/f.u.$, and the magnetic transition temperature (T_c^{MFA}) in the austenite phase satisfies 200 K $\leq T_c^{MFA} \leq$ 450 K condition. The condition on $M_{\rm A}$ is in accordance with the existing results on Heusler compounds showing reasonable MCE. A vast range of T_c^{MFA}, around the room temperature value of 300 K, is considered since MFA is known to overestimate or underestimate the transition temperature quite often.

(ii) Once the compounds satisfying conditions in (i) are selected, their formation energies are calculated to check the stabilities against decomposition into its components. The compounds having negative formation energies are selected for further inspection. Their total energy profiles as a function of tetragonal distortions are examined to check whether a tetragonal phase is energetically favorable. The ones with their austenite phases having the lowest total energies are finally selected for computations of the quantities related to MCE.

Summarizing the results in Fig. 5.1, in Table 5.1 we list the ranges of x, y, z over which the compounds satisfy the conditions given in (i). We find that, in comparison to Co-Cu cosubstituted compounds (Co@Ni-Cu@Mn), there are more number of Fe-Cu cosubstituted compounds (Fe@Ni-Cu@Mn) that satisfy the condition (i). For the former family, the comparatively less number is mostly due to very high values of T_c^{MFA}. In both families, most of the compounds which fail to satisfy the condition on $M_{\rm A}$ have the Mn spins anti-aligned, reducing the magnetic moments. The results on formation energies of the compounds selected based upon the condition (i) are shown in Table 5.2. For calculations of formation energies, we have considered bcc-Mn, bcc-Fe, hcp-Co, fcc-Ni, fcc-Cu, and trigonal-Sb as ground-state structures in their elemental phases. The formation energies show the following trend: (a) excess in Mn and deficiency in Sb decreases the stability of the system, (b) for a fixed Sb

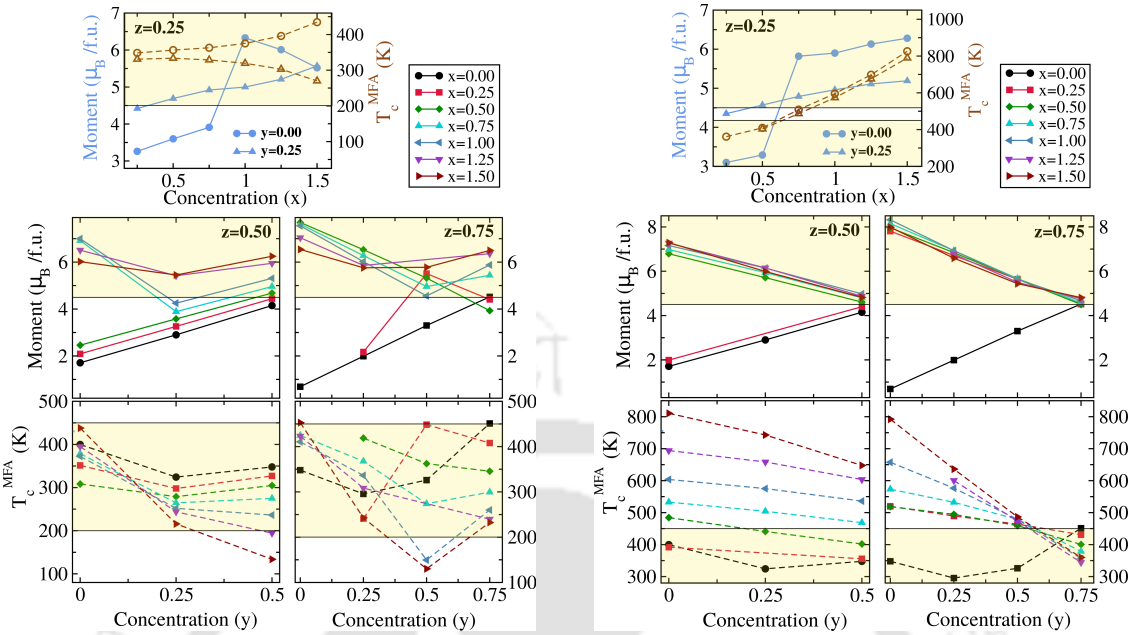

Figure 5.1: Variations in the calculated magnetic moments (M_A) and Mean field approximated Curie temperatures (T_c^{MFA}) with concentrations (x, y and z) in the austenite phases of (left) $Ni_{2-x}Fe_xMn_{1+z-y}Cu_ySb_{1-z}$(Fe@Ni-Cu@Mn) and (right) $Ni_{2-x}Co_xMn_{1+z-y}Cu_ySb_{1-z}$(Co@Ni-Cu@Mn) systems. Shaded regions mark the composition ranges that satisfy $M_A \geq 4.5\ \mu_B/f.u.$ and 200 K $\leq T_c^{MFA} \leq$ 450 K.

concentration, Cu substitution at the expense of Mn decreases the stability and for fixed concentration of substituted Mn and Cu, Fe/Co substitution at the expense of Ni further decreases the stability of the system, (c) Co substitution at the expense Ni is more favourable than Fe substituting Ni. These observations are in agreement with previous theoretical studies on Ni-Mn based Heusler compounds [229, 288]. In summary, all compounds in the family of Co@Ni-Cu@Mn can form from the point of enthalpy, while the amount of Fe is critical in formation of compounds in the family of Fe@Ni-Cu@Mn.

Table 5.1: The compositions of $Ni_{2-x}Fe_xMn_{1+z-y}Cu_ySb_{1-z}$ and $Ni_{2-x}Co_xMn_{1+z-y}Cu_ySb_{1-z}$ which satisfy the criterion of $M_A \geq 4.5\ \mu_B/f.u.$ and 200 K $\leq T_c^{MFA} \leq$ 450 K, as seen from results in Fig. 5.1, are summarized.

$Ni_{2-x}Fe_xMn_{1+z-y}Cu_ySb_{1-z}$			$Ni_{2-x}Co_xMn_{1+z-y}Cu_ySb_{1-z}$	
z=0.25	z=0.50	z=0.75	z=0.50	z=0.75
x=1.00, y=0.00	x=0.50, y=0.46-0.50	x=0.25, y=0.43-0.75	x=0.50, y=0.20-0.50	x=0.25, y=0.56-0.75
x=1.25, y=0.00	x=0.75, y=0.00-0.20 & 0.40-0.50	x=0.50, y=0.25-0.65		x=0.50, y=0.56-0.75
x=1.50, y=0.00	x=1.00, y=0.00-0.23 & 0.30-0.50	x=0.75, y=0.00-0.75		x=0.75, y=0.56-0.75
x=0.50, y=0.25	x=1.25, y=0.00-0.50	x=1.00, y=0.00-0.43 & 0.62-0.75		x=1.00, y=0.56-0.75
x=0.75, y=0.25	x=1.50, y=0.00-0.30	x=1.25, y=0.00-0.75		x=1.25, y=0.56-0.75
x=1.00, y=0.25		x=1.50, y=0.00-0.34 & 0.67-0.75		x=1.50, y=0.56-0.75
x=1.25, y=0.25				
x=1.50, y=0.25				

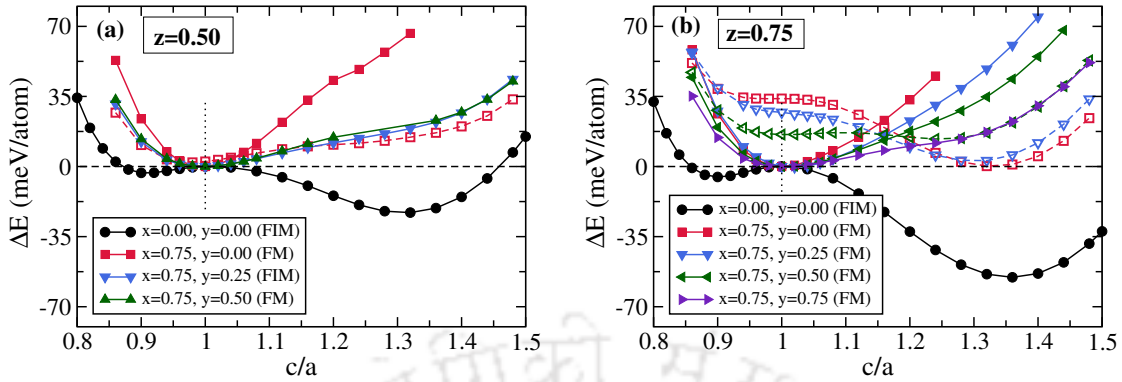

Figure 5.2: The variations of total energy difference (ΔE) between the austenite($L2_1$) and the martensite(tetragonal) phases as a function of tetragonal distortion i.e. c/a ratio for select compositions of (a) $Ni_{2-x}Fe_xMn_{1+z-y}Cu_ySb_{1-z}$ and (b) $Ni_{2-x}Co_xMn_{1+z-y}Cu_ySb_{1-z}$ systems. Energy profiles with solid lines and filled symbols correspond to calculations done in the ground state magnetic structure of the compound. The plots with dashed lines and open symbols represent calculations done in a different magnetic configuration.

Next, we check whether the compounds with negative formation energy undergo structural phase transformation under a tetragonal deformation. To this end, we distort the austenite $L2_1$ structure along the z-axis by keeping the volume at the equilibrium value of the austenite phase and compute the total energy of the system as a function of the tetragonal distortion given by (c/a). The calculations are done in the ground state magnetic configurations of the compounds. Additionally, calculations are done with ferrimagnetic (FIM) configuration (one where Mn spins at different sites anti-align) for the compositions where the ground state magnetic configuration is one where Mn spins at different sites align (denoted as FM). This is done to check the possibility of MPT in the system due to different magnetic structures in two structural phases. For example (see Fig. 5.2(a)), in $Ni_{2-x}Fe_xMn_{1+z-y}Cu_ySb_{1-z}$ family, MPT is observed in systems with Mn content, $z = 0.5$ and with no Fe or Cu; the ground state magnetic configuration being one with anti-parallel Mn spins. However, when Fe is substituted and having a concentration of $x = 0.75$, the ground state structure (FM) does not undergo MPT. Even a change in the magnetic structure does not show any possibility of MPT. Thus overall, the austenite phase is stable throughout the whole temperature range. Further, for Cu addition also, no possibility of MPT is observed for compounds with $y = 0.25$ and 0.50. Same analysis is done for $Ni_{2-x}Co_xMn_{1+z-y}Cu_ySb_{1-z}$ compounds (shown in Fig. 5.2(b) to decide the stability of the austenite phase. In Table 5.2, we list the structurally stable phase of each compound: there 'N' means a tetragonal phase has the lowest

energy implying an MPT will take place, and thus the austenite phase is not stable, while 'Y' denotes a stable austenite phase. Finally, we select only those compounds (the compositions of these compounds are the ones boldfaced in Table 5.2) which have negative formation energy and stable austenite phase (the condition (ii) above) for computations of their T_c (by more accurate MCS method) and the isothermal entropy change (ΔS_{mag}).

Table 5.2: Lattice parameter (a_0), magnetic moment (M_A), Mean field approximated Curie temperature (T_c^{MFA}), formation energies (E_f) for select compositions (Table 5.1) among $Ni_{2-x}Fe_xMn_{1+z-y}Cu_ySb_{1-z}$(Fe@Ni-Cu@Mn) and $Ni_{2-x}Co_xMn_{1+z-y}Cu_ySb_{1-z}$(Co@Ni-Cu@Mn) compounds in their austenite phases. The result on the stability of the austenite phase is also tabulated: 'Y' stands for the stability of the austenite phase down to low temperatures. Boldfaces indicate the compositions which satisfy the criteria of negative formation energy and stable austenite phase along with conditions on M_A and T_c^{MFA}. The Monte Carlo simulated Curie temperature (T_c^{MCS}) and maximum change in isothermal magnetic entropy (ΔS_{mag}) values around their corresponding T_c^{MCS} in an external field of 2 T are shown for these compositions only.

Compound & composition	a_0 (Å)	M_A ($\mu_B/f.u.$)	T_c^{MFA} (K)	E_f (eV/f.u.)	Stability of austenite	T_c^{MCS} (K)	- ΔS_{mag} ($J\,kg^{-1}\,K^{-1}$)
$Ni_{2-x}Fe_xMn_{1+z-y}Cu_ySb_{1-z}$							
z=0.25							
x=1.00, y=0.00	5.98	6.35	375.0	-0.181	Y	414	4.55
x=1.25, y=0.00	5.95	6.00	395.9	-0.116	Y	430	7.08
x=1.50, y=0.00	5.92	5.50	434.5	-0.029	Y	450	6.52
x=0.50, y=0.25	5.97	4.69	333.5	-0.348	Y	350	4.03
x=0.75, y=0.25	5.96	4.92	328.8	-0.222	Y	348	3.97
x=1.00, y=0.25	5.95	5.00	319.3	-0.082	Y	341	5.39
x=1.25, y=0.25	5.94	5.21	302.8	0.051			
x=1.50, y=0.25	5.94	5.57	270.0	0.173			
z=0.50							
x=0.50, y=0.50	5.89	4.65	304.9	-0.174	Y	286	4.49
x=0.75, y=0.00	5.92	6.89	378.6	-0.219	Y	400	4.19
x=0.75, y=0.50	5.89	4.94	275.0	-0.022	Y	260	3.29
x=1.00, y=0.00	5.91	7.00	372.5	-0.115	Y	419	3.88
x=1.00, y=0.50	5.88	5.31	236.4	0.143			
x=1.25, y=0.00	5.88	6.50	395.1	-0.031	Y	449	4.32
x=1.25, y=0.25	5.86	5.40	243.8	0.124			
x=1.25, y=0.50	5.90	5.93	194.5	0.261			
x=1.50, y=0.00	5.85	6.01	438.0	0.050			

Continuation of Table 5.2

Compound & composition	a_0 (Å)	M_A ($\mu_B/f.u.$)	T_c^{MFA} (K)	E_f (eV/f.u.)	Stability of austenite	T_c^{MCS} (K)	- ΔS_{mag} ($J\,kg^{-1}\,K^{-1}$)
x=1.50, y=0.25	5.84	5.40	215.8	0.214			
x=1.75, y=0.00	5.82	5.53	460.6	0.120			
x=1.75, y=0.25	5.84	5.65	163.0	0.306			
x=2.00, y=0.00	5.80	5.10	457.4	0.198			
x=2.00, y=0.25	5.84	5.87	155.5	0.397			
z=0.75							
x=0.25, y=0.50	5.83	5.53	448.4	-0.240	N		
x=0.25, y=0.75	5.81	4.43	407.9	-0.167	N		
x=0.50, y=0.25	5.84	6.54	418.8	-0.174	N		
x=0.50, y=0.50	5.81	5.33	362.4	-0.078	N		
x=0.75, y=0.25	5.82	6.27	367.7	-0.045	N		
x=0.75, y=0.50	5.79	4.95	273.8	0.079			
x=0.75, y=0.75	5.82	5.38	299.5	0.179			
x=1.00, y=0.00	5.83	7.51	410.5	-0.052	N		
x=1.00, y=0.25	5.79	6.02	336.3	0.076			
x=1.00, y=0.75	5.82	5.84	260.0	0.336			
x=1.25, y=0.00	5.80	7.02	423.1	0.033			
x=1.25, y=0.25	5.78	5.90	308.3	0.185			
x=1.25, y=0.75	5.84	6.30	239.8	0.460			
x=1.50, y=0.00	5.77	6.53	452.8	0.100			
x=1.50, y=0.25	5.76	5.73	242.6	0.255			
x=1.50, y=0.75	5.83	6.44	232.4	0.603			
$Ni_{2-x}Co_xMn_{1+z-y}Cu_ySb_{1-z}$							
z=0.50							
x=0.50, y=0.25	5.92	5.73	441.1	-0.752	N		
x=0.50, y=0.50	5.89	4.64	401.9	-0.696	Y	484	1.51
z=0.75							
x=0.25, y=0.50	5.84	5.62	464.1	-0.525	N		
x=0.25, y=0.75	5.81	4.53	430.9	-0.468	Y	420	1.90
x=0.50, y=0.50	5.83	5.66	459.5	-0.658	Y	503	2.40
x=0.50, y=0.75	5.80	4.53	400.5	-0.571	Y	442	1.71
x=0.75, y=0.50	5.82	5.71	479.0	-0.781	Y	552	2.79

Continuation of Table 5.2

Compound & composition	a_0 (Å)	M_A ($\mu_B/f.u.$)	T_c^{MFA} (K)	E_f (eV/f.u.)	Stability of austenite	T_c^{MCS} (K)	- ΔS_{mag} ($J\,kg^{-1}\,K^{-1}$)
x=**0.75**, y=**0.75**	5.79	4.52	378.9	-0.659	Y	440	2.00
x=**1.00**, y=**0.50**	5.80	5.62	479.0	-0.893	Y	560	3.62
x=**1.00**, y=**0.75**	5.78	4.68	356.7	-0.745	Y	389	1.33
x=**1.25**, y=**0.50**	5.78	5.44	473.4	-1.00	Y	535	4.26
x=**1.25**, y=**0.75**	5.78	4.75	344.2	-0.833	Y	330	2.49
x=**1.50**, y=**0.50**	5.77	5.34	486.6	-1.115	Y	494	4.74
x=**1.50**, y=**0.75**	5.77	4.81	360.0	-0.921	Y	370	3.19

5.3.2 Quantification of parameters important for MCE: calculations of Curie temperature by MCS method (T_c^{MCS}) and changes in magnetic entropy (ΔS_{mag})

Quantification of relevant physical quantities is important in order to assess the potentials of the compounds selected for magnetocaloric applications driven by a second-order magnetic transition. Having ascertained a stable cubic phase, a negative enthalpy of formation, and a substantial magnetic moment, we now compute the two most important quantities: the Curie temperature T_c and the maximum change in isothermal magnetic entropy (ΔS_{mag}). Although the T_c was already calculated once to select potential compounds, in here, we employ the more accurate MCS method for the purpose of quantification as accurate as possible. The results obtained by MCS on a Heisenberg model, denoted as T_c^{MCS}, are shown in Table 5.2. We find that, in general, T_c^{MCS} are higher than T_c^{MFA}. However, in about 50% cases, the disagreement is within 10-20 K. It is to be noted that, in general, it is the T_c^{MFA} that overestimates the experimental Curie temperature while T_C^{MCS} is closer to it. However, in case of Heusler compounds, there are cases [176, 311] where T_c^{MFA} are underestimated with respect to either the experimental results or T_c^{MCS}. In absence of experimental results in the present case, it is thus difficult to predict which approximation performs better.

Experimental results on the compounds considered in this work are yet to be available. Thus, in order for the quantitative estimations of ΔS_{mag} to be reliable and convincing, we first benchmark our calculations (see Appendix, Section A.2) against a similar system $Ni_2Mn_{1.4}In_{0.6}$, where experimentally a significant MCE was observed at second-order magnetic transition near room temperature [308]. We em-

ploy the procedure to compute ΔS_{mag} as a function of temperature in a magnetic field change of 2 T for all the select compounds (boldfaced in Table 5.2). The obtained maximum ΔS_{mag} values around their corresponding T_c^{MCS} values for all the compositions (Table 5.2) are found to be comparable to those of the prototype material Gd [33] as well as various Heusler compounds undergoing first-order magneto-structural transitions. For example, ΔS_{mag} of 7.08 J kg^{-1} K^{-1} obtained for $Ni_{0.75}Fe_{1.25}Mn_{1.25}Sb_{0.75}$ is comparable to 7.3 J kg^{-1} K^{-1} and 7.9 J kg^{-1} K^{-1} observed experimentally for $Ni_{1.72}Co_{0.28}Mn_{1.56}Sb_{0.44}$ and $Ni_{1.68}Co_{0.32}Mn_{1.56}Sb_{0.44}$, respectively, in a field of 1 T [134]. From our calculations, we find that though Co-Cu cosubstituted series has more compounds showing non-negligible MCE near room temperature, the entropy changes in Fe-Cu cosubstituted compounds are much higher. We also find that regardless of the series, both T_c and ΔS_{mag} decrease upon addition of Cu, when concentrations of other constituents are kept fixed.

Having observed significant MCE near second-order magnetic phase transition for a number of compounds obtained by cosubstitution in Ni-Mn-Sb, we now try to understand (i) the structural phase stability (ii) the nature of variations in the magnetic moments with changes in composition and (iii) variations in the T_c, as obtained from our calculations. These three were the important aspects of selecting compounds, potential for magnetocaloric applications; hence, a microscopic understanding is desirable.

5.3.3 Analysis of structural phase stability from electronic structures

In this subsection, we analyze the densities of states to understand the stabilization of the austenite phases in the compounds with changes in the compositions of the cosubstituents. For this, we show the total and atomic densities of states of compounds with z, x fixed at 0.5 and 0.75 respectively, and y varying from 0 to 0.5 in Fe@Ni-Cu@Mn family. The same is shown for compounds with z, x both fixed at 0.75 with y varying from 0 to 0.75 in Co@Ni-Cu@Mn family. Here we only analyze the minority densities of states because, in Ni-Mn-Sb compounds, the structural phase stability can be explained by features in the densities of states of the minority bands near Fermi level.

In Ni-Mn-Sb systems, a competition between the strength of the Jahn-Teller instability and the strength of the covalent bonding due to Ni-d and Sb-p minority states drives the phase stability, as understood in Chapter 3. In stoichiometric

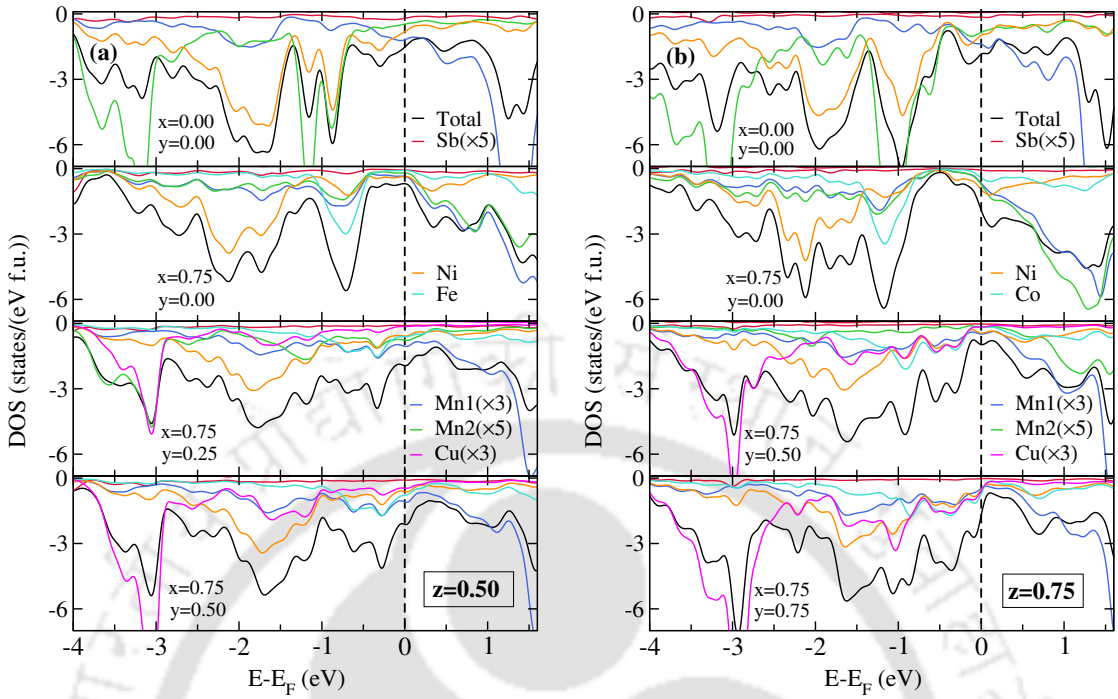

Figure 5.3: The minority band total and partial densities of states (DOS) for (a) $Ni_{2-x}Fe_xMn_{1+z-y}Cu_ySb_{1-z}$ and (b) $Ni_{2-x}Co_xMn_{1+z-y}Cu_ySb_{1-z}$ systems in their austenite phases. The zero energy is set at Fermi energy (E_F). Mn1 and Mn2 denote Mn atoms at its own site and at other sites in $L2_1$ structure, respectively.

Ni_2MnSb, the stability of the austenite phase is driven by the pseudo-gap at around 1 eV below the Fermi level, generated by Ni-Sb covalent bonding. When Mn is substituted at the expense of Sb ($z \neq 0$, $x = 0$, $y = 0$), the pseudo-gap is filled by states of Mn atoms at Sb site (i.e., Mn2 atoms), whose spins are anti-parallel to those of Mn1 atoms (the ones at original site of Mn). This results in weakening of the covalent bonding. Consequently, Jahn-Teller instability, manifested by the presence of substantial states at the Fermi level, increases, resulting in a martensitic phase transformation. It is to be noted that in Ni-Mn based compounds undergoing Jahn-Teller instability, Ni plays the key role in driving the instability and hence, a structural transformation. Thus, the concentration of Ni is a key factor in relative stabilities of structural phases in these compounds. Therefore, when Fe concentration, substituting Ni, exceeds a critical limit (here $x = 0.75$), the hybridization near Fermi level, driven by Ni, weakens, diminishing the Jahn-Teller instability. This is the reason behind the stabilization of austenite phase in Fe@Ni-Cu@Mn compounds shown in Fig. 5.3(a). The addition of Cu instead of Mn further weakens Ni-Mn hybridization stabilizing the austenite phases ($y = 0.25, 0.5$) more. The very similar features in the densities of states near Fermi level for Co@Ni-Cu@Mn compounds

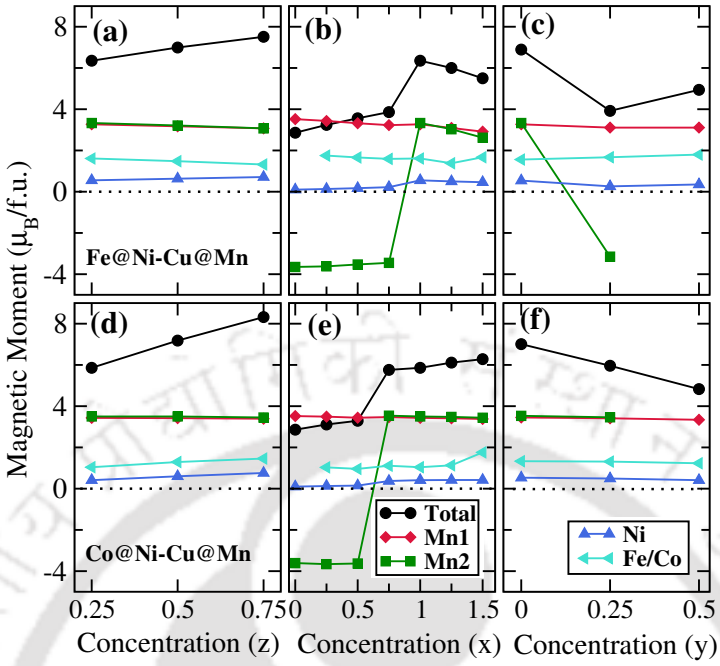

Figure 5.4: Variations in the calculated total and atomic magnetic moments (in $\mu_B/f.u.$) with z (x=1, y=0), x (y=0, z=0.25) and y (x=0.75, z=0.5) for ((a)-(c)) $Ni_{2-x}Fe_xMn_{1+z-y}Cu_ySb_{1-z}$ and ((d)-(f)) $Ni_{2-x}Co_xMn_{1+z-y}Cu_ySb_{1-z}$ systems in their austenite phases. Mn1 and Mn2 denote Mn atoms at its own site and at other sites in $L2_1$ structure, respectively.

(Fig. 5.3(b)) offer the same explanation behind the origin of the stability of austenite phases for the compounds with given compositions.

5.3.4 Understanding magnetic properties from effective exchange interactions

In this sub-section, we understand the fundamentals of the variations in magnetic moments and Curie temperatures by inspecting the magnetic exchange interactions. We find interesting trends in magnetic moments in some of the cases if we analyze the effects of substitutions with different elements systematically. For example, in $Ni_{2-x}Fe_xMn_{1+z-y}Cu_ySb_{1-z}$(Fe@Ni-Cu@Mn) family, a large magnetic moment is observed for high concentrations of Fe in systems with $y = 0$, $z = 0.25$. In Fig. 5.1, it can be seen that there is a slight increase in magnetic moment initially upon Fe substitution for compositions with $z = 0.25$, $y = 0$. In between the compositions with $x = 0.75$ and $x = 1$, a sudden jump in magnetic moment occurs; it decreases again linearly if more Fe is added to the system. However, the Curie temperature increases throughout the whole concentration range of Fe in this case. If z (Mn

concentration) is further increased, same behaviour of magnetization and T_c^{MFA} are obtained with less amount of Fe in the system. With a fixed Fe content, if Cu is added in this composition range, both magnetic moment and Curie temperature decrease in the system. In order to analyze the trends, we adopt the following procedure: we inspect the variations in the total and atomic moments by (a) first considering systems with no Cu ($y = 0$), fixed amount of Fe/Co ($x = 1$) and excess Mn ($z \geq 0.25$), (b) then considering systems with no Cu ($y = 0$), fixed concentration of excess Mn ($z = 0.25$) and amount of Fe/Co variable, and (c) finally considering systems where Fe/Co concentration and amount of excess Mn are fixed ($x = 0.75, z = 0.5$), the amount of Cu, y, being the only variable. The results are shown in Fig. 5.4. The variations in Curie temperatures are investigated by the same procedure and shown in Fig. 5.5. The effective inter-atomic exchange interactions $J_{\text{eff}}^{\mu\nu} = \sum_j J_{0j}^{\mu\nu}$; 0 fixed on sub-lattice μ and j sites belong to sub-lattice ν ($J_{ij}^{\mu\nu}$, the magnetic exchange parameters for the atoms i, j belonging to μ, ν sublattices), shown in Fig. 5.6, are used to analyse the results.

Figure 5.4(a) and 5.4(d) show that for a fixed and high content of substituted Fe/Co, the substitution of excess-Mn at the expense of Sb, leads to increase of the total magnetic moment with Mn content. This is somewhat counter-intuitive due to the following: stoichiometric Ni_2MnSb has a magnetic moment of nearly 4 $\mu_B/f.u.$ contributed primarily by Mn. Existing results show that the moment decreases gradually with excess-Mn content as the Mn spins at different sites align anti-parallel. An increasing trend of the moment is only seen when Fe substitutes Mn [140], or Co substitutes Ni [134, 135, 142]; the increases, however, were not as large as observed here. A look at the atomic moments reveals that Fe/Co being stronger magnets than Ni, along with the parallel alignment of Mn spins at different sites, are behind high magnetic moments of the system. In this case, the Curie temperature (T_c^{MFA}) also increases with z for both the systems, as can be seen in Fig. 5.5 (referred as Case-1). Insights into such qualitative behavior can be obtained from the variations of effective magnetic exchange interactions, shown in Fig. 5.6(a) and 5.6(d). We find that for both Fe and Co substituted systems, the dominant antiferromagnetic and ferromagnetic J_{eff} are due to the Mn1-Mn2 and Mn1(Mn2)-Ni pairs, respectively. The ferromagnetic component is strenghthened by the interactions between substituted Fe/Co and Mn. In case of Fe substituted system, the antiferromagnetic $J_{\text{eff}}^{\text{Mn1-Mn2}}$ increases slightly, although the dominant ferromagnetic J_{eff}s like $J_{\text{eff}}^{\text{Mn1(Mn2)-Ni}}$, $J_{\text{eff}}^{\text{Mn1-Fe}}$ increase significantly. The overall increase in ferromagnetic effective exchange interactions results into a growing trend

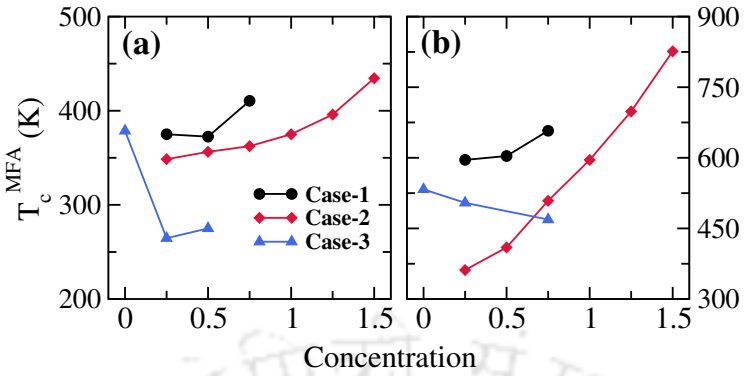

Figure 5.5: Variations of the Mean field approximated Curie Temperatures (T_c^{MFA}) with concentration x, y and z for (a) $Ni_{2-x}Fe_xMn_{1+z-y}Cu_ySb_{1-z}$ and (b) $Ni_{2-x}Co_xMn_{1+z-y}Cu_ySb_{1-z}$ systems in their austenite phases. Case-1 stands for variations with z (x=1, y=0). Case-2 shows variations with x (y=0, z=0.25). Case-3 is for variations with y (x=0.75, z=0.5).

in Curie temperature with z, the concentration of excess Mn (Fig. 5.6(a)). In case of Co substituted system, along with the increased ferromagnetic J_{eff}s, decreasing antiferromagnetic $J_{\text{eff}}^{\text{Mn1-Mn2}}$s as a function of z, (Fig. 5.6(d)), explains the trend in Curie temperature of the system (Fig. 5.5(b), Case-1). The higher Curie temperatures in Co-substituted systems, in comparison with Fe-substituted ones, can be interpreted as due to quantitatively larger ferromagnetic interactions in the former.

Interesting jumps in magnetization are observed (Fig. 5.4(b), 5.4(e)) at a critical concentration of Fe/Co in systems with no Cu and Mn content 25% in excess ($z = 0.25$, $y = 0$). The atomic moments reveal that such discontinuous jumps in magnetic moments are solely due to the change in orientation of the Mn spins: from an anti-parallel to a parallel alignment. The continuous increase in Curie temperature, as shown in Fig. 5.5 (Case-2), can be attributed to the significant increase in ferromagnetic J_{eff}s due to Mn1(Mn2)-Ni and Mn1(Mn2)-Fe pairs and the decrease in anti-ferromagnetic J_{eff} due to Mn pairs. One important difference between the two systems can be immediately noticed. While the T_c for Co-substituted system rises sharply to a very high value, this is not so for the Fe-substituted system. The origin of this difference is in the significant presence of anti-ferromagnetic interactions in Fe-substituted compounds for low concentrations of Fe.

The variations in moments with content of Cu (y) when Mn and Fe content held fixed ($z = 0.5$, $x = 0.75$), are shown in Fig. 5.4(c) and 5.4(f). For Fe@Ni-Cu@Mn system, the variation of the moment is non-monotonic. With the addition of Cu, the moment first decreases due to the anti-parallel alignment of Mn spins at different sites. With Cu content being 0.5 and beyond, there is no Mn at sites other

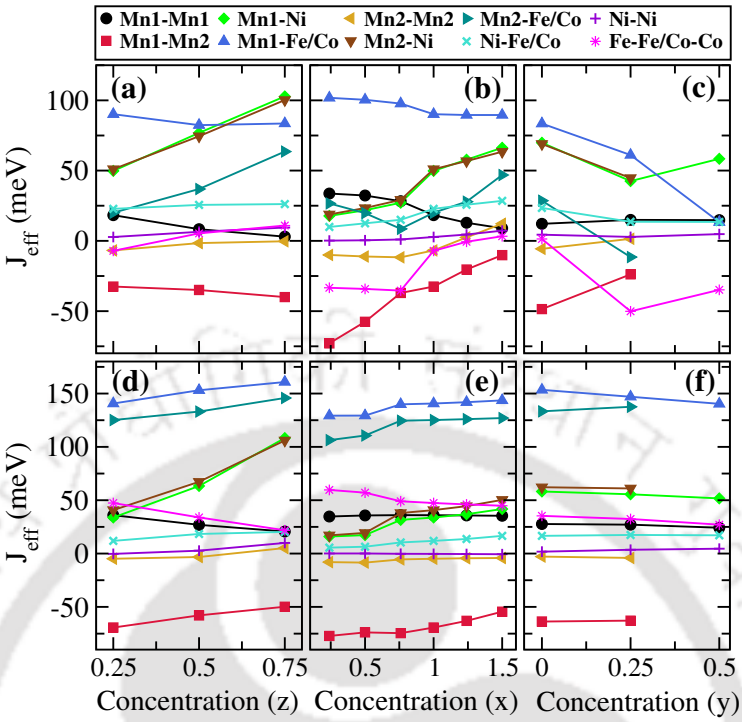

Figure 5.6: Variations of the calculated effective exchange coupling constants with z (x=1, y=0), x (y=0, z=0.25) and y (x=0.75, z=0.5) for ((a)-(c)) $Ni_{2-x}Fe_xMn_{1+z-y}Cu_ySb_{1-z}$ and ((d)-(f)) $Ni_{2-x}Co_xMn_{1+z-y}Cu_ySb_{1-z}$ systems in their austenite phases. Mn1 and Mn2 denote Mn atoms at its own site and at other sites in $L2_1$ structure, respectively.

than its original, for the spins to align anti-parallel. The total moment, therefore, increases again. In Co@Ni-Cu@Mn system, Cu addition does not affect the magnetic orientation of the Mn atoms leading to a monotonic variation of the total moment. The differences in the variations of the moments in these two cases are reflected in the variations of the Curie temperatures (Fig. 5.5, Case-3). The calculated effective exchange parameters (Fig. 5.6(c), 5.6(f)) show that the presence of substantial anti-ferromagnetic interactions at low concentrations of Cu and subsequent reductions in the dominant Mn-Co ferromagnetic interaction, due to reduced content of Mn in the Co@Ni-Cu@Mn system leads to monotonic decrease of its T_c with Cu concentration. In Fe@Ni-Cu@Mn system, the non-monotonic behavior of T_c, with y, can similarly be interpreted.

This analysis by systematic variations of the contents of the substituents implies that the contents of the substituents for cosubstitution are critical to obtain the target properties, as they renormalize the magnetic exchange interactions significantly. The reason for a larger number of compounds satisfying the criteria laid out in Section 5.3.1 in Co substituted family is due to substantially larger ferromagnetic

components in magnetic exchange interactions that pull the magnetic moments up. On the other hand, the addition of Cu in place of Mn reduces the possibilities of anti-ferromagnetic interactions bringing the moments down. At the same time, Cu addition reduces the strengths of the exchange interactions, pushing T_c closer to room temperature. The large and stable ferromagnetic exchange interactions in this family can also be correlated to the stable austenite phases in almost all select compounds in this family.

5.4 Conclusions

In this chapter, we have established that cosubstitution by transition metals Fe, Co and Cu in Mn-excess Sb-deficient Ni-Mn-Sb compounds can lead to significant changes in magnetic entropy, driven by a second-order magnetic transition near room temperature. Thus, cosubstitution in Ni-Mn-Z Heuslers compounds can emerge as an efficient way to obtain reversible magnetocaloric effect, exploiting the advantages of second-order phase transition over those in a first-order magneto-structural transition. We find that the cosubstitution provides a wider scope of tuning the physical parameters like magnetic moment and magnetic transition temperature as well as of stabilization of the Heusler phase down to very low temperatures. The calculated changes in the magnetic entropy, for most of the materials, are comparable to those obtained in off-stoichiometric Heusler compounds undergoing the first-order transition. This work, thus, offers a broader scope of synthesis and exploration of large MCE near room temperature by cosubstitution in other compounds of the Heusler family.

Chapter 6

Giant magnetocaloric effect driven by first-order magneto-structural transition in cosubstituted Ni-Mn-Sb Heusler compounds

6.1 Introduction

. In the previous chapter, we explored potential room-temperature magnetocaloric materials exploiting the advantages of second-order phase transition over those in a first-order magneto-structural transition in two cosubstituted families, $Ni_{2-x}Fe_xMn_{1+z-y}Cu_ySb_{1-z}$ (Fe@Ni-Cu@Mn) and $Ni_{2-x}Co_xMn_{1+z-y}Cu_ySb_{1-z}$ (Co@Ni-Cu@Mn). However, giant effect is generally observed in materials which undergo a first-order magneto-structural transition i.e. a structural phase transition, coupled with a magnetic one [17, 65, 67, 69, 88, 89, 123, 306, 307, 312–317], as discussed in chapter 1. From this point of view, the continuous search of new solid-state magnetic refrigerants that could exhibit a giant MCE, in an appropriate temperature range specially near room temperature, as well as the improvement of the existing ones, have been focus of research in this area.

Some recent investigations on the Ni-Mn-Sb family, carried out by single substitution of the Fe and Co atoms at Mn and Ni sites, respectively, resulted in significant positive values of ΔS_{mag} [134, 135, 140, 142] driven by the first-order magneto-structural transition. However, one major disadvantage observed was, that upon substitution, the working temperature, i.e., the martensitic transformation temper-

The contents of this chapter are accepted in Physical Review B

ature (T_M) falls below the room temperature. This is not desirable for operational purposes. The strategy of cosubstitution can be expected to be useful in achieving giant MCE with better tuning and adaptability of the important magnetic and structural properties. In the previous chapter, we found a delicate balance of the concentrations of different constituents and easy tunability of properties: austenite phase stability, magnetic moment, Curie temperature, in the cosubstituted Ni-Mn-Sb family. Therefore, in the present work, armed with the information in the previous chapter, we investigated the same two cosubstituted series, $Ni_{2-x}Fe_xMn_{1+z-y}Cu_ySb_{1-z}$ (Fe@Ni-Cu@Mn) and $Ni_{2-x}Co_xMn_{1+z-y}Cu_ySb_{1-z}$ (Co@Ni-Cu@Mn), but focused on the composition ranges in which a martensitic phase transformation (MPT) occurs, the ones not covered there. We aimed to explore whether an improved giant MCE due to magneto-structural coupling can be predicted in these compositions along with near room temperature T_M. Using a thermodynamic model in conjunction with first-principles electronic structure calculations, we made comparisons with the single substituted systems explored experimentally and provided predictions of new compounds, yet to be realized experimentally, that can exhibit significantly large MCE. This study established a systematic way to use the information on structural and magnetic properties obtained from first-principles calculations to screen the materials that are potential ones with target properties and the robustness of the formalism to accurate predictions of new compounds.

6.2 Computational Details

We have used the first-principles electronic structure calculations to gain information on the phase stability of the compounds explored and their magnetic properties. The electronic structure calculations were done with spin-polarised density functional theory (DFT) based on projector augmented wave (PAW) method as implemented in Vienna *Ab initio* Simulation Package (VASP) [177–179]. The valence electronic configurations used for the Mn, Fe, Co, Ni, Cu and Sb PAW pseudopotentials are $3d^64s$, $3d^74s$, $3d^84s$, $3d^84s^2$, $3d^{10}4s$ and $5s^25p^3$, respectively. For all calculations, we used the Perdew-Burke-Ernzerhof implementation of generalized gradient approximation for exchange-correlation functional [190]. An energy cut off of 550 eV, and a Monkhorst-Pack $11 \times 11 \times 11$ k-mesh were used for self-consistent calculations. The convergence criteria for the total energies and the forces on individual atoms were set to 10^{-6} eV and 10^{-2} eV/Å, respectively.

The stabilities of the compounds against decomposition into its components were

checked by computing the formation energies:

$$E_f = E_{tot} - \sum_i n_i E_i \tag{6.1}$$

E_{tot} is the total electronic energy of the systems, i represents the atoms in the unit cell, and n_i is the concentration of the i-th atom. E_i is the total energy of the element i in its bulk ground state.

To compute the Curie temperature T_c of a compound, we first calculated the magnetic pair exchange parameters using multiple scattering Green function formalism (KKR) as implemented in SPRKKR code [230]. In order to calculate the energy differences by the SPRKKR code, full potential spin-polarised scalar relativistic Hamiltonian with angular momentum cut-off $l_{max} = 3$ was used along with a converged k-mesh for Brillouin zone integrations. The Green's functions were calculated for 32 complex energy points distributed on a semi-circular contour in the complex plane. The energy convergence criterion was set to 10^{-5} eV for the self-consistent cycles. These exchange parameters were then used for the calculation of T_c. The Curie temperatures were estimated with two different approaches: the mean-field approximation (MFA) [223, 286] and the Monte Carlo simulation (MCS) method [182, 229, 236], as described in chapter 2. Magnetic exchange interactions $J_{ij}^{\mu\nu}$ for up to 20 neighbors surrounding each atom have been considered in the Heisenberg Hamiltonian. At each temperature, 80000 Monte Carlo steps have been performed to equilibrate the systems containing 8192 atoms. The Curie temperatures are obtained from the resulting M-T relationship, where M is the total magnetic moment of the system and T the temperature.

To estimate the MCE parameters, i.e., isothermal change in magnetic entropy (ΔS_{mag}) or adiabatic temperature change (ΔT_{ad}) due to the application of a magnetic field, we have used Monte Carlo simulation on a model Hamiltonian (H), incorporating the degenerate Blume-Emery-Griffiths (BEG) [173, 174] and a mixed q-states Potts model [111, 171, 172, 175, 176]. The model Hamiltonian was chosen such that it accommodates, along with magnetic and structural degrees of freedom, the coupling between the two [108, 111, 120, 172]. It consists of three parts: (a) the magnetic contribution due to the magnetic degrees of freedom of the system, H_m; (b) the elastic contribution due to the structural transformation from cubic to tetragonal phases, H_{els}; and (c) the contribution arising from the coupling of magnetic and structural interactions, H_{int}. The details are in chapter 2.

6.3 Results and Discussions

We investigated the two cosubstituted Mn-excess, Sb-deficient Ni-Mn-Sb families: (i) $Ni_{2-x}Fe_xMn_{1+z-y}Cu_ySb_{1-z}$ (denoted as Fe@Ni-Cu@Mn) and (ii) $Ni_{2-x}Co_xMn_{1+z-y}Cu_ySb_{1-z}$ (denoted as Co@Ni-Cu@Mn). As mentioned in the section 6.1, our motivation was to find compounds that give rise to large MCE driven by first-order magneto-structural transition. In order to model the compounds that have multi-sublattice chemical disorder, we have considered a 16 atom conventional cubic unit cell. This unit cell mimics the high temperature austenite ($L2_1$ Heusler) phase of the systems (space group 225). The consequence of the cell size is the inability to model compositions with arbitrary x, y, or z. Each one of the three variables can be changed by an amount of 0.25 only. The choice of the composition range to achieve ones with the target properties is crucial. For this, we took recourse to our previous chapters on the same system. Based upon the findings there, we restricted the value of x to 0.25, and the range of z between 0.50 and 0.75. The variable y is constrained to be less than or equal to the value of z. The compounds with these compositions are expected to exhibit a martensitic phase transformation.

Since, site occupancies in the compounds do not always follow a regular pattern (the excess atoms occupying the sites of deficient atoms in the reference system) [229, 253, 269, 287, 288, 318] affecting the MCE properties as a consequence, we first found out the minimum energy configuration for each composition by comparing the total energies of configurations with different site occupancy patterns and magnetic configurations. We found that the substituting Fe/Co atoms prefer to occupy the Ni sites, whereas the Cu atoms prefer to occupy the Sb sites, the same as found out in previous chapter. We also found that depending upon the composition, two types of magnetic configurations are found leading to minimum total energy; FM, where the two types of Mn can align parallel and FIM, where the two types of Mn can align antiparallel.

After fixing the lowest energy configurations, we first calculated the formation energies for all the compounds. Negative values of the formation energy for each of the composition (Table 6.1 and 6.2) indicated their stability against decomposition into its constituent elements. Subsequently, the following criteria were used to screen materials further to narrow down the ones which are potential large MCE materials:

(i) The materials should possess a high magnetic moment in their austenite phases.

(ii) The martensitic transformation temperature (T_M) should be near room temper-

ature or higher than that.
(iii) The MPT should be associated with a substantial change in magnetization. In other words, a magnetic structure in the martensite phase different than that in the austenite phase would be advantageous.
(iv) The second-order magnetic transition temperature, i.e., the Curie temperature (T_c^A) in the austenite phase, should be close to the martensitic transformation temperature (T_M). This would lead to a large change in entropy due to near simultaneous magnetic and structural transition. Otherwise, T_c^A should be higher than T_M so that the MPT can occur in a magnetically ordered phase.

In what follows, we present and analyze the results on the variations in the magnetic moments in the austenite phases, the relative stabilities of the structural phases and variations in the T_M and the variations in T_c^A with changes in the compositions by systematic variations in x, y and z. The analysis helps us in the prediction of new compounds that have potentials to exhibit large MCE. In here, we first understand the trends in the physical quantities due to cases with single substitution. For that, we extended the range of x up to 0.75 in all substituted compounds (Table 6.1). The outcome of the cosubstituted cases can be understood in the light of the results for single substituted compounds.

6.3.1 Magnetic moment in austenite phase

A correlation between enhancement of magnetization in the austenite phase and a large MCE for Ni-Mn-Sb system could be observed in the experiments [135, 142]. For $Ni_{1.8}Co_{0.2}Mn_{1.52}Sb_{0.48}$ [135], an enhanced magnetic moment in the austenite phase has been observed due to the Co substitution at Ni site. Subsequently, a large positive MCE was observed in the system, presumably an artifact of magneto-elastic coupling. In general, a significant enhancement of magnetic moment in the austenite phase leads to a possibility of large ΔM, the difference in magnetization between austenite and martensitic phases, the key to a first-order magneto-structural transition. We, therefore, focus on finding the possibility of enhancement of magnetic moment in austenite phases of Ni-Mn-Sb compounds upon substitution by 3*d*-elements at different sites. We present the results on total and atomic magnetic moments in Fig. 6.1 and Fig. 6.2. The panels (a)-(c) in each of the two figures show results for single substitution while (d)-(e) show results for cosubstitution. All results in Fig. 6.1 are for compounds with $z = 0.5$ that is with 50% excess Mn (with respect to stoichiometric Ni_2MnSb) while those in Fig. 6.2 are with $z = 0.75$. If we first look at

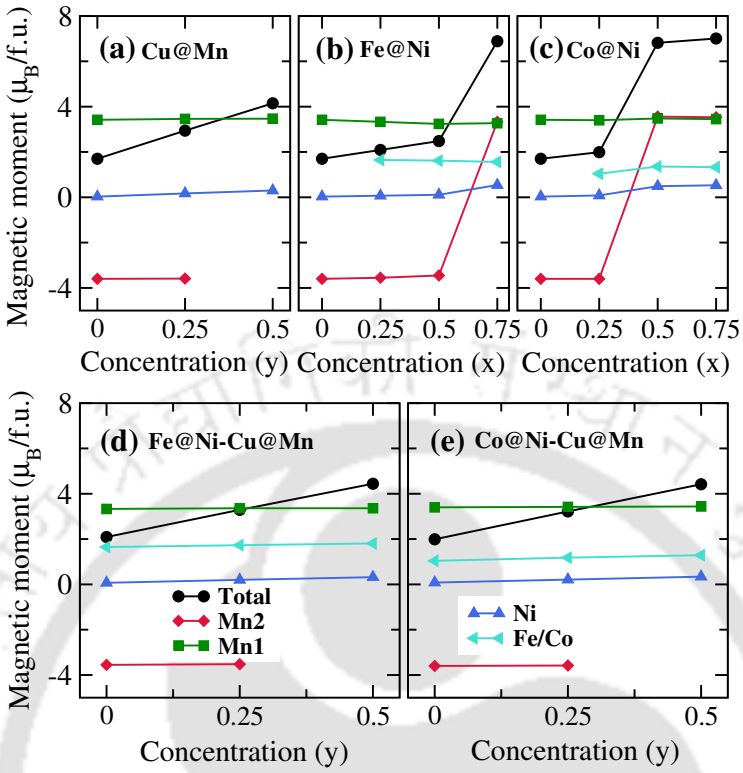

Figure 6.1: Variations in the calculated total and atomic magnetic moments (in $\mu_B/f.u.$) with (a) y (x=0), ((b)-(c)) x (y=0) and ((d)-(e)) y (x=0.25) for $Ni_{2-x}Fe_xMn_{1+z-y}Cu_ySb_{1-z}$ (Fe@Ni-Cu@Mn) and $Ni_{2-x}Co_xMn_{1+z-y}Cu_ySb_{1-z}$ (Co@Ni-Cu@Mn) systems in their austenite phases. z value is kept at 0.5 throughout. Mn1 and Mn2 denote Mn atoms at its own site and at other sites in $L2_1$ structure, respectively.

the compounds with single substitution (Table 6.1), we find that irrespective of z, Cu substitution at the Mn site allows the total moment to increase linearly with the Cu content y. This is due to the fact that the atomic moments of both Mn atoms stay nearly same and that the gradual replacement of Mn2 atoms by Cu reinforces the moment since Mn2, being aligned anti-parallel to Mn1, was reducing the total moment. When Fe or Co substitutes Ni, irrespective of the value of z, the behavior of magnetic moment with the concentration of Fe or Co, x, is qualitatively identical in the sense that a monotonic variation with x is either preceded or followed by a discontinuous jump at a critical value of x; the difference being in the critical value. Such discontinuous jump with at least two-fold increase in the total moment occurs due to the change in the magnetic structure from FIM to FM, driven by the orientations of the Mn atoms. The variations in the moments for cosubstitution with x fixed at 0.25, turn out to be the combined behavior of the two single-substituted cases, Fe or Co substituting Ni and Cu substituting Mn. Due to the presence of higher concentration of Mn2 atoms in compounds with $z = 0.75$, in comparison to

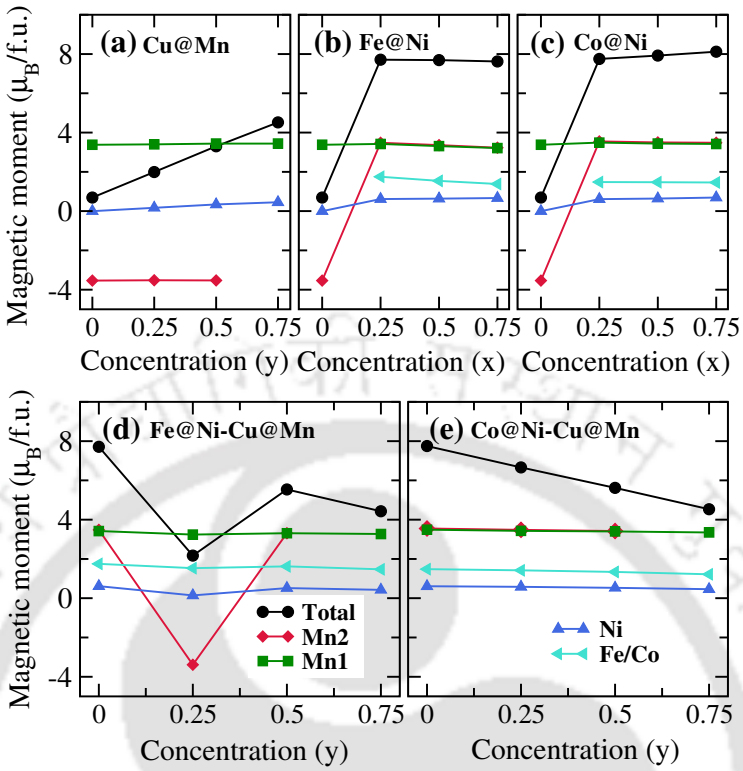

Figure 6.2: Variations in the calculated total and atomic magnetic moments (in $\mu_B/f.u.$) with (a) y (x=0), ((b)-(c)) x (y=0) and ((d)-(e)) y (x=0.25) for $Ni_{2-x}Fe_xMn_{1+z-y}Cu_ySb_{1-z}$ (Fe@Ni-Cu@Mn) and $Ni_{2-x}Co_xMn_{1+z-y}Cu_ySb_{1-z}$ (Co@Ni-Cu@Mn) systems in their austenite phases. z is kept at 0.75 throughout. Mn1 and Mn2 denote Mn atoms at its own site and at other sites in $L2_1$ structure, respectively.

those with $z = 0.5$, the overall moments in the former cosubstituted compounds are higher than that in the later (Table 6.2). The inference from these results is that the compositions with $z = 0.75$ may provide higher values of ΔM and thus better MCE than compounds with composition having $z = 0.5$, closest to the one on which experiments have been performed.

6.3.2 Martensitic transformation and magnetic structures across structural phases

Next, we investigate whether MPT occurs in our systems of investigation. To this end, we distort the austenite $L2_1$ structure along the z-axis by keeping the volume at the equilibrium value of the austenite phase and compute the total energy of the system as a function of the tetragonal distortion given by (c/a). Typical profiles of compounds undergoing MPT will have their minima at (c/a) $\neq 1$. For all compositions, we calculated the energy profiles as a function of tetragonal distor-

Table 6.1: Calculated values of equilibrium lattice constant (a_0), formation energies (E_f), and total magnetic moment (M_A) of the single substituted systems in their austenite phases with corresponding ground state magnetic configurations are shown. The total energy difference (ΔE) between the austenite($L2_1$) and the martensite(tetragonal) phases, the equilibrium value of tetragonal distortion (c/a), the differences in magnetic moments between the austenite and martensite phases (ΔM), the Mean-field approximated ($T_c^{A(MFA)}$) and Monte Carlo simulated ($T_c^{A(MCS)}$) Curie temperatures in the austenite phases are also shown. Boldfaces indicate the reference compositions on which experimental studies are available.

$Ni_{2-x}A_xMn_{1.50-y}Cu_ySb_{0.50}$($z$=0.50)

Composition x	y	Mag. Config.	a_0 (Å)	E_f (eV/f.u.)	M_A ($\mu_B/f.u.$)	ΔE (meV/atom)	c/a	$\lvert\Delta M\rvert$ ($\mu_B/f.u.$)	$T_c^{A(MFA)}$ (K)	$T_c^{A(MCS)}$ (K)
0.00	**0.00**	**FIM**	5.94	-0.552	1.71	27.64	1.34	0.16	397	422
0.00	0.25	FIM	5.92	-0.493	2.94	22.30	1.28	0.12	324	360
0.00	0.50	FM	5.90	-0.430	4.15	22.00	1.27	0.00	347	300
A=Fe										
0.25	0.00	FIM	5.92	-0.450	2.09	10.68	1.29	0.18	351	370
0.50	0.00	FIM	5.91	-0.332	2.48	4.81	1.24	0.26	308	335
0.75	0.00	FM	5.92	-0.219	6.89	No MPT	-	-	378	400
A=Co										
0.25	**0.00**	**FIM**	5.93	-0.670	1.99	20.97	1.30	0.04	391	410
0.50	0.00	FM	5.95	-0.796	6.82	16.19	1.28	4.85	484	500
0.75	0.00	FM	5.94	-0.941	7.01	4.95	1.28	4.90	532	565

$Ni_{2-x}A_xMn_{1.75-y}Cu_ySb_{0.25}$($z$=0.75)

Composition x	y	Mag. Config.	a_0 (Å)	E_f (eV/f.u.)	M_A ($\mu_B/f.u.$)	ΔE (meV/atom)	c/a	$\lvert\Delta M\rvert$ ($\mu_B/f.u.$)	$T_c^{A(MFA)}$ (K)	$T_c^{A(MCS)}$ (K)
0.00	0.00	FIM	5.86	-0.470	0.69	55.32	1.36	0.15	348	290
0.00	0.25	FIM	5.85	-0.427	1.99	49.09	1.33	0.17	295	280
0.00	0.50	FIM	5.84	-0.379	3.30	29.27	1.30	0.30	326	276
0.00	0.75	FM	5.82	-0.347	4.52	23.52	1.28	0.43	451	360
A=Fe										
0.25	0.00	FM	5.89	-0.352	7.71	41.22	1.38	6.27	498	406
0.50	0.00	FM	5.88	-0.250	7.69	28.00	1.40	5.64	469	421
0.75	0.00	FM	5.86	-0.147	7.62	16.30	1.41	5.06	424	447
A=Co										
0.25	0.00	FM	5.90	-0.615	7.75	37.25	1.34	6.78	519	450
0.50	0.00	FM	5.89	-0.786	7.92	16.65	1.33	6.84	518	535
0.75	0.00	FM	5.88	-0.950	8.12	No MPT	-	-	573	660

tion. The results are shown in Fig. 6.3. The results suggest that all the considered compounds, undergo MPT, a requirement for further consideration. However, for compounds with higher Mn content ($z = 0.75$), the magnetic ground states of the austenite phases are different than those in the martensitic phases except at the compound where $y = 0.75$. In all such cases, the austenite phase has FM magnetic structure (Table 6.2), while the martensitic phase has FIM magnetic structure. The results in Fig. 6.3(c)-(d) corroborate this. A consequence of this is a large value of ΔM (Table 6.2) for the compounds with $z = 0.75$ as compared to those with

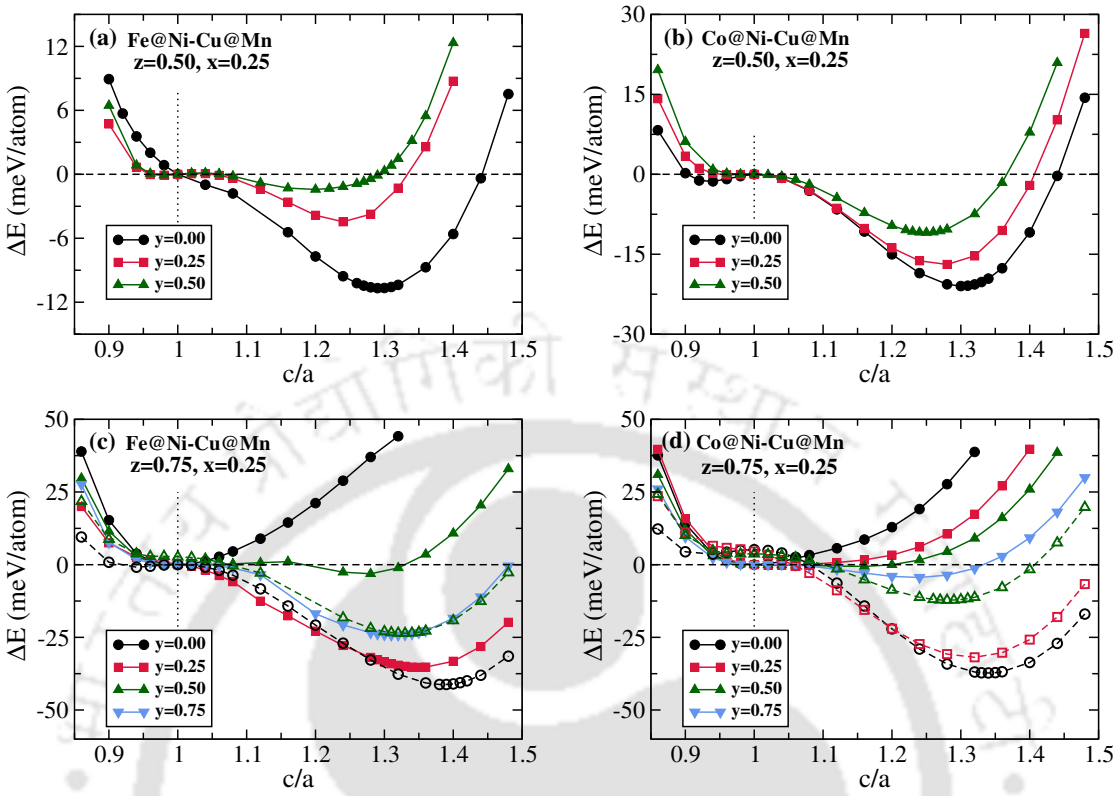

Figure 6.3: The variations of total energy difference (ΔE) between the austenite($L2_1$) and the martensite(tetragonal) phases as a function of tetragonal distortion i.e. c/a ratio in $Ni_{2-x}(Fe/Co)_xMn_{1+z-y}Cu_ySb_{1-z}$ ((Fe/Co)@Ni-Cu@Mn) compounds for different y with ((a)-(b)) z=0.50 and ((c)-(d)) z=0.75. x is fixed at the value 0.25 for all calculations.The magnetic configurations considered in each case is given in Table 6.2. The solid curves are for cases where magnetic configurations considered are same in both structural phases. The dotted curves in the panels (c) and (d) are for cases where the magnetic configurations in the tetragonal phases are different from those in the Heusler phases and provide minimum total energies.

$z = 0.5$. This makes the compounds with $z = 0.75$ potentially better to realize large MCE.

In order to make sure that this is indeed so, we looked at the variations in ΔE, the energy difference between the austenite and martensite phases in their respective ground states. The results for single-substituted compounds (Table 6.1) are shown in Fig. 6.4(a)-(c) while those for cosubstituted ones are shown in Fig. 6.4(d)-(e) and listed in Table 6.2. In literature, ΔE is routinely used to predict the martensitic transformation temperature (T_M) [229, 288, 302, 318, 319]. Here we have used it first to understand the trends in the T_M so that compositions with higher T_M can be screened. From Fig. 6.4, we find that the trends in variations of ΔE with compositions in cases of the cosubstituted compounds can be correlated with the

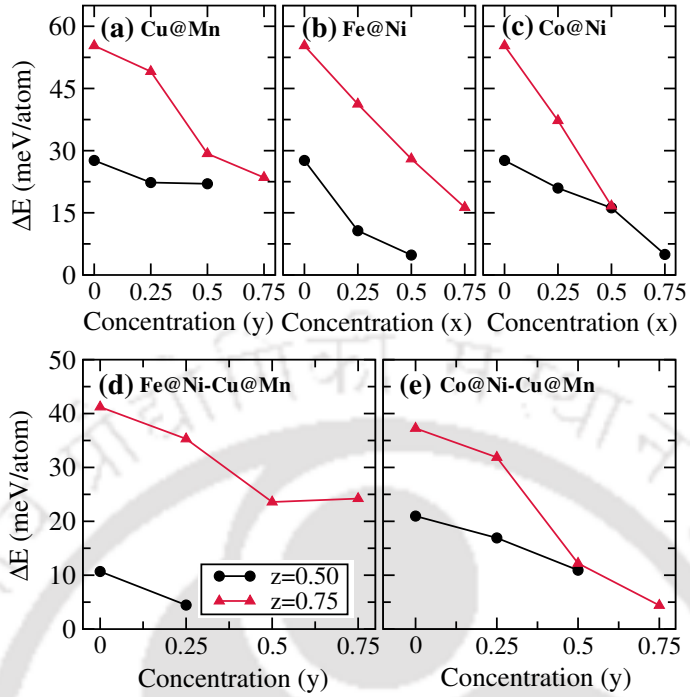

Figure 6.4: Variations in total energy difference, ΔE between the austenite($L2_1$) and the martensite(tetragonal) phases with (a) y (x=0), ((b)-(c)) x (y=0) and ((d)-(e)) y (x=0.25) for $Ni_{2-x}(Fe/Co)_xMn_{1+z-y}Cu_ySb_{1-z}$ compounds with different values of z.

trends in case of single-substituted ones. A general trend of $z = 0.75$ compounds having higher ΔE and thus higher T_M can be immediately inferred. Therefore, in both the counts of larger ΔM and higher T_M, the compounds with Mn-content as high as 1.75 can be considered promising to obtain large MCE.

6.3.3 Curie temperature in austenite phase

In Fig. 6.5, we present the calculated Curie temperature (T_c^A) in the austenite phase for all the compositions, using both the Mean-field approximation and the more accurate Monte Carlo simulation method. The results for single-substituted compounds are presented in Fig. 6.5(a)-(c), and those for the cosubstituted compounds are presented in Fig. 6.5(d)-(e). The T_c^A values for all the cosubstituted compositions are listed in Table 6.2. Here, too, the trends of variations in T_c^A for cosubstituted compounds can be correlated to the trends in cases of single-substitutions. Overall it can be concluded that for cosubstituted systems, the T_c^A values are higher for compounds with $z = 0.75$. This is more prominent for Co and Cu cosubstituted systems (Co@Ni-Cu@Mn). Thus cosubstituted Co@Ni-Cu@Mn family, with $z = 0.75$ have more possibility of fulfilling the target properties of a giant magnetocaloric material.

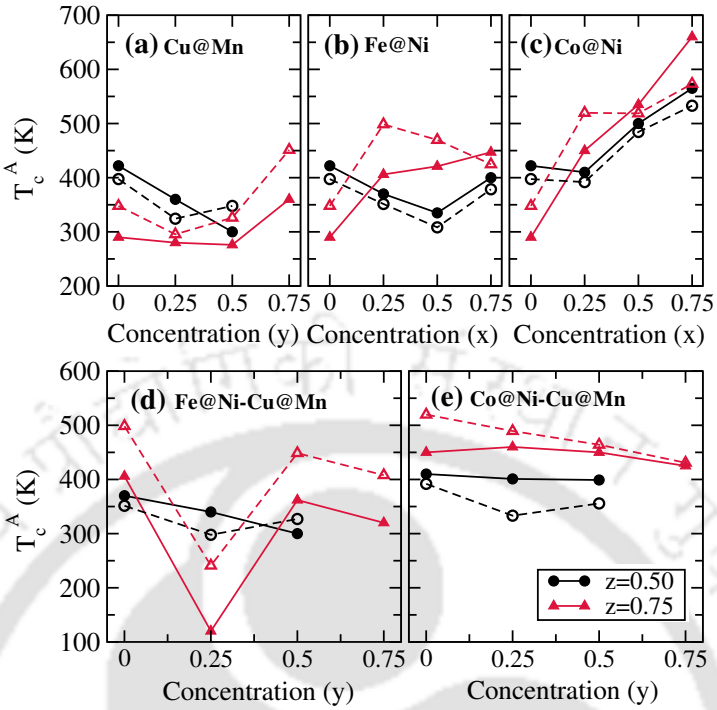

Figure 6.5: Variations in calculated Curie temperatures (T_c^A) in austenite phases with concentration (a) y (x=0), ((b)-(c)) x (y=0) and ((d)-(e)) y (x=0.25) for $Ni_{2-x}(Fe/Co)_xMn_{1+z-y}Cu_ySb_{1-z}$ systems with different z. Closed symbols and open symbols represent results calculated by Monte Carlo Simulation (MCS) and Mean Field Approximation (MFA) methods, respectively.

6.3.4 Prediction of new compounds

Based upon the results presented in the previous three sub-sections, we are now in a position to predict new compounds which can exhibit better MCE properties than that observed in the experimentally synthesized compounds. To this end, we first consider the compounds $Ni_2Mn_{1.5}Sb_{0.5}$ (i.e. x=0.00, y=0.00, z=0.50) and $Ni_{1.75}Co_{0.25}Mn_{1.5}Sb_{0.5}$ (i.e. x=0.25, y=0.00, z=0.50) (boldfaced in Table 6.2) as the reference ones with respect to which we assess the improvement in properties.

These compounds are chosen as the compositions in these compounds are very close to the experimentally investigated ones [132, 134, 135, 142, 243, 289, 305]. Comparing all the quantities, we predict four compositions (bold bordered in Table 6.2), two in Fe@Ni-Cu@Mn family, and the other two in Co@Ni-Cu@Mn family. In all the cases, $z = 0.75$ that is Mn atom is in excess by 75% in comparison to perfectly ordered Ni_2MnSb, the parent compound. For all the predicted compositions, the ground state magnetic configuration in the austenite phase is the FM one, where the two types of Mn atoms are aligned parallel, leading to larger magnetic moments

Table 6.2: Calculated values of equilibrium lattice constant (a_0), formation energies (E_f), and total magnetic moment (M_A) of the systems under considerations in their austenite phases. The corresponding ground state magnetic configurations are shown. The total energy difference (ΔE) between the austenite($L2_1$) and the martensite(tetragonal) phases, the equilibrium value of tetragonal distortion (c/a), the differences in magnetic moments between the austenite and martensite phases (ΔM), the Mean-field approximated ($T_c^{A(MFA)}$) and Monte Carlo simulated ($T_c^{A(MCS)}$) Curie temperatures in the austenite phases are also shown. Boldfaces indicate the reference compositions around which experimental studies [132, 135, 305] are available. The compositions shown within the borders are found to satisfy the criteria for considering them as efficient giant magnetocaloric materials with improved MCE properties than the reference ones.

$Ni_{2-x}A_xMn_{1.50-y}Cu_ySb_{0.50}$($z$=0.50)

Composition x	y	Mag. Config.	a_0 (Å)	E_f (eV/f.u.)	M_A ($\mu_B/f.u.$)	ΔE (meV/atom)	c/a	$\lvert\Delta M\rvert$ ($\mu_B/f.u.$)	$T_c^{A(MFA)}$ (K)	$T_c^{A(MCS)}$ (K)
0.00	**0.00**	**FIM**	5.94	-0.552	1.71	27.64	1.34	0.16	397	422
A=Fe										
0.25	0.00	FIM	5.92	-0.450	2.09	10.68	1.29	0.18	351	370
0.25	0.25	FIM	5.91	-0.386	3.29	4.45	1.24	0.08	297	340
0.25	0.50	FM	5.90	-0.317	4.44	No MPT	-	-	327	300
A=Co										
0.25	**0.00**	**FIM**	5.93	-0.670	1.99	20.97	1.30	0.04	392	410
0.25	0.25	FIM	5.91	-0.620	3.22	16.91	1.28	0.23	333	401
0.25	0.50	FM	5.90	-0.567	4.42	10.93	1.25	0.19	355	399

$Ni_{2-x}A_xMn_{1.75-y}Cu_ySb_{0.25}$($z$=0.75)

Composition x	y	Mag. Config.	a_0 (Å)	E_f (eV/f.u.)	M_A ($\mu_B/f.u.$)	ΔE (meV/atom)	c/a	$\lvert\Delta M\rvert$ ($\mu_B/f.u.$)	$T_c^{A(MFA)}$ (K)	$T_c^{A(MCS)}$ (K)
0.00	0.00	FIM	5.86	-0.470	0.69	55.32	1.36	0.15	348	290
A=Fe										
0.25	0.00	FM	5.89	-0.352	7.71	41.22	1.38	6.27	498	406
0.25	0.25	FIM	5.84	-0.312	2.17	35.30	1.35	0.19	241	120
0.25	**0.50**	**FM**	5.83	-0.240	5.54	23.58	1.33	3.33	448	362
0.25	**0.75**	**FM**	5.81	-0.167	4.43	24.22	1.32	1.22	408	320
A=Co										
0.25	**0.00**	**FM**	5.90	-0.615	7.75	37.25	1.34	6.78	519	450
0.25	**0.25**	**FM**	5.87	-0.576	6.66	31.87	1.32	4.66	489	460
0.25	0.50	FM	5.84	-0.525	5.62	12.20	1.28	2.53	464	450
0.25	0.75	FM	5.81	-0.468	4.53	4.40	1.24	0.27	431	425

compared to the reference systems. For these compounds, large values of change in magnetization (ΔM), compared to the reference compounds, are observed during the martensitic phase transformation. Finally, the conditions that the martensitic transformation temperature (T_M) and Curie temperature (T_c^A) either should nearly coincide or T_c^A should be higher than T_M, are satisfied for the predicted compounds. In order to establish this, we have made an estimation of T_M the following way: the value of ΔE corresponding to $Ni_{1.75}Co_{0.25}Mn_{1.50}Sb_{0.50}$ composition is mapped to the experimental martensitic transformation temperature (T_M) value of 262 K, found

for a compound with almost same composition $Ni_{1.8}Co_{0.2}Mn_{1.5}Sb_{0.5}$ [135]. Using this mapping, we found that approximate values of T_M are 294 K, 302 K, 465 K and 398 K for $Ni_{1.75}Fe_{0.25}Mn_{1.25}Cu_{0.5}Sb_{0.25}$, $Ni_{1.75}Fe_{0.25}MnCu_{0.75}Sb_{0.25}$, $Ni_{1.75}Co_{0.25}Mn_{1.75}Sb_{0.25}$ and $Ni_{1.75}Co_{0.25}Mn_{1.50}Cu_{0.25}Sb_{0.25}$, respectively. A look at Table 6.2, along with these mapped values, shows that the above mentioned conditions are satisfied for all four.

6.3.5 Computation of the MCE parameters

After screening the compounds, most suitable to exhibit giant MCE, we aimed at the calculations of the MCE parameters ΔS_{mag} and ΔT_{ad} to establish our predictions. Since there is no experimental result to compare in cases of the new cosubstituted compounds, it is imperative that our approach of using the DFT, in conjunction with the proposed model Hamiltonian, is validated. To this end, we used our approach to compute the MCE parameters for two compounds: $Ni_2Mn_{1.52}Sb_{0.48}$ and $Ni_{1.8}Co_{0.2}Mn_{1.52}Sb_{0.48}$ where experimental results are available [132, 135]. After validation, we computed the MCE parameters for $Ni_{1.75}Co_{0.25}Mn_{1.50}Cu_{0.25}Sb_{0.25}$, one of the compounds predicted. Due to the huge computational cost involved in cosubstituted compounds with multi-sublattice disorder, we restricted ourselves to only one out of the four new predicted compounds.

The compound $Ni_2Mn_{1.52}Sb_{0.48}$ was considered first. The Monte Carlo calculations were done using a simulation domain consisting of 8192 atoms obtained by replicating the unit cell, containing 16 atoms, eight times in each direction. The Mn2 atoms are randomly distributed on the Sb sub-lattices. The final simulation domain contains 983 Sb, 1065 Mn2, 2048 Mn1, 4096 Ni atoms.

For the magnetic interaction part of the Hamiltonian (H_m), the magnetic exchange parameters, J_{ij} were obtained from Fig. 6.6(a) and Fig. 6.6(b). The magnetic spin states (q) for Ni, Mn2, Mn1 atoms were taken as 3, 6, and 6, respectively, in accordance with the studies on other Heusler systems [120, 172]. The spin state of each magnetic atom site (S_i) were chosen randomly by generating a random number between 0 and 1 ($0 \leq r \leq 1$) and selecting the state as: if $0 \leq r \leq$ l/3, then q_{Ni} = l, l = 1, 2, 3, and if $0 \leq r \leq$ k/6, then $q_{\mathrm{Mn1(Mn2)}}$ = k, k = 1, 2, 3, . . . 6. We considered lattice sites up to the third coordination shells for Mn1-Mn1, Mn2-Mn2, Mn1-Mn2 pairs, and up to the first-coordination shell for Mn1(Mn2)-Ni and Ni-Ni atom pairs in the summation.

For elastic part of the Hamiltonian (H_{els}), the summation was taken over the

pairs up to the second-coordination shell. A similar procedure, as for choosing S_i values, had been used to assign the σ_i values randomly. Values of structural constants J and K were chosen such that the martensitic transformation temperature (T_M) could be adjusted around the experimental T_M, which is around the room temperature (≈300 K) [132, 243]. The constraint of $K/J \leq 0.5$ was imposed to get rid of any pre-martensitic phase. Although J and K could be obtained from *ab-initio* calculations, we used a simple procedure of tuning to reduce the complexity as well as computational cost. This had been followed in other investigations [111, 171] too. The degeneracy factor (p) for the cubic phase was taken as 2, since the cubic phase can distort along one of the three directions (here along the z-direction). The $K1$ was chosen to be negative since it was experimentally observed that T_M decreased under application of external magnetic field. The negative $K1$ fixed the ghost deformation state σ_g to -1. The value of $K1$ was chosen such that the maximum magnetic entropy change is obtained around the experimental martensitic transformation temperature.

In the magneto-elastic interaction part (H_{int}), the interaction parameters U_{ij} in cubic (U_c) and tetragonal (U_t) phases were tuned in such a way that the Curie temperature in the austenite phase is obtained around the experimental Curie temperature (350 K for the compound considered).

Thus, with an initial guess of J and K values, we adjusted the T_M, to bring it closer to the experimental value. Once a reasonable T_M is obtained, we tuned the parameter U_{ij} in both structural phases to obtain the experimental Curie temperature. These are done by adjusting the co-ordination shells over which summations are done. These were done in the absence of an external magnetic field, i.e., H_{ext}=0. Then we applied an external field of 5 T and tuned the $K1$ parameter so that T_M shifts in the direction observed in the experiment. This ensured a correct behavior of magnetic entropy change ΔS_{mag} as a function of temperature and ΔS_{mag}^{max} is achieved around the experimental T_M. Here, depending on the sign of $K1$, ghost deformation state σ_g was chosen. The simulation started with the initial values of σ_i as 1 for all the lattice sites and S_i, S_g as 1 for the magnetic atoms. The final values of all the parameters are presented in Table 6.3. For each temperature step, 2×10^5 MC steps were performed. The system was equilibrated for 1×10^5 MC steps, and the data, then, were collected for 10^5 steps. For each temperature step, energy of the system (H), magnetization (m), and structural distortion (ε) were averaged over 1000 data points collected after every 100 MC steps. These averaged quantities were then used to calculate the various thermodynamic quantities using equations,

given in Chapter 2.

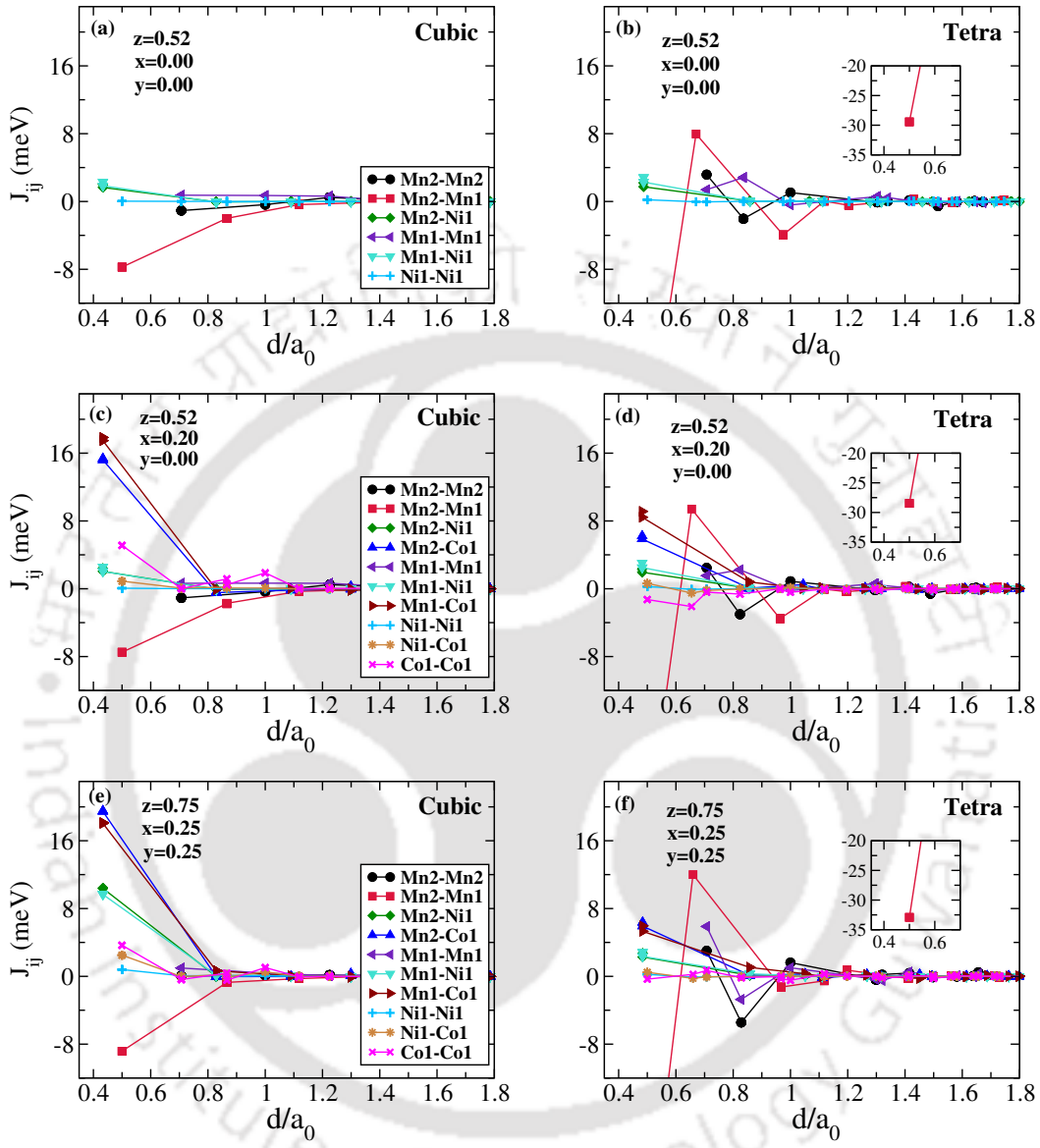

Figure 6.6: Inter-atomic magnetic exchange interactions in (a)-(b) parent composition $Ni_2Mn_{1.52}Sb_{0.48}$ and (c)-(d) Co substituted at Ni site, $Ni_{1.8}Co_{0.2}Mn_{1.52}Sb_{0.48}$ and ((e)-(f)) Co and Cu cosubstituted $Ni_{1.75}Co_{0.25}Mn_{1.50}Cu_{0.25}Sb_{0.25}$ compositions in the cubic ($c/a = 1$) and tetragonal ($c/a \neq 1$) phases as a function of distance d(in units of lattice constant a_0) between the pair of atoms.

Under zero field, the strain order parameter (ε) shows the structural transformation from austenite (undistorted phase with $\varepsilon = 0$) to martensite phases (distorted phase with $\varepsilon = 1$) with decreasing temperature (Fig. 6.7(a)). The transformation occurs around 300 K, which is in a good agreement with the experimental T_M. The magnetic order parameter (m) is almost zero at high temperatures indicating

Table 6.3: Values of structural, magneto-elastic and coupling parameters that are used in the present study for $Ni_{2-x}Co_xMn_{1+z-y}Cu_ySb_{1-z}$ compounds.

Concentrations			Parameters				
x	y	z	J meV	K meV	U_c meV	U_t meV	$K1$
0.00	0.00	0.52	1.67	0.25	1.36	3.54	-0.25
0.20	0.00	0.52	1.67	0.42	7.56	14.24	-0.8
0.25	0.25	0.75	2.00	0.32	7.56	14.24	-0.4

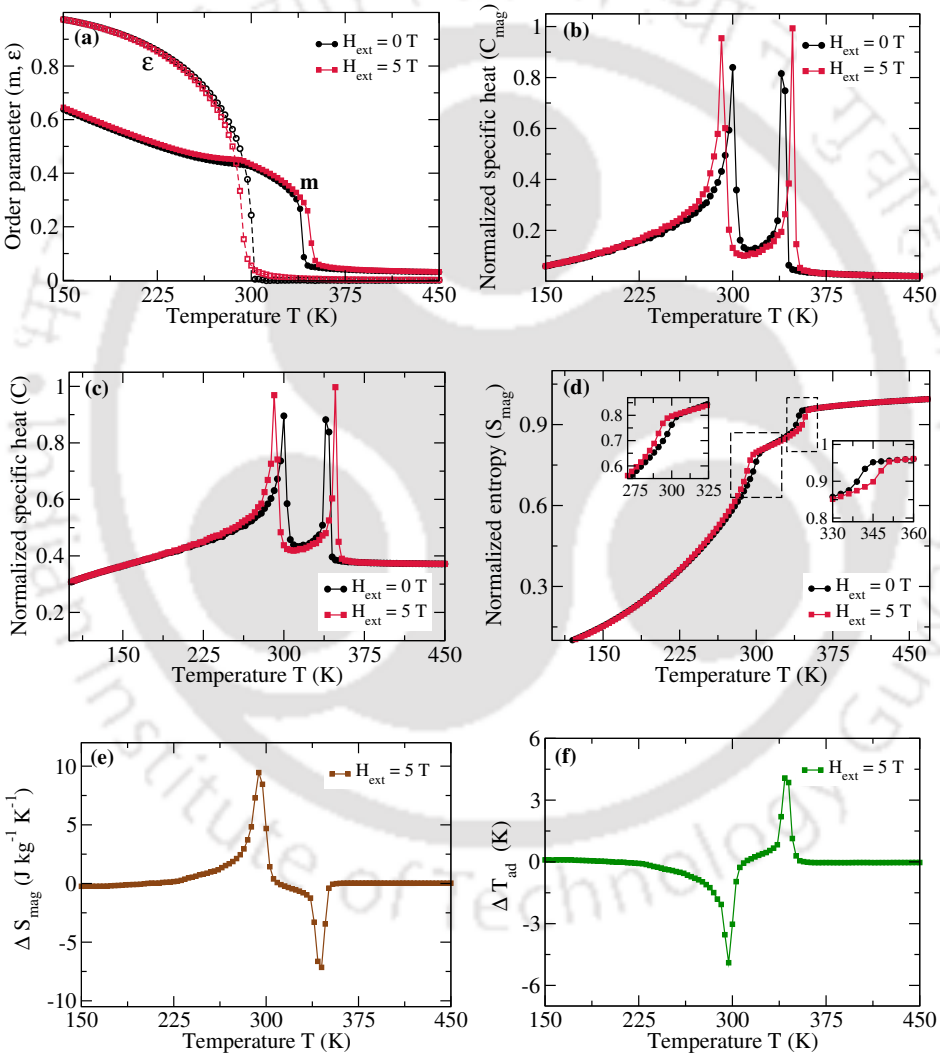

Figure 6.7: The calculated temperature dependence of (a) magnetic (m) and strain (ε) order parameters, (b)-(c) normalized magnetic and total specific heat (C_{mag} and C, respectively), (d) normalized magnetic entropy (S_{mag}) in an external field of 0 and 5 T and the temperature dependence of (e) the isothermal magnetic entropy change (ΔS_{mag}) and (f) adiabatic temperature change (ΔT_{ad}) due to change in the magnetic field from 0 to 5 T are shown. The results are for $Ni_{2-x}(Fe/Co)_xMn_{1+z-y}Cu_ySb_{1-z}$, with $z = 0.52, x = 0.00, y = 0.00$.

a paramagnetic phase. With a decrease in temperature, the magnetic order parameter increases gradually, indicating the transformation from the paramagnetic to a ferromagnetic phase around 350 K. Thus, the magnetic transition temperature (T_c^A) in the austenite phase also matches very well with the experimental value. With a further decrease in temperature, near the T_M, a small kink, indicating a weak magneto-elastic coupling, is observed in the magnetic order parameter (m). With an applied external magnetic field of 5 T, T_M decreases, and the T_c^A increases in agreement with the experimental trend.

The calculated magnetic specific heat (C_{mag}) is shown in Fig. 6.7(b). The total specific heat is also calculated as a function of temperature by calculating the lattice specific heat (C_{lat}). In absence of experimental result on this compound, the Debye temperature Θ_D was taken as 222 K, the experimental Θ_D of Ni_2MnSb [320]. Here, we assumed that the lattice specific heat does not contribute significantly to the isothermal entropy change, i.e., there is no significant impact of the application of magnetic field on C_{lat}. The isothermal entropy change, from lattice contributions across the magneto-structural transition, is not significant as long as the Debye temperature does not depend strongly on the magnetization and magnetic field. Two peaks can be observed in the specific heat curves, one at higher temperature corresponds to the second-order magnetic transition from paramagnetic to ferromagnetic phase, while the other at lower temperature corresponds to the structural transformation from austenite to martensite phases.

The magnetic entropy curve (in Fig. 6.7(d)) has been obtained by integrating the magnetic specific heat curves both at zero field and a field of 5 T. At very low temperatures, the calculated entropy has lower values, as expected, and increases with an increase in temperature, saturating at high temperatures beyond the magnetic transformation in the austenite phase. Upon application of the external magnetic field, the entropy of the system decreases as the system undergoes the magnetic transformation, while the entropy increases at the structural transformation. The insets of Fig. 6.7(d) show the changes in the entropy of the system when the structural (inset with lower temperature range) and magnetic (inset with higher temperature range) transformations take place.

The magnetic field induced isothermal entropy change, ΔS_{mag} and the adiabatic temperature change ΔT_{ad} are shown in Fig. 6.7(e) and Fig. 6.7(f) respectively. The maximum change in entropy is positive for structural transformation and negative for the magnetic transformation. Hence, we have an inverse magnetocaloric effect (cooling of the material in the presence of magnetic field) during structural

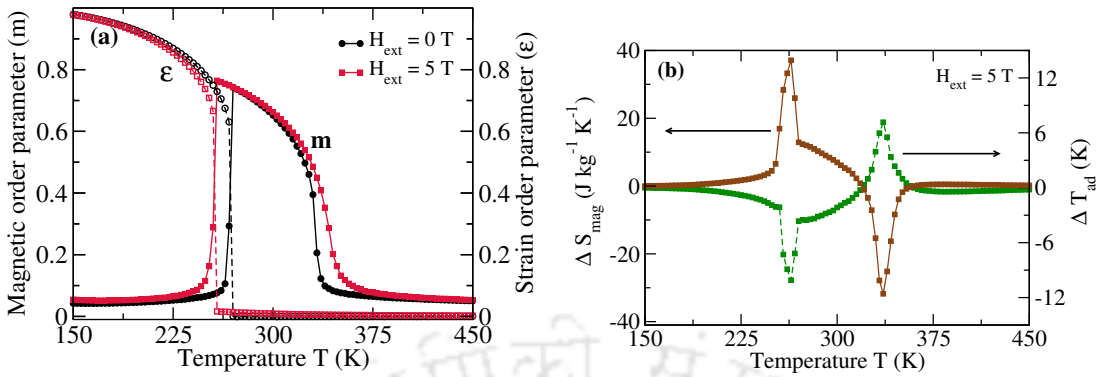

Figure 6.8: The calculated temperature dependence of (a) magnetic (m) and strain (ε) order parameter in an external field of 0 and 5 T and (b) the isothermal magnetic entropy change (ΔS_{mag}) and adiabatic temperature change (ΔT_{ad}) due to change in the magnetic field from 0 to 5 T in $Ni_{2-x}Co_xMn_{1+z-y}Cu_ySb_{1-z}$; $z = 0.52, x = 0.20, y = 0.00$.

transformation, while regular magnetocaloric effect (heating of the material in the presence of magnetic field) as the magnetic transformation takes place. A maximum value of isothermal entropy change of 9.8 $J\,kg^{-1}\,K^{-1}$ is obtained at the first order magneto-structural transition, in good agreement with the experimental observation [132, 135]. Our calculations predict a large value of nearly 5 K of ΔT_{ad} which, however, could not be compared with experiments due to the unavailability.

We next applied the same formalism to the Co substituted compound $Ni_{1.8}Co_{0.2}Mn_{1.52}Sb_{0.48}$. Due to the availability of experimental results [135], we could make a direct comparison. The results are shown in Fig. 6.8. The *ab initio* magnetic exchange parameters used here are shown in Fig. 6.6(c)-6.6(d). In here, the number of spin states for Co was taken to be q_{Co}=4. The parameters in the Hamiltonian were adjusted, such that the experimental value of T_M ($\approx$ 260 K) and T_c^A ($\approx$ 330 K) could be reproduced. This is evident from the curves of m and ε in Fig. 6.8(a).

The parameters used for this calculation are listed in Table 6.3. The directions of shifts in T_M and T_c^A under application of an external magnetic field of 5 T are in agreement with the experimental trends. One noteworthy point is that in contrast to the $Ni_2Mn_{1.52}Sb_{0.48}$, magnetization changes sharply at the structural transition in this case. This is important to obtain a giant MCE. This significant change in magnetization can be understood by analyzing the magnetic exchange interactions between different atom pairs in both structural phases (Fig. 6.6(c) and Fig. 6.6(d)). While for both $Ni_2Mn_{1.52}Sb_{0.48}$ and $Ni_{1.8}Co_{0.2}Mn_{1.52}Sb_{0.48}$, the dominant antiferromagnetic interaction between Mn atoms are four times larger in the tetragonal phase, in comparison to that in the austenite phase, larger ferromagnetic interactions due to the Mn1(Mn2)-Co atom pairs in the austenite phase appears for the

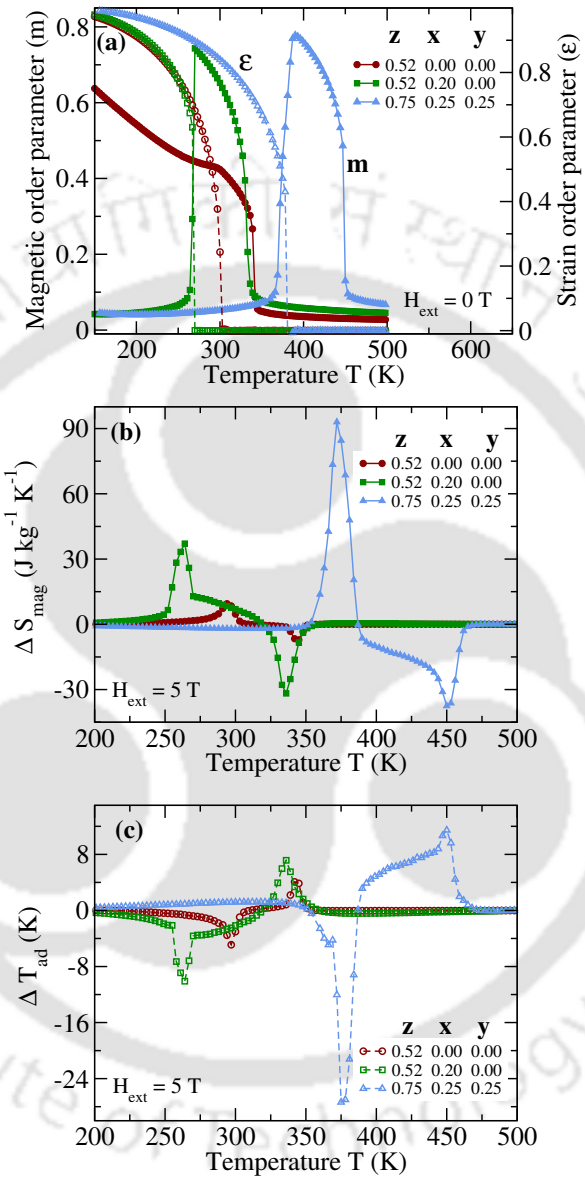

Figure 6.9: The calculated temperature dependence of (a) magnetic (m) and strain (ε) order parameter in absence of an external field, (b) the isothermal magnetic entropy change (ΔS_{mag}) and (c) adiabatic temperature change (ΔT_{ad}) due to change in the magnetic field from 0 to 5 T in $Ni_{2-x}Co_xMn_{1+z-y}Cu_ySb_{1-z}$; $z = 0.75, x = 0.25, y = 0.25$. Results for the reference compositions, $Ni_2Mn_{1.52}Sb_{0.48}$ and $Ni_{1.8}Co_{0.2}Mn_{1.52}Sb_{0.48}$ have also been included for comparison.

later compound. This can be correlated to the larger change in the magnetization for Co substituted compound. The MCE quantities ΔS_{mag} and ΔT_{ad}, calculated as a function of temperature, as shown in Fig. 6.8(b) and the maximum ΔS_{mag} of nearly 40 $\mathrm{J\,kg^{-1}\,K^{-1}}$, much larger than the $Ni_2Mn_{1.52}Sb_{0.48}$, is obtained due to the magneto-structural transition near T_M in an applied field of 5 T. This is in excellent agreement with the experimental value [135] of 35 $\mathrm{J\,kg^{-1}\,K^{-1}}$. We also obtained a large value of ΔT_{ad} that could not be verified in absence of experimental results.

The excellent agreement of the results obtained for the two compounds with the experimental observations validates the approach adopted here for computing the variables quantifying MCE. Therefore, we apply the same formalism for the cosubstituted compound $Ni_{1.75}Co_{0.25}Mn_{1.50}Cu_{0.25}Sb_{0.25}$. The results are presented in Fig. 6.9. The *ab initio* calculated exchange interactions used are shown in Fig. 6.6(e) and Fig. 6.6(f). The values of elastic and magneto-elastic parameters were tuned (Table 6.3) to fix the T_M at 398 K, as predicted in subsection 6.3.4, and T_c^A at 460 K as calculated through MCS in Table 6.2. For the purpose of comparison, we have included the results for $Ni_2Mn_{1.52}Sb_{0.48}$ and $Ni_{1.8}Co_{0.2}Mn_{1.52}Sb_{0.48}$. We find that cosubstitution leads to an increase in the working temperature (T_M). Also, the change in magnetization near MPT is larger (Fig. 6.9(a)). Both these characteristics were desired for a larger MCE in cosubstituted compounds. The calculated MCE quantities (Fig. 6.9(b) and 6.9(c)) meet this expectation. The results demonstrate that ΔS_{mag} four times higher than $Ni_2Mn_{1.52}Sb_{0.48}$ and two times higher than the $Ni_{1.8}Co_{0.2}Mn_{1.52}Sb_{0.48}$ are obtained. Stronger ferromagnetic interactions in the austenite phase of cosubstituted compound (Fig. 6.6(e)-6.6(f)), in comparison with the other two compounds, can be correlated to this amplified effect.

6.4 Conclusions

Using first-principles electronic structure calculations, we provide a protocol to systematically screen materials, potential to exhibit giant MCE driven by a first-order magneto-structural transition at temperatures near room temperature or above, among given Heusler family of compounds. We apply this approach to find target compounds in cosubstituted Ni-Mn-Sb family; the cosubstitution done at Ni and Mn sites. Our approach predicted four new compounds in the two cosubstituted families. In order to validate our predictions, we took recourse to a thermodynamic model to compute the MCE properties in one of these predicted compounds. The robustness and accuracy of the computational approach using the thermodynamic

model that takes into account magnetic, elastic and magneto-elastic effects in equal footing, is demonstrated by computing the MCE parameters in $Ni_2Mn_{1.52}Sb_{0.48}$ and Co substituted $Ni_{1.8}Co_{0.2}Mn_{1.52}Sb_{0.48}$ compounds where experimental results are available. Further computation of MCE parameters for one of the predicted compounds yields magnetic entropy change as large as four times in comparison to that observed experimentally. Thus, this established the protocol for screening materials from a large database adopted in this work. This work, apart from demonstrating the power of *ab initio* based approaches for computations of MCE parameters, offers experimentalists a broader scope to explore new materials where giant MCE driven by first-order magneto-elastic transition can be realized through cosubstitution in Heusler compounds.

Chapter 7

Conclusions and scopes for future work

7.1 Conclusions

The focus of this thesis is a detailed understanding of various important physical parameters related to the magnetocaloric effect, as well as on predicting the possibility of realizing efficient MCE in some new compounds in Ni-Mn-Sb based Heusler systems. In recent years, magnetocaloric effect, which is the driving force for magnetic refrigeration technology, led to intensive research due to its superiority over conventional gas refrigeration technology. Our investigation is mainly focused on off-stoichiometric Ni-Mn-Sb and 3d elements (Fe, Co and Cu) substituted Mn-excess Ni-Mn-Sb compounds. In brief, we have systematically explored the impacts of various factors, such as structural phase stability, site occupancy, magnetic structure, composition, magnetic interactions, mechanical properties, transition temperatures, on the magnetocaloric effect in a system, by first-principles electronic structure and Monte Carlo methods. We have developed a Monte Carlo code to calculate the MCE parameters i.e., the isothermal magnetic entropy change (ΔS_{mag}) and the adiabatic temperature change (ΔT_{ad}) and thus proposed some new compounds in Fe, Co and Cu substituted Mn-excess Ni-Mn-Sb Heusler alloys where significant magnetocaloric effect can be realized.

In the first chapter, the underlying concept of thermodynamics of caloric effect with a focus on magnetocaloric effect, its important applications and related research have been described. This is followed by a discussion on the usefulness of Heusler compunds as MCE materials. Importance of Ni-Mn based Heusler compounds have

been discussed in detail to set the ground for motivation behind the systems studied here. The importance of the theoretical approach, a combination of first-principles calculations and Monte Carlo simulations, adopted here, has also been reviewed.

In the next chapter, the theoretical methods that have been used in this thesis are discussed. A brief introduction of density functional theory (DFT) and its different implementations are first presented. Then Monte Carlo method, the model Hamiltonians to compute the finite temperature magnetic and magneto-structural properties, e.g., the Curie temperature (T_c) and the magnetocaloric quantities i.e., the isothermal change in magnetic entropy (ΔS_{mag}) and the adiabatic temperature change (ΔT_{ad}), are discussed.

In chapter 3, we have performed a comprehensive and systematic investigation into the roles of composition, site occupancies and magnetic configurations in affecting the structural stabilities or the possibility of martensitic phase transformation, that is observed to be leading to a giant change in magnetic entropy, in Ni and Mn-excess Ni_2MnSb compositions. We find that the site occupancy pattern and associated magnetic alignment of Mn atoms play the central role in de-stabilizing the high temperature Heusler phase and consequently stabilizing a tetragonal martensite at low temperature. We find that unless the system is significantly Sb-deficient, a martensitic phase transformation is difficult to obtain, unless the system stays in a meta-stable state due to the process of annealing or is grown by non-equilibrium methods. The patterns in phase stability, as obtained from our total energy calculations, can be understood from the features in the densities of states in the minority spin bands. Shear modulus (C') and electron to atom ratio (e/a) both turn out to be good predictors of structural transition temperature in Ni-Mn-Sb. This work helps understand the reason behind experimentalists choice of Mn-excess Sb-deficient systems for observing giant magnetocaloric effect in Ni-Mn-Sb Heusler family. An important outcome of this work is the identification of $Ni_{2+x}MnSb_{1-x}$ as a potential new shape memory alloy where the martensitic transformation takes place even at high Sb composition. This input widens the scope of the experimentalists to explore functional properties in Ni-Mn-Sb systems.

In chapter 4, we have explored the potentials of Mn-excess, Sb-deficient Ni_2MnSb compounds, as efficient magnetocaloric materials by substitution of Ni and Mn with $3d$ transition metals Fe, Co, and Cu. Apart from being able to explain the trends

of variations in quantities like magnetic moments, the martensitic transformation temperature and magnetic transition temperature, observed in handful of experiments on this system, we have provided insights into the possibilities of significant magnetocaloric effects in this group of compounds $Ni_2Mn_{1.5-y}Co_ySb_{0.5}$ and $Ni_2Mn_{1.5-y}Cu_ySb_{0.5}$; $y \sim 0.25$, the ones which are yet to be synthesized. Thus our investigation unveiled the physics behind the variations of physical properties associated with the magnetocaloric effect and also interpreted the available experimental results successfully. The structural stabilities and possibility of significant magnetocaloric effect in these systems are correlated to the magnetic exchange interactions and their variations. The approach adopted and knowledge obtained from this work can be used to investigate a wider pool of materials, boosting the possibility of discovering more materials with large MCE.

Armed with the information from chapter 3 and chapter 4, in chapter 5, we explored potential room temperature magnetocaloric materials near second-order magnetic transition by cosubstitution in the Ni-Mn-Sb family. Our investigation on two cosubstituted families, $Ni_{2-x}Fe_xMn_{1+z-y}Cu_ySb_{1-z}$ and $Ni_{2-x}Co_xMn_{1+z-y}Cu_ySb_{1-z}$ with the composition range $0 \leq x \leq 1.5$, $0.25 \leq z \leq 0.75$, $y \leq z$ discovered significant numbers of compounds exhibiting substantial changes in magnetic entropy due to second-order magnetic phase transition near room temperature, the changes comparable to that observed in the compounds showing inverse magnetocaloric effect near a first-order magneto-structural transition. We find that the cosubstitution provides a wider scope of tuning the physical parameters like magnetic moment and magnetic transition temperature as well as of stabilization of the Heusler phase down to very low temperatures. The work, thus, offers a broader scope of synthesis and exploration of large reversible MCE near room temperature by cosubstitution in other compounds of the Heusler family.

In the next chapter, we have extended our investigations on the two cosubstituted families, $Ni_{2-x}Fe_xMn_{1+z-y}Cu_ySb_{1-z}$ and $Ni_{2-x}Co_xMn_{1+z-y}Cu_ySb_{1-z}$ further to realize giant magnetocaloric effect driven by the first-order magneto-structural transition. We focussed on the concentration range complementary to the ones used in chapter 5. With help of the full thermodynamic study, using the techniques employed in chapter 5, we predict four new compounds with potentials to achieve the target properties. Our computations of the thermodynamic parameters, relevant for magnetocaloric applications, show that the improvement in the parameters in the

predicted cosubstituted compounds can be as large as four times in comparison to the off-stoichiometric Ni-Mn-Sb and a compound derived by single substitution of Co at the Ni site. This work establishes a protocol to select new compounds that can exhibit giant magnetocaloric effects and demonstrate cosubstitution as a route for more flexible tuneability to achieve outcomes, better than the existing ones.

7.2 Scopes for future work

In this dissertation, we have systematically explored various factors that can influence the magnetocaloric effect in a system. In the process, we have been able to offer microscopic interpretations of the experimental results. We have also developed a Monte Carlo method based code to realize the simultaneous presence of a first-order structural transition coupled with a magnetization change and a second-order magnetic phase transition and to calculate the MCE parameters. However, different possible future extensions of the work presented in the thesis have been left. In the following, some future research plans are listed:

An important property related to the magnetocaloric effect in a system is the magnetocrystalline anisotropy in the martensite phase. In Ni_2MnGa, it is observed that greater the magnetic anisotropy in the martensite phase, larger is the value of the inverse magnetocaloric effect. Thus it would be interesting to investigate in detail the interrelation between the magnetocrystalline anisotropy and the MCE in a system.

The in-house Monte Carlo code deals with Heulser families. A further generalization of the code is needed to explore other groups of magnetocaloric materials.

The Hamiltonian used in the Monte Carlo code includes structural, magnetic, and magneto-structural coupling interaction parameters. The magnetic interaction parameters are calculated from *ab initio* methods, while the structural and coupling parameters are tuned in the simulation process to achieve the experimental martensitic transformation temperature. If the martensitic transformation temperature is calculated through a free energy approach or can be estimated using machine learning techniques, then new magnetocaloric systems can be designed with more accuracy without any prior knowledge from experiments.

Appendix A

Benchmarking the In-house Monte Carlo Code

A.1 Calculation of second order magnetic transition temperature (T_c) within Heisenberg model

A.1.1 Ni_2MnGa and Mn_2NiGa

We have developed the Monte Carlo method based code implementing the Heisenberg Model (as mentioned in chapter 2); the parameters are obtained from *ab initio* calculations. We have first applied the code to two very well studied magnetic Heusler systems: Ni_2MnGa (space group no. 225) and Mn_2NiGa (space group no. 216). The magnetic exchange interactions (J_{ij}) calculated by *ab initio* method have been shown for Ni_2MnGa and Mn_2NiGa in Fig. A.1(a) and Fig. A.1(c), respectively. Using these parameters in the model Hamiltonian, the systems were simulated at finite temperatures. The temperature dependent behavior of magnetization is shown in Fig. A.1(b) and Fig. A.1(d), respectively. The steps followed in the Monte Carlo simulation have been discussed in chapter 2. Curie temperatures from the susceptibility curves are found to be 370 K for Ni_2MnGa and 630 K for Mn_2NiGa, which are in good agreement with the experimental results (360 K for Ni_2MnGa and 588 K for Mn_2NiGa) [321–323]. At each temperature, 80000 Monte Carlo steps have been performed to equilibrate the systems containing 8192 atoms.

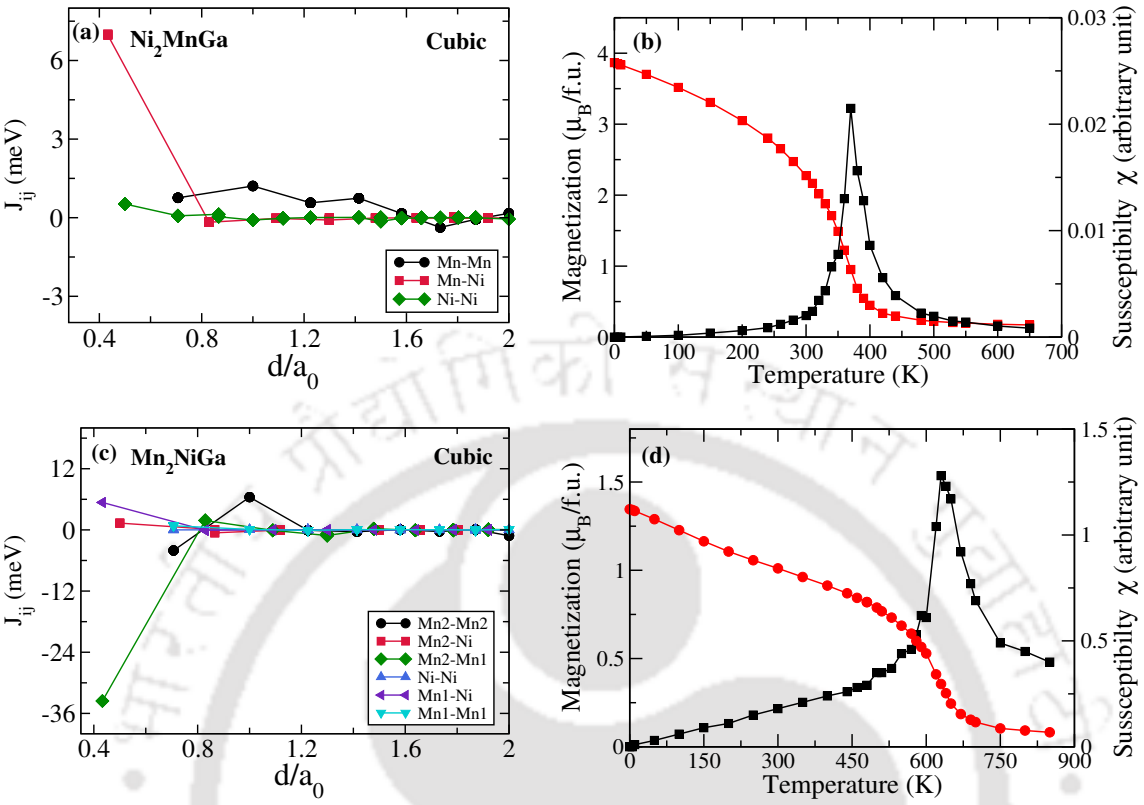

Figure A.1: ((a) and (c)): The calculated magnetic exchange parameters as a function of distance d between two atom pairs (in units of lattice constant a_0). ((b) and (d)): Magnetization and susceptibility curves as a function of temperature in zero magnetic field for Ni_2MnGa and Mn_2NiGa, respectively. Calculations are done using the Heisenberg Model for magnetic interactions.

A.1.2 $Ni_2Mn_{1+x}Sn_{1-x}$

Next, we extend our calculations for more complex compositions like off-stoichiometric $Ni_2Mn_{1+x}Sn_{1-x}$ system (x varies from 0 to 0.4), where the Ni atoms occupy the 8c((0.25, 0.25, 0.25), (0.75, 0.75, 0.75)) sites, Mn and Sn atoms occupy 4b(0.5, 0.5, 0.5) (referred as MnI) and 4a(0, 0, 0) sites respectively in the Heusler lattice. The excess Mn atoms occupy the Sn sublattice (referred as MnII). With this site occupancy of the constituent atoms, the system is referred to as 0% disordered. y% disordered system refers to the composition $(Sn_{1-x-y}MnII_{y+x})Ni(MnI_{1-y}Sn_y)Ni$, that is, Sn with concentration y occupies the MnI sublattice. We calculated the magnetic exchange parameters in *ab initio* way and used them in the Mone Carlo simulation, to obtain the magnetization curves for different x values for $y = 0$ and $y = 25\%$ (Fig. A.2(a) and A.2(b) respectively). Then from the magnetization curves we have calculated the Curie temperatures for both 0% and 25% disordered systems and compared those with the existing numerical [223] and experimental results [324] as

shown in Fig. A.3.

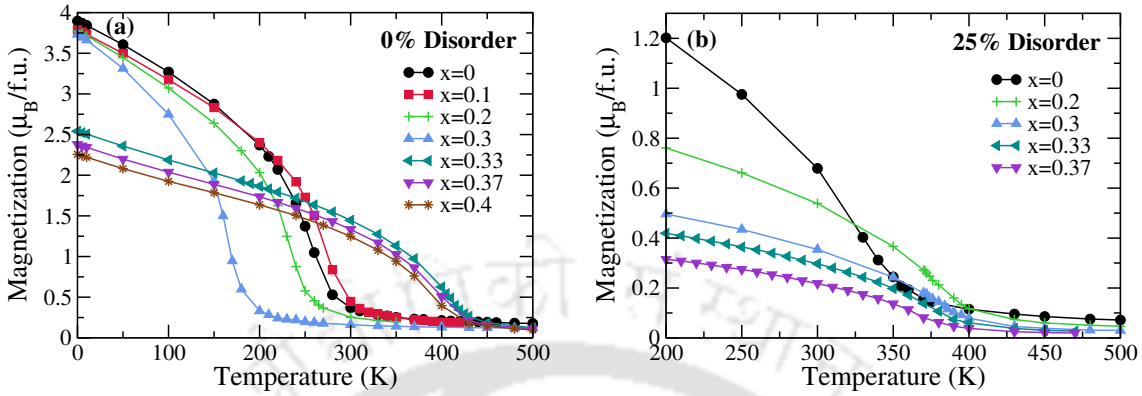

Figure A.2: Magnetization curves as a function of temperature in zero magnetic field for $Ni_2Mn_{1+x}Sn_{1-x}$ (x varies from 0 to 0.4) with (a) 0% disorder and (b) 25% disorder.

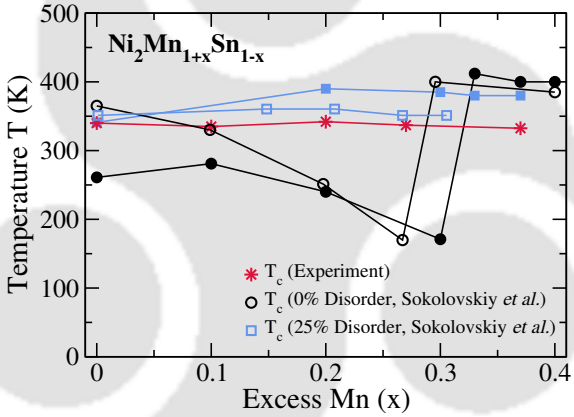

Figure A.3: Experimental [324] (T, x) phase diagram of $Ni_2Mn_{1+x}Sn_{1-x}$ to which the present calculated (filled symbols) and existing MC simulated results [223] (open symbols) have been added.

Our observed trends for Curie temperatures agree well with the previous existing numerical results, both qualitatively and quantitatively. From Fig. A.3, it can also be seen that the trend of experimental Curie temperatures matches with our results only when the effect of disorder is considered.

A.1.3 Fe/Co substituted Mn_2NiGa

Next, we study the composition dependencies of Curie temperatures for two systems: Fe and Co substituted Mn_2NiGa [229]. Experimental results are available for these systems. Fe and Co have been substituted at different crystallographic sites and we have considered four different concentrations 25%, 50%, 75% and 100%. Site

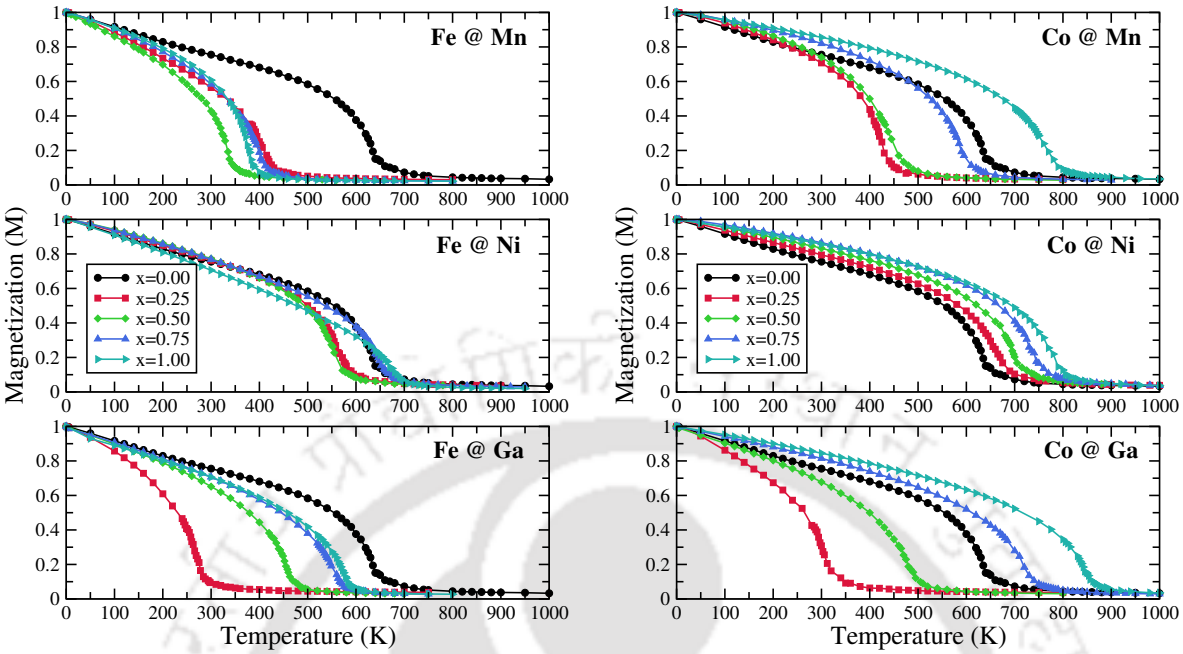

Figure A.4: Magnetization curves as a function of temperature in zero magnetic field for Fe and Co substituted Mn_2NiGa alloys with different concentration of the substituent atoms. X@Y denotes that X(X=Fe, Co) atom substitutes Y(Y=Mn, Ni, Ga) atom.

preference of the substituted atoms has been taken care in the calculation as the site occupancies have an important impact on the magnetic properties of the system. At high temperature, Mn_2NiGa crystallizes in the Hg_2CuTi (inverse Heusler) structure with four inequivalent Wyckoff positions (4a, 4b, 4c, 4d) in a fcc unit cell. Mn atoms occupying the 4a(0,0,0) and 4c(0.25, 0.25, 0.25) Wyckoff positions are denoted as MnI and MnII respectively. The 4b(0.5, 0.5, 0.5) and 4d(0.75, 0.75, 0.75) positions are occupied by Ni and Ga, respectively. It was observed that for substitution of Fe and Co at the Mn site, the substituted atoms prefer the MnI sites. Substitution at Ni site also show the normal site occupancy. The substitution at the Ga site, however, follows a different pattern, depending on the substituting element. The abnormal site occupancies are preferable for Fe and Co substitution at Ga sites in Mn_2NiGa which means that Fe/Co prefers to occupy the MnI sites pushing the remaining MnI atoms to Ga sites (henceforth denoted as MnIII). In Fig. A.4 and Fig. A.5, we show the composition dependencies of magnetization and Curies temperatures (T_c), respectively, for Fe and Co substituted Mn_2NiGa.

The MCS results are found to be close to experimental results for a variety of systems. The available experimental results in these compounds are included in fig. A.5. From the MCS results, we find that all the end compounds obtained by complete substitution of Fe or Co in any of the sites have very high T_c, the largest being close

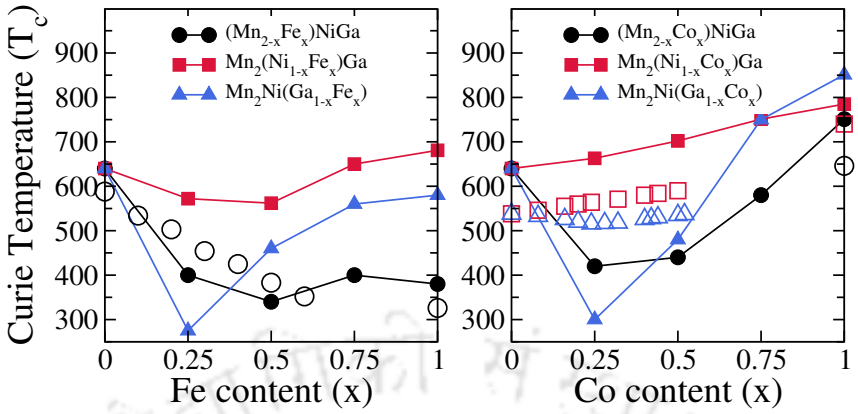

Figure A.5: Calculated Curie temperatures as a function of substituent (a) Fe concentration and (b) Co concentration for substitution at different sites in Mn_2NiGa. Open symbols represent the experimental results which are adopted from Refs. [325–328].

to 900 K for Mn_2NiCo. The qualitative variation of T_c for $Mn_2(Ni_{1-x}Co_x)Ga$ agrees well with the experiment [325, 326], although the MCS results are a little overestimated. The quantitative agreement between the MCS results and the experimental results [327, 328] for $(Mn_{2-x}Fe_x)NiGa$ is better. There is a significant disagreement, both qualitatively and quantitatively, for $Mn_2Ni(Ga_{1-x}Co_x)$ systems. The MCS calculations show a sharp decrease in T_c for 25% Co substitution after which the T_c rises sharply with increase in x. In case of the experiment [325], the change is very nominal. It may be noted that the T_c reported in Ref. [325] is lower by 50 K in comparison to T_c obtained from other experiments [322, 327]. Such discrepancies may be due to antisite disorder or off-stoichiometric compositions present in the samples used by the authors of Ref. [325]. Nevertheless, the agreement between the MCS results and the experiments for the end compounds, wherever available, is remarkable.

A.2 Calculation of MCE parameters for $Ni_2Mn_{1.4}In_{0.6}$ near second-order magnetic transition

In order to calculate magnetocaloric quantity, the isothermal change in magnetic entropy (ΔS_{mag}) as a function of temperature, Monte Carlo simulation is employed on a q-state Potts model Hamiltonian in presence of an external magnetic field (discussed in chapter 2). We calculated the isothermal magnetic entropy change for $Ni_2Mn_{1.4}In_{0.6}$ system, experimentally investigated by Singh *et al.* [308]. To this end, we have first calculated the *ab initio* magnetic exchange parameters (J_{ij}) con-

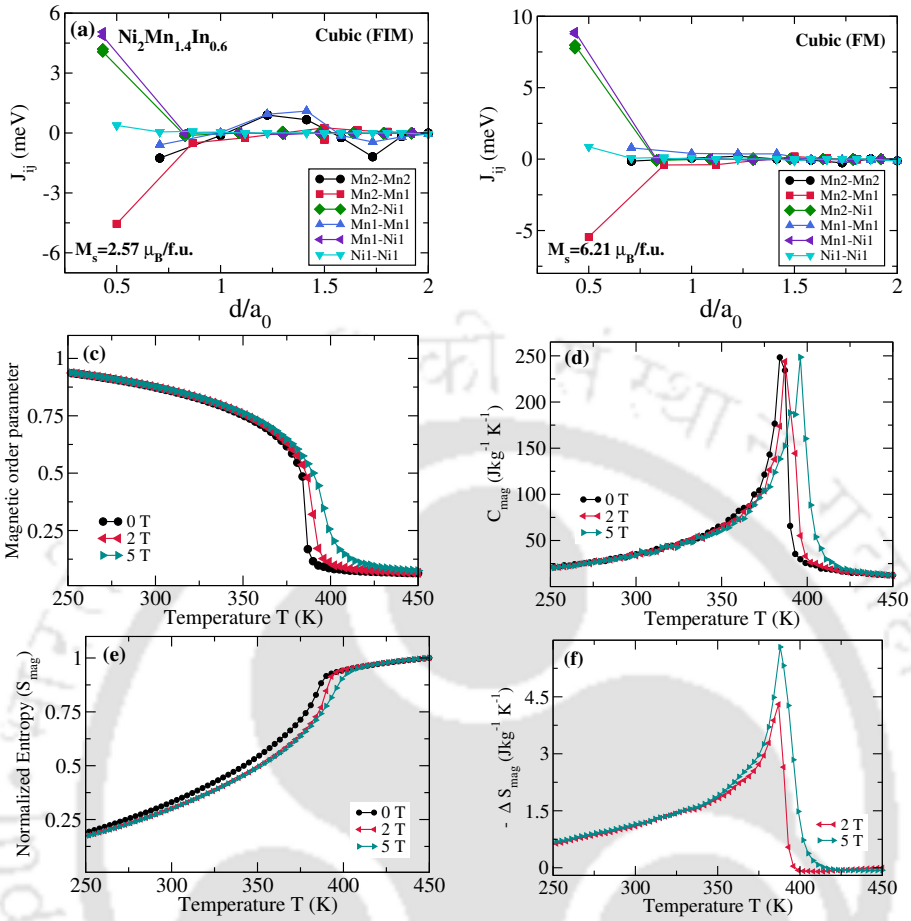

Figure A.6: The calculated ((a)-(b)) magnetic exchange parameters in FIM and FM magnetic configurations (c) temperature dependence of magnetic order parameter (d) magnetic specific heat (C_{mag}) (e) normalized magnetic entropy (S_{mag}) in an external field of 0, 2 T and 5 T, (f) temperature variation in the isothermal magnetic entropy change (ΔS_{mag}) due to change in the magnetic field from 0 to 2 T and 5 T in $Ni_2Mn_{1.4}In_{0.6}$, to compare with the experimental observation [308].

sidering two magnetic configurations: (i) ferrimagnetic (FIM), where the Mn spins at different sites align antiparallel and (ii) ferromagnetic (FM) configuration, where the Mn spins at different sites align parallel. Calculated J_{ij}s for both of them are shown in Figure A.6(a) and A.6(b). We find that the saturation magnetization (M_s) has a larger value of 6.21 $\mu_B/f.u.$ in FM configuration compared to that in the FIM configuration, in agreement with the large magnetization value observed in experiment. Using the magnetic exchange parameters (J_{ij}) obtained with FM configuration, we then calculate the Curie temperature through Monte Carlo simulation on the Heisenberg model. The calculated T_c comes out to be about 380 K, a little higher than the experimental value of 315 K, still reasonable for further consideration. Next, Monte Carlo simulation is done on the Potts model, for cal-

culation of temperature dependent magnetization. The result is shown in Figure A.6(c). For this calculation, we have used a simulation cell containing 8192 atoms and performed 80000 Monte Carlo steps to attain equilibrium at each temperature. We have used three and five spin states for Ni and Mn, respectively. To adjust the exchange interactions within a reasonable and computationally tractable number of coordination shells, we have used the Curie temperature, calculated using the Heisenberg model, as reference. These are done in absence of an external field i.e. H_{ext}=0. Then, for different applied external fields (here 2 T and 5 T), we have simulated the system at different temperatures, and from those we have calculated the magnetic specific heat (C_{mag}) as a function of temperature in 0, 2 T and 5 T external field. The results are shown in Figure A.6(d). Finally, normalized magnetic entropy as a function of temperature, (shown in Figure A.6(e)) is calculated and used further to calculate isothermal changes in magnetic entropy values in presence of an external field (shown in Figure A.6(f)). The calculated maximum ΔS_{mag} values, -4.3 $\mathrm{J\,kg^{-1}\,K^{-1}}$ and -5.81 $\mathrm{J\,kg^{-1}\,K^{-1}}$ in an applied field of 2 T and 5 T around T_c=388 K are in good agreement with the experimental observations [308] of -3.3 $\mathrm{J\,kg^{-1}\,K^{-1}}$ and -6.3 $\mathrm{J\,kg^{-1}\,K^{-1}}$ in 2 T and 5 T respectively. The agreement between theory and experiment, thus, validate our approach.

A.3 Calculation of MCE parameters near first-order magneto-structural transition

The giant magnetocaloric effect in Heusler compounds is associated with the first order magneto-structural transition. The simultaneous presence of second order magnetic transition is also observed in these systems. Hence to address both the transitions, in addition to the q-state Potts model, the Blume-Emery-Griffiths (BEG) model has been incorporated in the Monte Carlo code. This implementation allows simultaneous structural and magnetic transformations, as described in details in chapter 2.

With the in-house Monte Carlo code, we have first studied the temperature dependence of the magnetic and strain order parameters for three different Heusler systems: (i) $Ni_2Mn_{1.36}In_{0.64}$ (ii) $Ni_{2.18}Mn_{0.82}Ga$ and (iii) $Ni_2Mn_{0.75}Cu_{0.25}Ga$. The systems are chosen as results on them are available in literature. In the simulations, the simulation domain consists of 8192 atoms and for each temperature 10^5 MCS steps have been considered. The system has been equilibrated for first 60000 MCS.

Finally, the system energy (H), magnetic order parameter (m) and strain order parameter (ε) have been averaged over the last 40000 steps.

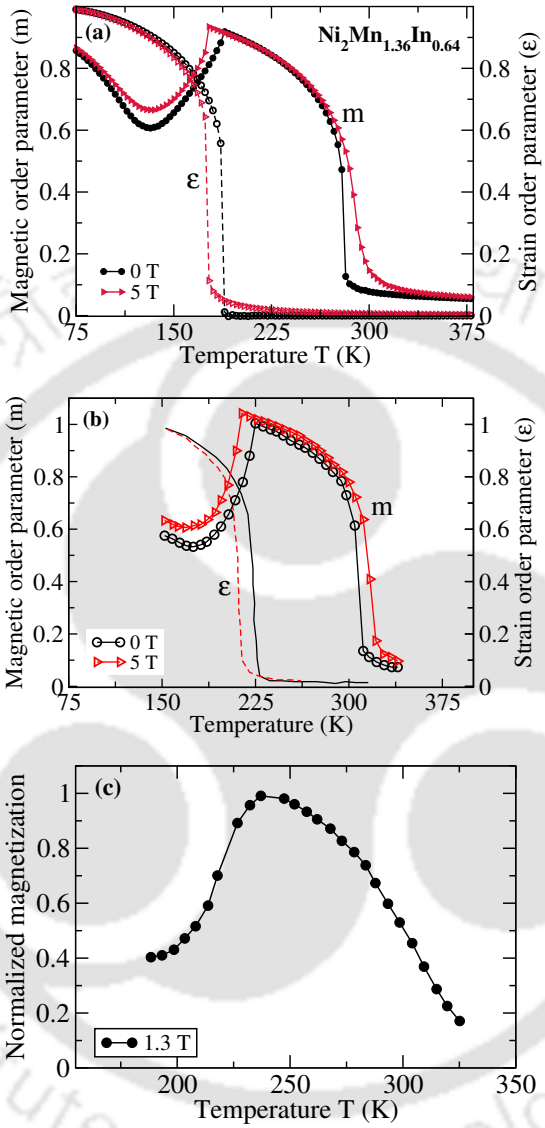

Figure A.7: The calculated temperature dependence of (a) magnetic order parameter(m) and strain order parameter(ε) in external magnetic field of 0 T and 5 T for $Ni_2Mn_{1.36}In_{0.64}$. Existing results from numerical simulation [108] and experimental [296] are shown in (b) and (c) respectively.

The temperature dependence of the magnetic and strain order parameters for $Ni_2Mn_{1.36}In_{0.64}$ in both absence and presence of external magnetic field have been shown in Fig. A.7(a). The existing numerical [108] as well as available experimental [296] results are shown in Fig. A.7(b) and Fig. A.7(c). In Fig. A.7(a), in absence of external magnetic field we observe two phase transitions, the PM-FM transition in austenite phase at ($T_c^A \approx$)290 K and the magneto-structural transition from FM

cubic state to mixed AFM-FM tetragonal phase at ($T_M \approx$)180 K. The behavior of the strain order parameter (ε) shows the onset of the structural phase transformation around 180 K. The calculated magnetization and distortion curves coincide in the phase transition region which points to a coupled magneto-structural phase transition. When an external magnetic field of 5 T is applied, T_M decreases, whereas T_c^A increases. All these observations are in very good agreement with the existing trends observed in numerical simulations [108] and experiment [296].

Next, we investigate the other two systems, $Ni_{2.18}Mn_{0.82}Ga$ and $Ni_2Mn_{0.75}Cu_{0.25}Ga$. The calculated magnetic and structural transition behaviors along with a comparison to the existing simulation results [111, 172] (in absence of external magnetic field) have been shown in Fig. A.8. Our results are in excellent agreement with the existing ones implying robustness and accuracy of our simulation.

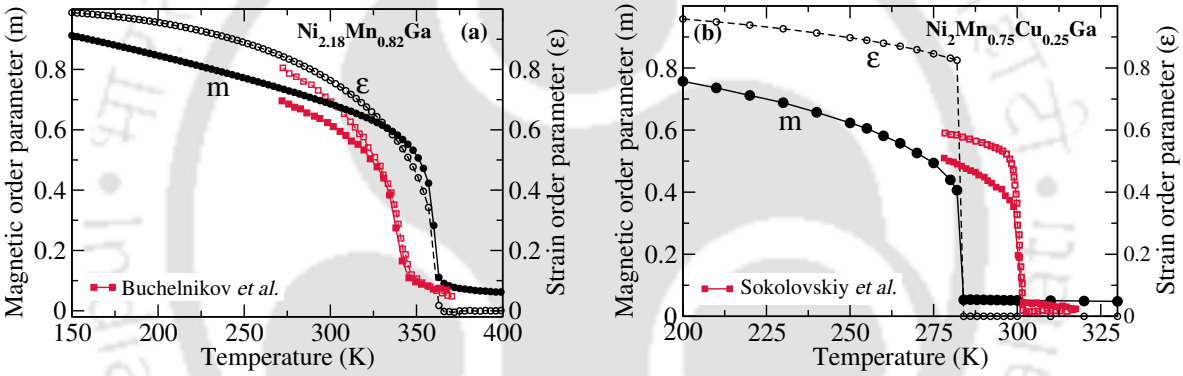

Figure A.8: The calculated temperature dependence of magnetic order parameter(m) and strain order parameter(ε) in absence of external magnetic field for (a) $Ni_{2.18}Mn_{0.82}Ga$ and (b) $Ni_2Mn_{0.75}Cu_{0.25}Ga$. The simulation results present in literature [111, 172] have also been included.

Final benchmarking is done by calculating the magnetocaloric parameters associated with the first-order magneto-structural transition. To this end, two systems, $Ni_{2.18}Mn_{0.82}Ga$ and Fe substituted Ni-Mn-Ga ($Ni_{2.104}Mn_{0.876}Ga_{0.968}Fe_{0.052}$) have been considered. The simulated results for the two systems are shown in Fig. A.9 and Fig. A.10. The tuned parameters used for the simulations in different considered systems are listed in Table A.1. The Monte Carlo calculations were done using a simulation domain consisting of 8192 atoms obtained by replicating the unit cell, containing 16 atoms, eight times in each direction. For each temperature step, 2×10^5 MC steps were performed. The systems were equilibrated for 10^5 MC steps, and the data, then, were collected for 10^5 steps. For each temperature step, energy of the system (H), magnetization (m), and structural distortion (ε) were averaged over 1000 data points collected after every 100 MC steps.

Table A.1: Values of structural, magneto-elastic and coupling parameters that are used in the present study for $Ni_{2.18}Mn_{0.82}Ga$ and $Ni_{2.104}Mn_{0.876}Ga_{0.968}Fe_{0.052}$ systems.

Systems	Parameters				
	J meV	K meV	U_c meV	U_t meV	$K1$
$Ni_{2.18}Mn_{0.82}Ga$	2.00	0.25	0.3	0.3	0.25
$Ni_{2.104}Mn_{0.876}Ga_{0.968}Fe_{0.052}$	2.01	0.4	0.3	0.3	-0.4

A.3.1 $Ni_{2.18}Mn_{0.82}Ga$

We first consider the $Ni_{2.18}Mn_{0.82}Ga$ system under three different fields 0 T, 1.85 T and 5 T. In absence of any external magnetic field, the strain order parameter (ε) shows the structural transformation from austenite (undistorted phase with $\varepsilon = 0$) to martensite phases (distorted phase with $\varepsilon = 1$) as temperature decreases (Fig. A.9(a)). The transformation occurs around 362 K. The magnetic order parameter (m) is almost zero at high temperatures indicating a paramagnetic phase. With a decrease in temperature, the magnetic order parameter increases gradually, indicating the transformation from the paramagnetic to a ferromagnetic phase around the same temperature as that of the structural transition. Thus for this system, a coinciding T_M and T_c^A is attainable, leading to the possibility of a giant magnetocaloric effect. Due to the application of external magnetic field of 1.85 T and 5 T, the transition temperature increases. The magnetic specific heat (C_{mag}) and total specific heat (C) were calculated then as a function of temperature. The magnetic entropy curve (in Fig. A.9(b)) has been obtained by integrating the magnetic specific heat curves using equations in chapter 2. At very low temperatures, the calculated entropy has lower values, as expected. It increases with an increase in temperature, leading to saturation at high temperatures. Upon application of the external magnetic field, the entropy of the system decreases. The magnetic field induced isothermal entropy change, ΔS_{mag} and the adiabatic temperature change ΔT_{ad} are shown in Fig. A.9(c) and Fig. A.9(d), respectively. A negative change in entropy for the magneto-structural transformation occurs and hence a regular magnetocaloric effect (heating of the material in the presence of magnetic field) takes place. The maximum values of isothermal entropy change of -13 $J\,kg^{-1}\,K^{-1}$ and -29 $J\,kg^{-1}\,K^{-1}$ in an external field of 1.85 T and 5 T are obtained around 364 K, in very good agreement with the experimental observation [111](Fig. A.9(e)). Our values are, however, higher than the existing simulated result in case of applied field of 5 T.

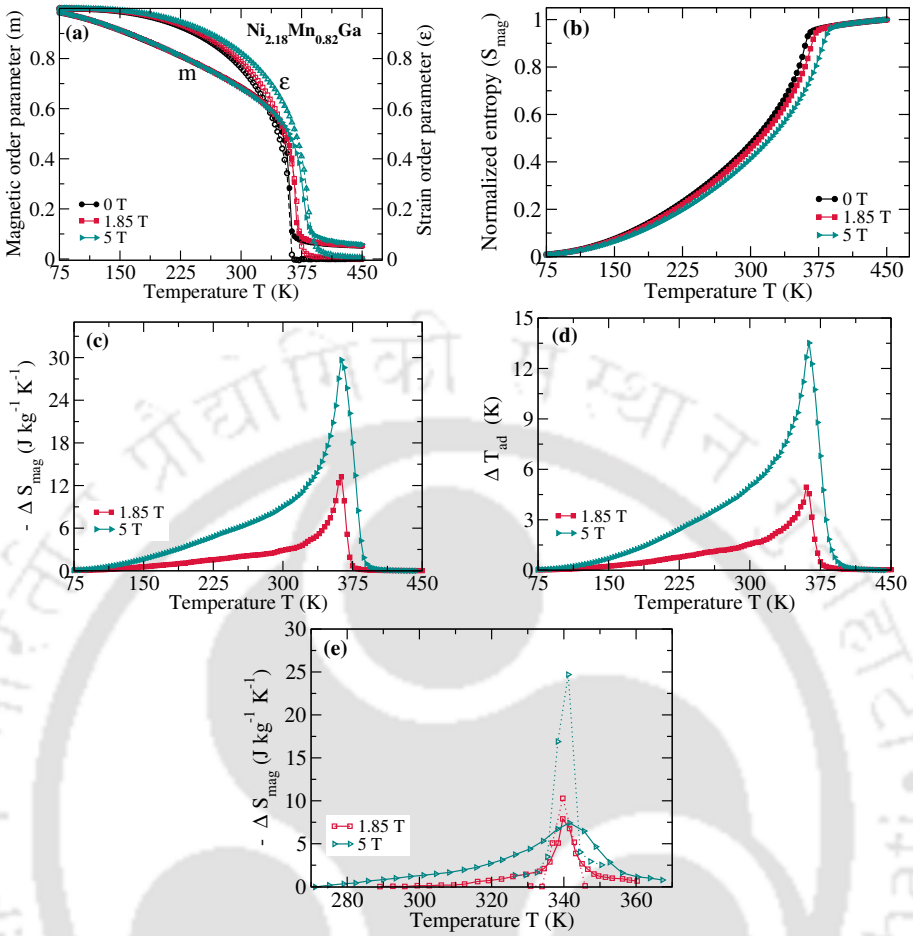

Figure A.9: The calculated temperature dependence of (a) magnetic (m) and strain (ε) order parameters, (b) normalized magnetic entropy (S_{mag}) in an external field of 0, 1.85 T and 5 T, (c) isothermal magnetic entropy change (ΔS_{mag}) and (d) adiabatic temperature change (ΔT_{ad}) due to change in the magnetic field from 0 to 1.85 T and 5 T for $Ni_{2.18}Mn_{0.82}Ga$ system are shown. The temperature dependent ΔS_{mag} observed in previous numerical (solid lines) and experimental (dotted lines) results [111] are presented in (e) for comparison.

A.3.2 Fe substituted off-stoichiometric Ni_2MnGa

Next, we consider the other system $Ni_{2.104}Mn_{0.876}Ga_{0.968}Fe_{0.052}$. In contrast to the $Ni_{2.18}Mn_{0.82}Ga$, the first-order magneto-structural transition and second order magnetic transition temperatures do not coincide for this system. Thus, both the inverse MCE associated with the magneto-structural transition and regular MCE due to the magnetic transition can be realized. Our results are shown in Fig. A.10. The maximum positive ΔS_{mag} of +2 $J\,mol^{-1}\,K^{-1}$ at (T_M=)322 K and -0.55 $J\,mol^{-1}\,K^{-1}$ at (T_c^A=)387 K (Fig. A.10(c)) associated with first-order magnetostructural transition and secon order magnetic transition, respectively, in an applied field of 2 T are in

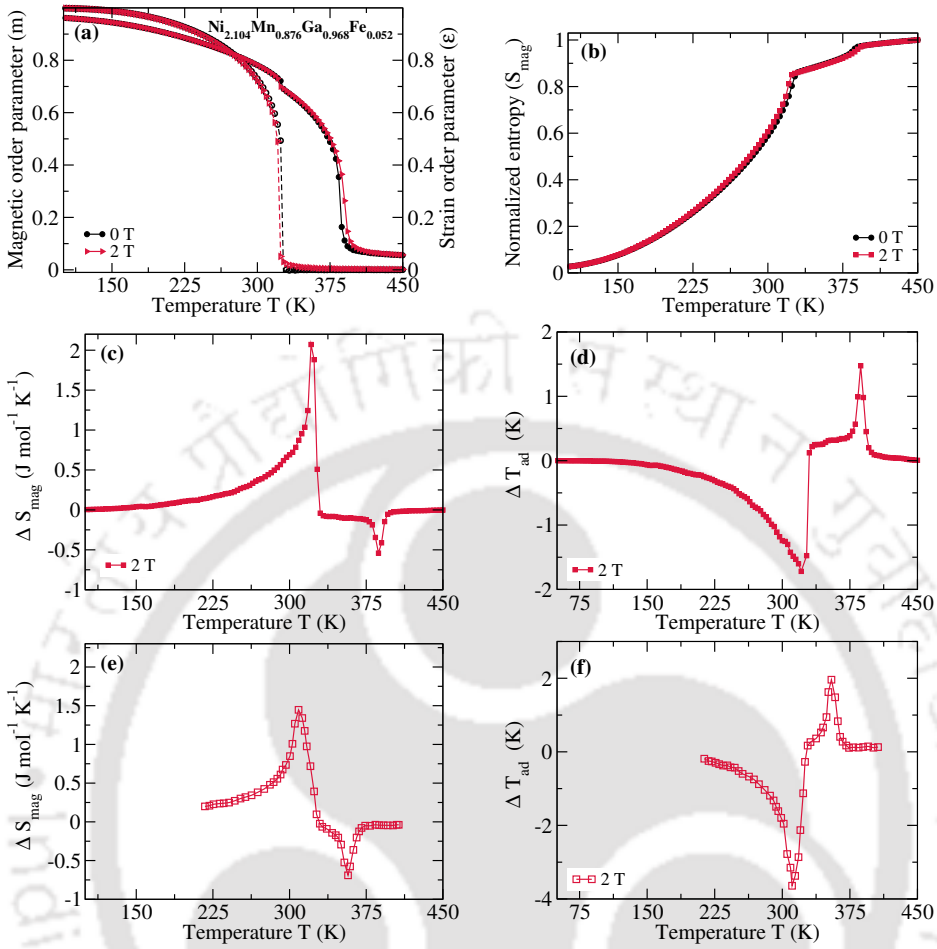

Figure A.10: The calculated temperature dependence of (a) magnetic (m) and strain (ε) order parameters, (b) normalized magnetic entropy (S_{mag}) in an external field of 0 and 2 T, and the temperature dependence of the (c) isothermal magnetic entropy change (ΔS_{mag}) and (d) adiabatic temperature change (ΔT_{ad}) due to change in the magnetic field from 0 to 2 T for $Ni_{2.104}Mn_{0.876}Ga_{0.968}Fe_{0.052}$ are shown. Also temperature dependent (e) ΔS_{mag} and (f) ΔT_{ad} observed in previous numerical simulation results [171] have been compared.

a good agreement with the existing result [171, 329] (shown in Fig. A.10(e)). The value of our calculated adiabatic temeprature change also (ΔT_{ad}) matches well with the previous result (Fig. A.10(d) and Fig. A.10(f)).

The results obtained by the in-house Monte Carlo code on a number of systems, benchmarked against available results in the literature, validate the implementation of the thermodynamic model, in conjunction with results from *ab initio* calculations, used in this thesis. The predictions made in this thesis based on simulations alone thus turn out to be robust and accurate.

Bibliography

[1] O. Gutfleisch, M. A. Willard, E. Brück, C. H. Chen, S. Sankar, and J. P. Liu, Adv. Mater. **23**, 821 (2011).

[2] O. Gutfleisch and V. Franco, Scr. Mater. **6**, 521 (2012).

[3] M. Sivak, American Scientist **101**, 330 (2013).

[4] X. Moya, S. Kar-Narayan, and N. D. Mathur, Nat. Mater. **13**, 439 (2014).

[5] A. Kitanovski, U. Plaznik, U. Tomc, and A. Poredoš, Int. J. Refrig **57**, 288 (2015).

[6] X. Moya, E. Defay, V. Heine, and N. D. Mathur, Nat. Phys. **11**, 202 (2015).

[7] L. Mañosa and A. Planes, Adv. Mater. **29**, 1603607 (2017).

[8] J. Tušek, K. Engelbrecht, R. Millán-Solsona, L. Mañosa, E. Vives, L. P. Mikkelsen, and N. Pryds, Adv. Energy Mater. **5**, 1500361 (2015).

[9] F. Bruederlin, L. Bumke, C. Chluba, H. Ossmer, E. Quandt, and M. Kohl, Energy Technology **6**, 1588 (2018).

[10] J. Tušek and A. Kitanovski, Magnetocaloric energy conversion: From theory to applications, 2015.

[11] V. Franco, J. Blázquez, J. Ipus, J. Law, L. Moreno-Ramírez, and A. Conde, Prog. Mater Sci. **93**, 112 (2018).

[12] T. Gottschall et al., Adv. Energy Mater. **9**, 1970130 (2019).

[13] A. Kitanovski, Adv. Energy Mater. **10**, 1903741 (2020).

[14] M. Ožbolt, A. Kitanovski, J. Tušek, and A. Poredoš, Int. J. Refrig **40**, 174 (2014).

[15] J. Shi et al., Joule **3**, 1200 (2019).

[16] V. Nikiforov, Russian Physics Journal **50**, 913 (2007).

[17] A. M. Tishin and Y. I. Spichkin, *The magnetocaloric effect and its applications*, CRC Press, 2016.

[18] A. Kitanovski, J. Tušek, U. Tomc, U. Plaznik, M. Ozbolt, and A. Poredoš, *Magnetocaloric energy conversion*, Springer, 2016.

[19] V. Pecharsky, K. Gschneidner Jr, A. Pecharsky, and A. Tishin, Phys. Rev. B **64**, 144406 (2001).

[20] N. De Oliveira and P. Von Ranke, Phys. Rev. B **77**, 214439 (2008).

[21] J. Joule, The London, Edinburgh, and Dublin Philosophical Magazine and Journal of Science **23**, 347 (1843).

[22] P. Weiss and A. Piccard, (1917).

[23] P. Weiss and A. Piccard, Comptes Rendus **166**, 352 (1918).

[24] P. Debye, Annalen der Physik **386**, 1154 (1926).

[25] W. Giauque, J. Am. Chem. Soc. **49**, 1864 (1927).
[26] W. Giauque and D. MacDougall, Phys. Rev. **43**, 768 (1933).
[27] D. Coulomb, The iir and environmental challenges facing the refrigeration sector, in *Proceedings of IIR International Conference on Magnetic Refrigeration at Room Temperature*, pages 11–13, 2007.
[28] L. P. Oliva, Pace Envtl. L. Rev. **7**, 213 (1989).
[29] J. Banks, 2002 Report of the Methyl Bromide Technical Options Committee, UNEP (2002).
[30] T. Tegusi et al., *Novel materials for magnetic refrigeration*, Universiteit van Amsterdam [Host], 2003.
[31] N. Mezaal, K. Osintsev, and T. Zhirgalova, Review of magnetic refrigeration system as alternative to conventional refrigeration system, in *IOP Conference Series: Earth and Environmental Science*, volume 87, page 032024, IOP Publishing, 2017.
[32] C. Zimm, A. Jastrab, A. Sternberg, V. Pecharsky, K. Gschneidner, M. Osborne, and I. Anderson, Description and performance of a near-room temperature magnetic refrigerator, in *Adv. Cryog. Eng.*, pages 1759–1766, Springer, 1998.
[33] G. Brown, J. Appl. Phys. **47**, 3673 (1976).
[34] Premiere of cutting-edge cooling appliance at ces., https://www.basf.com/global/en/media/news-releases/2015/01/p-15-100.html., 2015.
[35] J. R. Gómez, R. F. Garcia, A. D. M. Catoira, and M. R. Gómez, Renewable Sustainable Energy Rev. **17**, 74 (2013).
[36] E. Zatsepnia, A. Tishin, P. Egolf, and D. Vuarnoz, Proceedings of the 3rd International Conference on Magnetic Refrigeration at Room Temperature (2009).
[37] A. Tishin and Y. Spichkin, Int. J. Refrig **37**, 223 (2014).
[38] M. Falk and R. Issels, Int. J. Hyperth. **17**, 1 (2001).
[39] Q. A. Pankhurst, J. Connolly, S. K. Jones, and J. Dobson, J. Phys. D: Appl. Phys. **36**, R167 (2003).
[40] P. Wust et al., The lancet oncology **3**, 487 (2002).
[41] P. R. Stauffer, T. C. Cetas, A. M. Fletcher, D. W. Deyoung, M. W. Dewhirst, J. R. Oleson, and R. B. Roemer, IEEE Trans. Biomed. Eng. , 76 (1984).
[42] S. Mornet, S. Vasseur, F. Grasset, and E. Duguet, J. Mater. Chem. **14**, 2161 (2004).
[43] A. M. Tishin, Patent WO **135270** (2006).
[44] M. R. Barati, C. Selomulya, K. G. Sandeman, and K. Suzuki, Appl. Phys. Lett. **105**, 162412 (2014).
[45] S. Pandey, A. Quetz, A. Aryal, I. Dubenko, D. Mazumdar, S. Stadler, and N. Ali, Int. J. Hyperth. **33**, 779 (2017).
[46] Y. Cao et al., J. Mater. Sci. , 1 (2020).
[47] V. Balanov, A. Kiseleva, E. Krivoshapkina, E. Kashtanov, R. Gimaev, V. Zverev, and P. Krivoshapkin, J. Sol-Gel Sci. Technol. , 1 (2020).
[48] O. Gutfleisch et al., Philosophical Transactions of the Royal Society A: Mathemat-

ical, Physical and Engineering Sciences **374**, 20150308 (2016).
[49] B. Yu, Q. Gao, B. Zhang, X. Meng, and Z. Chen, Int. J. Refrig **26**, 622 (2003).
[50] K. A. GschneidnerJr, V. Pecharsky, and A. Tsokol, Reports on progress in physics **68**, 1479 (2005).
[51] V. Pecharsky and K. Gschneidner Jr, J. Appl. Phys. **90**, 4614 (2001).
[52] T. Hashimoto, T. Kuzuhara, M. Sahashi, K. Inomata, A. Tomokiyo, and H. Yayama, J. Appl. Phys. **62**, 3873 (1987).
[53] A. Tishin, K. Gschneidner Jr, and V. Pecharsky, Phys. Rev. B **59**, 503 (1999).
[54] H. Takeya, V. Pecharsky, K. Gschneidner Jr, and J. Moorman, Appl. Phys. Lett. **64**, 2739 (1994).
[55] C. Zimm, E. Ludeman, M. Severson, and T. Henning, Materials for regenerative magnetic cooling spanning 20k to 80k, in *Adv. Cryog. Eng.*, pages 883–890, Springer, 1992.
[56] A. Tomokiyo, H. Yayama, H. Wakabayashi, T. Kuzuhara, T. Hashimoto, M. Sahashi, and K. Inomata, Specific heat and entropy of rni 2 (r: Rare earth heavy metals) in magnetic field, in *Adv. Cryog. Eng. Materials*, pages 295–301, Springer, 1986.
[57] S. Benford, J. Appl. Phys. **50**, 1868 (1979).
[58] S. Y. Dan'kov, A. Tishin, V. Pecharsky, and K. Gschneidner Jr, Rev. Sci. Instrum. **68**, 2432 (1997).
[59] S. Benford and G. Brown, J. Appl. Phys. **52**, 2110 (1981).
[60] S. Y. Dan'Kov et al., Phys. Rev. B **57**, 3478 (1998).
[61] A. Tishin, Handbook of magnetic materials **12**, 395 (1999).
[62] A. Smaili and R. Chahine, J. Appl. Phys. **81**, 824 (1997).
[63] V. K. Pecharsky and K. A. Gschneidner Jr, Appl. Phys. Lett. **70**, 3299 (1997).
[64] V. K. Pecharsky and K. A. Gschneidner Jr, J. Magn. Magn. Mater. **200**, 44 (1999).
[65] V. K. Pecharsky and K. A. Gschneidner Jr, Phys. Rev. Lett. **78**, 4494 (1997).
[66] F. Hu, X. Qian, J. Sun, G. Wang, X. Zhang, Z. Cheng, and B. Shen, J. Appl. Phys. **92**, 3620 (2002).
[67] S. Fujieda, A. Fujita, and K. Fukamichi, Appl. Phys. Lett. **81**, 1276 (2002).
[68] F.-x. Hu, B.-g. Shen, J.-r. Sun, Z.-h. Cheng, G.-h. Rao, and X.-x. Zhang, Appl. Phys. Lett. **78**, 3675 (2001).
[69] H. Wada and Y. Tanabe, Appl. Phys. Lett. **79**, 3302 (2001).
[70] F. Guillou, H. Yibole, G. Porcari, L. Zhang, N. Van Dijk, and E. Brück, J. Appl. Phys. **116**, 063903 (2014).
[71] A. He, V. Svitlyk, and Y. Mozharivskyj, Inorg. Chem. **56**, 2827 (2017).
[72] M. Annaorazov, S. Nikitin, A. Tyurin, K. Asatryan, and A. K. Dovletov, J. Appl. Phys. **79**, 1689 (1996).
[73] C. M. Wayman, Macmillan Siries in Materials Science (1964).
[74] L. Chang and T. Read, JOM **3**, 47 (1951).
[75] W. J. Buehler, J. Gilfrich, and R. Wiley, J. Appl. Phys. **34**, 1475 (1963).
[76] T. Graf, C. Felser, and S. S. Parkin, Prog. Solid State Chem. **39**, 1 (2011).
[77] G. Liu, X. Dai, H. Liu, J. Chen, Y. Li, G. Xiao, and G. Wu, Phys. Rev. B **77**,

014424 (2008).
[78] H. C. Kandpal, G. H. Fecher, and C. Felser, J. Phys. D: Appl. Phys. **40**, 1507 (2007).
[79] Y. Feng et al., Phys. Rev. B **63**, 165109 (2001).
[80] T. Burch, T. Litrenta, and J. Budnick, Phys. Rev. Lett. **33**, 421 (1974).
[81] A. Planes, L. Mañosa, and M. Acet, J. Phys.: Condens. Matter **21**, 233201 (2009).
[82] K. Ullakko, J. Huang, C. Kantner, R. O'handley, and V. Kokorin, Appl. Phys. Lett. **69**, 1966 (1996).
[83] S. J. Murray, M. Marioni, S. Allen, R. O'handley, and T. A. Lograsso, Appl. Phys. Lett. **77**, 886 (2000).
[84] A. Sozinov, A. Likhachev, N. Lanska, and K. Ullakko, Appl. Phys. Lett. **80**, 1746 (2002).
[85] M. Chmielus, X. Zhang, C. Witherspoon, D. Dunand, and P. Müllner, Nat. Mater. **8**, 863 (2009).
[86] J. Marcos, A. Planes, L. Mañosa, F. Casanova, X. Batlle, A. Labarta, and B. Martínez, Phys. Rev. B **66**, 224413 (2002).
[87] F.-x. Hu, B.-g. Shen, J.-r. Sun, and G.-h. Wu, Phys. Rev. B **64**, 132412 (2001).
[88] T. Krenke et al., Phys. Rev. B **75**, 104414 (2007).
[89] M. Pasquale, C. P. Sasso, L. H. Lewis, L. Giudici, T. Lograsso, and D. Schlagel, Phys. Rev. B **72**, 094435 (2005).
[90] C. Biswas, R. Rawat, and S. Barman, Appl. Phys. Lett. **86**, 202508 (2005).
[91] V. Sharma, M. Chattopadhyay, K. Shaeb, A. Chouhan, and S. Roy, Appl. Phys. Lett. **89**, 222509 (2006).
[92] R. Kainuma et al., Nature **439**, 957 (2006).
[93] R. Kainuma et al., Appl. Phys. Lett. **88**, 192513 (2006).
[94] V. Khovaylo, K. Skokov, O. Gutfleisch, H. Miki, R. Kainuma, and T. Kanomata, Appl. Phys. Lett. **97**, 052503 (2010).
[95] Z. Li, C. Jing, J. Chen, S. Yuan, S. Cao, and J. Zhang, Appl. Phys. Lett. **91**, 112505 (2007).
[96] M. Khan, I. Dubenko, S. Stadler, and N. Ali, Appl. Phys. Lett. **91**, 072510 (2007).
[97] F.-x. Hu, B.-g. Shen, and J.-r. Sun, Appl. Phys. Lett. **76**, 3460 (2000).
[98] P. O. Castillo-Villa et al., Phys. Rev. B **83**, 174109 (2011).
[99] V. Srivastava, Y. Song, K. Bhatti, and R. D. James, Adv. Energy Mater. **1**, 97 (2011).
[100] J. Marcos, L. Mañosa, A. Planes, F. Casanova, X. Batlle, and A. Labarta, Phys. Rev. B **68**, 094401 (2003).
[101] L. Pareti, M. Solzi, F. Albertini, and A. Paoluzi, The European Physical Journal B-Condensed Matter and Complex Systems **32**, 303 (2003).
[102] A. Aliev et al., J. Magn. Magn. Mater. **272**, 2040 (2004).
[103] F. Albertini et al., J. Magn. Magn. Mater. **272**, 2111 (2004).
[104] A. Cherechukin, T. Takagi, M. Matsumoto, and V. Buchel'Nikov, Physics Letters A **326**, 146 (2004).
[105] J. Duan et al., J. Magn. Magn. Mater. **309**, 96 (2007).

[106] A. K. Pathak, I. Dubenko, H. E. Karaca, S. Stadler, and N. Ali, Appl. Phys. Lett. **97**, 062505 (2010).
[107] A. Brzoza, A. Wierzbicka-Miernik, T. Czeppe, E. Cesari, and M. Szczerba, Intermetallics **109**, 157 (2019).
[108] V. Buchelnikov et al., J. Phys. D: Appl. Phys. **44**, 064012 (2011).
[109] V. Sokolovskiy, A. Grünebohm, V. Buchelnikov, and P. Entel, Entropy **16**, 4992 (2014).
[110] D. Comtesse et al., Phys. Rev. B **89**, 184403 (2014).
[111] V. Buchelnikov et al., Phys. Rev. B **81**, 094411 (2010).
[112] F. Albertini et al., Reverse magnetostructural transitions by co and in doping nimnga alloys: Structural, magnetic, and magnetoelastic properties, in *Materials Science Forum*, volume 684, pages 151–163, Trans Tech Publ, 2011.
[113] N. V. Rama Rao, R. Gopalan, V. Chandrasekaran, and K. G. Suresh, Applied Physics A **99**, 265 (2010).
[114] F. Liu, Q. Wang, W. Ao, Y. Yu, L. Pan, and J. Li, J. Magn. Magn. Mater. **324**, 514 (2012).
[115] J. Ren, H. Li, S. Feng, Q. Zhai, J. Fu, Z. Luo, and H. Zheng, Intermetallics **65**, 10 (2015).
[116] A. K. Pathak, I. Dubenko, S. Stadler, and N. Ali, J. Phys. D: Appl. Phys. **41**, 202004 (2008).
[117] V. Sharma, M. Chattopadhyay, S. Nath, K. Sokhey, R. Kumar, P. Tiwari, and S. Roy, J. Phys.: Condens. Matter **22**, 486007 (2010).
[118] V. Sharma, M. Chattopadhyay, and S. Roy, J. Phys. D: Appl. Phys. **43**, 225001 (2010).
[119] D. Bourgault, J. Tillier, P. Courtois, D. Maillard, and X. Chaud, Appl. Phys. Lett. **96**, 132501 (2010).
[120] V. Sokolovskiy, V. Buchelnikov, S. Taskaev, V. Khovaylo, M. Ogura, and P. Entel, J. Phys. D: Appl. Phys. **46**, 305003 (2013).
[121] V. Sokolovskiy, V. Buchelnikov, V. Khovaylo, S. Taskaev, and P. Entel, Int. J. Refrig **37**, 273 (2014).
[122] V. Sokolovskiy, V. Buchelnikov, and P. Entel, Journal of Experimental and Theoretical Physics **115**, 662 (2012).
[123] T. Krenke, E. Duman, M. Acet, E. F. Wassermann, X. Moya, L. Mañosa, and A. Planes, Nat. Mater. **4**, 450 (2005).
[124] F. Liu, Q. Wang, S. Li, W. Ao, and J. Li, Physica B Condens. Matter **412**, 74 (2013).
[125] D. Zhao et al., Intermetallics **70**, 68 (2016).
[126] X. Zhang, H. Zhang, M. Qian, and L. Geng, Sci. Rep. **8**, 1 (2018).
[127] S. E. Muthu, S. Singh, R. Thiyagarajan, G. K. Selvan, N. R. Rao, M. M. Raja, and S. Arumugam, J. Phys. D: Appl. Phys. **46**, 205001 (2013).
[128] M. N. Inallu, P. Kameli, A. G. Varzaneh, I. A. Sarsari, D. Salazar, I. Orue, and

V. Chernenko, J. Phys. D: Appl. Phys. **52**, 235001 (2019).
[129] A. Grünebohm, D. Comtesse, A. Hucht, M. E. Gruner, A. Maslovskaya, and P. Entel, IEEE Trans. Magn. **50**, 1 (2014).
[130] N. Duc, T. Thanh, N. Yen, P. Thanh, N. Dan, and T. Phan, J. Korean Phys. Soc. **60**, 454 (2012).
[131] J. Du, Q. Zheng, W. Ren, W. Feng, X. Liu, and Z. Zhang, J. Phys. D: Appl. Phys. **40**, 5523 (2007).
[132] M. Khan, N. Ali, and S. Stadler, J. Appl. Phys. **101**, 053919 (2007).
[133] W. Feng, J. Du, B. Li, W. Hu, Z. Zhang, X. Li, and Y. Deng, J. Phys. D: Appl. Phys. **42**, 125003 (2009).
[134] Z. Han, D. Wang, C. Zhang, H. Xuan, J. Zhang, B. Gu, and Y. Du, J. Appl. Phys. **104**, 053906 (2008).
[135] A. K. Nayak, K. Suresh, and A. Nigam, J. Phys. D: Appl. Phys. **42**, 035009 (2009).
[136] R. Sahoo, A. K. Nayak, K. G. Suresh, A. K. Nigam, R. Mittal, A. K. Chauhan, and R. Mukhopadhyay, AIP Conference Proceedings **1447**, 1225 (2012).
[137] R. Sahoo, A. K. Nayak, K. Suresh, and A. Nigam, J. Appl. Phys. **109**, 07A921 (2011).
[138] R. Zhang et al., J. Magn. Magn. Mater. **428**, 464 (2017).
[139] N. Nong et al., Mater. Sci. Eng.,B **176**, 1322 (2011).
[140] R. Sahoo, A. K. Nayak, K. Suresh, and A. Nigam, J. Appl. Phys. **109**, 123904 (2011).
[141] M. Khan et al., Appl. Phys. Lett. **102**, 112402 (2013).
[142] A. K. Nayak, K. Suresh, and A. Nigam, J. Phys. D: Appl. Phys. **42**, 115004 (2009).
[143] M. Zelenỳ, A. Sozinov, L. Straka, T. Björkman, and R. M. Nieminen, Phys. Rev. B **89**, 184103 (2014).
[144] V. V. Sokolovskiy, P. Entel, V. Buchelnikov, and M. Gruner, Phys. Rev. B **91**, 220409 (2015).
[145] A. Perez-Checa, J. Feuchtwanger, J. Barandiaran, A. Sozinov, K. Ullakko, and V. Chernenko, Scr. Mater. **154**, 131 (2018).
[146] W. J. Feng, J. Du, B. Li, W. J. Hu, Z. D. Zhang, X. H. Li, and Y. F. Deng, J. Phys. D: Appl. Phys. **42**, 125003 (2009).
[147] P. Hohenberg and W. Kohn, Phys. Rev. **136**, B864 (1964).
[148] W. Kohn and L. J. Sham, Phys. Rev. **140**, A1133 (1965).
[149] R. M. Martin and R. M. Martin, *Electronic structure: basic theory and practical methods*, Cambridge university press, 2004.
[150] J. Korringa, Physica **13**, 392 (1947).
[151] W. Kohn and N. Rostoker, Phys. Rev. **94**, 1111 (1954).
[152] D. J. Singh and L. Nordstrom, *Planewaves, Pseudopotentials, and the LAPW method*, Springer Science & Business Media, 2006.
[153] P. Blaha, K. Schwarz, P. Sorantin, and S. Trickey, Comput. Phys. Commun. **59**, 399 (1990).

[154] J. C. Slater, Phys. Rev. **51**, 846 (1937).
[155] J. Slater, Adv. Quantum Chem. **1**, 35 (1964).
[156] J. Kubler, K.-H. Hock, J. Sticht, and A. Williams, J. Phys. F: Met. Phys. **18**, 469 (1988).
[157] L. Sandratskii, Adv. Phys. **47**, 91 (1998).
[158] L. Nordström and D. J. Singh, Phys. Rev. Lett. **76**, 4420 (1996).
[159] D. Hobbs, G. Kresse, and J. Hafner, Phys. Rev. B **62**, 11556 (2000).
[160] S. Y. Savrasov, Phys. Rev. B **54**, 16470 (1996).
[161] S. Baroni, S. De Gironcoli, A. Dal Corso, and P. Giannozzi, Rev. Mod. Phys. **73**, 515 (2001).
[162] I. Turek, V. Drchal, J. Kudrnovskỳ, M. Sob, and P. Weinberger, *Electronic structure of disordered alloys, surfaces and interfaces*, Springer Science & Business Media, 2013.
[163] R. McCormack and D. De Fontaine, Phys. Rev. B **54**, 9746 (1996).
[164] J. Amaral, N. Silva, and V. Amaral, Appl. Phys. Lett. **91**, 172503 (2007).
[165] P. Álvarez, P. Gorria, and J. Blanco, Phys. Rev. B **84**, 024412 (2011).
[166] K. SzaŁowski, T. Balcerzak, and A. Bobák, J. Magn. Magn. Mater. **323**, 2095 (2011).
[167] C. Triguero, M. Porta, and A. Planes, Phys. Rev. B **73**, 054401 (2006).
[168] E. Nobrega, N. de Oliveira, P. Von Ranke, and A. Troper, J. Phys.: Condens. Matter **18**, 1275 (2006).
[169] V. D. Buchelnikov, V. Sokolovskiy, S. Taskaev, and P. Entel, Theoretical modeling of magnetocaloric effect in heusler ni-mn-in alloy by monte carlo study, in *Materials Science Forum*, volume 635, pages 137–142, Trans Tech Publ, 2010.
[170] E. Nóbrega, N. de Oliveira, P. von Ranke, and A. Troper, Phys. Rev. B **72**, 134426 (2005).
[171] N. Singh and R. Arróyave, J. Appl. Phys. **113**, 183904 (2013).
[172] V. Sokolovskiy et al., J. Appl. Phys. **114**, 183913 (2013).
[173] M. Blume, V. Emery, and R. B. Griffiths, Phys. Rev. A **4**, 1071 (1971).
[174] E. Vives, T. Castán, and P.-A. Lindgård, Phys. Rev. B **53**, 8915 (1996).
[175] P. Meyer, School of Mathematics and Computing, University of Derby (2000).
[176] N. Singh, E. Dogan, I. Karaman, and R. Arróyave, Phys. Rev. B **84**, 184201 (2011).
[177] P. E. Blöchl, Phys. Rev. B **50**, 17953 (1994).
[178] G. Kresse and D. Joubert, Phys. Rev. B **59**, 1758 (1999).
[179] G. Kresse and J. Furthmüller, Phys. Rev. B **54**, 11169 (1996).
[180] H. Ebert et al., *The Munich SPR-KKR package, version 6.3*, University of Munich, Munich, Germany, 2012.
[181] E. Şaşıoğlu, L. Sandratskii, and P. Bruno, Phys. Rev. B **70**, 024427 (2004).
[182] D. P. Landau and K. Binder, *A guide to Monte Carlo simulations in statistical physics*, Cambridge university press, 2014.
[183] M. Born and R. Oppenheimer, Annalen der physik **389**, 457 (1927).
[184] D. R. Hartree, The wave mechanics of an atom with a non-coulomb central field. part

i. theory and methods, in *Mathematical Proceedings of the Cambridge Philosophical Society*, volume 24, pages 89–110, Cambridge University Press, 1928.
[185] V. Fock, Zeitschrift für Physik **61**, 126 (1930).
[186] L. H. Thomas, The calculation of atomic fields, in *Mathematical Proceedings of the Cambridge Philosophical Society*, volume 23, pages 542–548, Cambridge University Press, 1927.
[187] E. Fermi, Rend. Accad. Naz. Lincei **6**, 32 (1927).
[188] P. A. Dirac, Note on exchange phenomena in the thomas atom, in *Mathematical Proceedings of the Cambridge Philosophical Society*, volume 26, pages 376–385, Cambridge University Press, 1930.
[189] J. P. Perdew, P. Ziesche, and H. Eschrig, Electronic structure of solids' 91, 1991.
[190] J. P. Perdew, K. Burke, and M. Ernzerhof, Phys. Rev. Lett. **77**, 3865 (1996).
[191] J. P. Perdew and W. Yue, Phys. Rev. B **33**, 8800 (1986).
[192] A. Alkauskas, P. Deák, J. Neugebauer, A. Pasquarello, and C. G. Van de Walle, *Advanced Calculations for Defects in Materials: Electronic Structure Methods*, John Wiley & Sons, 2011.
[193] J. Kohanoff, *Electronic structure calculations for solids and molecules: theory and computational methods*, Cambridge University Press, 2006.
[194] J. Hubbard, Proceedings of the Royal Society of London. Series A. Mathematical and Physical Sciences **276**, 238 (1963).
[195] V. I. Anisimov, J. Zaanen, and O. K. Andersen, Phys. Rev. B **44**, 943 (1991).
[196] V. I. Anisimov, I. Solovyev, M. Korotin, M. Czyżyk, and G. Sawatzky, Phys. Rev. B **48**, 16929 (1993).
[197] R. Albers, N. E. Christensen, and A. Svane, J. Phys.: Condens. Matter **21**, 343201 (2009).
[198] V. I. Anisimov, F. Aryasetiawan, and A. Lichtenstein, J. Phys.: Condens. Matter **9**, 767 (1997).
[199] S. Hüfner and G. Wertheim, Phys. Rev. B **7**, 5086 (1973).
[200] S. Banik et al., J. Phys.: Condens. Matter **26**, 335502 (2014).
[201] I. Solovyev, P. Dederichs, and V. Anisimov, Phys. Rev. B **50**, 16861 (1994).
[202] T. Wehling, E. Şaşıoğlu, C. Friedrich, A. Lichtenstein, M. Katsnelson, and S. Blügel, Phys. Rev. Lett. **106**, 236805 (2011).
[203] B. Himmetoglu, R. M. Wentzcovitch, and M. Cococcioni, Phys. Rev. B **84**, 115108 (2011).
[204] F. Nilsson, R. Sakuma, and F. Aryasetiawan, Phys. Rev. B **88**, 125123 (2013).
[205] N. Ashcroft and N. Mermin, Google Scholar , 404 (1976).
[206] D. Vanderbilt, Phys. Rev. B **41**, 7892 (1990).
[207] K. Laasonen, R. Car, C. Lee, and D. Vanderbilt, Phys. Rev. B **43**, 6796 (1991).
[208] K. Laasonen, A. Pasquarello, R. Car, C. Lee, and D. Vanderbilt, Phys. Rev. B **47**, 10142 (1993).
[209] G. Kresse and J. Hafner, Phys. Rev. B **47**, 558 (1993).

[210] G. Kresse and J. Hafner, Phys. Rev. B **49**, 14251 (1994).
[211] S. Cottenier et al., Instituut voor Kern-en Stralingsfysica, KU Leuven, Belgium **4**, 41 (2002).
[212] G. Kresse et al., *Vienna ab-initio simulation package (VASP)*, Vienna University, Vienna, Austria, 2001.
[213] P. Soven, Phys. Rev. **156**, 809 (1967).
[214] D. Taylor, Phys. Rev. **156**, 1017 (1967).
[215] B. Gyorffy, Phys. Rev. B **5**, 2382 (1972).
[216] L. Vitos, *Computational quantum mechanics for materials engineers: the EMTO method and applications*, Springer Science & Business Media, 2007.
[217] F. Murnaghan, Proc. Natl. Acad. Sci. USA **30**, 244 (1944).
[218] G. Grimvall, *Thermophysical properties of materials*, Elsevier, 1999.
[219] W. Voigt, Ann. Phys. Chem **274**, 573 (1889).
[220] A. Reuss, Z. Angew. Math. Mech. **9**, 49 (1929).
[221] R. Hill, Proceedings of the Physical Society. Section A **65**, 349 (1952).
[222] R. Hill, J. Mech. Phys. Solids **11**, 357 (1963).
[223] V. Sokolovskiy, V. Buchelnikov, M. Zagrebin, P. Entel, S. Sahoo, and M. Ogura, Phys. Rev. B **86**, 134418 (2012).
[224] T. Roy, D. Pandey, and A. Chakrabarti, Phys. Rev. B **93**, 184102 (2016).
[225] S. Pugh, The London, Edinburgh, and Dublin Philosophical Magazine and Journal of Science **45**, 823 (1954).
[226] T. Roy, M. E. Gruner, P. Entel, and A. Chakrabarti, J. Alloys. Compd. **632**, 822 (2015).
[227] S. O. Kart and T. Cagın, J. Alloys. Compd. **508**, 177 (2010).
[228] D. Pettifor, Mater. Sci. Technol. **8**, 345 (1992).
[229] A. Kundu, S. Ghosh, and S. Ghosh, Phys. Rev. B **96**, 174107 (2017).
[230] H. Ebert, D. Koedderitzsch, and J. Minar, Reports on Progress in Physics **74**, 096501 (2011).
[231] A. I. Liechtenstein, M. Katsnelson, V. Antropov, and V. Gubanov, J. Magn. Magn. Mater. **67**, 65 (1987).
[232] M. Methfessel and J. Kubler, J. Phys. F: Met. Phys. **12**, 141 (1982).
[233] K. Binder, D. Heermann, L. Roelofs, A. J. Mallinckrodt, and S. McKay, Comput. Phys. **7**, 156 (1993).
[234] N. Metropolis, A. W. Rosenbluth, M. N. Rosenbluth, A. H. Teller, and E. Teller, J. Chem. Phys. **21**, 1087 (1953).
[235] E. Şaşıoğlu, L. Sandratskii, P. Bruno, and I. Galanakis, Phys. Rev. B **72**, 184415 (2005).
[236] M. Zagrebin, V. Sokolovskiy, and V. Buchelnikov, J. Phys. D: Appl. Phys. **49**, 355004 (2016).
[237] M. Newman and G. Barkema, *Monte carlo methods in statistical physics chapter 1-4*, Oxford University Press: New York, USA, 1999.
[238] K. Koyama et al., Appl. Phys. Lett. **89**, 182510 (2006).

[239] S. Yu et al., Appl. Phys. Lett. **89**, 162503 (2006).
[240] M. K. Ray, B. Maji, M. Modak, and S. Banerjee, J. Magn. Magn. Mater. **429**, 110 (2017).
[241] Z. Han, D. Wang, C. Zhang, H. Xuan, B. Gu, and Y. Du, Appl. Phys. Lett. **90**, 042507 (2007).
[242] S. Aksoy et al., Philos. Mag. **89**, 2093 (2009).
[243] M. Khan, I. Dubenko, S. Stadler, and N. Ali, J. Phys.: Condens. Matter **20**, 235204 (2008).
[244] Q.-M. Hu, C.-M. Li, R. Yang, S. E. Kulkova, D. I. Bazhanov, B. Johansson, and L. Vitos, Phys. Rev. B **79**, 144112 (2009).
[245] C.-M. Li, H.-B. Luo, Q.-M. Hu, R. Yang, B. Johansson, and L. Vitos, Phys. Rev. B **86**, 214205 (2012).
[246] A. Kundu and S. Ghosh, J. Phys.: Condens. Matter **30**, 015401 (2017).
[247] N. Lanska, O. Söderberg, A. Sozinov, Y. Ge, K. Ullakko, and V. Lindroos, J. Appl. Phys. **95**, 8074 (2004).
[248] A. Zayak, W. Adeagbo, P. Entel, and K. Rabe, Appl. Phys. Lett. **88**, 111903 (2006).
[249] T. Mehaddene, J. Neuhaus, W. Petry, K. Hradil, P. Bourges, and A. Hiess, Phys. Rev. B **78**, 104110 (2008).
[250] Y. Xin, Y. Li, C. B. Jiang, and H. B. Xu, Martensitic transformations of ni54mn25ga21-xalx shape memory alloys, in *Materials Science Forum*, volume 475, pages 1991–1994, Trans Tech Publ, 2005.
[251] V. Kokorin and I. Osipenko, Phys. Met. Metallogr.(USSR) **67**, 173 (1989).
[252] C. Seguí, J. Pons, and E. Cesari, Acta Mater. **55**, 1649 (2007).
[253] V. Sánchez-Alarcos, V. Recarte, J. Pérez-Landazábal, and G. Cuello, Acta Mater. **55**, 3883 (2007).
[254] M. Khan et al., Appl. Phys. Lett. **100**, 172403 (2012).
[255] X. Ren and K. Otsuka, Why does the martensitic transformation temperature strongly depend on composition, in *Materials science forum*, volume 327, pages 429–432, 2000.
[256] X. Ren, K. Otsuka, and T. Suzuki, J. Alloys. Compd. **355**, 196 (2003).
[257] M. Stipcich, L. Mañosa, A. Planes, M. Morin, J. Zarestky, T. Lograsso, and C. Stassis, Phys. Rev. B **70**, 054115 (2004).
[258] A. Chakrabarti, C. Biswas, S. Banik, R. Dhaka, A. Shukla, and S. Barman, Phys. Rev. B **72**, 073103 (2005).
[259] J. Chen, Y. Li, J. Shang, and H. Xu, Appl. Phys. Lett. **89**, 231921 (2006).
[260] V. D. Buchelnikov, V. V. Sokolovskiy, M. A. Zagrebin, M. A. Tufatullina, and P. Entel, J. Phys. D: Appl. Phys. **48**, 164005 (2015).
[261] N. Rama Rao et al., J. Appl. Phys. **109**, 07A907 (2011).
[262] G. Grimvall, Phys. Scr. **13**, 59 (1976).
[263] B. Johansson and P. Söderlind, Thermochim. Acta **218**, 145 (1993).
[264] B. L. Gyorffy, A. J. Pindor, J. Staunton, G. M. Stocks, and H. Winter, J. Phys. F:

Met. Phys. **13**, 979 (1983).
[265] G. Grimvall, Phys. Rev. B **39**, 12300 (1993).
[266] Y. Yang et al., Scr. Mater. **116**, 31 (2016).
[267] W. He, H. Huang, Z. Liu, and X. Ma, Intermetallics **90**, 140 (2017).
[268] Y. Ma, H. Hao, X. Liu, H. Luo, F. Meng, and H. Liu, Intermetallics (2017).
[269] A. Ghosh and K. Mandal, Appl. Phys. Lett. **104**, 031905 (2014).
[270] C.-M. Li, H.-B. Luo, Q.-M. Hu, R. Yang, B. Johansson, and L. Vitos, Phys. Rev. B **82**, 024201 (2010).
[271] H.-B. Luo, C.-M. Li, Q.-M. Hu, R. Yang, B. Johansson, and L. Vitos, Acta Mater. **59**, 971 (2011).
[272] O. Nittono and Y. Koyama, Jpn. J. Appl. Phys. **21**, 680 (1982).
[273] B. Gao, J. Shen, F. Hu, J. Wang, J. Sun, and B. Shen, Applied Physics A **97**, 443 (2009).
[274] J.-M. Lee, Y.-M. Oh, K. Euh, and S.-B. Kang, Met. Mater. Int. **15**, 459 (2009).
[275] M. Khan, I. Dubenko, S. Stadler, and N. Ali, J. Appl. Phys. **97**, 10M304 (2005).
[276] D. Soto-Parra et al., Philos. Mag. **90**, 2771 (2010).
[277] A. K. Pathak, I. Dubenko, C. Pueblo, S. Stadler, and N. Ali, J. Appl. Phys. **107**, 09A907 (2010).
[278] A. Gomes, M. Khan, S. Stadler, N. Ali, I. Dubenko, A. Takeuchi, and A. Guimarães, J. Appl. Phys. **99**, 08Q106 (2006).
[279] S. Stadler et al., Appl. Phys. Lett. **88**, 192511 (2006).
[280] D. Soto et al., Phys. Rev. B **77**, 184103 (2008).
[281] A. Cherechukin et al., Physics Letters A **291**, 175 (2001).
[282] H. Wang, F. Chen, Z. Gao, W. Cai, and L. Zhao, Mater. Sci. Eng.,A **438**, 990 (2006).
[283] C. Jing, Z. Li, H. Zhang, J. Chen, Y. Qiao, S. Cao, and J. Zhang, The European Physical Journal B **67**, 193 (2009).
[284] T. Krenke, E. Duman, M. Acet, X. Moya, L. Mañosa, and A. Planes, J. Appl. Phys. **102**, 033903 (2007).
[285] B. Gao, F. Hu, J. Shen, J. Wang, J. Sun, and B. Shen, J. Magn. Magn. Mater. **321**, 2571 (2009).
[286] M. Meinert, J.-M. Schmalhorst, and G. Reiss, J. Phys.: Condens. Matter **23**, 036001 (2010).
[287] C.-M. Li, H.-B. Luo, Q.-M. Hu, R. Yang, B. Johansson, and L. Vitos, Phys. Rev. B **84**, 024206 (2011).
[288] A. Chakrabarti, M. Siewert, T. Roy, K. Mondal, A. Banerjee, M. E. Gruner, and P. Entel, Phys. Rev. B **88**, 174116 (2013).
[289] R. Sahoo, K. Suresh, and A. Das, J. Magn. Magn. Mater. **371**, 94 (2014).
[290] A. Vasiliev et al., J. Phys. D: Appl. Phys. **43**, 055004 (2010).
[291] Z. Han, D. Wang, B. Qian, J. Feng, X. Jiang, and Y. Du, Jpn. J. Appl. Phys. **49**, 010211 (2010).
[292] J. Pérez-Landazábal, V. Recarte, V. Sánchez-Alarcos, C. Gómez-Polo, and E. Cesari,

Appl. Phys. Lett. **102**, 101908 (2013).
[293] A. K. Nayak, K. Suresh, and A. Nigam, J. Appl. Phys. **107**, 09A927 (2010).
[294] W. Feng, L. Zuo, Y. Li, Y. Wang, M. Gao, and G. Fang, Mater. Sci. Eng.,B **176**, 621 (2011).
[295] V. Buchelnikov et al., Phys. Rev. B **78**, 184427 (2008).
[296] X. Moya, L. Mañosa, A. Planes, S. Aksoy, M. Acet, E. F. Wassermann, and T. Krenke, Phys. Rev. B **75**, 184412 (2007).
[297] A. Vasil'ev et al., Phys. Rev. B **59**, 1113 (1999).
[298] Z. Liu et al., J. Appl. Phys. **92**, 5006 (2002).
[299] C.-M. Li, Q.-M. Hu, R. Yang, B. Johansson, and L. Vitos, Appl. Phys. Lett. **98**, 261903 (2011).
[300] M. Siewert et al., Advanced Engineering Materials **14**, 530 (2012).
[301] X. Chen, F. Yang, X. Lu, and Z. Qin, Phys. Status Solidi (b) **244**, 1047 (2007).
[302] V. Sokolovskiy, M. Zagrebin, and V. Buchelnikov, J. Phys. D: Appl. Phys. **50**, 195001 (2017).
[303] S. Banik et al., Phys. Rev. B **75**, 104107 (2007).
[304] I. P. Ezekiel and T. Moyo, AIP Advances **8**, 075120 (2018).
[305] J. Du, Q. Zheng, W. J. Ren, W. J. Feng, X. G. Liu, and Z. D. Zhang, J. Phys. D: Appl. Phys. **40**, 5523 (2007).
[306] A. K. Pathak, M. Khan, I. Dubenko, S. Stadler, and N. Ali, Appl. Phys. Lett. **90**, 262504 (2007).
[307] S. E. Muthu, N. R. Rao, M. M. Raja, D. R. Kumar, D. M. Radheep, and S. Arumugam, J. Phys. D: Appl. Phys. **43**, 425002 (2010).
[308] S. Singh et al., Adv. Mater. **28**, 3321 (2016).
[309] S. Ghosh, A. Ghosh, and K. Mandal, J. Alloys. Compd. **746**, 200 (2018).
[310] G. Cavazzini et al., Scr. Mater. **170**, 48 (2019).
[311] M. Meinert, J.-M. Schmalhorst, and G. Reiss, J. Phys.: Condens. Matter **23**, 116005 (2011).
[312] V. K. Pecharsky and K. A. Gschneidner Jr, Adv. Mater. **13**, 683 (2001).
[313] A. De Campos et al., Nat. Mater. **5**, 802 (2006).
[314] O. Tegus, E. Brück, and L. Zhang, Physica B **319**, 174 (2002).
[315] Z. Li, J. L. Sánchez Llamazares, C. F. Sánchez-Valdés, Y. Zhang, C. Esling, X. Zhao, and L. Zuo, Appl. Phys. Lett. **100**, 174102 (2012).
[316] Z. Li, Y. Zhang, C. F. Sánchez-Valdés, J. L. Sánchez Llamazares, C. Esling, X. Zhao, and L. Zuo, Appl. Phys. Lett. **104**, 044101 (2014).
[317] T. Krenke, M. Acet, E. F. Wassermann, X. Moya, L. Mañosa, and A. Planes, Phys. Rev. B **72**, 014412 (2005).
[318] S. Ghosh and S. Ghosh, Phys. Rev. B **99**, 064112 (2019).
[319] S. Ghosh and S. Ghosh, Phys. Rev. B **101**, 024109 (2020).
[320] S. Podgornykh, S. Streltsov, V. Kazantsev, and E. Shreder, J. Magn. Magn. Mater. **311**, 530 (2007).
[321] P. Webster, K. Ziebeck, S. Town, and M. Peak, Philos. Mag. B **49**, 295 (1984).

[322] G. Liu, J. Chen, Z. Liu, X. Dai, G. Wu, B. Zhang, and X. Zhang, Appl. Phys. Lett. **87**, 262504 (2005).
[323] G. Liu et al., Phys. Rev. B **74**, 054435 (2006).
[324] T. Kanomata et al., Magnetic and crystallographic properties of shape memory alloys ni2mn1+ xsn1-x, in *Materials Science Forum*, volume 583, pages 119–129, Trans Tech Publ, 2008.
[325] L. Ma et al., Phys. Rev. B **84**, 224404 (2011).
[326] K. Minakuchi, R. Umetsu, K. Kobayashi, M. Nagasako, and R. Kainuma, J. Alloys Compd. **645**, 577 (2015).
[327] H. Luo et al., J. Appl. Phys. **107**, 013905 (2010).
[328] V. Alijani, J. Winterlik, G. H. Fecher, S. S. Naghavi, and C. Felser, Phys. Rev. B **83**, 184428 (2011).
[329] D. Soto-Parra et al., Appl. Phys. Lett. **96**, 071912 (2010).

List of Publications

1. Ashis Kundu, **Sheuly Ghosh**, Subhradip Ghosh. *Effect of Fe and Co substitution on the martensitic stability and the elastic, electronic, and magnetic properties of Mn_2NiGa: Insights from ab initio calculations.* Physical Review B **96**, 174107 (2017)

2. **Sheuly Ghosh**, Subhradip Ghosh. *Role of composition, site ordering, and magnetic structure for the structural stability of off-stoichiometric Ni_2MnSb alloys with excess Ni and Mn.* Physical Review B **99**, 064112 (2019)*

3. **Sheuly Ghosh**, Subhradip Ghosh. *Understanding the origin of the magnetocaloric effects in substitutional Ni-Mn-Sb-Z(Z=Fe, Co, Cu)compounds: Insights from first-principles calculations.* Physical Review B **101**, 024109 (2020)*

4. **Sheuly Ghosh**, Subhradip Ghosh. *Cosubstitution in Ni-Mn-Sb Heusler compounds: Realization of room-temperature reversible magnetocaloric effect driven by second-order magnetic transition.* Physical Review Materials **4**, 025401 (2020)*

5. **Sheuly Ghosh**, Subhradip Ghosh. *Giant magnetocaloric effect driven by first-order magneto-structural transition in cosubstituted Ni-Mn-Sb Heusler compounds: predictions from Ab initio and Monte Carlo calculations.* Accepted in Physical Review B (arXiv:2008.13479)*

6. **Sheuly Ghosh**, Subhradip Ghosh. *Understanding the discrepancy between DFT and experimental results regarding low temperature structural phases in Mn_2NiSn and Mn_2NiIn.* Manuscript under preparation

7. **Sheuly Ghosh**, Ashis Kundu, Subhradip Ghosh. *Effect of Pd substitution on structural and magnetic properties in Co_2MnSi.* Manuscript under preparation

Publications marked with * are included in the thesis

Schools/Workshops/Conferences attended

1. International School on *Fundamental Crystallography and workshop on Structural Phase transitions*, January 30-September 4 (2017), **Department of Physics and Astronomy, National Institute of Technology Rourkela**, Odisha, India.

2. Sorbonne-JNCASR School on *Advanced Computational Materials Science (SJSACMS-2018)*, February 29-February 2, (2018), **Thematic Unit of Excellence in Computational Materials Science, JNCASR**, Bengaluru, India.

3. International Workshop on *Evolution of Electronic Structure Theory and Experimental Realization (EESTER-2018)*, September 11-15, (2018), **SRM Institute of Science and Technology & Indian Institute of Technology Madras in Association with MRSI Computational Materials Science subject group**, Chennai, India.

4. International Conference on on *Current Trends in Functional Materials (CTFM-2020)*, January 15-17, (2020), **National Institute of Technology Karnataka (NITK)**, Surathkal, Mangalore, India.